PHD

Characterisation of thermal sprayed hydroxyapatite coatings for use as a biological attachment system for prosthetic devices

Brown, Steven R.

Award date:
1996

Awarding institution:
University of Bath

Characterisation of Thermal Sprayed Hydroxyapatite Coatings for use as a Biological Attachment System for Prosthetic Devices

Submitted by Steven R Brown for the degree of Doctor

of Philosophy of the University of Bath.

1996.

S. R. Brown.

ProQuest LLC
789 East Eisenhower Parkway
P.O. Box 1346
Ann Arbor, MI 48106-1346

Characterisation of Thermal Sprayed Hydroxyapatite Coatings for use as a Biological Attachment System for Prosthetic Devices.

Abstract.

Orthopaedic surgery has progressed at an amazing rate from the introduction of the cemented hip prostheses in the early 1960's by Sir John Charnley. This prostheses gives thousands of people each year the opportunity to walk again after being crippled by the painful disease osteoarthritis. The clinical results have shown that this prostheses and generic copies using PMMA cement have a 90% success rate over a 10 year period for patients over 60 years of age. For younger more active patients a revision operation may be required in as little as 3 years. The main cause of post-operative failure is aseptic loosening which has been attributed to a change in the mechanical properties of the PMMA cement. To increase the life span of a hip prostheses a new method of fixing the implant to the bone, known as cementless fixation, has been developed. One of the cementless fixation techniques utilises an hydroxyapatite coating on the surface of the implant. Hydroxyapatite is the mineral component of bone and therefore when implanted in the body does not invoke an immune reaction and has been shown to encourage bone growth.

This thesis will look at three thermal spraying processes which have been used to produce hydroxyapatite coatings. Two conventional processes Air & Vacuum Plasma Spraying and the novel process of High Velocity Oxy Fuel thermal spraying. The morphology and composition of these coatings has been determined using many standard and novel characterisation techniques. The three coating processes produced coatings with different compositions and morphologies. The effect of heat-treatment and *in vitro* ageing on the coatings has also been investigated. One can conclude from this work that by selecting an appropriate process, powder and spraying parameters an hydroxyapatite coating can be produced to a given specification.

Table of Contents.

1. Introduction.

Osteoarthritis is a crippling and painful disability which affects the mobility of joints in the body. The disease is associated with the elderly but can also affect young people. The Total Hip Replacement (THR) operation provides immense relief from pain and disability to around 40 000 patients each year in Britain alone [1]. With patients in the 65+ year age group there is a 90% success rate for a total hip replacement over a 10 year period but for those in the 16-24 year age group, who are generally more active than the elderly, it can be expected that a revision operation will have to be performed approximately three years after initial surgery [2]. The revision operation, for young or old patients, is a much more severe and complicated operation. With an increasingly ageing population, the demand for surgery to replace the hip joint will go on rising. Therefore improvements to increase the life span of hip replacement joints, especially in younger patients, would significantly reduce the number of revision operations required and free surgeons to undertake more primary surgery.

There are considerable stresses exerted on the hip joint and these need to be met by the artificial implant. The environment of the human body with a temperature of 37°C, pH 7.2, saline solutions and a host of other biological and chemical agents is extremely corrosive. Materials implanted in the body need to be biocompatible, corrosion resistant and withstand physiological forces such as fatigue and stress corrosion without failure [3].

Failure of the total hip replacement is not generally associated with stem fracture or cup wear, but with infection or, in the majority of cases, with stem or cup loosening. A well fixed component has a bone-cement interface which displays a thin interfacial membrane, termed as the 'quiescent' interfacial membrane (QIM). The QIM consists of bland and densely textured collagenous tissue, with fibres oriented parallel to the surface. Sharpey like fibres emerge at irregular intervals from the bone and combine with the collagenous fibres of the QIM, which anchor the implant in position. A loosened joint replacement exhibits a thick pathological or aggressive interfacial membrane. This membrane is known as the 'lytic' interfacial membrane (LIM) because mediatory substances increase the inflammatory cell reactions therein causing bone resorption. The LIM consists of a three layered structure an inner synovial-like layer, a middle inflammatory-granulomatous layer and an outer scarified layer. The formation of LIMs is a result of many contributing factors. The friction between articulating surfaces results in wear debris which migrates to the implant bone interface. Macrophages act to encapsulate the wear debris and stimulate osteoclasts, giving rise to bone resorption and, thus, to loss of osseointegration and stability. The loss of stability leads to macromotion and the increase in the production of wear debris and hence the increase of the rate at which the LIM is formed. The wear debris is commonly from the polyethylene acetabular cup and also to a lesser extent from the degradation of the

PMMA cement in cemented prostheses. Other factors which are known to contribute to loosening are the mismatch of stiffness between bone and the implant materials and misalignment of the prostheses during implantation. The heat of polymerisation for the PMMA cement can cause necrosis of hard and soft bony tissues, and the presence of monomeric methylmethacrylate as well as N,N-dimethyl-toluidine would be expected to result in a functionally adverse interfacial membrane. The combination of these problems and the degradation of the cement after prolonged periods has lead to the development of the cementless prostheses [4].

Uncemented fixation is concerned with the close contact of the bone to the implant surface. It is essentially dependent on bone being able to form around the implant and maintain the bond. This has led to the study of the interface between bone and either an inert porous surface which allows bony ingrowth or a bioactive coating such as hydroxyapatite which promotes bony ingrowth [5] .

The use of a bioactive coating is not confined to hip replacements; these coatings are used in other prostheses and dental implants [6]. Hydroxyapatite is used as a bone filler to bridge large breaks in bones and reconstructive surgery, research has also been carried out on impregnating hydroxyapatite with drugs to prevent infection and promote bone growth [7].

1.1 History of prosthetic devices.

Materials have been used as orthopaedic implants for many years. First attempts at a hip replacement were by Gluck in 1891, which involved gluing an ivory ball and socket to the bone. Modern hip replacement began in 1957, when Charnley designed his artificial hip joint consisting of a stainless-steel sphere articulating in a socket, or cup, made from PTFE. The stem and cup were fixed in position using an acrylic cement, which was a major break through in orthopaedic surgery. After initially good results he found that the PTFE cup was disintegrating due to the body environment accelerating wear. Charnley tested a wide range of materials using a machine he devised that would simulate the wear of the component over many years of use. He found that a high molecular weight polyethylene was best suited for use as the cup and developed the first acceptable prosthesis.

John Scales was also working on a total hip replacement at the same time as Charnley. His contribution to overcoming the wear and friction of an artificial hip joint was to give them a metal stem and a small ball in a polyethylene socket, a variation on Charnley's design. Using the acrylic cement the modified Charnley prosthesis is the mainstay of today's artificial hip replacements. [2]

1.2 Biomedical Materials

A definition of a biomaterial is given by D.F.Williams.[6]

"Biomaterials are those materials which come into intimate and sustained contact with tissues of the body, generally being implanted within the tissues. They may be distinguished from other materials in that they possess a combination of properties, including chemical, physical, and biological, that render them safe, effective and reliable for use within a physiological environment."

This definition gives a broad outline of the properties required of a material for it to be biocompatible. It covers all materials implanted in the body, for example hip and knee joints, total artificial heart, replacement of the lens in the eye, kidney machines and pacemakers. One of the oldest examples of the use of materials within the body is that of sutures, the thin fibres which hold tissue together after injury and during repair. Although occasionally a metal wire will be used for this purpose, it is polymers, either natural or synthetic, which dominate this field.

When it comes to the repair of bone the most commonly used materials are metals. The advantage of using metal is that it possesses adequate strength and rigidity for load bearing applications and also excellent fatigue properties. The metals which are commonly in use are austenitic stainless steels, cobalt chrome and titanium alloys [3]. These alloys show a high strength, corrosion resistance and fatigue life compared to other engineering alloys. Stainless steel alloys were used in the earliest implants and showed good results, although failures were reported due to stress corrosion cracking and metallosis of surrounding tissue. The cobalt chrome alloys are stiffer and more stable in the body than stainless steel. The disadvantages of cobalt chrome are its weight, being the heaviest of the three alloys, and the high stiffness causes a large disruption to the stress field in the bone. Bone has been shown to remodel to accommodate the change in stress distribution with greater bone losses proximally than distally [8]. The tissue reaction to cobalt chrome alloys is less severe than to stainless steel but the metal which has proven to be the most biocompatible is titanium. The titanium alloy which has become the standard alloy used in prosthetics is the Ti-6Al-4V, BS 3531. This alloy has excellent fatigue properties and was originally designed for use in the aerospace industries. The combination of a high strength to weight ratio and excellent biocompatibility has lead to this alloy being used for load bearing skeletal implants. The wear properties of the titanium alloy are poor compared to the cobalt chrome alloy and to overcome this problem ceramics or cobalt chrome alloy are often attached to the titanium at articulating joints. An example of this is a ceramic ball attached to a titanium hip stem to replace the femoral head. The ceramics used are alumina and yitria stabilised zirconia, which are very hard and exhibit good toughness.

Other materials which have been considered for skeletal replacement have been designed to match the stiffness of bone. An example of this is a composite of polyethylene filled with particles of the bioactive mineral hydroxyapatite, the idea is to get a material with a similar structure to bone that can be osseointegrated [3]. Another example is a carbon fibre composite structure with a similar modulus to bone, the problem with this material is that fragments of carbon fibre in the body trigger a macrophage reaction and rapidly form a LIM. This material functions well until fatigue or wear generates particulate debris.

1.2.1 Implant/Tissue Attachment.

The highest incidence of failure of hip and knee joint prostheses is found with the loosening phenomena and this is attributed to the difficulty of obtaining and retaining a close apposition between implant material and bone. The main problem is that the natural reaction of the body to a material in the bone is to encase the material in a soft fibrous tissue. While some may say this is beneficial as a resilient shock absorbing component, it is generally thought desirable to have direct apposition or attachment to the bone [5].

There have been two approaches to improving the bone/material interface. It has long been assumed that direct attachment to the synthetic, manufactured components of joint replacements is impossible under clinical conditions. This has led to the vast majority of prostheses being designed for use with a bone cement. The cement is used not as an adhesive but to fill the gap between the bone and the implant making a mechanical bond. The cement is typically a polymethyl methacrylate (PMMA) polymer. Although this gives quite satisfactory results this rather brittle polymer does eventually break down at the bone/polymer interface with resultant loosening of the implant. [3]

The other approach is towards uncemented fixation and three possibilities are being explored in this area. The first method involves the use of materials with extreme inertness in the body, producing a minimal stimulus to inflammation and subsequent generation of a QIM. For this reason titanium and its alloys have been the target of much interest. It has been shown that titanium produces good results because of its excellent corrosion resistance and the body's reaction to the metal is to encapsulate it in a thin fibrous layer similar to the QIM [10, 11].

The second approach is an extension of the chemical inertness principle by incorporating a porous surface to create a mechanical bond with the bone. If the porosity is the correct size and interconnecting the bone can grow into the voids and thus produce an anchorage. Porous surfaces have been created using several techniques including sintering and plasma spraying and although bone ingrowth has been reported into several metals, titanium and its alloys are reported to be the best option. There are concerns about the corrosion resistance of the highly increased surface area of the implant, the strength of the porous layer and it's attachment to the substrate, and the fate of the bone once it has grown into the porosity [5, 12, 13].

The third possibility moves away from metals and looks toward materials which play an active part in controlling the tissue response. These materials are generally known as 'bioactive' materials, which encourage the growth of bone at the interface rather than fibrous tissue. The main group of materials being the ceramics and glasses of calcium phosphate, with hydroxyapatite $Ca_{10}(PO_4)_6(OH)_2$ showing the best combination of bioactivity and *in vivo* stability [14, 15, 16]. Hydroxyapatite (HA) is essentially chemically equivalent to the mineral phase of the bone and may be prepared synthetically. Although too brittle to be used as a monolithic component the material can be deposited on the surface of an implant to form a coating using primarily plasma spraying, as well as other coating deposition techniques.

1.3 Hydroxyapatite.

Hydroxyapatite is used as a bone substitute for filling bone defects and as a coating for orthopaedic and dental implants. Commercial hydroxyapatites are prepared from the coral exoskeleton of the Porites Goniopora [17] or by synthesis [18, 19], which involves a reaction between ammonium solutions of compounds like ammonium phosphate and soluble calcium salts.

Monolithic components of hydroxyapatite have the characteristic properties of ceramic materials, a low tensile strength and low resistance against fatigue failure, making them unsuitable for orthopaedic applications. The application of a coating of bioactive hydroxyapatite to implants is attracting considerable interest, with emphasis on the use of plasma spraying to deposit the coating [20]. This combines the superior mechanical performance of the metal component with the excellent biological response to hydroxyapatite. Plasma sprayed hydroxyapatite coatings with their macroporous surface can also significantly improve bone ingrowth. The hydroxyapatite should also act as a biological barrier to reduce concerns over the toxic responses caused by the release of metallic ions from the metal substrate into the body. The strength of the hydroxyapatite coating on the metal substrate is at its optimum when the coating thickness is $< 100\mu$ m. The reason for a thin coating being more favourable than a thick coating is that residual stresses are higher in thicker coatings which tend to fracture at lower stresses when subjected to bending or shear forces [21, 22] . Since bone bonding to the prosthesis can be enhanced by an hydroxyapatite coating in the early stages after implantation, bonding at the coating/substrate interface becomes more crucial in the long term for stability of the implant. The stability can also be strongly influenced by both the nature of the surface and the presence of phases which can be dissolved and therefore influence cell behaviour [23, 24].

Much work has been done on the biocompatibility of several calcium phosphates using *in vivo* [25→39] and *in vitro* [40→49] testing. The results show that hydroxyapatite has been found to be totally biocompatible; it promotes bone growth and direct apposition to bone has been reported. The *in vivo* stability of bioactive materials has been investigated and the results show crystalline hydroxyapatite as the most stable bioactive material with these other bioactive materials, β-Tri Calcium Phosphate (β-TCP) > amorphous hydroxyapatite > α-Tri Calcium Phosphate (α-TCP) > bioactive glasses, listed in order of *in vivo* stability. The advantage of the less stable bioactive materials is that they tend to be more bioactive. *In vitro* testing has been used to study the cellular reaction and stability of calcium phosphates. These tests are designed to simulate the environment found in the body and expose materials to this environment without the use of animal test subjects. The reason behind *in vitro* testing is that scientists can achieve a good idea of how a material will react when implanted into the body. The advantage of *in vitro* testing over *in vivo* testing is the relatively low cost and short test periods. Therefore most initial studies on a material to establish the bodies reaction are performed *in vitro.* The disadvantage of the *in vitro* testing is that it is almost impossible to simulate the body environment for a prolonged period. The body is constantly rejuvenating and reacting to changes in the environment which is almost impossible to mimic in the laboratory. Therefore *in vitro* testing can give scientists a good idea of how a material will react when implanted into the body although the true reaction of the body to an implanted material can only be established via an *in vivo* test. As the bodies environment is so complex simplified *in vitro* solutions have been devised which simulate the bodies environment. One such Simulated Body Fluid (SBF) is Ringers solution which has been used by many researchers and is also the solution used in this work. Ringers solution is used as a physiological buffer and has the composition shown in table 1.3.1. Ringers SBF contains no biological constituent and shows the corrosive resistance of the material and not the effect of biological agents. Ringers and other none biological SBF solutions have been used to study hydroxyapatite and other calcium phosphates. Researchers studied the dissolution of the different calcium phosphates and found the stability to be similar to the results obtained from the *in vivo* tests. *In vitro* tests to assess how bioactive, by measuring cellular activity, hydroxyapatite and related calcium phosphates have closely matched the results obtained from *in vivo* experiments. With the highly unstable calcium phosphates showing the highest cell growth rates. The dissolution of the material provides a local source of calcium and phosphorous that the body can utilise to form new bone. It has been shown that these less stable bioactive materials show new bone formation at an earlier stage than crystalline hydroxyapatite. The disadvantage of these less stable bioactive coatings is that the material is dissolved and eventually there is no coating attached to the implant, leaving the implant material exposed to the body environment. This can be an advantage where new bone needs to be encouraged to grow to fill a gap caused by a severe break or reconstructive facial surgery. For the coating of an orthopaedic implant it is generally considered to be advantageous for the coating to remain in contact with the implant for many years and therefore a crystalline hydroxyapatite coating is considered to be the ideal.

Chemical composition	Quantity (g/l)
KCl	0.300
$CaCl_22H_2O$	.200
NaCl	6.0
$NaC_3H_2O_2$	3.1

Table 1.3.1. Chemical composition of Ringers solution.

The coating of implants with hydroxyapatite is usually carried out using the plasma spraying techniques. These spraying techniques involve using a high temperature plasma flame which reaches temperatures in excess of 20,000°C. This high temperature can have a detrimental effect on the hydroxyapatite causing phase changes to occur. Another problem associated with the plasma spraying process is the inherent rapid cooling rate which can cause an amorphous phase to form on impact with the substrate [50→57]. Ellies et al. [51] investigated the air plasma spraying of a near stoichiometric and calcium deficient hydroxyapatite using an Argon/Hydrogen gas mixture. The current and percentage Hydrogen were varied and the subsequent crystallographic changes in the sprayed coating were measured using X-Ray diffraction (XRD). The effect of increasing the current and hydrogen percentage is to raise the temperature of the plasma flame. The results indicated that the calcium deficient hydroxyapatite powder produced predominantly β-TCP with ≈5% hydroxyapatite and as the hydrogen percentage and current were increased the formation of CaO rose to a maximum of 35%. The stoichiometric hydroxyapatite powder produced a >95% compositional hydroxyapatite coating at low hydrogen percentages. As the current and hydrogen percentage are increased the hydroxyapatite degrades to CaO, although there is >35% hydroxyapatite present. This work shows that by varying the plasma spraying parameters the composition of the hydroxyapatite coating can be altered. As previously stated the *in vivo* stability of the β-TCP, CaO and hydroxyapatite are different and therefore a coating which is stable or more bioactive can be designed by varying the plasma spraying parameters.

With vacuum plasma spraying the loss of H_2O can occur and this can lead to a transformation of hydroxyapatite into α-TCP if the temperature is > 1125°C and to β-TCP if the temperature < 1125°C. The transformation reaction is:

$$Ca_{10}(OH)_2(PO_4)_6 \rightarrow 2Ca_3(PO_4)_2 + Ca_4P_2O_9 + H_2O$$

hydroxyapatite → α-TCP + calcium oxide phosphate + water

If hydroxyapatite is heated in steam, it is stable up to 1400°C [54]. In an ordinary atmosphere crystalline hydroxyapatite is stable up to 1200°C, beyond 1200°C hydroxyapatite loses its (OH) groups gradually and transforms to oxyapatite. At 1450°C it dissociates into the products α-TCP, $Ca_2P_2O_7$ and $Ca_4P_2O_9$ [56]. If the hydroxyapatite is not totally crystalline and contains some amorphous calcium phosphate or other calcium phosphate phases the thermal stability of hydroxyapatite and the resultant phase transformations which occur are different to the pure crystalline hydroxyapatite [58]. The phase diagrams for calcium phosphate have been published in the American Ceramic Society Journal [59]. Figures 1.3.1 and 1.3.2 show the phase diagrams for calcium phosphate from 1200 to 1700°C, anhydrous and at 500mm water pressure.

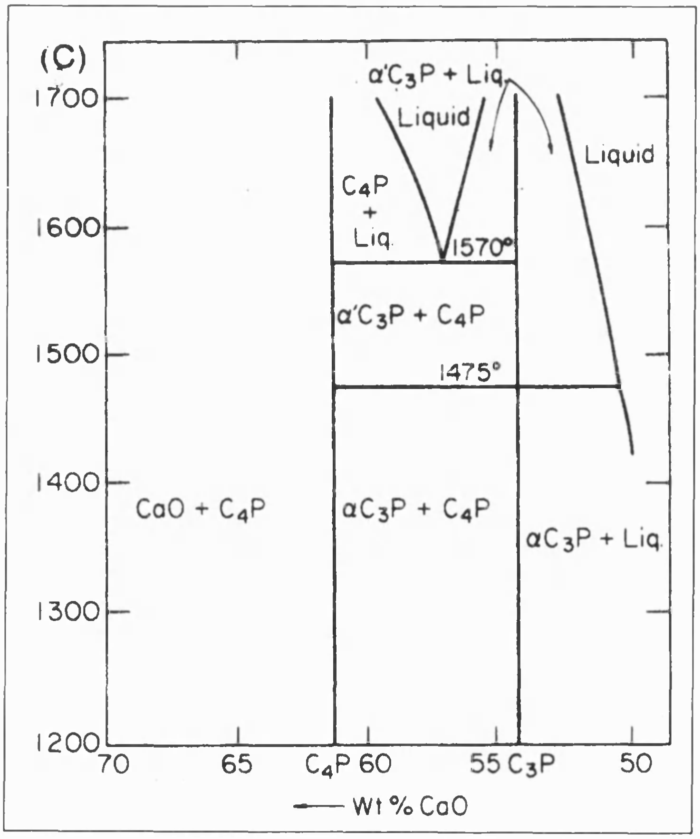

Figure 1.3.1. Phase diagram of anhydrous calcium phosphate.[59]

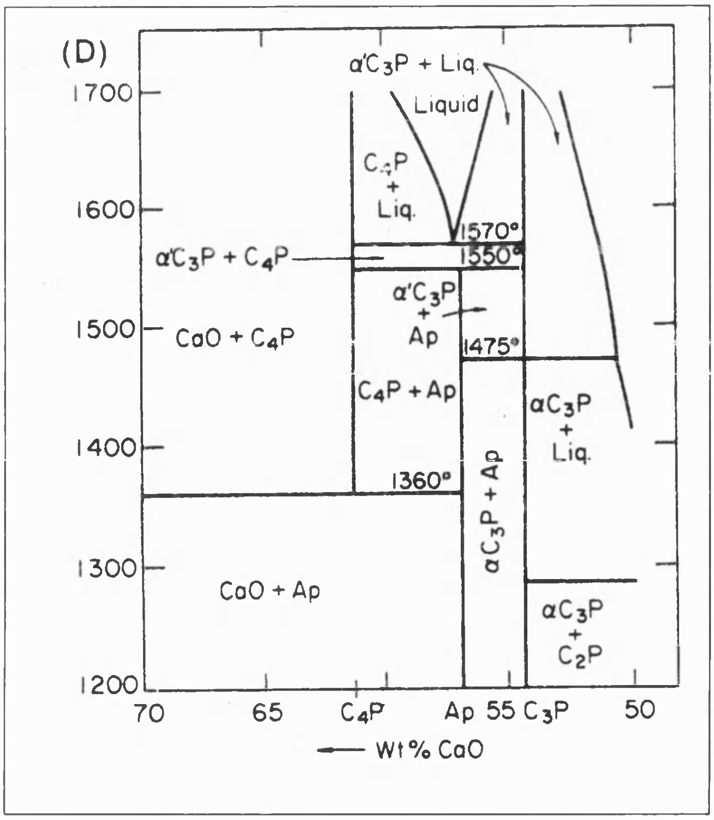

Figure 1.3.2. Phase diagram of calcium phosphate at 500mm water pressure.[59]

The presence of water vapour has a marked effect on the phase diagram of calcium phosphate. Several authors have looked at the effect of heat-treating plasma sprayed hydroxyapatite coatings [50, 52, 53, 54, 57, 60, 61]. Chen et al. [50] used two particle size distributions of 1-75 and 1-125μm to obtain two coatings with different crystallinity. These coatings were then heat-treated at a temperature of 600°C for either 1 or 10 hours. The results showed that the original crystallinity of the coatings which ranged between 23-30%, by XRD measurement, was increased by ≈5% after the 1 hour heat-treatment and ≈15% after the 10 hour heat-treatment. Zyman and

Weng et al. [57, 60] also used a heat-treatment temperature of 630°C; they found a similar result to Chen in that the heat-treatment caused crystallisation of the amorphous phase in the as-sprayed hydroxyapatite coating. When the as-sprayed coatings and the heat-treated coatings were tested in an acidic solution, 0.15M lactic acid at 25°C, for a short period the authors observed efflorescent dicalcium phosphate dihydrate crystals on the surface of the as-sprayed coating and very little change on the heat-treated coating. The crystals were attributed to the dissolution and recrystallisation of the amorphous phase. Fillaggi et al. [52] and Ji et al. [53] heat-treated a plasma sprayed hydroxyapatite coating on a titanium substrate under vacuum at 960 and 950°C respectively. Fillaggi investigated the effect of the heat-treatment on fracture toughness and tensile bond strength, the heat-treatment showed promise by increasing the bond strength. At the interface between the titanium and the hydroxyapatite, there was diffusion of phosphorous 50nm into the titanium and a higher Ca/P ratio in the coating near the interface. The diffusion of phosphorous was also detected by Ji and by using transmission electron microscopy a titanium phosphide (Ti_3P) phase was identified at the titanium/hydroxyapatite interface. An increase in mechanical strength, reported by Fillaggi, can be attributed to the formation of this chemical bond. Fillaggi also found that the heat-treated coating spontaneously debonded from the substrate if the sample was left in the laboratory atmosphere. This phenomena was attributed to either relief of the compressive residual forces at the interface, or tensile residual stresses being built up due to volumetric changes associated with the transformation at the interface. This heat-treatment also caused minor degradation of the hydroxyapatite coating with the formation of α-TCP, β-TCP [53] and tetra calcium phosphate [52]. Zyman et al. heat-treated hydroxyapatite coatings between the temperatures of 100-1000°C. The results showed that crystallisation of the amorphous phase started to occur at 630°C and the hydroxyapatite transformed into other calcium phosphate phase (α-TCP, β-TCP and tetra calcium monoxide diphosphate) from 800°C. As the temperature or heat-treatment time increases the quantity of these other calcium phosphate phases increases and that of the hydroxyapatite decreases.

1.4 Thermal Spraying techniques.

There are several types of thermal spraying process all of which use a similar principle. A high temperature, high gas velocity flame is used to melt and accelerate powder particles towards a substrate and on impact they are cooled rapidly and adhere to the substrate to form a coating. This is a line of sight overlay process in which relatively thick coatings can be applied due to the rapid deposition rates achievable. Thermal spraying provides a near net shape production method for thin film ceramics and coatings [62].

1.4.1 Air Plasma spraying.

The air and vacuum plasma spraying processes involve initiating a high intensity arc between a rod shaped cathode and a nozzle shaped water cooled anode (figure 1.4.1). Gas is then introduced alongside this cathode either axially or with an additional swirl component, which improves arc stability in the vicinity of the cathode and rotates the root of the arc, reducing anode erosion. The gas is heated to plasma temperatures by the arc and emerges from the (anode) nozzle as a plasma jet flame. The velocity of the gas is usually high enough to produce a highly turbulent jet with a visible length of a few centimetres. The maximum temperature depends on the design and operating parameters, i.e., arc current, mass flow rate, plasma velocity, operating voltage and type of gas used. The gases mainly used are argon and mixtures of argon and other noble or molecular gases (He,H_2,N_2,etc.). The effect of adding these gases to argon is to drastically increase the enthalpy of the plasma, affecting the arc voltage and the plasma "power", which is important for complete particle melting (figure 1.4.2) [63].

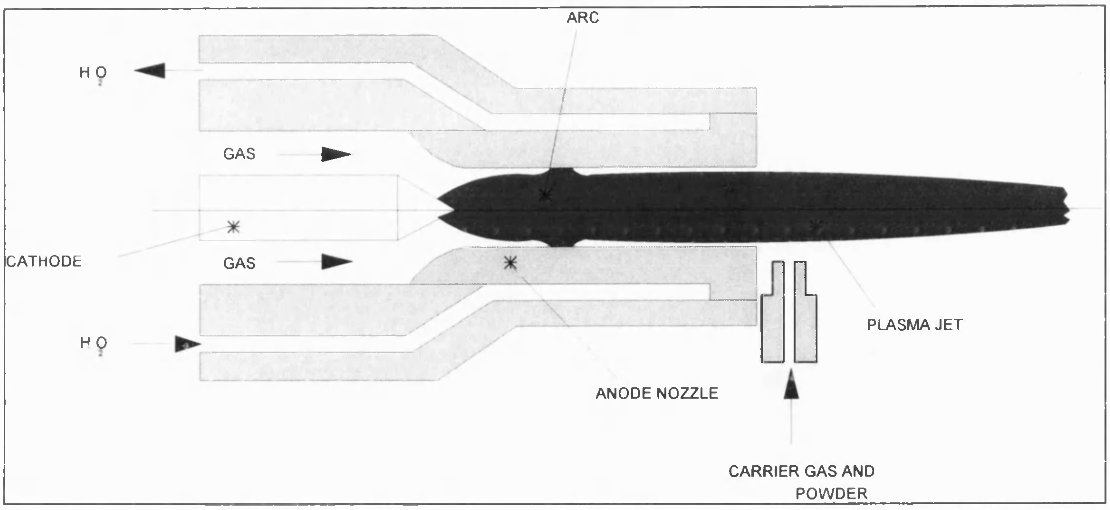

Figure 1.4.1. Schematic of a plasma torch

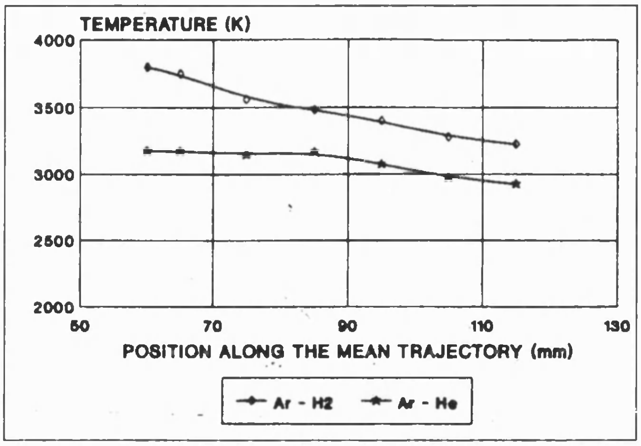

Figure 1.4.2. Evolution along their mean trajectory of the mean surface temperature of ZrO_2 + 8wt% Y_2O_3 particles injected in Ar (75slm) - H_2 (15slm) plasma jet at 31kW or in an Ar (40slm) - He (60slm) jet at 23.4kW. [63]

Particle melting is a consequence of ionised and dissociated gas recombining on the particle surface and releasing considerable energy. The plasma velocity is governed by the nozzle selected and the flow rate of the plasma gases. A high flow rate produces a high plasma velocity which gives a higher power or density of plasma. This also results in the powder particle having less dwell time in the plasma, which could result in the particle not completely melting and giving a low density coating. If the flow rate is too slow the density of the plasma may not be high enough to cause sufficient melting of the particle and again produce a low density coating.

The particle size and distribution is also important as these parameters determine the extent to which melting may occur. If particles are too big only the surface may melt, while if too small they may vaporise. Too wide a distribution will result in a fraction of the particles either vaporising or not melting.

The powder is suspended in a non reactive carrier gas and can be injected into the plasma jet either before or after it leaves the nozzle. The particles are melted and accelerated towards the substrate, both flow velocity and plasma temperature vary with distance from the nozzle as in Figure 1.4.3 and 1.4.4 [63, 64]. The molten particles impinge on the surface of the substrate, producing a dense, layered coating of fused splattered powder droplets. The morphology of the flattened particle and hence the properties of the coating, are dependent on the velocity and temperature of the particle upon impact with the surface, because the wetting and flow characteristics of the droplets influence porosity. The flow and solidification of molten particles upon the substrate is subject to interactions between heat transfer and crystal growth.

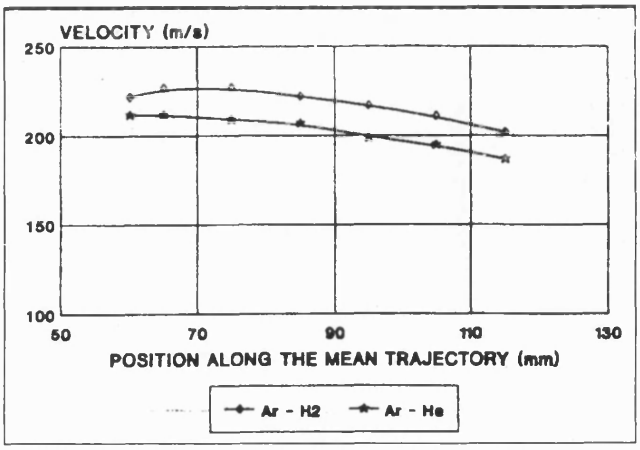

Figure.1.4.3. Evolution along their mean trajectory of the mean velocity of ZrO_2 + 8wt% Y_2O_3 particles injected in Ar (75slm) - H_2 (15slm) plasma jet at 31kW or in an Ar (40slm) - He (60slm) jet at 23.4kW. [63]

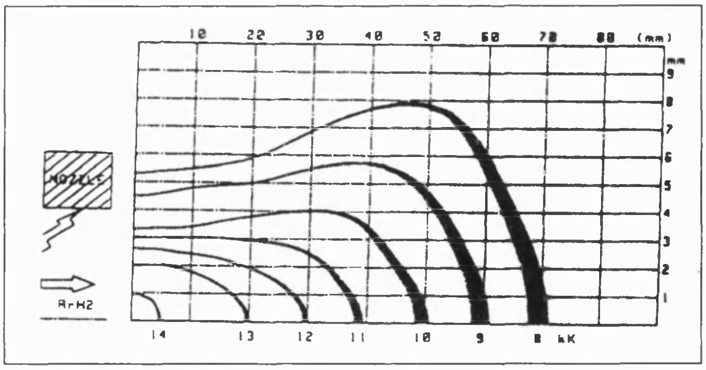

Figure 1.4.4. Plasma temperature distribution in a controlled atmosphere chamber. Pressure 10^5Pa; I=450A; Ar=45slm; H_2=15slm.[64]

The main difference between vacuum and air plasma spraying is that vacuum plasma spraying is performed at a reduced pressure. This has several advantages over air plasma spraying:

(i) The plasma flame is longer giving more time for particles to melt.

(ii) Particles which are susceptible to oxidation can be sprayed without oxidising using this technique.

(iii) The velocity of the particles is increased.

The result of combining these three advantages is that a more dense, homogeneous coating can be produced, but the cost is significantly higher and it is not suitable for spraying all powders, especially volatile powders.

Both air plasma spray (APS) and vacuum plasma spray (VPS) coating processes have been widely used for producing hydroxyapatite coatings. The VPS process produces a more dense coating than the APS process, but both processes suffer from phase changes of the hydroxyapatite during plasma spraying. This can be detrimental to the coating as it can be absorbed more rapidly when in the body. The coating is applied for several reasons:

- To provide a bioactive surface for rapid bone apposition.
- To shield the metal from environmental attack and prevent metal ion release.
- To be stable and provide a good fixation to the bone over many years.

The first aim has been achieved with APS and VPS, it is the other two aims where improvements could be made. This would require increasing the density and homogeneity of the coating and with the inherently high temperature of APS and VPS the homogeneity could be difficult to achieve due to phase changes of the hydroxyapatite. This is where the new high velocity Continuous Detonation System (CDS) may have an advantage over plasma techniques.

1.4.3 High Velocity Oxy-Fuel Thermal Spraying

CDS is the Plasma Technik variation of the high velocity oxy fuel (HVOF) process. CDS is a thermal spray process in which the chemical reaction of a fuel gas with oxygen is converted into thermal and kinetic energy for heating and accelerating coating materials. The fuel gases used are propane (C_3H_8) and propylene (C_3H_6), depending on the local supply conditions. A supersonic gas jet is produced with velocities up to 1500m/sec using a specially developed gun shown in fig. 1.4.4. The supersonic gas jet is stabilised in the reaction zone of the CDS gun using continuously controlled fuel gas and oxygen flows. The powder particles are heated uniformly and accelerated to a very high velocity (350 - 1000 m/s) in a gas jet at approximately 2500°C. The CDS process can be controlled to give varied coating conditions by adjusting the oxygen to fuel gas ratio and also the gas speed passing through the gun. The coating builds up in a similar way to the plasma spraying techniques. The diamonds which can be seen in the gas jet (fig. 1.4.4) are caused by gas speeds exceeding the speed of sound and these are known as shock diamonds [65, 66, 67].

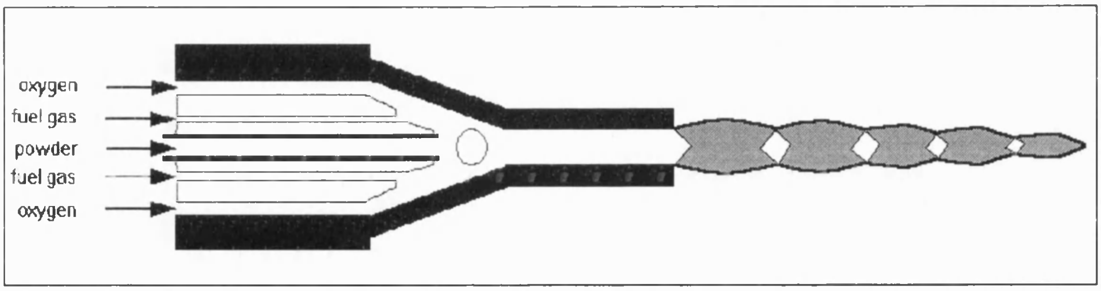

Figure 1.4.4. Cross section of the CDS-100 gun.

The very high kinetic energy of the powder particles results in a CDS coating with the following properties:

- very high adhesion to the substrate.
- very high interparticle cohesion.
- minimal porosity.

The high velocity of the jet ensures a short particle dwell time in the jet. This gives a relatively shorter and lower temperature thermal cycle compared to plasma spraying techniques. This makes the CDS process especially useful for spraying materials which detrimentally change during high temperature plasma spraying. CDS is not suitable for materials with high melting points and those which require an inert atmosphere when spraying. Figure 1.4.5 shows the thermal/kinetic energy diagram comparing APS, VPS, CDS and flame spraying.

It has been reported that since hydroxyapatite is unstable above 1300°C phase changes have occurred as a result of plasma spraying [54]. The phases usually produced are β-TCP and CaO, which are less stable in the body than hydroxyapatite and could lead to the coating spalling off. The lower temperature of the CDS process therefore makes it attractive as a process for spraying hydroxyapatite coatings.

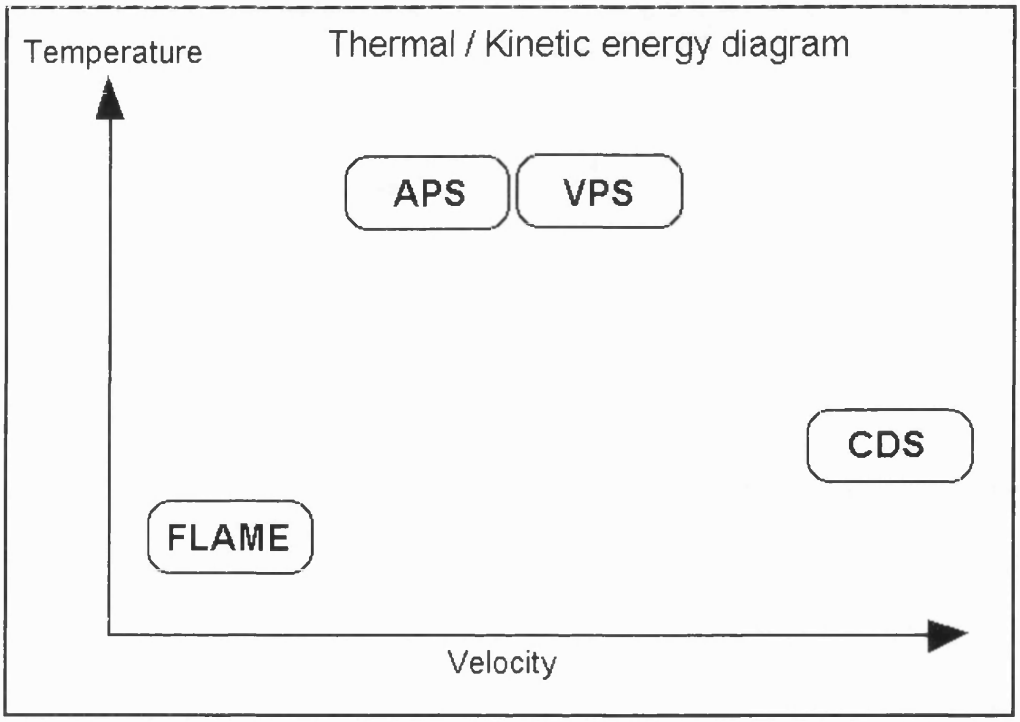

Figure 1.4.5. Thermal / kinetic energy diagram comparing 4 coating processes.

The HVOF process has been used to produce hydroxyapatite coatings in Japan by Hitoshi Oguchi et al. [68, 69, 70]. They produced a high density coating with good adhesive strength to the substrate (18.2MPa) and showed by *in vivo* testing that the coating was biologically compatible. Terashima et al. [71] found similar results when using the Jet-Kot II(Cabot Co. Ltd) spraying process, which is a HVOF thermal spraying gun, to produce a dental implant. They found the coating to have a good adhesion with the substrate and *in vivo* studies were very positive. Wolke et al. [72] compared hydroxyapatite coatings prepared by a HVOF, APS and VPS techniques. They used an hydroxyapatite powder with a particle size distribution of 1-125μm for all three spraying techniques. They showed that the VPS had the highest adhesion strength and the APS was the most dense. This was probably due more melting of the powder particles during spraying, compared to the HVOF process, allowing more flow and a closer contact with the substrate. It was apparent more melting had occurred in these two coatings from the XRD and the scanning electron microscope examination. The HVOF coating was the most crystalline and showed the least degradation from the spraying powder. This was probably due to the lower temperature of the process and this coating was also the most stable when subjected to *in vitro* testing.

1.5 Coating analysis techniques.

To characterise the hydroxyapatite coatings the two main techniques which are in common use are optical and Scanning Electron Microscopy (SEM) and X-Ray Diffraction (XRD). Other techniques which are used include Infra-Red spectroscopy (IR) [75, 76, 77, 78], Thermo-Gravimetric Analysis (TGA)

[54, 56], X-ray Photon Spectroscopy (XPS) [78, 79] and electron microscope elemental characterisation techniques [29, 80, 81, 82].

Optical microscopy can be used to examine the coating morphology by looking at polished cross-sections. The coating thickness and porosity can be calculated using the optical microscope techniques. The surface of the coating is often too rough and translucent for an optical microscope to obtain sufficient resolution for a clear image. By staining the bone cells *in vivo* samples can be examined in cross-section to examine the cellular reaction to implants, and in the case of hydroxyapatite calculate the percentage of bone in contact with the coating [10, 13, 20, 21, 23, 26, 27, 28, 31, 33, 34, 37, 83 - 87].

SEM has the advantage of a larger depth of field than optical microscopy therefore the surface of thermal sprayed coatings can be characterised. By examining the coating surface the extent of particle melting on spraying can be estimated and surface cracks and porosity measured. After *in vivo* or *in vitro* testing the coating surface can be analysed to examine new bone formation and to see where coating dissolution has occurred [29, 31, 32, 50, 51, 53, 57, 73, 74, 81, 82, 88-93]. SEM and Transmission Electron Microscopy (TEM) can also be used to characterise the interface between the hydroxyapatite and the substrate. In one study TEM was used to show a TiP_3 phase at the interface of the hydroxyapatite and titanium [53]. Other electron microscope analysis techniques can be used to calculate the calcium phosphorous ratio and look at the diffusion of elements across the interface between the hydroxyapatite and the substrate.

XRD is the main tool for analysing the purity of hydroxyapatite coatings. Using this technique the crystallinity, the quantity of other phases present and the residual stress in the coating can be calculated. By comparing the XRD diffractograms obtained from the powders and coatings with ASTM standard diffraction files the purity and phase composition can be determined. The lattice parameters and crystal groups for hydroxyapatite and other calcium phosphates are shown in table 1.5.1. XRD has been used by many authors to compare the powder used for spraying with the resultant coating. The effect of heat-treatment and *in vitro* testing has also been studied [18, 24, ,29, 42, 49, 50, 51, 53, 56, 57, 73, 75, 76, 81, 82, 90, 94-98]. Residual stress in thermal sprayed coatings is usually measured by a mechanical deformation process, for example deformation of the substrate or coating during spraying [99-103]. XRD can be used to measure the residual stress in coatings by calculating the strain at an atomic level [104]. This is a non-destructive technique and can be applied to coatings on thick substrates where the deformation due to spraying is too small to measure.

Acoustic emission analysis measures the energy emitted as noise when a material is stressed. The energy is detected by an acoustic emission transducer which is attached to the sample. The energy detected is caused by cracks propagating through the sample or some other failure mechanism. Acoustic emission analysis is a technique which has been employed by the composite scientist to measure failure mechanisms due to fatigue or large deformation of composites. The reason for using this technique for composites is that the two types of fibre failure possible in composites, fibre pullout and fibre fracture, produce very different acoustic emission signals. The pull out of a fibre produces a large number of low energy event, whereas fibre fracture produces a single high energy event [105]. This technique has also been employed to analyse the failure mechanism of plasma sprayed coatings [106]. This work shows that large cracks produced high energy acoustic emission events and cracks which branched through the coating and ran along the interface produced low energy events. This technique is useful to predict the failure mode of the coating, which may be important when assessing whether an hydroxyapatite coating will perform well in the body under fatigue loading conditions.

Name	Crystal Structure	ASTM card No.	Lattice Parameters **d** (Å)		
			a	b	c
Hydroxyapatite. $Ca_5(PO_4)_3(OH)$	Hexagonal	9-432	9.418	9.418	6.884
β-Tri Calcium Phosphate β-$Ca_3(PO_4)_2$	Rhombohedral	9-169	10.429	10.429	37.38
α-Tri Calcium Phosphate α-$Ca_3(PO_4)_2$	Orthorhombic	9-348	15.22	20.71	9.109
Calcium Oxide Phosphate $Ca_4O(PO_4)_2$	Monoclinic	24-1137	7.018	11.980	9.469
Calcium Oxide CaO	Cubic	37-1497	4.81	4.81	4.81

Table 1.5.1. ASTM data for several calcium phosphate materials.

2.0 Experimental techniques.

2.1 Powder Characterisation.

The three hydroxyapatite powders used to produce the hydroxyapatite coatings were:

(1) Powder HA044, supplied by Sultzer for use with the CDS process.

(2) Powder Amdry 6020, supplied by Sultzer for use with the APS process.

(3) Powder XPT W 601, supplied by Sultzer for use with the VPS process.

2.1.1 X-ray diffraction.

The Phillips PW 1730/10 4kW X-ray generator, using Philips PC-APD diffraction software for data collection and analysis was used to analyse the hydroxyapatite powders. Standard ASTM powder analysis techniques were used.

The β-TCP percentage was calculated using the I_{100} peaks for β-TCP and hydroxyapatite in the following formula.

$$\%\beta - TCP = \frac{I_{100}^{\beta-TCP}}{I_{100}^{\beta-TCP} + I_{100}^{\beta-TCP}} \times 100\%$$

I_{100}^{HA} = Intensity of maximum hydroxyapatite peak.

$I_{100}^{\beta-TCP}$ = Intensity of maximum β-TCP peak.

2.1.2 Particle size analysis.

The particle size distribution was measured for the APS, VPS and CDS hydroxyapatite powders using the Malvern Instruments System 3601 particle size analyser. This instrument uses a laser diffraction technique to determine the particle size distribution. The powders were dispersed in distilled water using the ultrasonic cell strirrers. The suspension was passed through a cell in the path of the laser and the data collected and analysed by Malvern Instruments computer software.

2.1.3 Scanning electron microscopy.

The hydroxyapatite powders were prepared for electron microscopy, by sprinkling the powder on to a conductive adhesive applied to an aluminium dish; the excess powder was removed by shaking. The samples were coated with carbon, to prevent charging of the powder particles during SEM examination. The Jeol 6310 scanning microscope was used for examination of particle size and morphology. The accelerating voltage used was either 10 or 15kV.

2.1.4 Energy dispersive X-ray analysis.

EDX analysis was carried out on the hydroxyapatite powders. The SEM samples prepared in section 2.1.3 were used for analysis. The Joel 6310 scanning microscope was used with the Link Analytical AN-10000 EDX system to obtain the EDX pattern for the powders. The software was used to calculate the integrated intensities of the calcium and phosphorous peaks to obtain a calcium to phosphorous ratio.

2.2 Thermal Spraying of Hydroxyapatite coatings.

In all cases a 2mm thick sheet of Ti-6Al-4V alloy, BS3531, was used as the substrate.

2.2.1 Air Plasma Spraying.

The air plasma sprayed hydroxyapatite coatings were manufactured at Plasma - Technik Ltd, Newport. The titanium alloy sheet was cut into oblong samples measuring 75×20mm. To prepare the surface for plasma spraying the samples were grit blasted, using a 60 grit alumina at 80psi. Both sides of each sample were grit blasted to prevent distortion of the substrate caused by the grit blasting process. The samples were plasma sprayed in batches of at least 5 samples. The robot controlling the plasma spray gun was programmed to do a standard raster pattern. The spraying parameters used are shown in table 2.1. Six sets of parameters were produced with the aim of showing the standard conditions used and the extremes of over and under heating the powder by varying the gas ratio and applied current.

Torch: APS F4	Powder: Amdry 6020			Nozzle: 6mm		
Test	1	2	3	4	5	6
Ar (slpm)	20	20	30	30	20	25
N_2 (slpm)	15	27	13	0	0	0
He (slpm)	0	0	0	60	80	50
Current (amps)	450	550	400	700	800	650
Voltage (volts)	69	68	40	52	53	49
Distance (mm)	75	75	75	115	115	115
No. Cycles	2	2	2	8	4	10
Thickness (μm)	100	200	100	85	150	150

(SLPM: Standard Litres Perm Minute)

Table 2.1. Spraying parameters for air plasma sprayed coatings.

2.2.3 Vacuum Plasma Spraying.

The vacuum plasma sprayed (VPS) hydroxyapatite coatings were sprayed at Plasma - Technique AG, Switzerland. The substrate size and surface preparation was the same as section 2.2.2. The spraying parameters used are specified in table 2.2.

Powder	XPT W 601	Chamber pressure	100 mbar
Distance	275 mm	Powder feed rate	18 g/min
Gas mixture	Ar: 15 slpm	H_2: 4 slpm	He: 30 slpm
Current	600 A		

(SLPM: Standard Litres Perm Minute)

Table 2.2. Spraying parameters for vacuum plasma sprayed coatings.

2.2.4. High Velocity Oxy-Fuel Thermal Spraying.

The high Velocity Oxy-Fuel (HVOF) hydroxyapatite coatings were sprayed at Plasma - Technik, Newport using the Continuous Detonation System (CDS). Substrate size and preparation was the same as for section 2.2.2. Two sets of spraying parameters were used and these are shown in table 2.3 and 2.4.

Torch:	CDS	Material:	HA044
Barrel:	3 inch	Oxygen nozzle:	standard
Powder injector:	2,0	Fuel nozzle:	standard
Carrier gas:	20 slpm, N_2	Powder feed setting	30
Powder spreading	NL	Suction piece:	NL
Stirrer speed:	≈90 rpm	Powder feed rate	≈6 g/min
Substrate cooling:	Air, 2×90°		

(SLPM: Standard Litres Perm Minute)

Table 2.3. CDS set up parameters.

Translation programme:			
Surface speed (m/min):	30	Step (mm/pass)	4.5
Spraying Parameters		Set 1	Set 2
Coating Distance, angle	(mm : °)	250 : 90	225 : 90
Fuel gas C_3H_8	(slpm)	50	50
Oxygen	(slpm)	200	250
No. of passes		6	6
Coating Thickness	(μm)	160	140

(SLPM: Standard Litres Perm Minute)

Table 2.4. CDS spraying parameters.

2.3 Hydroxyapatite coating characterisation.

2.3.1 X-ray diffraction.

A Philips PW 1730/10 4kW X-ray generator, using Philips PC-APD diffraction software for data collection and analysis was used to analyse the coatings from all three plasma spraying processes. The coating thickness was sufficient to prevent penetration into the titanium substrate and hence no interference was caused by the substrate.

2.3.1.1. Crystallinity of Hydroxyapatite coatings.

The Philips PW 1730/10 4kW X-ray generator, using Philips PC-APD diffraction software for data collection and analysis was used to obtain the XRD patterns for all thermal sprayed coatings. The XRD pattern was stored as an ASCI data file and imported into an Microsoft Excel spreadsheet where the XRD pattern could be generated as a digital image. This image was then transferred to the image analysis software package OPTIMAS and the total area under the peaks (area A) of the XRD pattern was calculated. The peaks were then manually erased from the background and amorphous hump in the pattern, and the area of the amorphous hump (area B) measured. The two areas can be seen in figure 2.1.

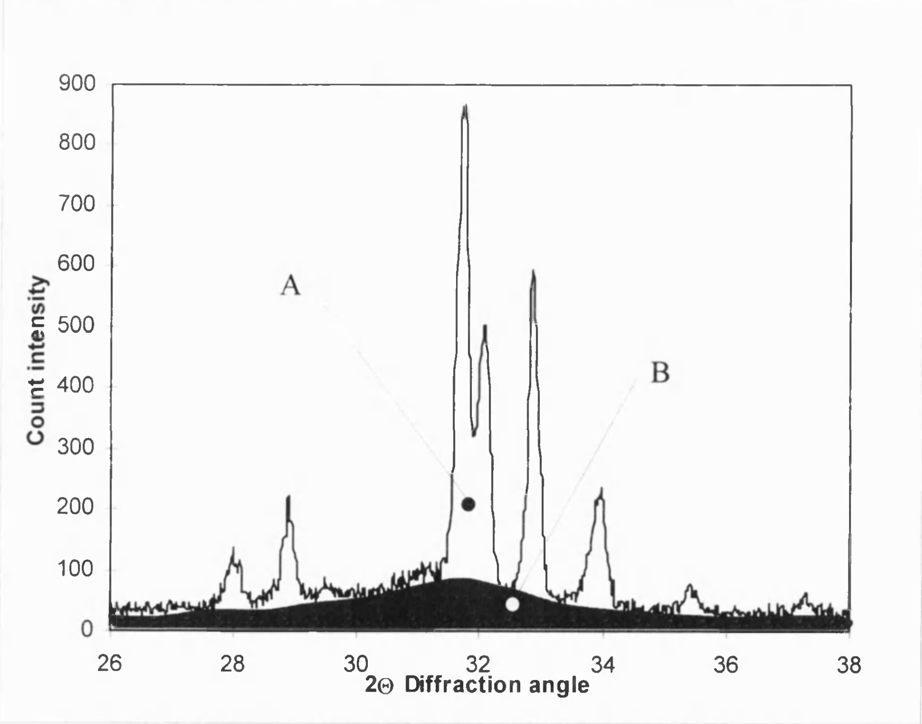

Figure 2.1. XRD pattern showing areas used for % crystallinity calculation.

A simple rule of mixtures formula can be applied to calculate the percentage of crystalline phase present in the coating, as shown in equation 2.3.1.

$$\%Crystallinity = \frac{A-B}{A} \times 100\% \qquad \text{Equation 2.3.1.}$$

2.3.1.2. Residual stress in hydroxyapatite coatings.

The Philips PW 1730/10 4kW X-ray generator, with Philips PC-APD diffraction software for data collection and analysis was used to obtain the XRD patterns for all thermal sprayed coatings. The residual stress in a coating can be calculated from the accurately measured position of a relevant peak in the XRD pattern. Using the PC-APD software for analysing XRD patterns the position of a peak can be accurately measured. It is important to select an appropriate peak, with a reasonable relative intensity to the I_{100} hydroxyapatite peak and simple *hkl* indices so that the calculations are not too complex. The peaks selected were for the 300 and 004 planes, which give the stress in the two major planes of the hydroxyapatite structure. Since the hydroxyapatite structure is hexagonal,

a = **b** ≠ **c**, the **a** and **c** lattice parameters can be calculated from the relationship

$$\frac{1}{d^2} = \frac{4}{3}\left(\frac{h^2 + hk + l^2}{a^2}\right) + \frac{l^2}{c^2} \qquad \text{Equation 2.3.2}$$

using the plane 300 this simplifies to

$$a = \sqrt{12d^2} = 2\sqrt{3}d \qquad \text{Equation 2.3.3}$$

and similarly for the plane 004

$$c = \sqrt{16d^2} = 4d \qquad \text{Equation 2.3.4}$$

where *d* is the plane spacing calculated from the XRD pattern using Braggs' law, which rearranges to

$$d = \frac{\lambda}{Sin\theta} \qquad \text{Equation 2.3.5}$$

where λ is the wavelength of the incident beam and θ is the measured diffraction angle.

Once the lattice parameters have been determined for the powder and the coatings, the lattice strain can be worked out and by using a suitable modulus for hydroxyapatite the residual stress in the coating can be calculated. The hydroxyapatite powders used for spraying the coatings were used as standards for the residual stress calculations.

2.3.2 Optical microscopy.

A Zeiss ICM 405 optical microscope using normal reflective light was employed to examine the cross-section of the coatings, as prepared in section 2.3.2.1. For increased contrast, differential interference contrast (DIC) was used to view the samples (See Appendix 1).

2.3.2.1 Sample preparation.

A cross-section of the coating was prepared by impregnating with a low viscosity epoxy resin under a vacuum of 500mmHg to extract any air trapped in the coating and then pressuring the resin into the pores and cracks of the coating. The pressure was maintained while the resin was curing. This procedure was followed to prevent the coating from cracking and flaking when cut into suitably sized pieces for microscopic analysis. The samples were polished using a Buehler Motopol 12 automatic polishing and grinding machine. Two polishing protocols have been used with the aim of highlighting different morphological characteristics of the coating, the sequence of grinding and polishing steps for both protocols are shown in table 2.5.

Polishing route	Surface & abrasive	Wheel speed (rpm)	Sample rotation	Force per sample (lbs)	Duration (mins)
S & D	240 grit SiC	150	comp	5	2
S & D	Metlap 4, 9µm ♦ oil based	25	contra	5	6
S & D	Ultrapol, 3µm ♦ oil based	200	comp	5	4
S & D	Texmet 1, 1µm ♦ oil based	240	comp	5	4
D	RAM cloth, ¼µm ♦ oil based	150	comp	5	15
S	Texmet 1, coll. silica 0.05µm	100	comp	5	10

S = Colloidal Silica Polishing route, D = ¼µm diamond polishing route, ♦ = diamond, comp = same rotation of polishing wheel, contra = opposite to rotation of polishing wheel.

Table 2.5. Polishing procedure for plasma sprayed hydroxyapatite coatings.

2.3.2.2. Porosity measurements.

The percentage porosity of the hydroxyapatite coatings was measured by looking at the polished cross-section of the coatings, prepared in section 2.3.2.1, using an optical microscope. A video camera connected to the microscope provided a digital image which was processed with a computer based image analyser (Data Cell Optimas image processing software in windows) and the percentage porosity measured for all the hydroxyapatite coatings.

2.3.2.3. Coating thickness measurements.

The image analysis system used in the porosity measurements (2.3.2.2) was also used to measure the hydroxyapatite coating thickness.

2.3.3. Scanning electron microscopy.

A Joel 6310 scanning electron microscope was used for examining the cross-section, as prepared in section 2.3.2.1, and surface of the hydroxyapatite coatings. The cross-sections and surfaces were coated with either gold or carbon to prevent charging of the samples during electron microscope examination.

2.3.4 Surface roughness measurement.

The surface roughness characteristics of all the HA coatings was measured using a computer controlled Talysurf. The diamond stylus was moved over the HA surface a distance of 5mm and the computer software calculated the roughness measurement parameters.

2.4 Shear testing of HA coatings.

The test coupons prepared in section 2.2 were used for testing the shear strength of the coatings. A simple lap shear test was used to measure the shear strength of the coatings. The test samples were made by gluing a similar sized sample to the hydroxyapatite coating as shown in figure 2.4.1. A clamping jig was employed to align the samples and compress the adhesive. The adhesive was a heat-curing structural adhesive, Redux 312, manufactured by Ciba-Geigy Plastics.

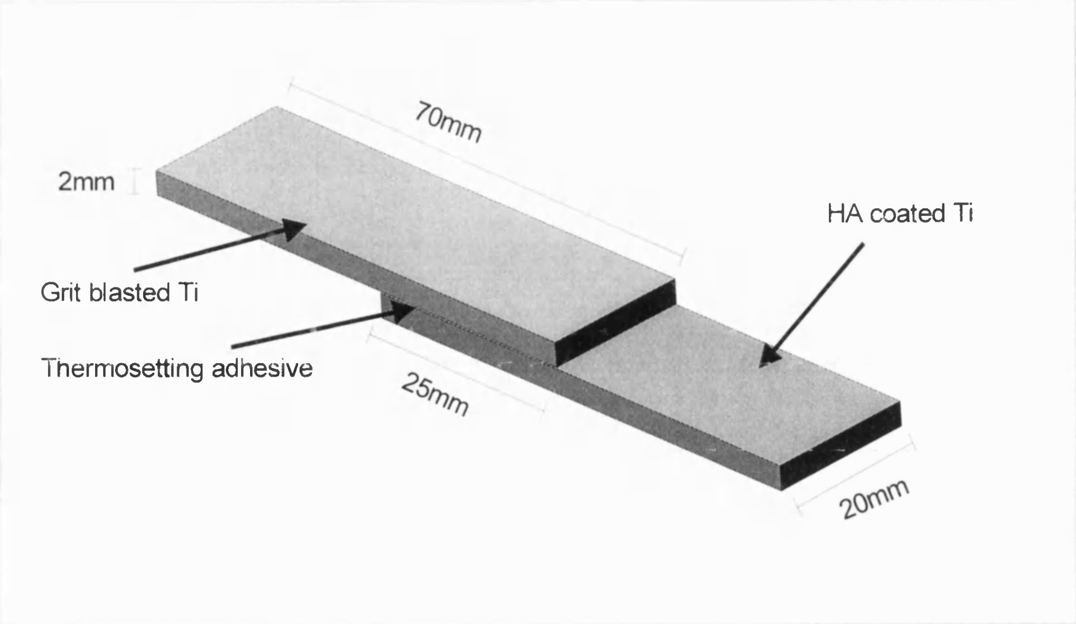

Figure 2.4.1. Shear test sample.

The samples were tested using an Instron 1195 tensometer. The extension rate was set at 1mm/min. The force at failure was measured and used to calculate the shear strength of the coating as shown in equation 2.4.1.

$$\text{shear strength} = \frac{F}{A} \qquad \text{Equation 2.4.1}$$

F = Force at failure, A = Contact area of lap joint.

A minimum of 5 samples were tested for all coating types and the average shear strength was calculated.

2.5 Tensile testing of hydroxyapatite coatings.

The tensile bond strength of the hydroxyapatite coatings was measured using a variation of ASTM C633. The hydroxyapatite coating was sprayed onto the end of a titanium cylinder 25mm in diameter. The spraying surface was prepared by degreasing and grit blasting, as for previously sprayed samples. The spraying parameters used are shown in section 2.2. The tensile strength samples were prepared by gluing a titanium cylinder with a hydroxyapatite coating to an uncoated grit blasted cylinder, as shown in figure 2.5.1. A clamping jig was used to align the samples and compress the adhesive. The adhesive was a structural heat curing adhesive, Redux 312, manufactured by Ciba-Geigy. The tensile strength samples were tested using an Instron 1195 tensometer, the strain rate was set at 1mm/min. A minimum of 10 samples were tested for each set of spraying parameters and the force at failure was used to calculate the average tensile strength.

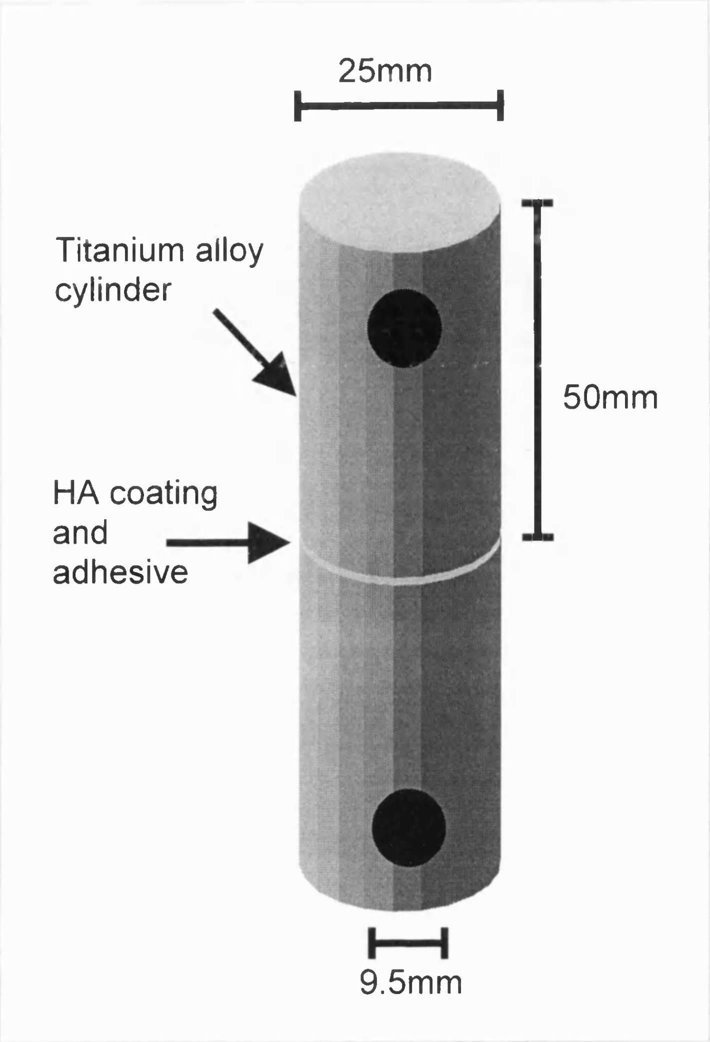

Figure 2.5.1 Tensile strength test sample.

2.6 Acoustic emission of hydroxyapatite coatings.

The hydroxyapatite coatings prepared in section 2.2 were used for the acoustic emission test. The hydroxyapatite coated coupons were bent using a four point bend test, with the acoustic emission transducer in contact with the coating, as shown in figure 2.6.1. The rate of deflection was set at 1mm/min. The ends of the hydroxyapatite test coupons were cleaned of hydroxyapatite coating to prevent noise being generated from the coating abrading the bars of the four point bend test rig.

The transducer was amplified by a 60dB preamplifier which had a frequency range of 100kHz to 1mhz. A Marandy MR1004 unit was used to collect the acoustic emission data. This system is a 25 channel amplitude sorter and ringdown counter which is used in association with an IBM compatible PC. The threshold on the MR1004 is variable but has a minimum value of 10mV at channel 1 and a maximum threshold of 10V at channel 26. Channels 1 to 25 are 2.4dB wide and events of amplitude greater than 10V are recorded as over range in channel 26.

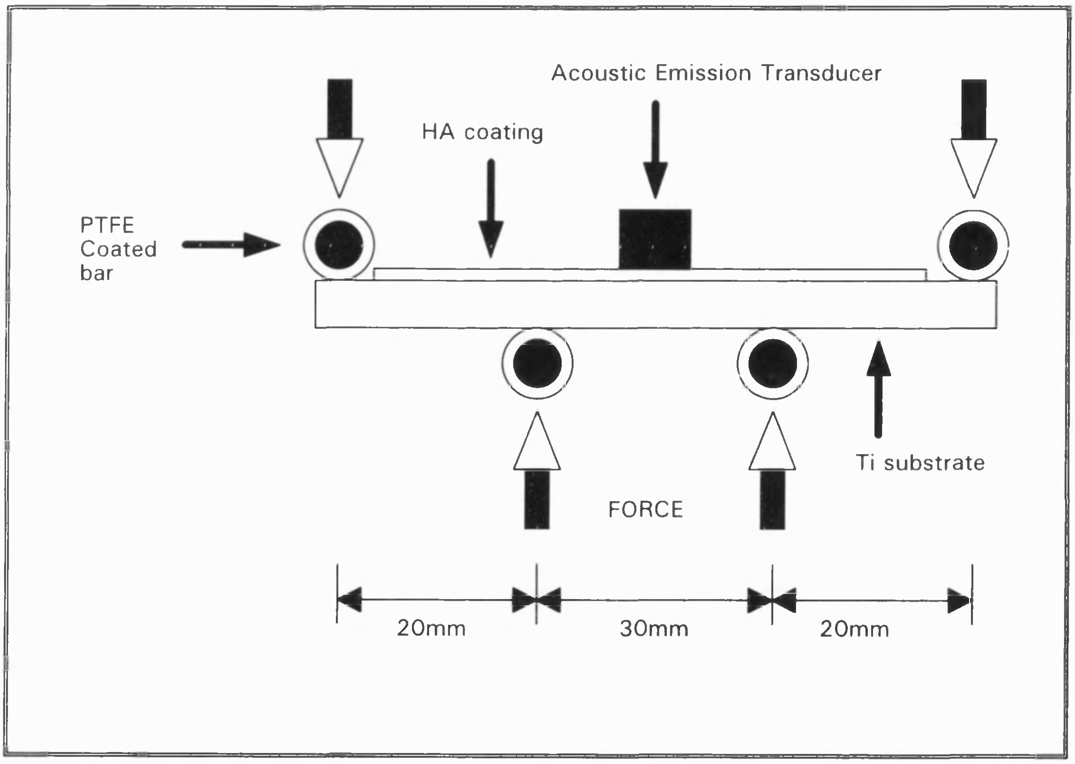

Figure 2.6.1 Acoustic emission test set-up.

2.7 Heat-treatment of hydroxyapatite coatings.

The hydroxyapatite coated test coupons manufactured in section 2.2 were subjected to a heat-treatment process. A carbolite muffle furnace with an air atmosphere was preheated to 600°C. The hydroxyapatite coated test coupon was placed in the furnace for 30 minutes and then removed to cool in air. Two samples from each set of spraying parameters were heat-treated at this and all following heat-treatment temperatures. The furnace was then preheated to 700, 800 and 900°C and the heat-treatment repeated with previously unheat-treated test coupons.

These heat-treated hydroxyapatite coatings were then characterised using the procedures described in section 2.3.

2.8 *In vitro* testing of hydroxyapatite coatings.

The hydroxyapatite coatings prepared in section 2.2 were tested for *in vitro* stability by soaking in Ringers *in vitro* solution at pH 7.2 and 4.5. The pH of the Ringers solution was maintained constant by buffering with 1M hydrochloric acid or 1M tri(hydroxymethyl)aminomethane. The temperature was kept stable at 37.7°C by using a circulatory heater. For each set of spraying parameters a test coupon was soaked in the Ringers solution for 1, 2 and 4 weeks at both pHs. The invitro tested hydroxyapatite coatings were then characterised using the procedures described in section 2.3.

3.0 Results.

3.1 Powder Characterisation.

3.1.1 X-Ray Diffraction.

Figure 3.1.1 shows the XRD pattern obtained from powder Amdry 6020. The pattern was analysed for relevant peaks using the PC-APD software and was found to be characteristic of hydroxyapatite according to ASTM powder diffraction files. There were no peaks other than those corresponding to hydroxyapatite in this pattern.

Figure 3.1.2 shows the XRD pattern obtained from powder HA044. The pattern was analysed for relevant peaks using the PC-APD software and was found to be characteristic of hydroxyapatite according to ASTM powder diffraction files. A peak was detected at $2\theta=31.05°$, which corresponds to the strongest XRD line of β-TCP. Using the formula stated in section 2.1.1 the %β-TCP was calculated to be 2.32%.

Figure 3.1.3 shows the XRD pattern obtained from powder XPT W 601. The pattern was analysed for relevant peaks using the PC-APD software and was found to be characteristic of hydroxyapatite according to ASTM powder diffraction files. There were no peaks other than those corresponding to hydroxyapatite in this pattern.

3.1.2 Particle Size Analysis.

The particle size distribution for powders Amdry 6020, HA 044 and XPT W 601 are shown in figures 3.1.4, 3.1.5 and 3.1.6 respectively.

The main characteristics of particle size distribution for the three powders are shown in table 3.1.1.

	d (0.5) (μm)	d (0.1) (μm)	d (0.9) (μm)	Specific surface area (m^2/g)
Amdry 6020	128.22	59.94	240.16	0.0867
HA 044	14.09	9.07	19.25	0.4695
XPT W 601	34.31	25.32	43.18	0.1861

Table 3.1.1. Summary of particle size distribution data.

d (0.5) = Median particle size diameter.

d (0.1) = Particle size of the 10% volume distribution cut off.

d (0.9) = Particle size of the 90% volume distribution cut off.

3.1.3 Scanning Electron Microscopy.

Figure 3.1.7 shows a typical selection of particles from powder Amdry 6020. The particles range in size from 50 to 150μm and are very angular in appearance. A single particle of powder Amdry 6020 can be seen in figure 3.1.8. The particle looks as though it is an agglomerate of smaller particles 1 to 2μm in size.

A typical selection of particles from powder HA 044 are shown in figure 3.1.9. The powder appears to consist of two particle morphologies, a spherical particle and rectangular particle. The distribution of spherical and rectangular particles seems to be equal and both these particles appear to be of similar size ranging from 5 to 20μm. Figure 3.1.10 shows a single rectangular particle from powder HA 044. This particle looks like it is a dense agglomerate of smaller particles of size less than 1μm. The spherical particle is shown in figure 3.1.11. The particle appears to be a porous agglomerate of particles less than 1μm in size with interconnecting porosity of a similar size.

Figure 3.1.12 shows a typical selection of particles from powder XPT W 601. The particles are angular in appearance and range in size from 10 to 40μm. A single particle of XPT W 601 can be seen in figure 3.1.13. The particle looks dense with finer particulate debris ≈1μm in size adhering to the surface of the particle.

3.1.4 Energy Dispersive X-ray Analysis.

EDX analysis was carried out on the hydroxyapatite powders. The SEM samples prepared in section 2.1.3 were used for analysis. The Joel 6310 scanning microscope was used with the Link Analytical AN-10000 EDX system to obtain the EDX pattern for the powders. The computer software was used to calculate the percentage of calcium and phosphorous present in the hydroxyapatite particles. The percentage of calcium and phosphorous and also the ratio of calcium to phosphorous are shown in table 3.1.2 for all three powders.

	% Calcium ± std	% Phosphorous ± std	Ca/P mass ratio ± std	Ca/P molar ratio ± std
Amdry 6020	41.97 ± 2.96	20.99 ± 1.55	2.000 ± 0.014	1.545 ± 0.011
XPT W 601	39.55 ± 2.26	19.62 ± 0.96	2.015 ± 0.020	1.557 ± 0.015
HA 044 rectangular*	40.12 ± 5.85	20.31 ± 3.06	1.976 ± 0.014	1.527 ± 0.011
HA 044 spherical*	36.72 ± 3.43	18.41 ± 1.94	1.997 ± 0.060	1.543 ± 0.046

* Powder HA 044 consisted of two particle morphologies and the EDX results are shown for both particle types

Table 3.1.2. EDX analysis results of hydroxyapatite powders.

3.1.5 Discussion of Results

The XRD results for powder Amdry 6020 and XPT W 601 showed a crystalline hydroxyapatite which is characteristic of a powder which had been manufactured by a precipitation, sintering and crushing route. The SEM examination showed the particles of both powders to consist of smaller sintered particles and had an angular appearance suggesting that the particles were produced by crushing. Powder Amdry 6020 has been used by other authors and the XRD results agree strongly with the published work [46]. The size distribution between Amdry 6020 and XPT W 601 is different as the two spraying techniques require powders with different thermal capacities. The APS spraying process uses a hot slow plasma flame, this means that a particle injected into the plasma will have a relatively high dwell time in the flame and absorb a large quantity of energy. Therefore a powder which is used with the APS process requires the particles to have a sufficiently high thermal capacity that it does not vaporise or detrimentally degrade during spraying. A large particle requires more energy to be melted than a small particle, if the particle does not melt sufficiently for it to flow when impacting the substrate it will bounce off and the coating will not be deposited. Therefore large particles are more suitable for the APS process. The VPS process uses similar temperatures to APS but the plasma gas velocity is significantly higher, therefore the particles have a shorter dwell time in the plasma and absorb less energy than the APS process. This requires a smaller particle size distribution, so that the particles can absorb enough energy to melt sufficiently for a coating to be deposited. The other advantage of a small particle distribution is that the coatings produced tend to be more dense and any porosity which is present is small and less likely to affect the properties of the coating. The high plasma velocity of the VPS process also aids the production of dense coatings.

The powder HA044 used to produce the CDS HA coating showed an impurity of 2.3% β-TCP, from the XRD results. The powder morphology is different to Amdry 6020 and XPT W 601, with two distinct particle shapes. Both these shapes are regular and are probably manufactured using the spray drying or powder precipitation production techniques. Spray drying and precipitation preparation routes are very sensitive to changes in temperature and Ca/P ratio, and these parameters will dictate the phases which form. The pH of the reaction solutions also needs to be controlled when the precipitation preparation route is being used. Both these techniques are susceptible to other calcium phosphate phases being produced, which explains the presence of the β-TCP impurity. The particle size is smaller than the other two powders. The CDS process has a much lower processing temperature of ≈2500°C, as compared to the APS or VPS plasma temperature of ≈20000°C, therefore the process requires a powder particle with a much lower thermal capacity. The CDS process utilises the high velocity of the flame, exceeding Mach 4, to accelerate the particle to a high velocity and use this kinetic energy as well as the thermal energy to deposit the coating.

The EDX analysis results of the hydroxyapatite powders showed that there is no significant difference in the calcium to phosphorous ratio between the different powders. The difference in percentage of calcium and phosphorous detected by the EDX technique can be attributed to the different morphologies of the particles. Although the particles were polished (as described in section 2.1.3) and apparently exhibited flat surfaces for the EDX analysis the density of particles varied. The spherical HA 044 particles had a sponge like structure and therefore a low density and hence a low calcium and phosphorous percentage. Powder Amdry 6020 was dense with only a small amount of porosity and hence gave a higher calcium and phosphorous percentage. The difference in calcium and phosphorous percentages had a minimal effect on the calcium to phosphorous ratio as the change in density would effect the quantity of emitted X-rays from the calcium and phosphorous to a similar extent. For stoichiometric hydroxyapatite the molar calcium to phosphorous ratio is 1.66 and the mass ratio is 2.148. Powder HA044 contained 2.32% β-TCP which has a Ca/P ratio of 1.5 and would therefore cause a small drop in the overall Ca/P ratio to 1.656. A 0.01 change in the Ca/P ratio is not within the measurement accuracy of the EDX technique and therefore powder HA044 would be expected to have a very similar Ca/P ratio to the other hydroxyapatite powders. The EDX results for calcium to phosphorous ratio for the hydroxyapatite powders are consistently lower by ≈0.12 than the calculated stoichiometric ratio. From the XRD results the powders are >97% hydroxyapatite and therefore the calcium to phosphorous ratio for these powder would be expected to be close to the stoichoimetric ratio. The difference between the measured and stoichiometric calcium to phosphorous ratio can be attributed to a consistent error caused by the calibration of the system. The calibration for the elements calcium and phosphorous is done using calibration standards such as calcite and galium phosphide. The calibration error occurs due to the calcium and phosphorous in the calibration standards having a slightly different emitance of X-rays caused by a difference in the surface roughness or density of the standard from the powder samples. To overcome this error an hydroxyapatite standard would need to be used, which was unfortunately unavailable.

Although the measured calcium to phosphorous values are probably incorrect the results show that there is very little difference in calcium to phosphorous ratio between the different powders.

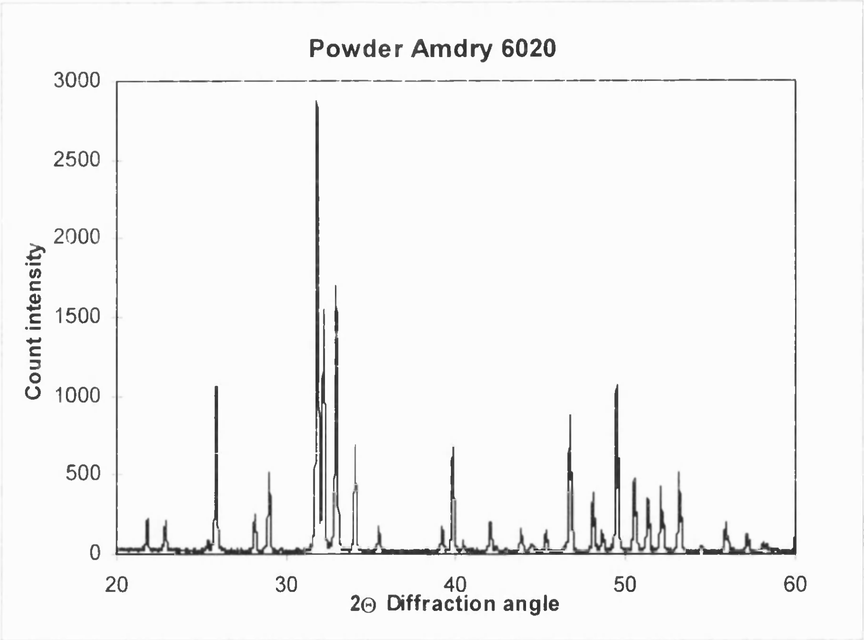

Figure 3.1.1. XRD pattern of powder Amdry 6020.

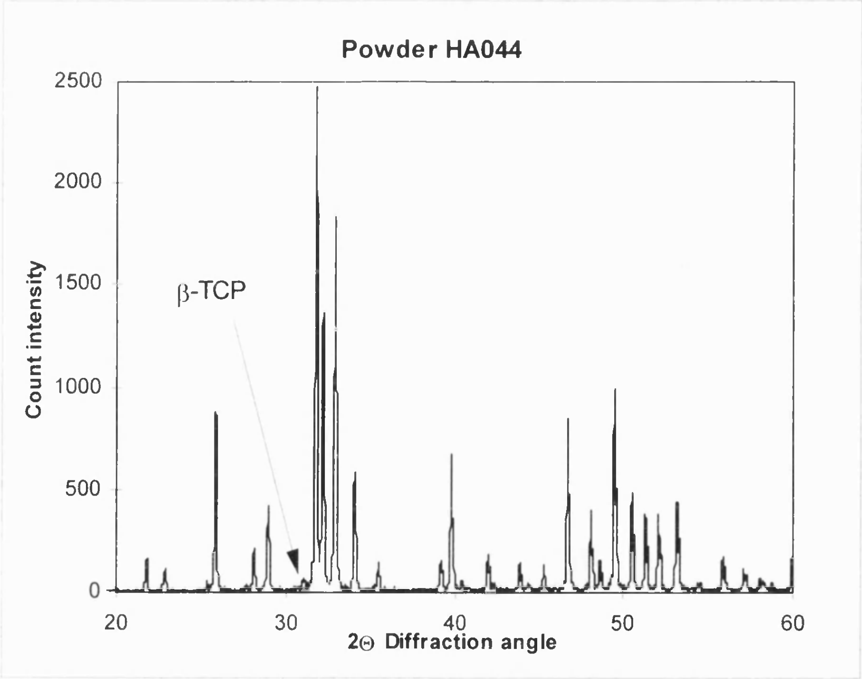

Figure 3.1.2. XRD pattern of powder HA044.

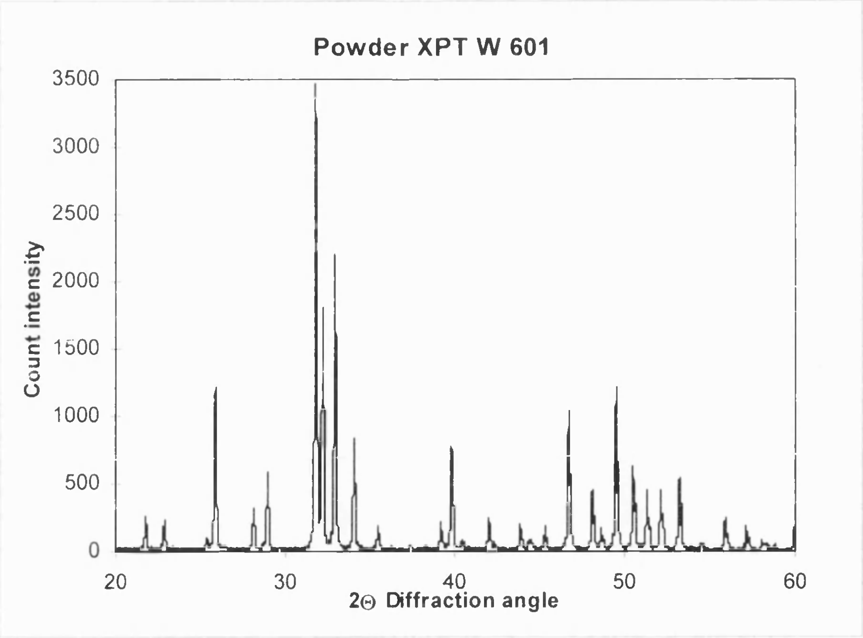

Figure 3.1.3. XRD pattern of powder XPT W 601.

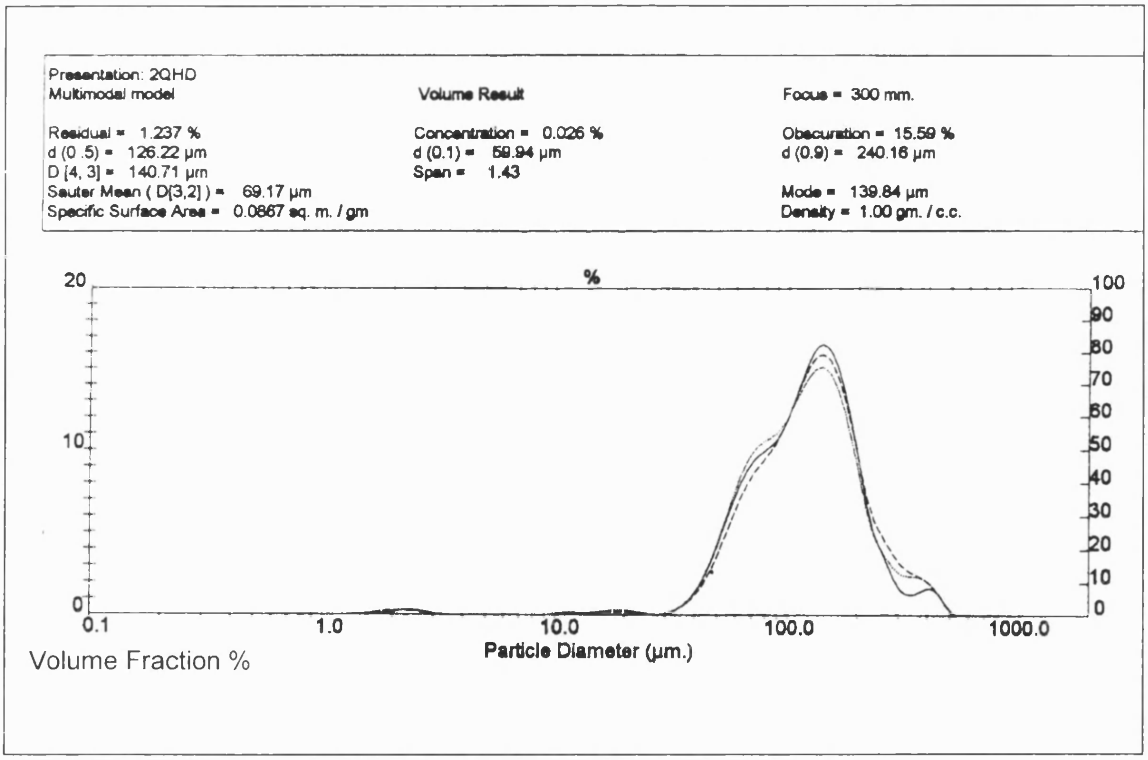
Presentation: 2QHD
Multimodal model

Residual = 1.237 %
d (0 .5) = 126.22 µm
D [4, 3] = 140.71 µm
Sauter Mean (D[3,2]) = 69.17 µm
Specific Surface Area = 0.0867 sq. m. / gm

Volume Result

Concentration = 0.026 %
d (0.1) = 59.94 µm
Span = 1.43

Focus = 300 mm.

Obscuration = 15.59 %
d (0.9) = 240.16 µm

Mode = 139.84 µm
Density = 1.00 gm. / c.c.

Figure 3.1.4. Particle size distribution for powder Amdry 6020.

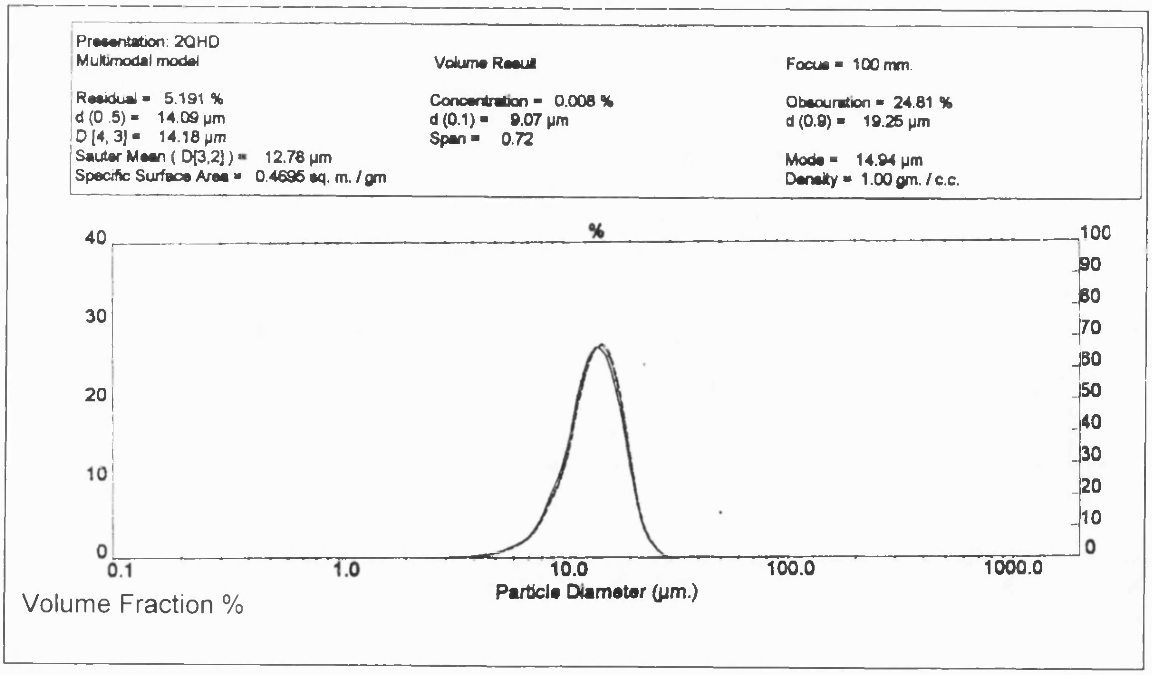

Presentation: 2QHD
Multimodal model

Volume Result

Focus = 100 mm.

Residual = 5.191 %
d (0 .5) = 14.09 µm
D [4, 3] = 14.18 µm
Sauter Mean (D[3,2]) = 12.78 µm
Specific Surface Area = 0.4695 sq. m. / gm

Concentration = 0.008 %
d (0.1) = 9.07 µm
Span = 0.72

Obscuration = 24.81 %
d (0.9) = 19.25 µm

Mode = 14.94 µm
Density = 1.00 gm. / c.c.

Figure 3.1.5. Particle size distribution for powder HA 044.

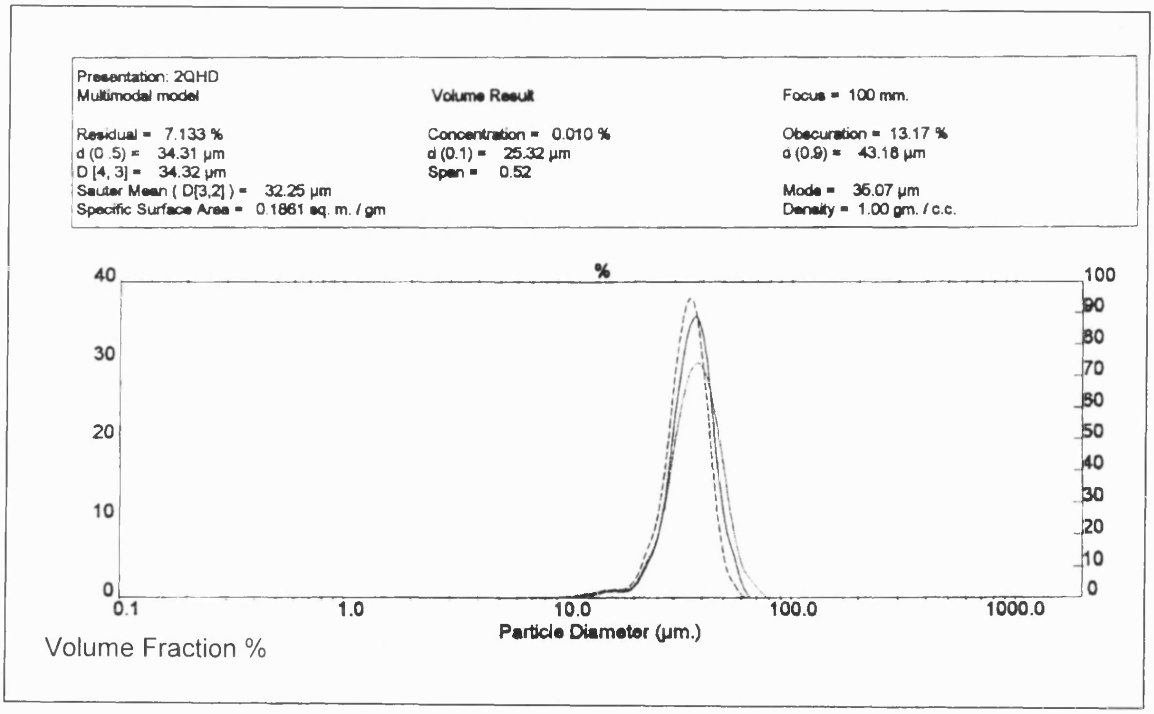

Presentation: 2QHD
Multimodal model

Volume Result

Focus = 100 mm.

Residual = 7.133 %
d (0 .5) = 34.31 µm
D [4, 3] = 34.32 µm
Sauter Mean (D[3,2]) = 32.25 µm
Specific Surface Area = 0.1861 sq. m. / gm

Concentration = 0.010 %
d (0.1) = 25.32 µm
Span = 0.52

Obscuration = 13.17 %
d (0.9) = 43.18 µm

Mode = 35.07 µm
Density = 1.00 gm. / c.c.

Figure 3.1.6. Particle size distribution for powder XPT W 601.

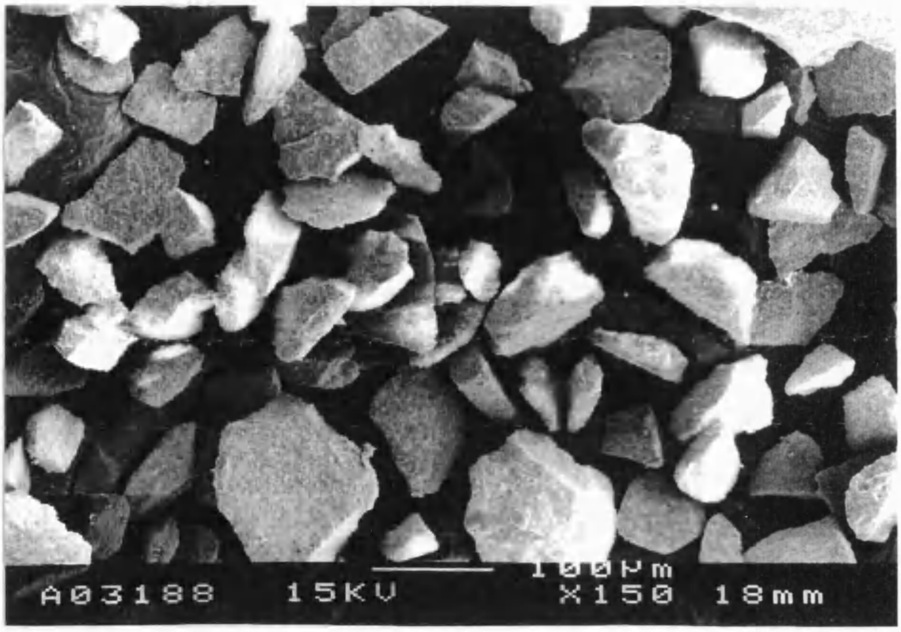

Figure 3.1.7. SEM micrograph showing a typical selection of particles from powder Amdry 6020, mag. ×150.

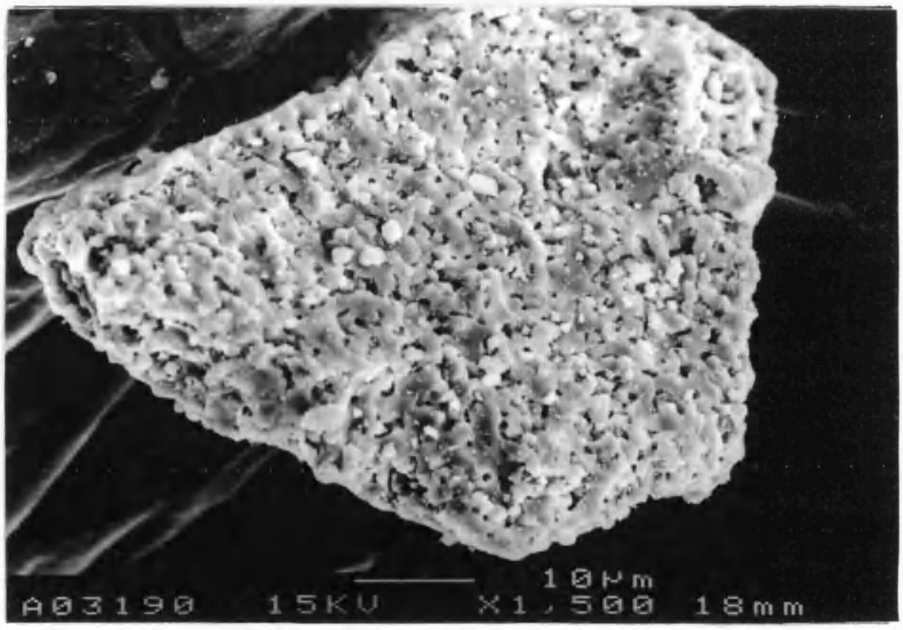

Figure 3.1.8. SEM micrograph showing a single particle of powder Amdry 6020, mag. ×1500.

Figure 3.1.9. SEM micrograph showing a typical selection of particles from powder HA 044, mag. ×1000.

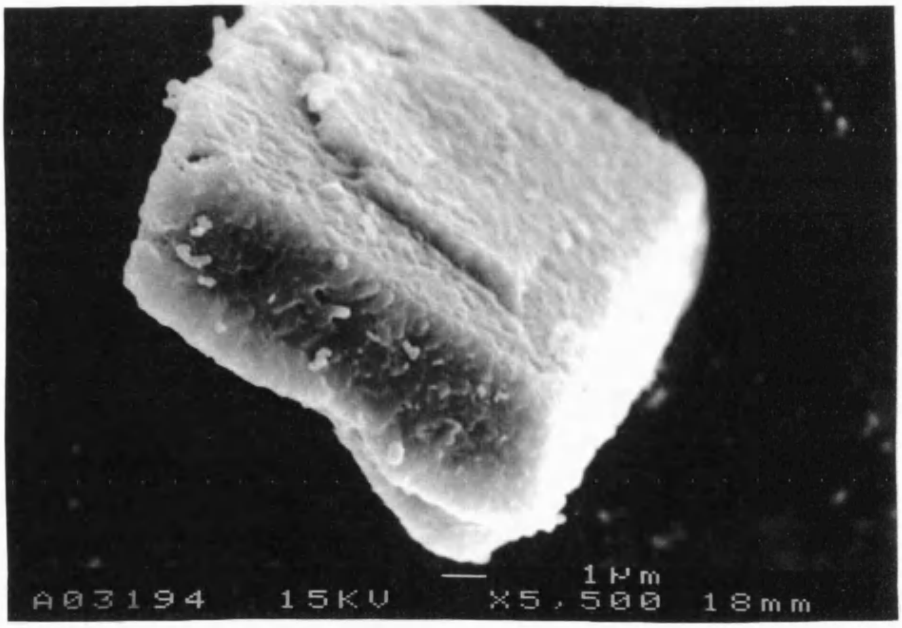

Figure 3.1.10. SEM micrograph showing a single blocky particle of powder HA 044, mag.×5500.

Figure 3.1.11. SEM micrograph showing a spherical particle of powder HA 044, mag ×10000.

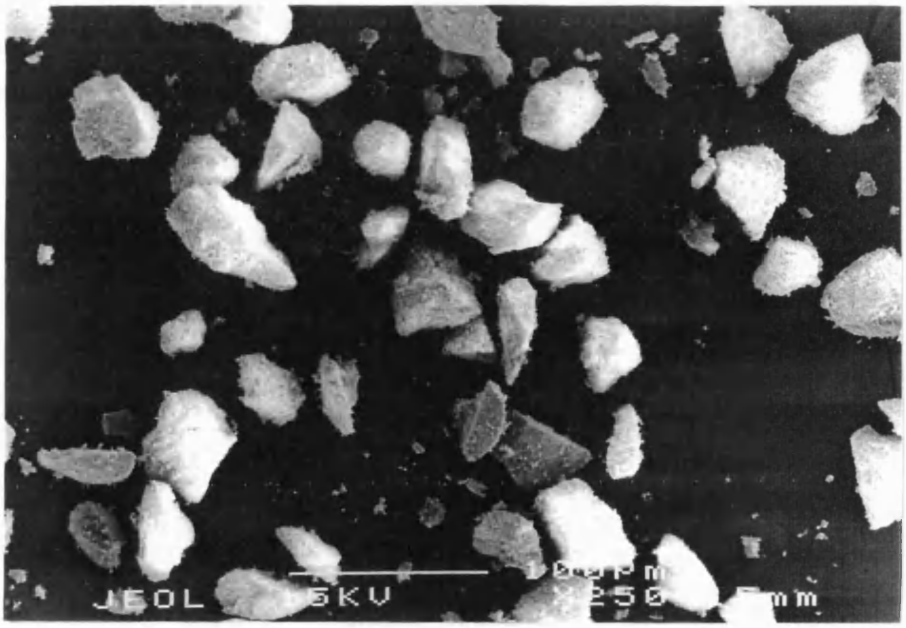

Figure 3.1.12. SEM micrograph showing a typical selection of particles from powder XPT W 601, mag. ×250.

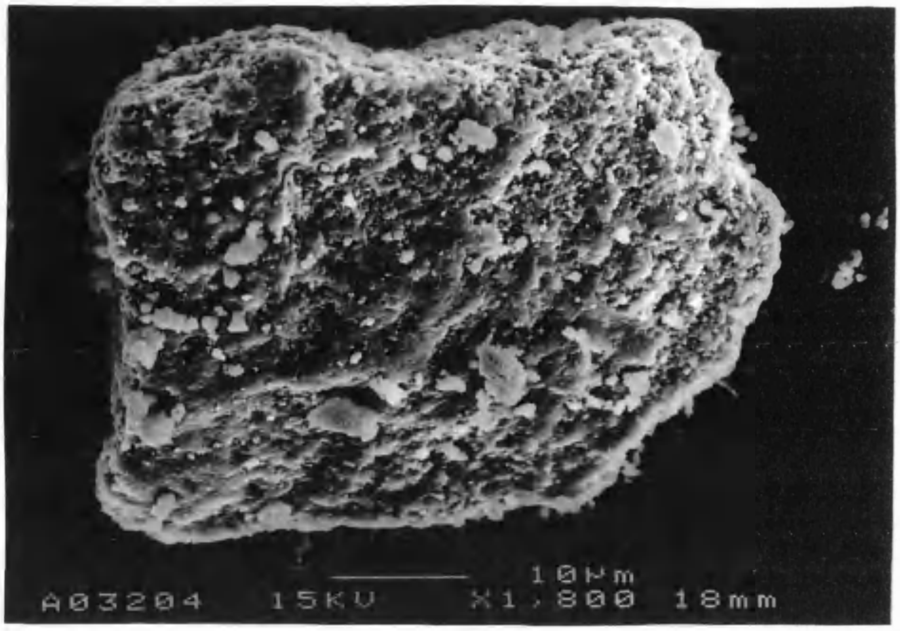

Figure 3.1.13. SEM micrograph showing a single particle of powder XPT W 601, mag ×1800.

3.2 Hydroxyapatite coating characterisation.

3.2.1 X-ray diffraction.

After XRD, the coatings showed a slight colour change in the area which had been exposed to X-rays. The colour change varied, in that for the APS and VPS coating the colour was a pale greyish green and for the CDS coating the colour was pale brown. The common features in the XRD patterns for the air plasma sprayed coatings were a higher and noisier background and lower peak intensities than the XRD pattern for the powder Amdry 6020. There were some differences in the XRD patterns between the different spraying parameters and these are stated as follows;

APS1:- (Figure 3.2.1) This pattern had a CaO peak at $2\theta=37.28°$, this corresponds to the I_{100} peak for CaO. Approximately 5% β-TCP was present in this coating. The peak width for the I_{100} hydroxyapatite peak had increased from 0.1°, in the Amdry 6020 powder, to 0.12°.

APS2:- (Figure 3.2.2) In this pattern the I_{100} peaks for β-TCP and CaO can be found. The % β-TCP can be calculated using the formula stated previously and this gives the value 8.4%. The peak width of 0.1° for the I_{100} hydroxyapatite peak is the same as the powder Amdry 6020.

APS3:- (Figure 3.2.3) There was no detectable β-TCP found in the pattern but some CaO was present, similar to APS1. The peak width for the I_{100} hydroxyapatite peak was 0.2°, which is a larger increase than in APS1.

APS4:- (Figure 3.2.4) This coating, as well as APS5 and APS6, had a higher background noise than the other coatings. There was no β-TCP or CaO detected in the pattern. The peak width of the I_{100} hydroxyapatite peak is 0.12°, wider than for the powder Amdry 6020.

APS5:- (Figure 3.2.5) The pattern for this sample is very similar to APS4.

APS6:- (Figure 3.2.6) The pattern for this sample is very similar to APS4.

The XRD patterns for samples CDS1 and CDS3 were very similar, figure 3.2.7. The background noise had increased, the peak intensities decreased and the peak widths had generally increased compared to the XRD pattern for powder HA044. A small peak was detected which corresponded to I_{100} β-TCP peak, this was present in both coatings but fractionally larger in CDS1 than CDS3. This peak was broad and represented approximately 4% β-TCP. All the other peaks in the pattern could be attributed to hydroxyapatite.

The XRD pattern for sample VPS1 showed mainly hydroxyapatite peaks, figure 3.2.8. The background noise had increased compared to that of the spraying powder and some β-TCP has formed due to spraying. The β-TCP peak in the XRD pattern for sample VPS1 corresponds to approximately 6% β-TCP.

3.2.1.1. Crystallinity of HA coatings.

The crystallinity of all the HA coatings are shown in table 3.2.1.

The error on crystallinity measurements is ≈±3%.

	APS1	APS2	APS3	APS4	APS5	APS6	CDS	VPS
crystallinity %	59	68	63	67	76	74	62	70

Table 3.2.1. Crystallinity measurements for HA coatings.

3.2.1.2. Residual stress in HA coatings.

The residual stress measurement for the HA coatings are shown in figure 3.2.9. The residual stresses in the coatings are calculated from the measurement of 2 peak positions in the XRD scan. The error in measuring the peak position is ±0.005° 2ϑ, which corresponds to an error in residual stress of ±15 MPa. The highest residual stress is in the VPS coating and the lowest in the CDS coating.

The HA coating APS2 was polished back parallel to the substrate and XRD scans were acquired at different coating depths. The residual stress in the coating was calculated at each depth through the coating. The residual stress measurements through the thickness of coating APS2 are shown in figure 3.2.10.

3.2.2. Optical microscopy.

DIC optical micrographs are shown of all HA coatings, figures 3.2.11 to 3.2.18. DIC was used rather than reflective light microscopy as the structure of the coating can be more readily seen using this technique.

In sample APS1, figure 3.2.11, there are splats running parallel to the surface and what appear to be unmelted particles containing fine porosity. A few lateral cracks can be seen running across the splats as well as from the surface. The interface between the coating and the substrate is good, with close contact between the two. Sample APS2, figure 3.2.12, has a much coarser structure with fewer unmelted particles than APS1. The flow lines caused by the particles splatting on the surface are broader than in other coatings. There are large lateral cracks in the coating and also some large pores. Sample APS3, figure 3.2.13, is very similar to APS1 but appears more porous. Samples APS4, 5 and 6, figures 3.2.14, 3.2.15 and 3.2.16 respectively, are very similar. Porosity is present in all three coatings, although the pores are smaller than those found in samples APS1 - 3. The structure is finer than samples APS1 - 3, without long flow lines. The structure of APS6 is finer than APS4 and APS5.

It can be seen that the structure of the CDS coating, figure 3.2.17, is fine and there are two phases in approximately equal quantity. The coating appears to be relatively dense with close contact at the interface with the substrate. There are some small pores in the coating, which mainly appear in the lighter of the two phases present. A few cracks are present in the coating, which run from the surface to approximately two thirds of the way through the coating. Near the middle of the coating some of cracks branch and propagate parallel to the surface. These cracks were found along the coating length at approximately equal distance in both of the CDS coatings.

The morphology of the VPS HA coating can be seen in figure 3.3.18. The coating is built up of parallel splats similar to samples APS1-3, but the structure is finer and there is less porosity. The coating to substrate interface is good with the coating being in close contact with the interface. There are some grit particles at the interface, which originate from the grit blasting process prior to plasma spraying.

3.2.2.1. Porosity measurements.

The porosity in the HA coatings, measured by image analysis of the polished coating cross-sections, are shown in table 3.2.2.

	APS1	APS2	APS3	APS4	APS5	APS6	CDS	VPS
porosity %	10	11.7	12.00	12.9	15.4	12.7	7.5	5.6
Standard dev.	2.1	1.6	1.8	2.1	2.2	1.8	1.3	0.6

Table 3.2.2. Percentage porosity for HA coatings.

A graphical presentation of the percentage porosity of the HA coatings is shown in figure 3.2.19. The porosity in the CDS and VPS coatings is much lower than the APS coatings.

3.2.2.2. Coating thickness measurements.

The thicknesses of the HA coatings are shown in table 3.2.3 and graphically in figure 3.2.20. The coating thickness deposited for each thermal spraying cycle is shown in table 3.2.4 and graphically in figure 3.2.21. The coating thickness deposited per cycle is a measure of the efficiency of the different spraying parameters, as the powder feed rate is constant for all APS coatings.

	APS1	APS2	APS3	APS4	APS5	APS6	CDS1	CDS3	VPS
coating thickness (μm)	96.2	212.4	112.8	108.7	126.4	156.0	148.0	167.2	128.4
STD (μm)	14.6	19.7	11.9	11.4	12.4	11.1	7.6	12.6	9.5

Table 3.2.3. HA coating thickness measurement.

	APS1	APS2	APS3	APS4	APS5	APS6
coating thickness per cycle (μm)	48.1	106.2	56.4	13.6	31.6	13.0
STD (μm)	7.3	9.9	6.0	1.4	3.1	0.9

Table 3.2.4. Thickness of HA coating for 1 thermal spraying cycle.

3.2.3. Scanning electron microscopy of HA coatings.

The surface of sample APS1, figure 3.2.22, clearly shows splats of hydroxyapatite. It can be seen that the particles have melted and flow has taken place. Porosity is visible in the surface of the coating, ranging in size from 1 to 10μm. On sample APS2, figure 3.2.23, it is even more evident that melting has occurred, the surface being quite smooth apart from some nodules. Cracks can also be seen on the surface of this coating. Sample APS3, figure 3.2.24, is very similar to sample APS1 but with far more nodules 1 to 4μm in size clustered on the surface. Sample APS4, figure 3.2.25, has a very fine structure with many small fragmented particles on the surface. At a higher magnification, figure 3.2.26, it can be seen that melting has occurred and there are small pores on the surface ranging in size from 1 to 10μm. Samples APS5 and APS6 are very similar to sample APS4.

The surface of samples CDS1 and CDS3 are very similar, figure 3.2.27, the coatings are made up of small melted particles and pores can be seen on the surface ranging in size from 1 to 10μm. Sample VPS, figure 3.2.28, has a molten surface with small nodules 1 to 10μm in size adhering to it.

The scanning electron microscope images of the cross sections of the air plasma sprayed coating showed no additional detail that had not already been observed using the reflected light and DIC optical microscope techniques.

The scanning electron microscope images of the cross sections of the CDS coating showed 2 different phases, figure 3.2.29. The cross section of the VPS coating, figure 3.2.30, shows the coating morphology in a similar way to the DIC technique. Also pores are shown more clearly using the scanning electron microscope image, indicating a higher porosity than apparent from optical microscopy techniques.

3.2.4. Surface roughness of HA coatings.

The surface roughness of the HA coatings, measured by talysurf, are shown in table 3.2.5. Several parameter were determined by the computer software employed to run the talysurf, these are:

Ra = Roughness measurement of mean peak height

Rp = Highest peak

Rv = Lowest trough

Rt = Peak to trough height

S = Mean peak spacing.

From these results it can be seen that CDS and VPS coatings are smoother than the APS coatings. Samples APS1 and APS2 the Ar/N gas mixture APS coatings have the roughest surfaces, the other APS coating have similar roughness between 7μm and 8.2μm Ra.

	Ra (μm)	Rp (μm)	Rv (μm)	Rt (μm)	S (μm)
APS1	10.87	41.45	34.79	76.24	45.38
APS2	9.59	33.46	28.26	61.72	42.14
APS3	8.19	28.38	26.71	55.09	38.35
APS4	7.07	31.71	28.59	60.30	35.06
APS5	7.99	27.34	26.78	54.12	39.06
APS6	7.78	26.78	20.79	47.58	32.23
CDS	4.03	21.51	15.02	36.54	26.68
VPS	3.91	15.93	13.88	29.81	25.77

Table 3.2.5. Surface roughness measurements of HA coatings.

3.2.5. Discussion of Results.

The microscopy of the air plasma sprayed coatings showed the morphology of the coatings and the differences between the spraying conditions. Sample APS2, with spraying parameters which used the Ar/N_2 gas mixture, was sprayed using the highest power plasma flame. This coating was thicker than any of the other coatings due to the high temperature plasma flame having sufficient energy to melt larger particles than with the other sets of spraying parameters. This can also be seen by the thicker flow lines in the coating. Image analysis proved this set of parameters to have the highest coating deposition efficiency. There were some large pores in the coating probably caused by gas being trapped in the coating during deposition, also there were some wide cracks running laterally across the coating and some fine cracks running laterally between flow lines. These are caused by the build up of residual stress in the coating, which is due to the different expansion coefficient and thermal conductivity between the coating and the substrate. Sample APS1 was produced using the normal spraying parameters with the Ar/N_2 gas mixture to deposit the hydroxyapatite coating . This produced a good coating with a reasonable coating thickness. There were some partially melted particles in the coating which can be recognised as round particles with fine porosity. Some lateral cracks are present in the coating caused by residual stress. These were not as large as some of the cracks in sample APS2, which is probably due to a thinner coating and the powder particles being cooler when impacting the substrate resulting in a lower residual stress. The interface between the coating and substrate is good with close contact between the substrate and coating for a majority of interface viewed. Sample APS3 was produced using the lowest powered plasma flame for the Ar/N_2 gas mixture, there is very little difference between APS1 and APS3. Sample APS3 may have fractionally more unmelted particles and there are more lateral cracks in the coating. The presence of a greater number of lateral cracks could be due to the powder particles being cooler than the particles sprayed using the APS1 parameters. The particles may not flow very well on impact due to being very close to their melting point and may solidify rapidly. When a liquid solidifies, in most cases, it undergoes a rapid volume shrinkage which can cause residual stress to build up. If there is not sufficient time for the stress to be relieved higher residual stress would build up in the coating. Samples APS3 and APS1 had very similar coating deposition efficiency, but in general coating APS1 was of a higher quality due to a lower porosity and more uniform coating structure.

Samples APS4, APS5 and APS6 were very similar, these were sprayed using an Ar/He gas mixture which has a lower power than the Ar/N_2 gas mixture due to a lower enthalpy of dissociation and ionisation. All of these coatings have a finer structure than the Ar/N_2 gas mixture coatings. This is a result of the plasma not having sufficient power to melt the large particles in the powder and hence these would bounce off the substrate. The substrate/coating interface was good, with close contact at the interface for the majority of the interface viewed. A good interface should produce a good coating/substrate bond strength. Sample APS5 had a higher coating deposition efficiency than samples APS4 and APS6 and this was the highest power set of parameters for the Ar/He gas mixture. Samples APS4 and APS6 had very similar coating deposition efficiency. The Ar/He gas mixture coating had a higher porosity than the Ar/N_2 gas mixture coatings with sample APS5 having the highest porosity. The porosity in the Ar/He gas mixture coatings was finer than in the Ar/N_2 gas mixture coatings. The higher porosity was probably due to particles not flowing on impact with the substrate and the building up of pores between splatted particles where the impacting particle does not flow into the space between other particles.

The XRD patterns for the Ar/N_2 gas mixture APS HA coatings all had CaO present in the coating and the background noise had increased compared to the XRD pattern for spraying powder Amdry 6020. The increase in background noise can be related to an increase in amorphous calcium phosphate present in the coating; also the formation of CaO can occur when hydroxyapatite has been over heated and starts to dissociate. Sample APS2 has some β-TCP present, this has been reported to occur when the spraying powder has been significantly over-heated, and also at the interface with the substrate where the cooling rate is the fastest [29]. The variation in peak width between the samples can be attributed to an increase in residual stress [36], the larger the increase is, the larger the residual stress will be.

The vacuum plasma sprayed sample showed a good quality coating with a high density, this is expected when using this technique. There was close contact at the coating/substrate interface but there were some grit particles at the interface which were probably left over from grit blasting of the substrate surface prior to plasma spraying. The XRD pattern for this sample showed a β-TCP peak, this has been reported previously and is a problem when using a reduced pressure atmosphere to spray hydroxyapatite.

The CDS sprayed samples showed a two phase structure, this could possibly have been caused by the spraying powder HA044 being made up of two different types of particle. The two phases were in approximately equal proportions like the two different particles in powder HA044. If this is the reason for the two phase structure, it is difficult to say why the particles ,once they have been sprayed, still remain different. As the particles are required to melt, and if both particles have the same chemical structure, on impacting the substrate no memory of their previous form should be translated to the coating. Possibly the two particles experience different heat cycles in the CDS gas jet because the two particle morphologies have different thermal properties. This could explain the two phase structure observed. The coatings were relatively dense, with nearly the same porosity as the vacuum plasma sprayed samples. There was close contact between the substrate and coating, indicating a good interfacial bond strength. The XRD pattern for the CDS sprayed coating showed that the background noise and peak width had increased compared to the powder HA044. This could be attributed to amorphous calcium phosphate being formed during spraying and also a residual stress increase. There was also a small peak which corresponded to a β-TCP phase, this phase was present in the powder HA044 and the increase in β-TCP from powder to coating was approximately 2-3%.

It is a well known phenomena in crystals of alkali halides that these crystals which would normally be clear appear to be coloured. The reason is that impurities and defects in the crystal alter the electronic structure by putting energy levels between the valence and conduction bands. Light, in the visible range, is absorbed by electrons being excited to these energy levels. The defects which cause the phenomena are called colour centres. The colour centre which absorbs the most visible light is known as the F centre. Colour centres are also seen in other materials, it has been reported that F centres can be readily generated in crystals that contain Ca^{2+} or hydroxyl ions. This would suggest that hydroxyapatite is particularly susceptible to the formation of F centres. Other defects such as interstitials and vacancies also cause colour centres. Defects are formed when the material is subjected to an external energy force. X-ray diffraction provides sufficient energy to cause the formation of F centres and other defects. This would explain the observed colour change of the plasma sprayed coating after X-ray diffraction. The different colour of the CDS sprayed sample to the APS and VPS sprayed sample could possibly be due to the start powders having minute differences in impurities, or the sprayed coating having a different composition due to the lower temperature and higher kinetic energy.

The residual stress in the coating was measured using XRD. The X-ray beam penetrates only a few microns into the coating, therefore the values calculated for residual stress correspond to residual stress near the surface of the coating. This tends to be the maximum residual stress in the coating, as the maximum stress in a bent beam is always at the surface of the beam. The stresses are tensile for all the sprayed coatings, which is undesirable for a biomedical coating. Tensile stresses increase the chance of cracks forming in the coating, which can lead to seepage of body fluids and eventually cause the coating to spall off. There is a difference between the stresses calculated for the **a** and **c** directions, this is probably due to the **a** and **c** directions having different moduli and possibly some directionality in the coating. No values for the moduli of the crystallographic directions in hydroxyapatite have been reported in the literature. Thermal sprayed coatings are a non-homogeneous mixture of different phases of the sprayed material. The modulus used to calculate the residual stress using XRD was obtained from ultrasonic measurement of sintered HA. Therefore the modulus of the coating is probably considerably lower than the measured value of the sintered HA. This would cause all the residual stress measurements to be a factor lower than stated. The modulus of thermal sprayed HA coatings has not been published in the literature to date, and for comparative purposes the modulus of sintered HA will suffice. As the XRD technique measures strain at an atomic level similar to the ultrasonic technique, this value of modulus seems appropriate to use. Residual stress is related to coating thickness and this can be seen in figure 3.2.10 for the HA coating APS2. Ideally the lower the tensile residual stress the longer the coating should last, as the fatigue life would improve. The Ar/He gas mixture air plasma sprayed samples have lower residual stresses than the Ar/N_2 gas mixture sprayed samples. This is probably due to the slower build up of the coating as more cycles of the plasma gun are required to deposit the Ar/He gas mixture coatings than the Ar/N_2 gas mixture. The CDS sprayed coatings appear to have a lower residual stress than the air plasma sprayed samples. Although the different spraying processes use different powders for depositing the coatings and it is the change in residual stress from powder to coating that is calculated and not the actual residual stress in the coating. The number and frequency of cracks in a coating is also a good comparative guide to how large the residual stress is. Using microscopy the size and frequency of cracks in the coating can be measured. The VPS coating has some of the largest cracks of all the sprayed coatings and it has the largest residual stress according to the XRD results. The VPS process uses a reduced pressure atmosphere which can cause problem when cooling the substrate material, as convection cooling is reduced. This can result in very different cooling characteristics and in this case has resulted in a high residual stress in the coating.

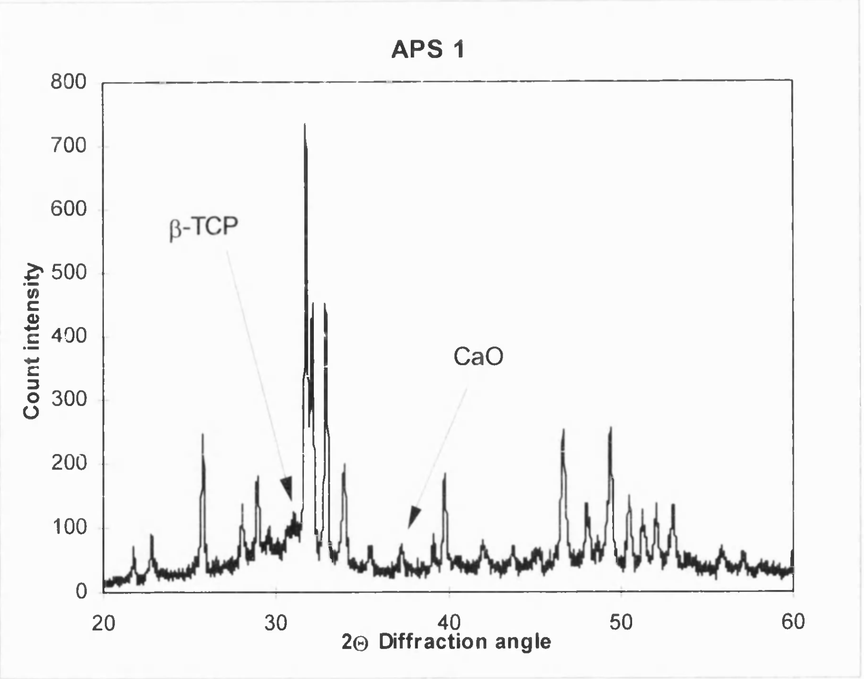

Figure 3.2.1. XRD pattern of APS1 coating.

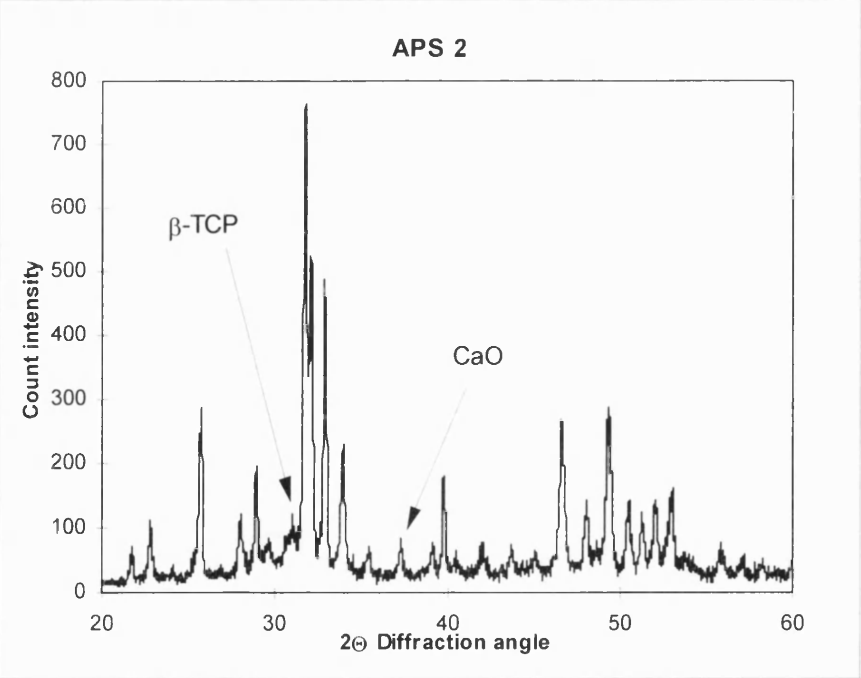

Figure 3.2.2. XRD pattern of APS2 coating.

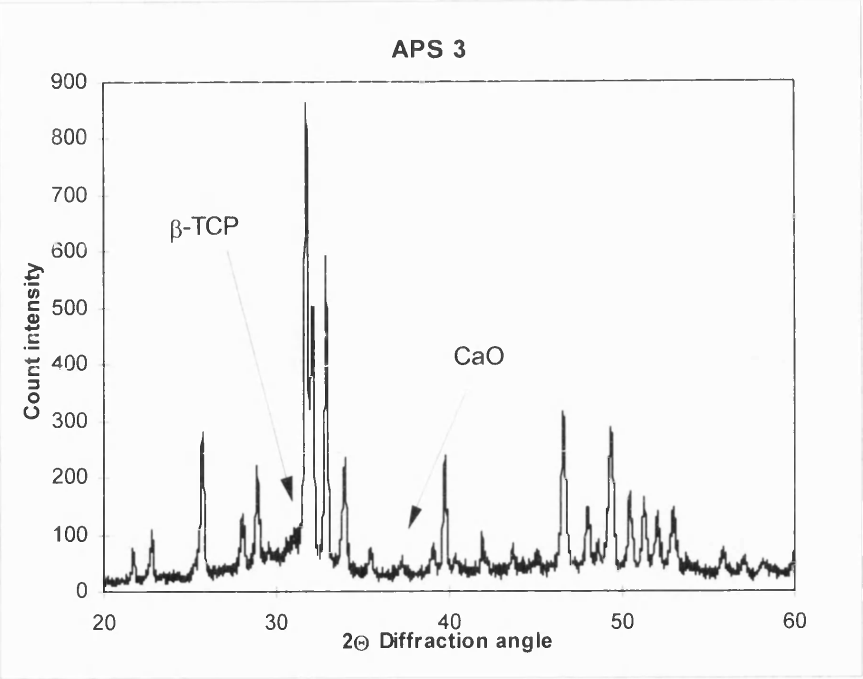

Figure 3.2.3. XRD pattern of APS3 coating.

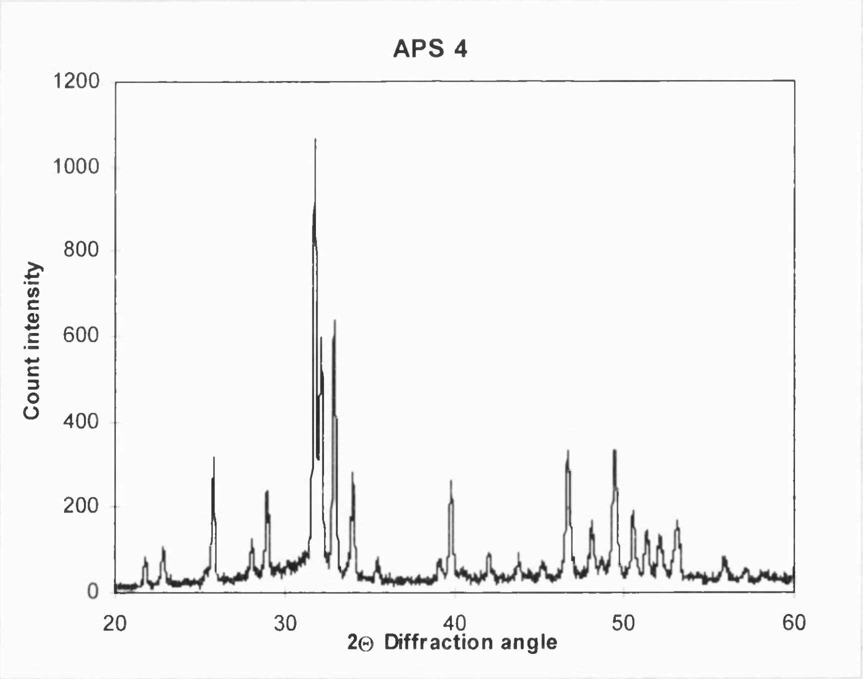

Figure 3.2.4. XRD pattern of APS4 coating.

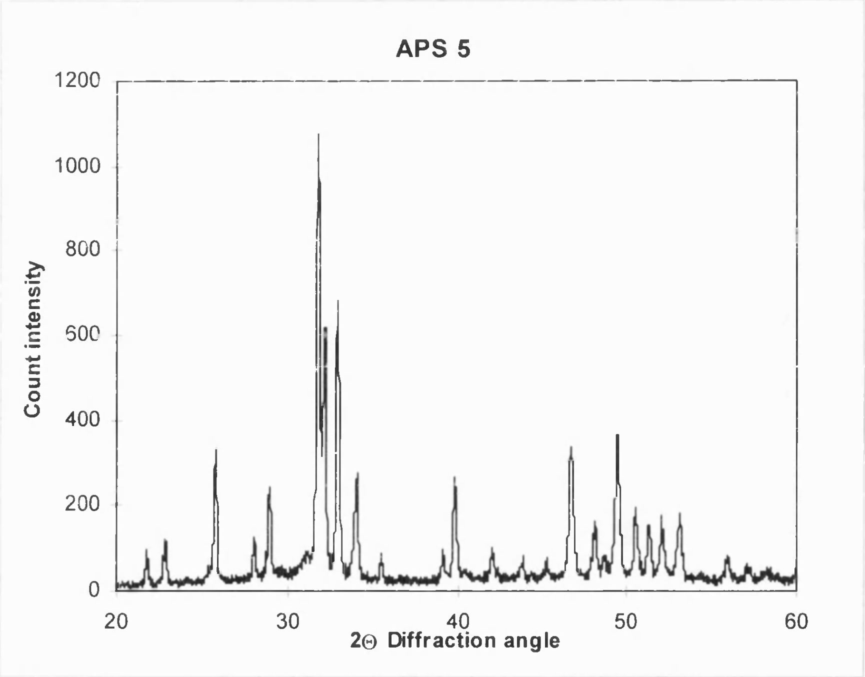

Figure 3.2.5. XRD pattern of APS5 coating.

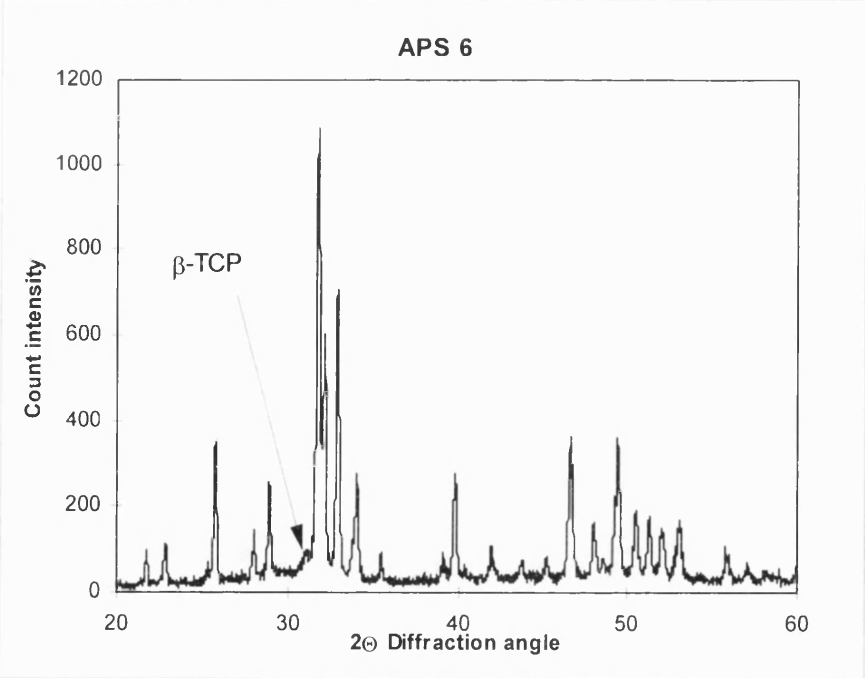

Figure 3.2.6. XRD pattern of APS6 coating.

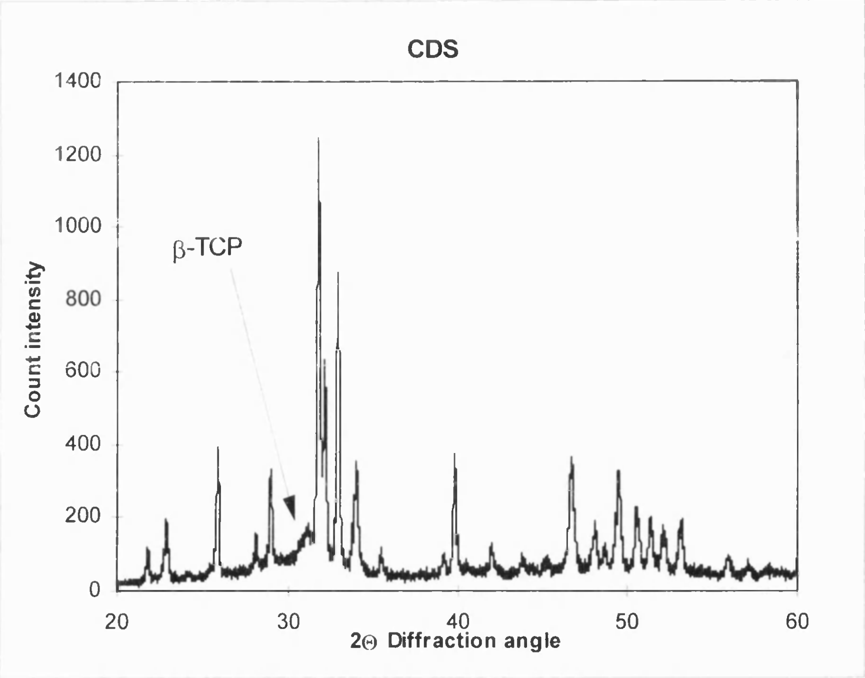

Figure 3.2.7. XRD pattern of CDS coating.

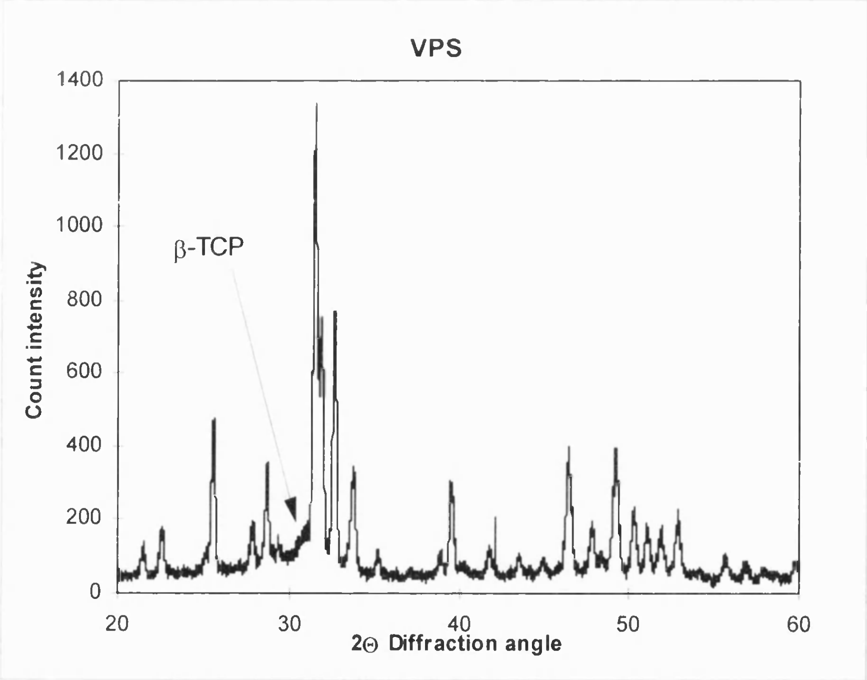

Figure 3.2.8. XRD pattern of VPS coating.

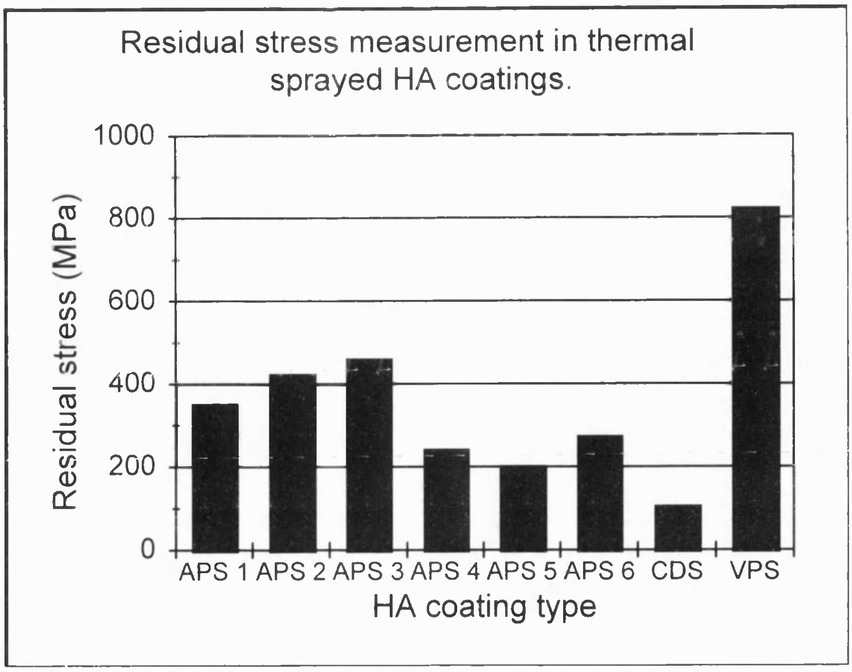

Figure 3.2.9. Residual stress measurement in HA coatings.

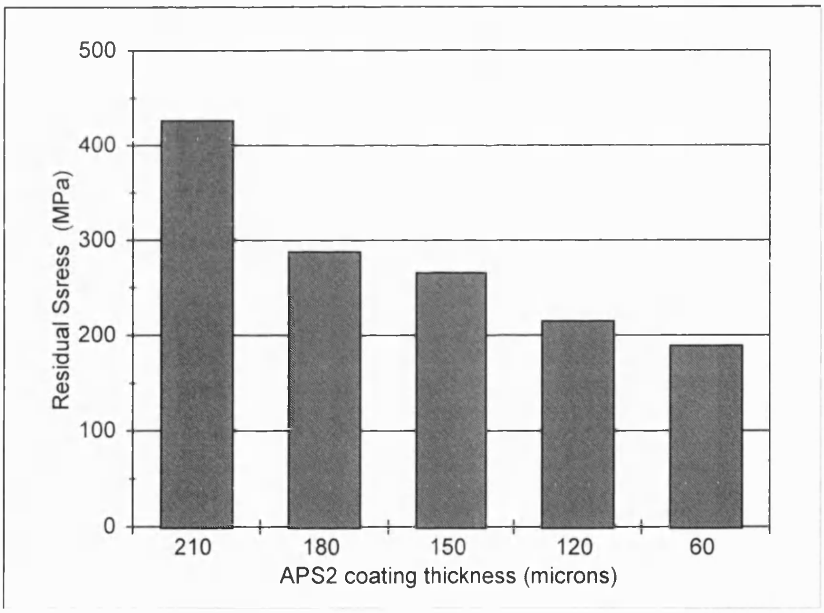

Figure 3.2.10. Residual stress measurement through the thickness of HA coating APS2.

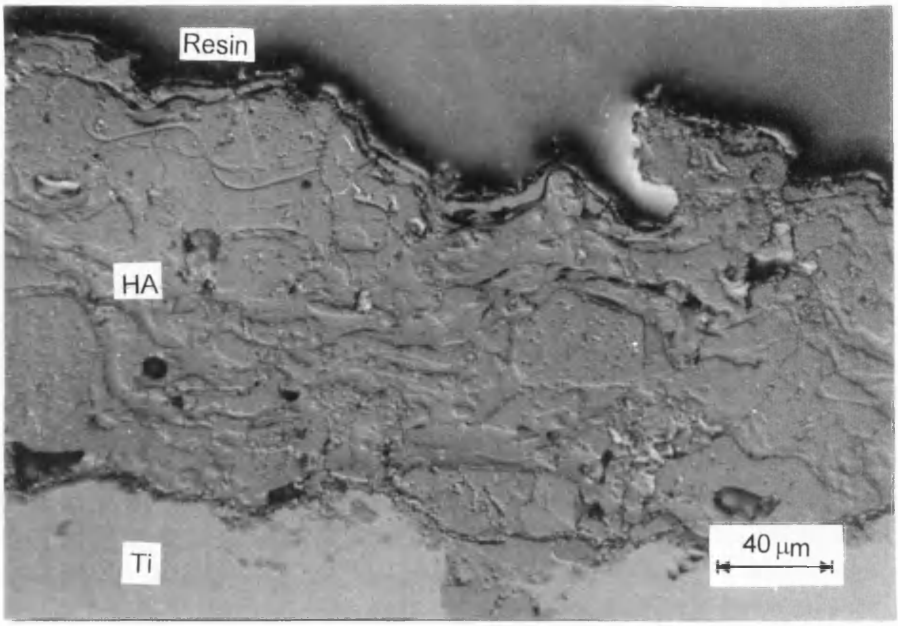

Figure 3.2.11. DIC optical micrograph of HA coating APS1, mag. ×400 .

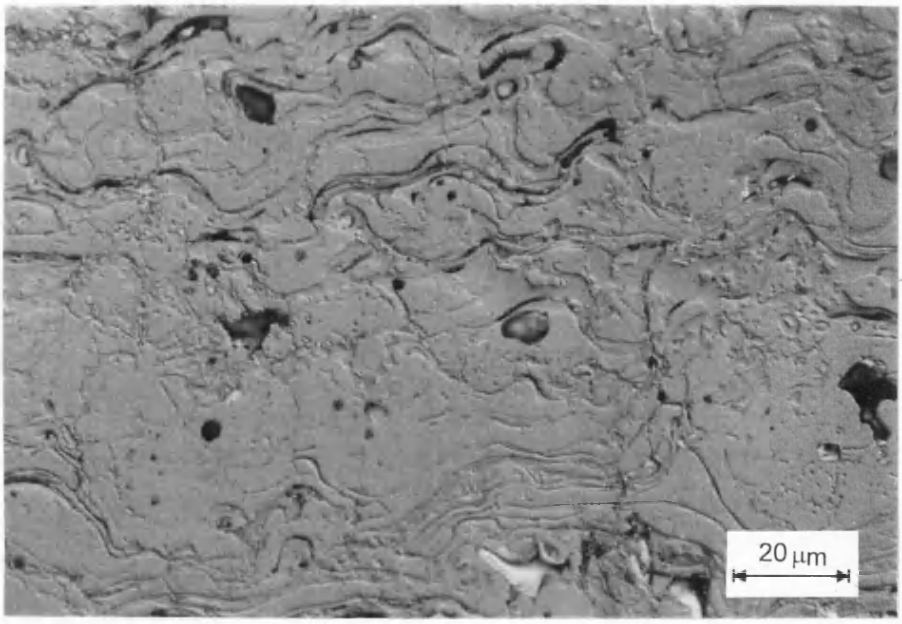

Figure 3.2.12. DIC optical micrograph of HA coating APS2, mag. ×400 .

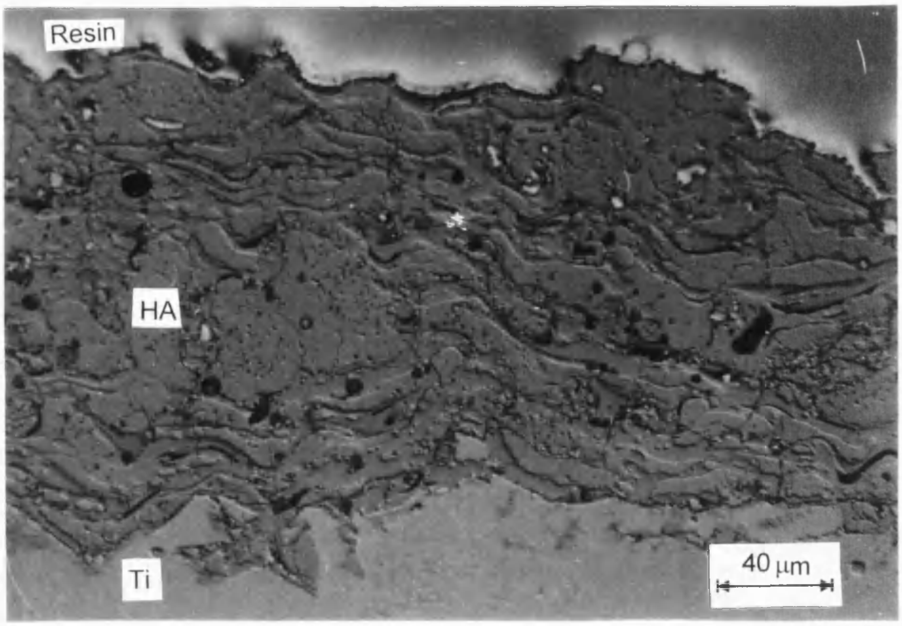

Figure 3.2.13. DIC optical micrograph of HA coating APS3, mag. ×400 .

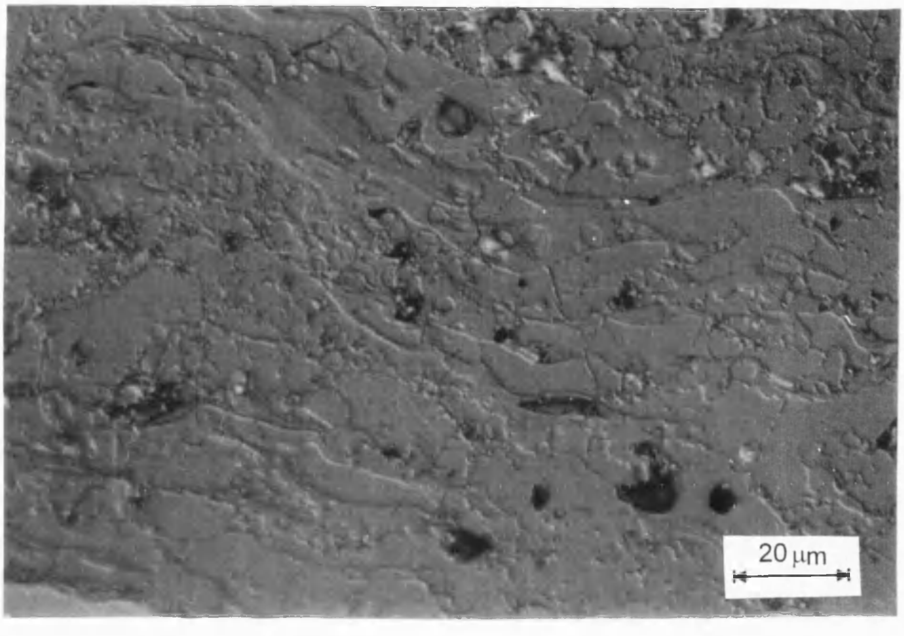

Figure 3.2.14. DIC optical micrograph of HA coating APS4, mag. ×800 .

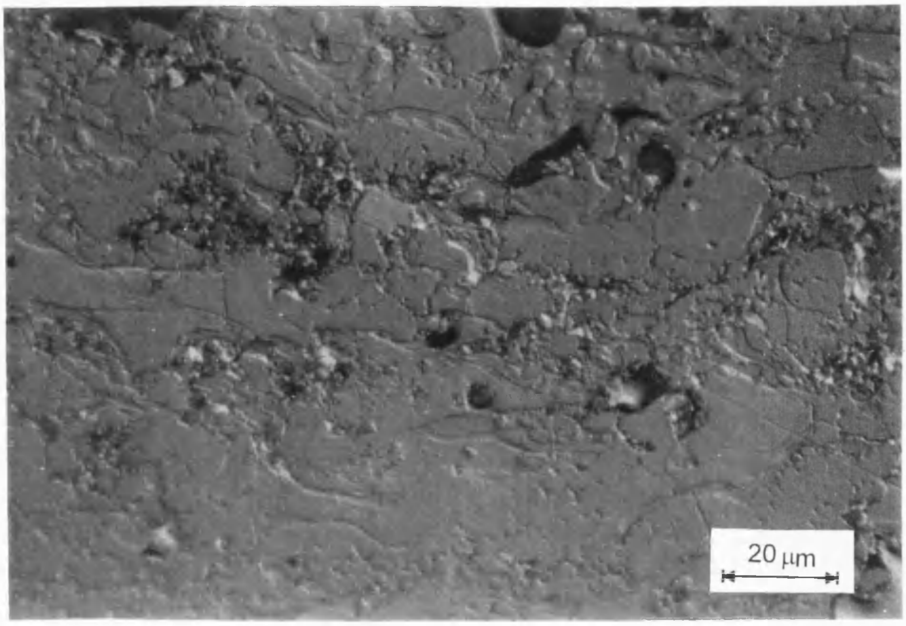

Figure 3.2.15. DIC optical micrograph of HA coating APS5, mag. ×800.

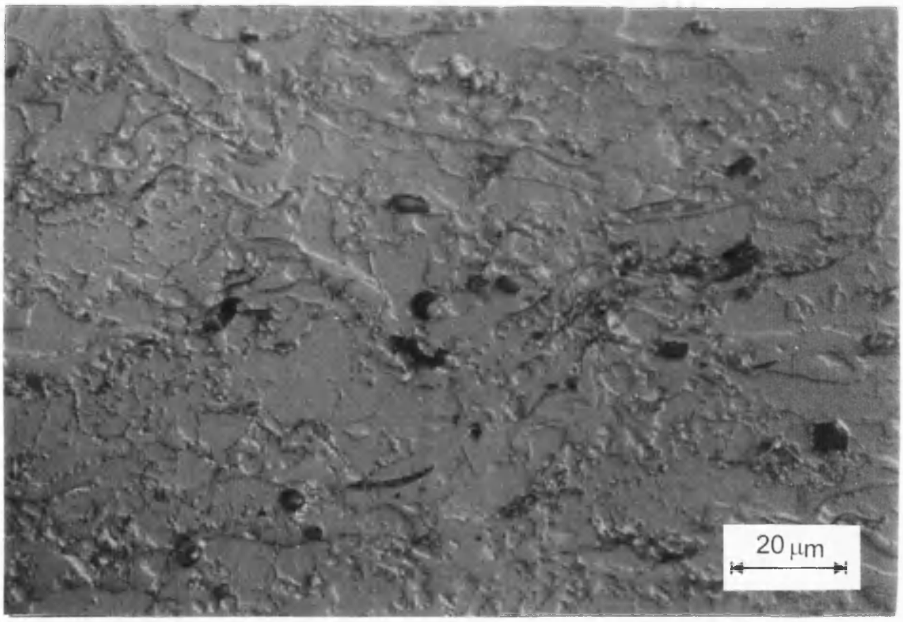

Figure 3.2.16. DIC optical micrograph of HA coating APS6, mag. ×800.

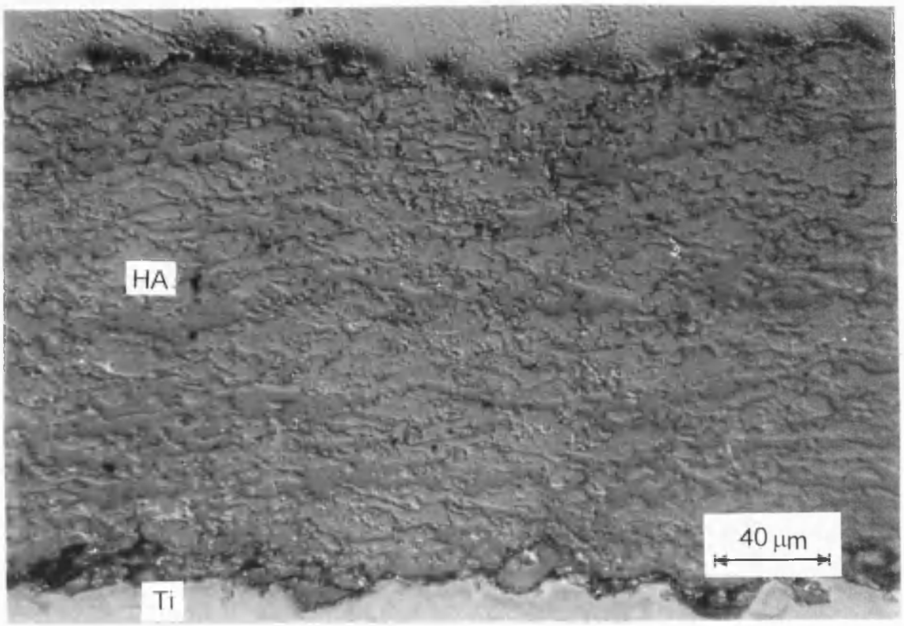

Figure 3.2.17. DIC optical micrograph of HA coating CDS, mag. ×400 .

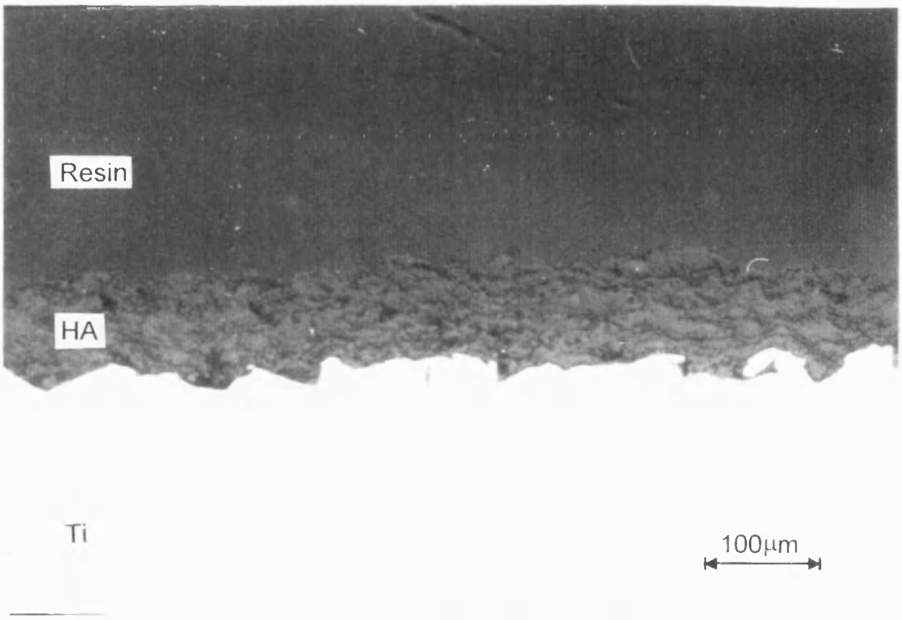

Figure 3.2.18. DIC optical micrograph of HA coating VPS, mag. × 160.

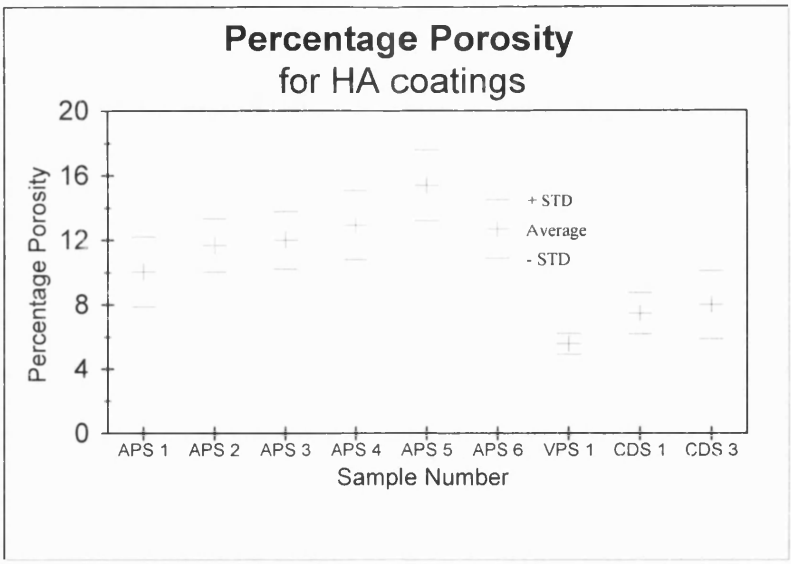

Figure 3.2.19. Percentage porosity in HA coatings.

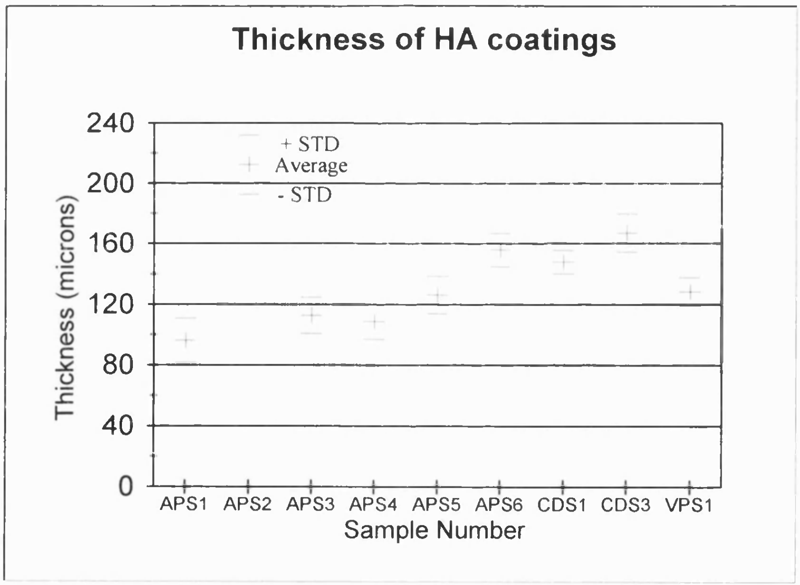

Figure 3.2.20. Thickness of HA coatings.

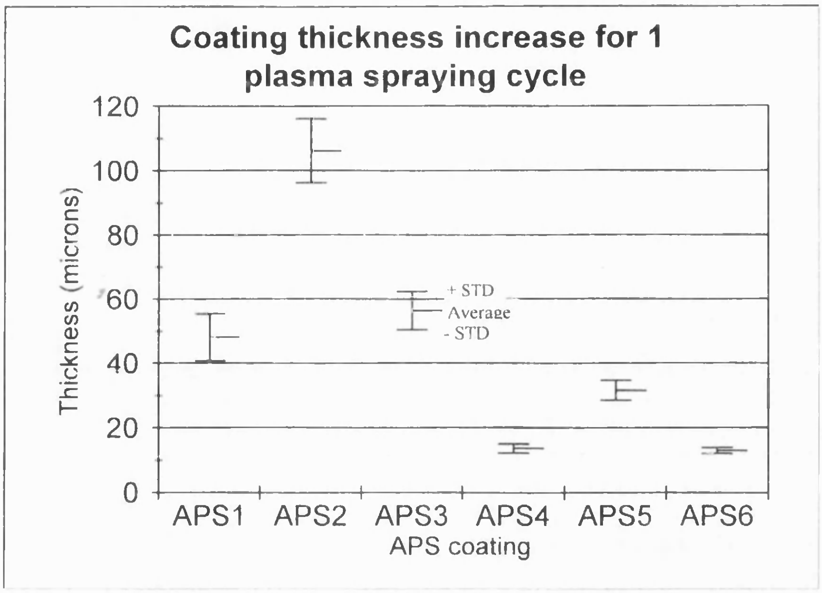

Figure 3.2.21. HA coating deposited for each thermal spraying cycle.

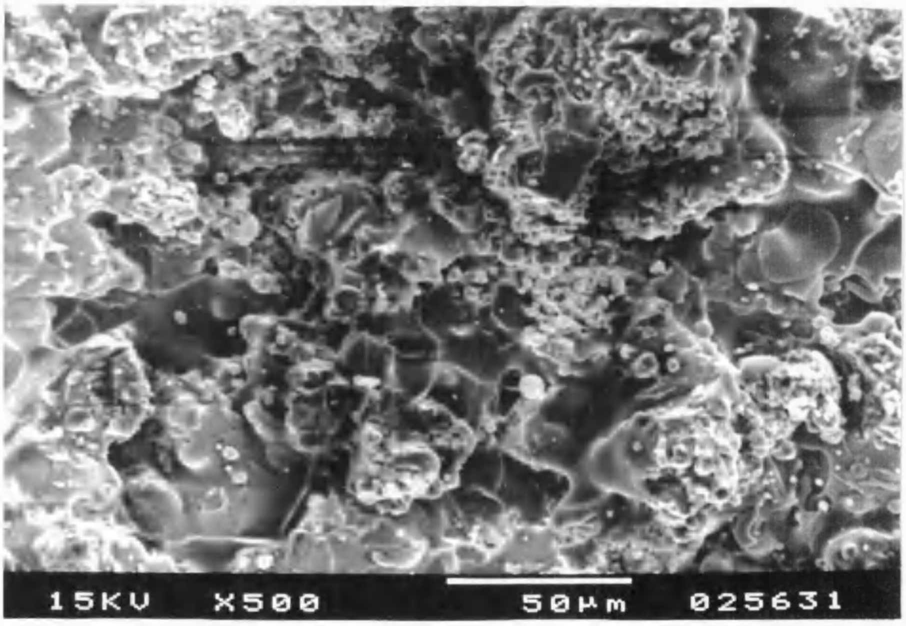

Figure 3.2.22. Scanning electron micrograph of the surface of APS1. mag. ×500.

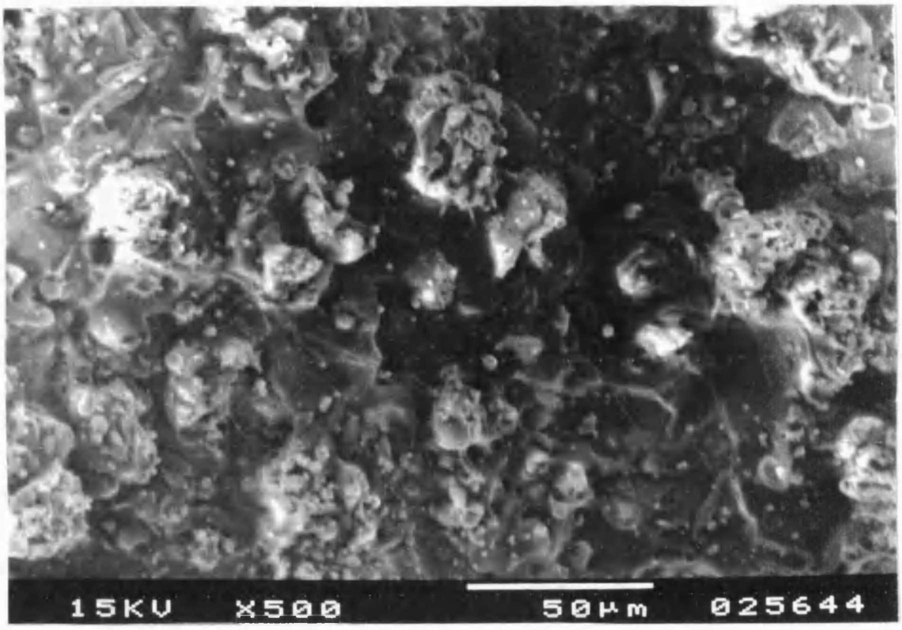

Figure 3.2.23. Scanning electron micrograph of the surface of APS2. mag.×500.

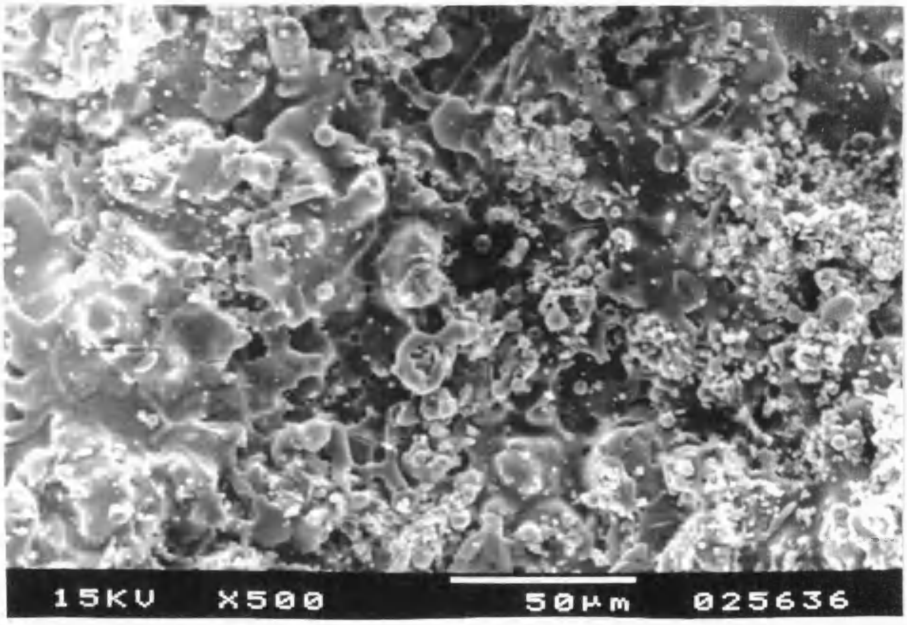

Figure 3.2.24. Scanning electron micrograph of the surface of APS3. mag. ×500.

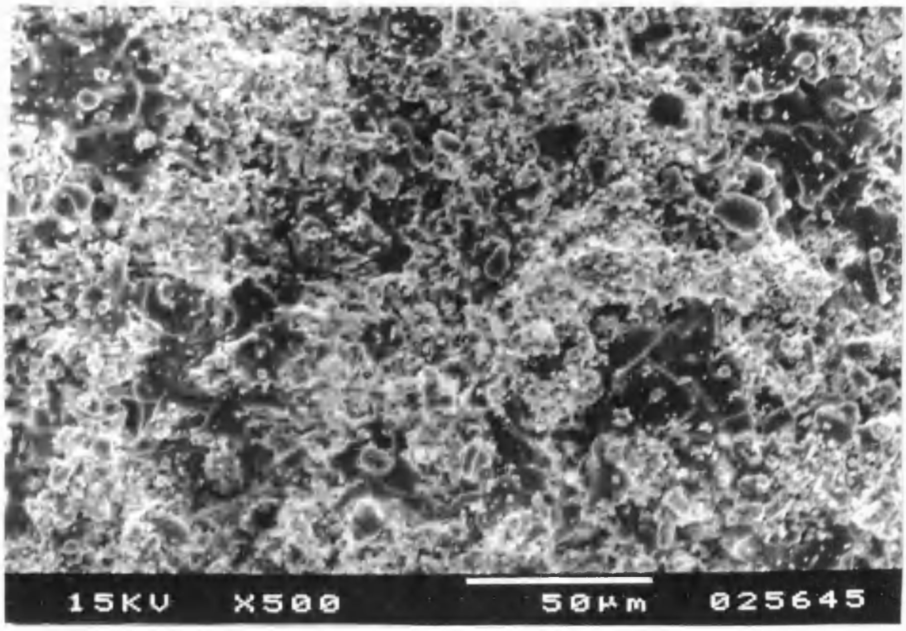

Figure 3.2.25. Scanning electron micrograph of the surface of APS4. mag. ×500.

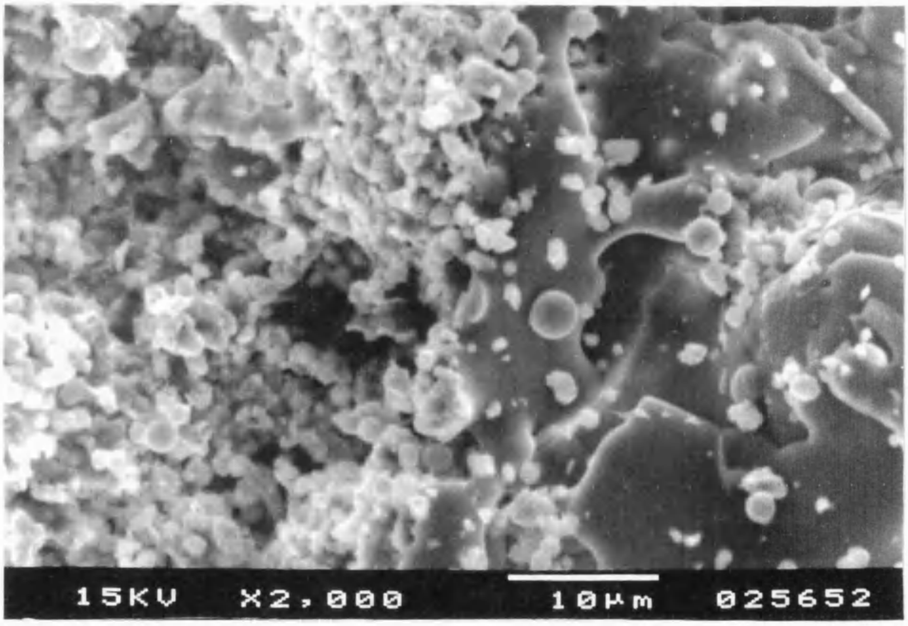

Figure 3.2.26. Scanning electron micrograph of the surface of APS4. mag. ×2000.

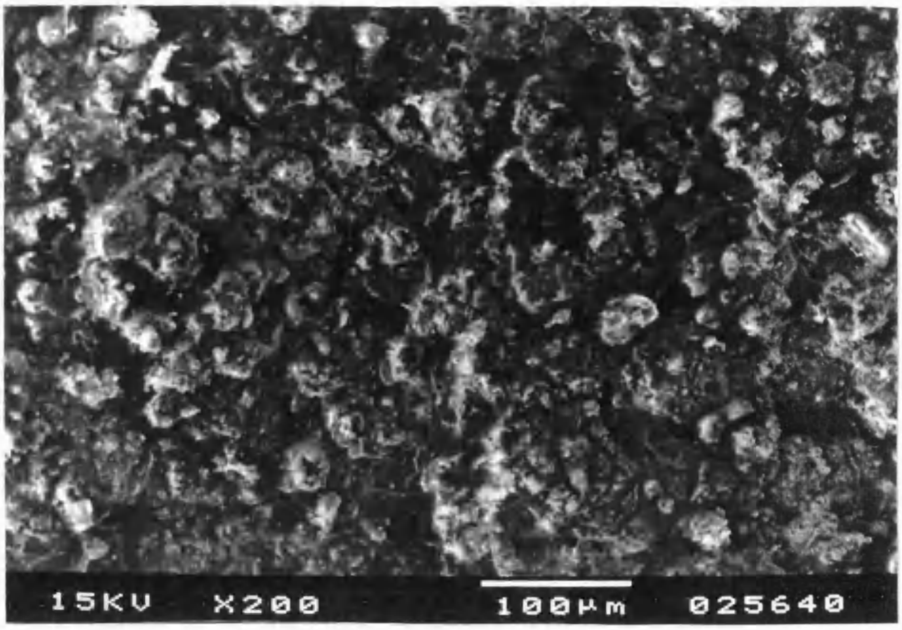

Figure 3.2.27. Scanning electron micrograph of the surface of the CDS coating. mag. ×1000.

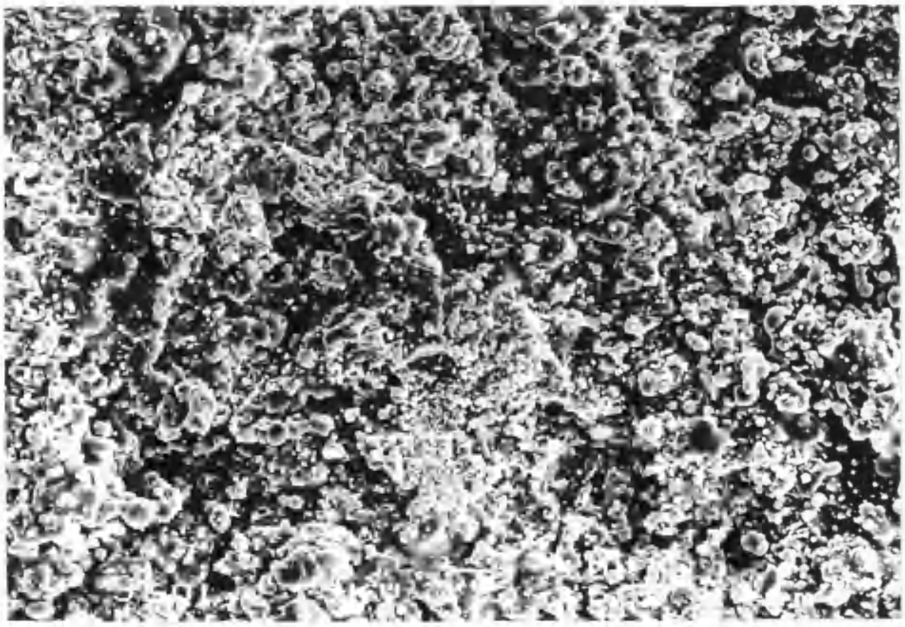

Figure 3.2.28. Scanning electron micrograph of the surface of the VPS coating. mag. ×500.

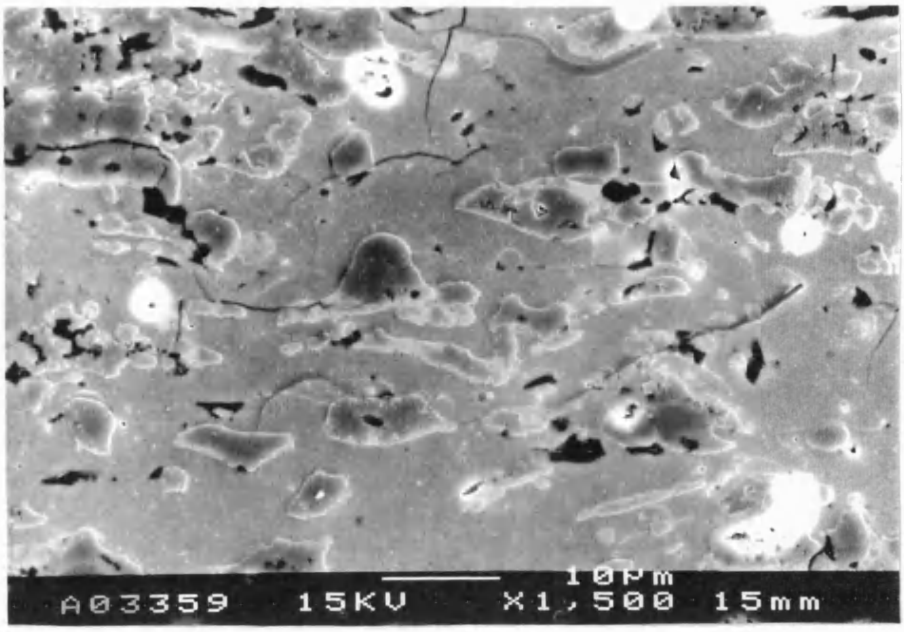

Figure 3.2.29. Scanning electron micrograph of a cross-section through a CDS coating. mag. ×1500.

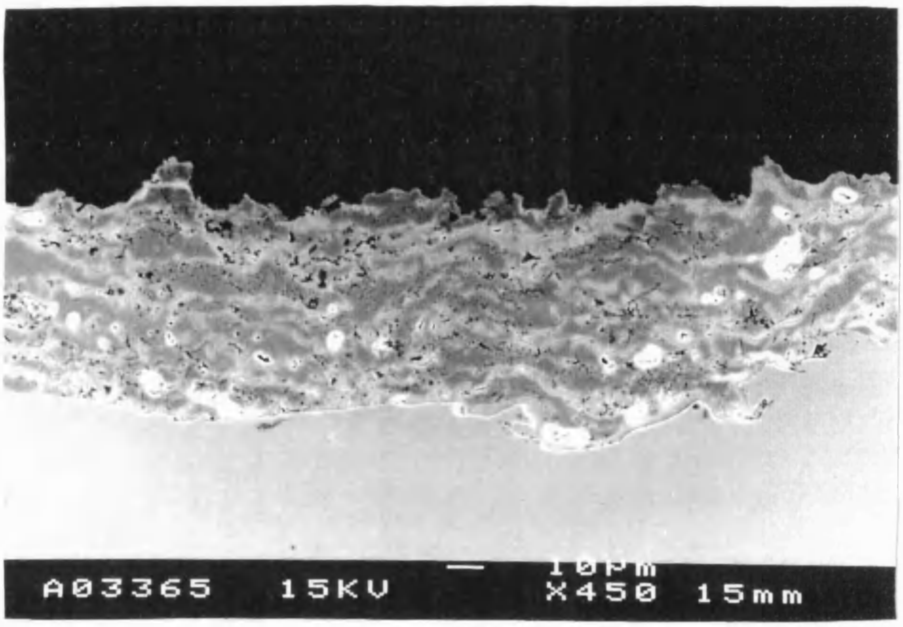

Figure 3.2.30. Scanning electron micrograph of a cross-section through a VPS coating. mag. ×450.

3.3. Shear Testing of HA Coatings.

The shear strengths of the HA coatings are shown in table 3.3.1 and graphically in figure 3.3.1. The coatings with the highest shear strength are APS2 and VPS, the lowest shear strength is the CDS coating.

3.3.1. Discussion of Results.

The shear test results approximately agree with shear and *in vivo* pushout test results published in the literature [22, 28, 32, 35]. Where the pushout test measures the adhesive shear strength of bone to an implant. The HA coated implants have typically shown values of ≈12MPa after 4 weeks of implantation, and failure is predominantly at the HA coating/implant interface. The shear test employed for the work in this thesis does not produce a true shear force at the coating/titanium interface due to the substrate bending and causing a peeling of the coating from the substrate. Although the shear strength is not a true measurement, the actual shear strength should be higher than this measured value, and for comparative purposes the test produces reasonably consistent results.

The difference in the shear test results between the different spraying parameters is possibly due to the temperature at which the particles impact the substrate. A high temperature molten particle would take longer to solidify than a low temperature molten particle as more energy needs to be absorbed by the substrate. This would give a longer time for the particle to flow and have a more intimate contact with the substrate and surrounding particles giving a coherent coating and a high adhesive strength. The high temperature molten particle is more likely to form a chemical bond with the substrate, such as the TiP_3 phase, which has been reported in the literature [53]. The higher temperature particles would also have a slower cooling rate and this would give a more crystalline coating. The crystallinity and shear strengths for the HA coatings are shown graphically in figure 3.3.2. A similar trend between the shear strength and crystallinity measurements can be seen. The highest energy Ar/N gas mixture APS coating, APS2, has the highest crystallinity for the Ar/N gas mixture coatings and the highest shear strength of all the HA coatings. The highest energy Ar/He gas mixture coating, APS5, has the highest crystallinity of all the HA coatings and the highest shear strength for the Ar/He gas mixture coatings. The reason for this coating not having as higher shear strength as the Ar/N gas mixture coatings is probably due to the lower temperature of the Ar/He plasma not melting the powder particles sufficiently to get a coating as coherent as the Ar/N APS coatings. The VPS coating also has a high shear strength and only an average crystallinity. The high shear strength of this coating is probably due to the increased velocity of the particles forming a more coherent coating compared to the APS process. The CDS coating has the lowest shear strength and this is probably due to the CDS process not melting the particles sufficiently to form a cohesive bond with the titanium alloy substrate. The CDS process relies on the high velocity of the particles rather than temperature to give enough energy to deposit a coating.

	APS1	APS2	APS3	APS4	APS5	APS6	CDS	VPS
No. of tests	11	4	5	10	10	8	5	5
average (MPa)	8.6	11.3	9.8	8.6	10.3	9.3	7.3	11.2
std (MPa)	2.36	1.99	1.06	1.05	1.38	0.87	1.18	0.63

Table 3.3.1. Shear strength of HA coatings.

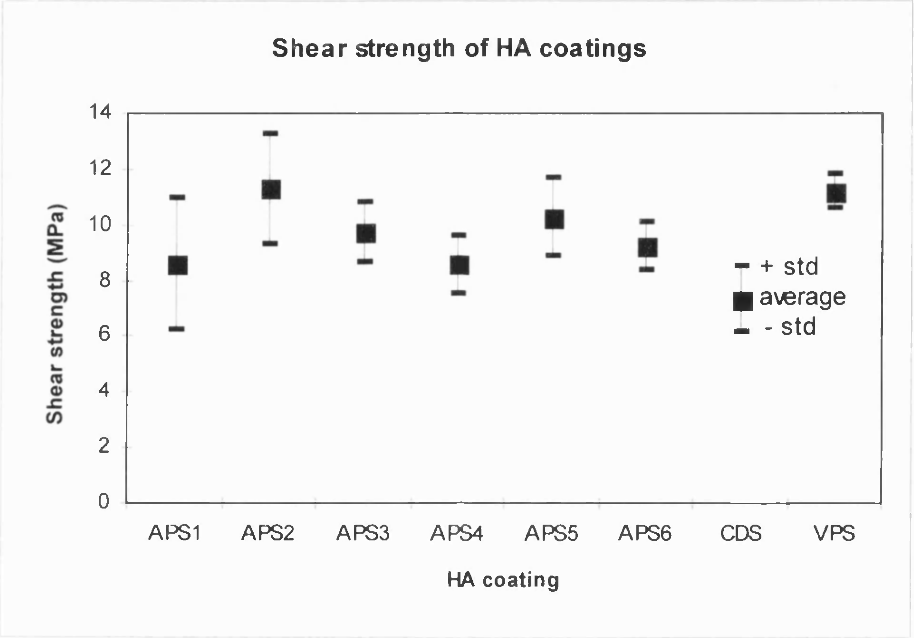

Figure 3.3.1. Shear strength of HA coatings.

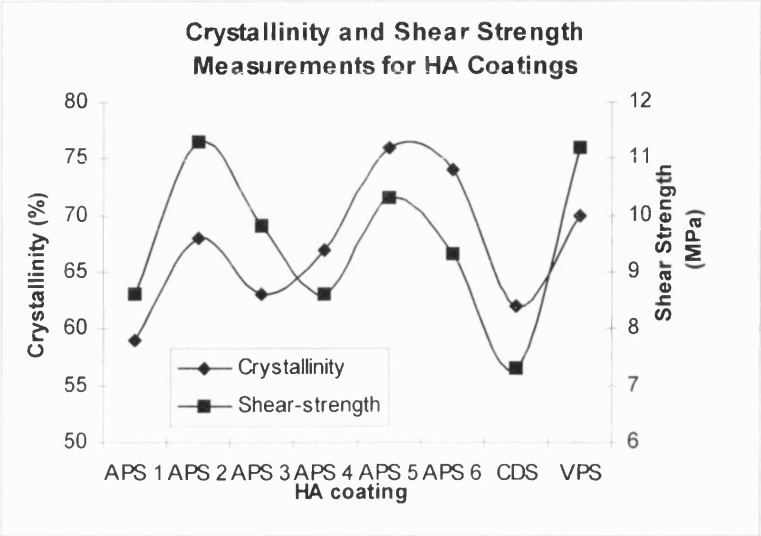

Figure 3.3.2. Crystallinity and shear strength measurement for HA coatings.

3.4 Tensile testing of HA coatings.

The tensile bond strength of the HA coatings is shown in table 3.4.1. The average tensile bond strength is calculated from a sample of 10 tensile test results. The standard deviation is nearly 50% of the tensile bond strength in the case of APS5, APS6 and the CDS coatings. This degree of inaccuracy is too high to draw any valid conclusions from these results and therefore tensile bond strength measurement was not carried out on samples APS1, APS2 and APS3. The variability in the tensile bond strength is caused by a combination of factors, the main factor being alignment of the test sample during gluing. If a sample is misaligned the initial applied force will act to straighten the test sample, which effectively causes a bending moment and a high stress concentration at the edge of the bond line which can initiate a crack and lead to premature failure.

Unfortunately the alignment could not be improved within the time scale of this project and as previously stated the full program of tests was not completed.

	APS4	APS5	APS6	VPS	CDS
Tensile strength (MPa)	23.2	6.5	8.1	22.6	8.0
STD (MPa)	4.83	2.91	3.05	3.82	3.33

Table 3.4.1. Tensile bond strength of HA coatings.

3.5 Acoustic emission of HA coatings.

The four point bend test was run for a duration of ≈400 seconds until the titanium alloy substrate was permanently deformed, which corresponded to a deflection of ≈6.6mm and ≈6% strain in the tensile surface of the substrate. Tests which were run past the elastic limit of the titanium alloy showed evidence of debonding of the HA coating and a rapid increase in AE events.

The acoustic emission (AE) events were recorded for the duration of the test. The computer software sorts the AE events by measuring the amplitude of the event and counting into channels of 2.4dB width. The number of counts in each channel is updated every second, which gives a cumulative event count for the duration of the test. The threshold was set at channel 2, excluding events with energy less than 4.8dB which where mainly noise created by the tensometer and surroundings. The number of events in each channel at the end of the test can be shown as a bar chart. Figure 3.5.1 shows a typical cumulative event count for HA coating APS1. All HA coatings showed a similar cumulative event count to that of APS1, with a high number of low energy events and an almost exponential decay in the number of counts as the event energy increases.

The total number of events, low and high energy, for a given time period can be calculated from the AE results. The force at a given time was also recorded by the computer and the force and total number of AE events are plotted against time in figure 3.5.2 for HA coating APS4. All HA coatings showed a similar trend once the titanium alloy substrate had yielded, which was an increase in the rate of AE events. The total number of AE events recorded varied within sample batches and between different spraying parameters. Therefore the total AE event count was normalised for all tests to give a maximum of 1000 events for a test duration of 400 seconds which is just before the substrate yields. A correlation between samples with the same set of spraying parameters could be seen. Figure 3.5.3 shows 2 independent tests on the HA coating APS1, the two curves have a similar shape with a high event count rate in the initial 100 seconds. A parameter to describe the shape of the curve was proposed to allow quantitative comparison of the different HA coatings. This parameter was calculated by generating a straight line from 0 seconds and 0 AE events to 400 seconds and 1000 AE events. The difference between the straight line AE events and the measured AE events at each second was calculated. The average of these differences gives the parameter which will be referred to as **D**. A positive value of **D** indicates a curve with a high AE event count rate in the early stages of the test. A negative value of **D** suggests a high AE event count rate near the end of the test. The magnitude of **D** indicates how much higher the initial or late AE event count rate is compared to other HA coatings. Figures 3.5.4 to 3.5.10 show the normalised AE event count and the calculated **D** value for HA coatings APS2, APS3, APS4, APS5, APS6, CDS and VPS. Table 3.5.1 shows the **D** values for all HA coating.

	APS1	APS2	APS3	APS4	APS5	APS6	CDS	VPS
D	+174	-200	+1	+52	+28	-50	+8	+107

Table 3.5.1. **D** parameter for HA coatings.

A cross-section through the HA coating was taken along the long axis of the deformed sample. The sectioning and polishing techniques used are described in section 2.2.3.1. Optical and scanning electron microscopy was used to characterise the morphology of the deformed coatings. Optical microscopy shows no obvious damage in the coatings, despite the permanent deformation in the substrate. Using electron microscopy the cracks in the coating are clearly defined. Figure 3.5.11 shows an optical micrograph of the deformed HA coating of APS1. At first glance the coating looks very similar to the as-sprayed coating, a closer examination shows small cracks traversing the coating approximately a third of the coating thickness in length. Using electron microscopy, figure 3.5.12, these cracks are shown to propagate to the HA/Ti interface. Compared to other coatings there are an average number of cracks spaced approximately 200 to 500μm apart. Optical microscopy shows that APS2 and APS3 are very similar to the as-sprayed coating, figure 3.5.13. The few cracks which can be seen using optical microscopy are hairline cracks and there are apparently fewer cracks than APS1. Using the electron microscope APS2 can be seen to have more hairline cracks than are apparent using optical microscopy, figure 3.5.14. Electron microscope micrographs of APS3 show a similar appearance to

APS1, figure 3.5.15. Cracks can be seen to have initiated at the surface and propagated to the interface and are spaced approximately 300μm apart. The optical micrograph of APS4, figure 3.5.16, has a similar appearance to APS1 with cracks traversing the coating. Electron microscope micrographs of APS4 show similar images to the optical micrographs. At a higher magnification the coating layers near the surface of APS4 appears to have hairline cracks which do not proagate to the HA/Ti inteface, figure 3.5.17. APS5 and APS6 are very similar to the as-sprayed coating with only a few small cracks in the coating. Electron microscope images shows that APS5 and APS6 are similar with cracks running from the surface to the HA/Ti interface and also hairline cracks near the surface of the coatings, figure 3.5.18. The CDS HA coating has some small cracks which appear to have initiated at pores within the coating, an optical micrograph of the CDS coating is shown in figure 3.5.19. The electron microscope micrograph, figure 3.5.20, shows a similar result to the optical micrograph. The electron microscope micrograph also shows that a crack appears to be running parallel to the HA/Ti interface, suggesting that the coating is debonding from the substrate. The VPS coating appears to be similar to the as-sprayed HA coating, there are some large cracks traversing the coating and also some small cracks within the coating, figure 3.5.21. The electron microscopy of the VPS coating confirms the optical microscopy results.

3.5.1. Discussion of Results.

The acoustic emission and microscopy results for the HA coatings suggest that failure occurs by microcracking in the coating. If failure had occurred by the coating debonding from the substrate or large cracks propagating from the coating surface to the interface a high number of high energy AE events would be expected, as figure 3.5.1 shows this in not the case. Also from the microscopy of the deformed coatings debonding from the substrate and large cracks traversing the coating are not apparent.

The thicker of the coatings APS1, APS4 and VPS all had positive **D** values. The thinnest coating APS2 had the highest negative **D** parameter. This would suggest that a thicker coating would sustain more microcracking in the initial stages of deformation than a thin coating. The microcracking would probably initiate near the coating surface where the bending stress is greatest. For a thin coating the bending stress near the surface would be less for a similar deflection, therefore a lower microcracking rate in the initial stages of the test would be expected and hence a negative **D** parameter.

It has been shown previously that the Ar/He gas mixture APS coatings 4, 5 and 6 have lower residual stresses than the Ar/N gas mixture coatings APS1, 2 and 3. This could indicate why APS4, although the thickest coating, has a lower **D** parameter than APS1 which showed a similar shaped curve for the normalised AE event count. A coating with a high tensile residual stress would be expected to fail earlier, as the deflection to achieve a critical stress limit would be less.

Cracks formed in the coatings at regular intervals are consistent with the 4 point bend test. This is due to a uniform stress distribution at the coating surface. As the coating is deformed it will crack to relieve the stress when the stress reaches a critical value. The cracks will be approximately equal distance apart as the coating will relieve the stress in a uniform manor.

The **D** parameter may be useful in predicting the performance of an hydroxyapatite coating when subjected to a high load or cyclic loading. A coating with a low **D** parameter would be expected to have a good fatigue life as little damage is generated in the coating at low loads. Further work will be required to assess the usefulness of the **D** parameter.

In summary:

- HA coatings fail by microcracking when subjected to a bending stress.
- Thin coatings withstand higher deformation before substantial microcracking occurs.
- The higher residual stress in the APS Ar/N gas mixture coatings results in higher **D** parameters for similar thickness coatings.
- SEM results show APS2 to have a large number of hairline microcracks, probably due to the higher power of the APS2 plasma producing a glassy coating which is more susceptible to brittle fracture.

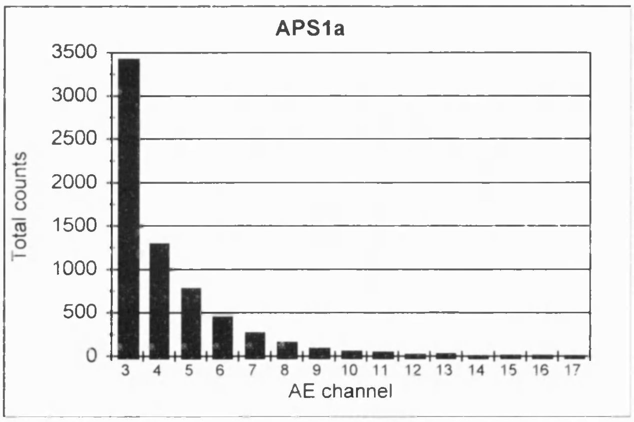

Figure 3.5.1. Cumulative event count per channel for HA coating APS1.

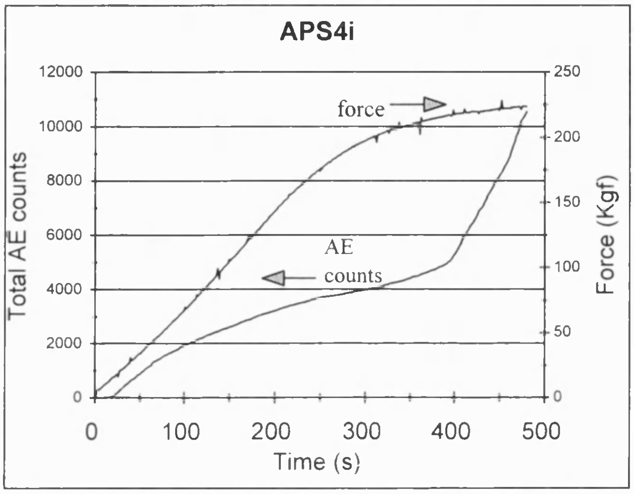

Figure 3.5.2. Force and total AE event count for HA coating APS4.

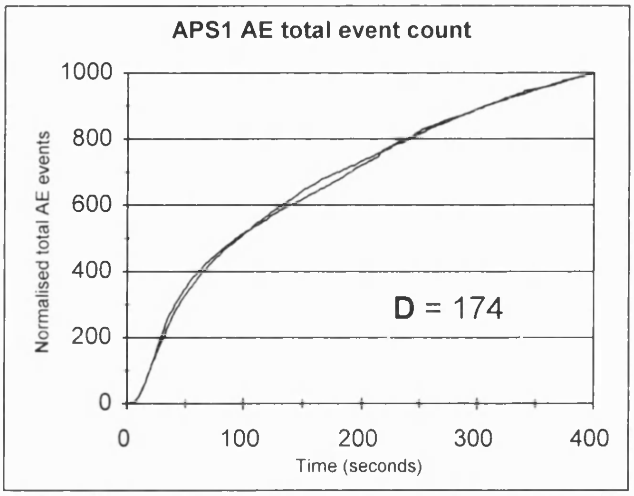

Figure 3.5.3. Normalised total AE event count for 2 APS1 HA tested samples

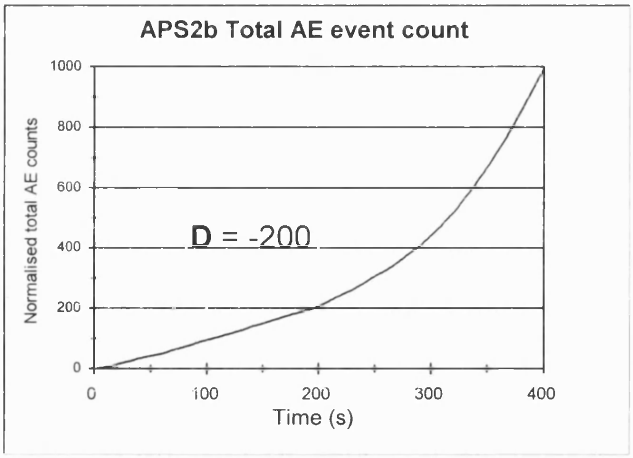

Figure 3.5.4. Normalised total AE event count for APS2 HA coating.

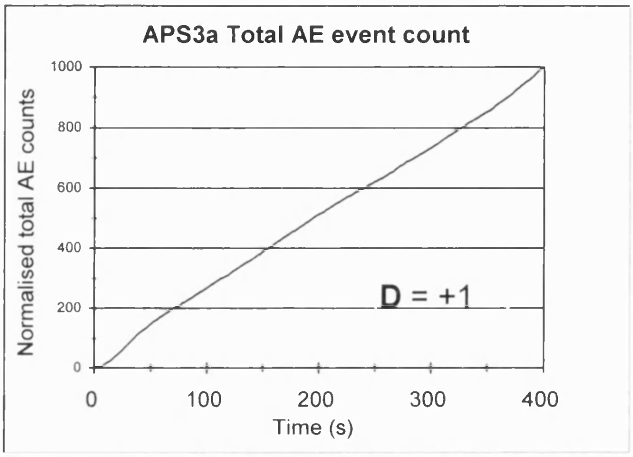

Figure 3.5.5. Normalised total AE event count for APS3 HA coatings.

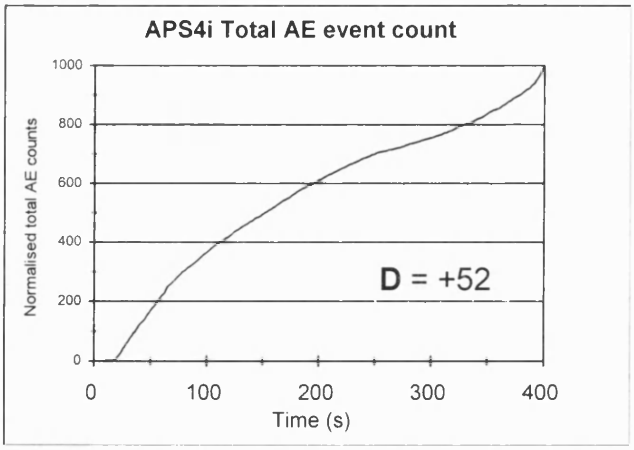

Figure 3.5.6. Normalised total AE event count for APS4 HA coating.

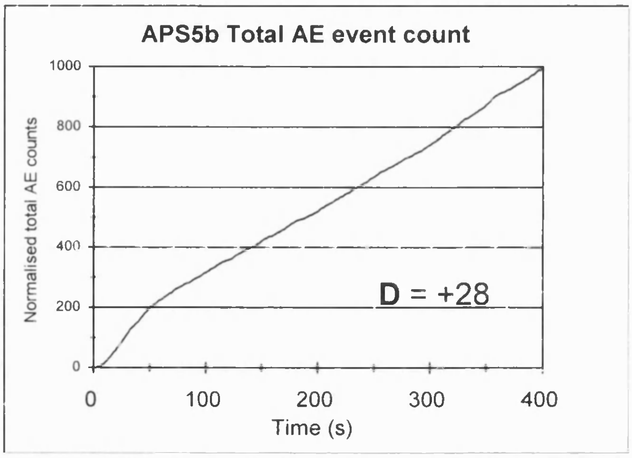

Figure 3.5.7. Normalised total AE event count for APS5 HA coating.

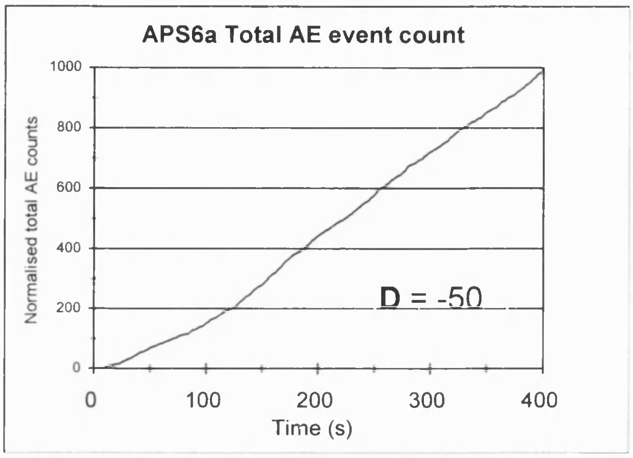

Figure 3.5.8. Normalised total AE event count for APS3 HA coating.

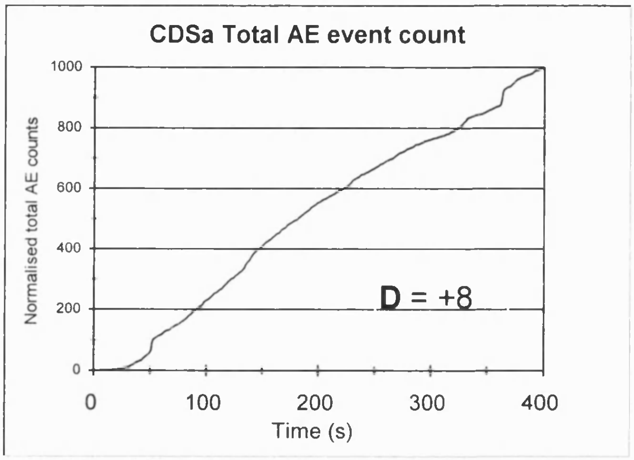

Figure 3.5.9. Normalised total AE event count for CDS HA coating.

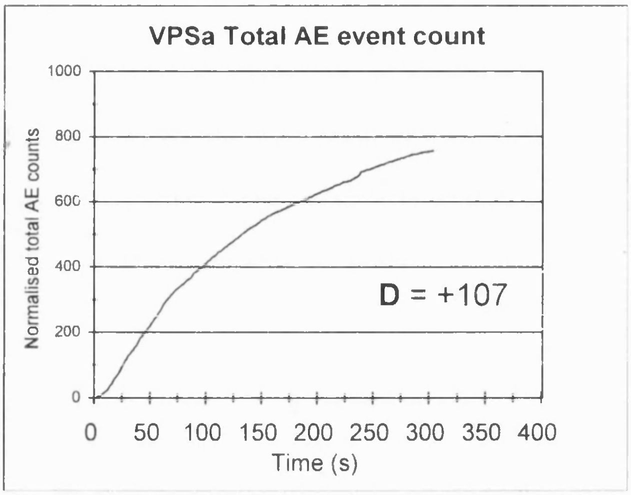

Figure 3.5.10. Normalised total AE event count for VPS HA coating.

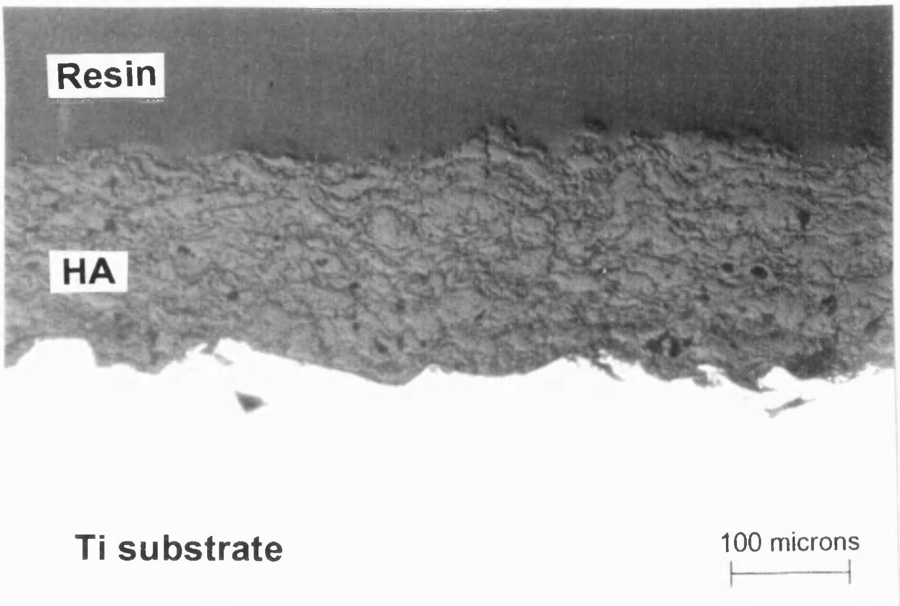

Figure 3.5.11. DIC optical micrograph of deformed HA coating APS1. Mag.x160.

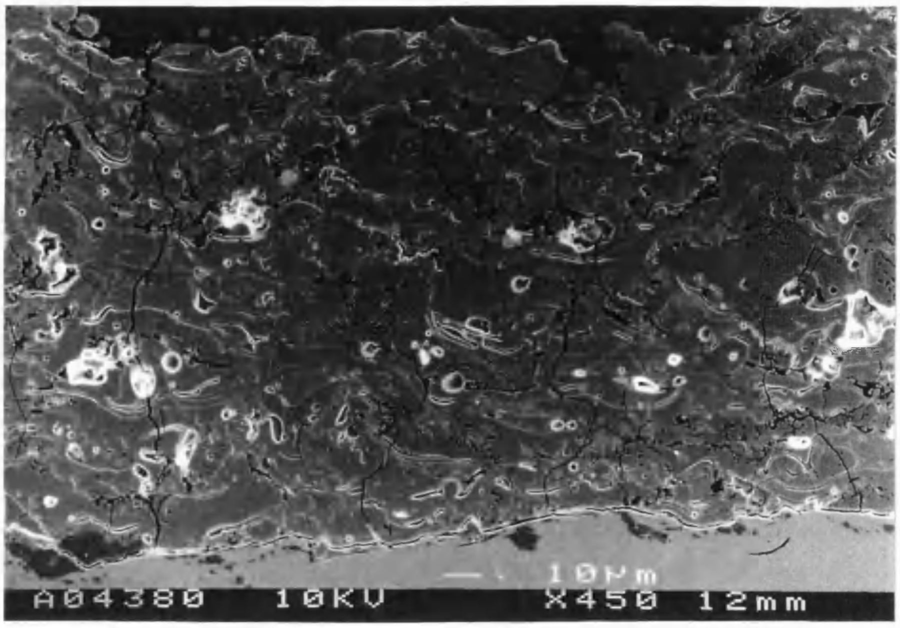

Figure 3.5.12. SEM micrograph of deformed HA coating APS1. Mag.x450.

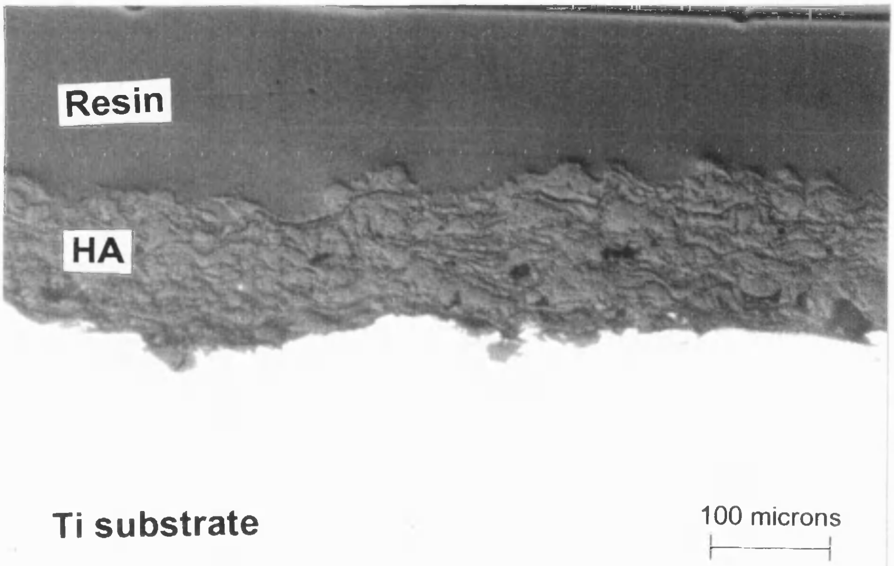

Figure 3.5.13. DIC optical micrograph of deformed HA coating APS3. Mag.x160.

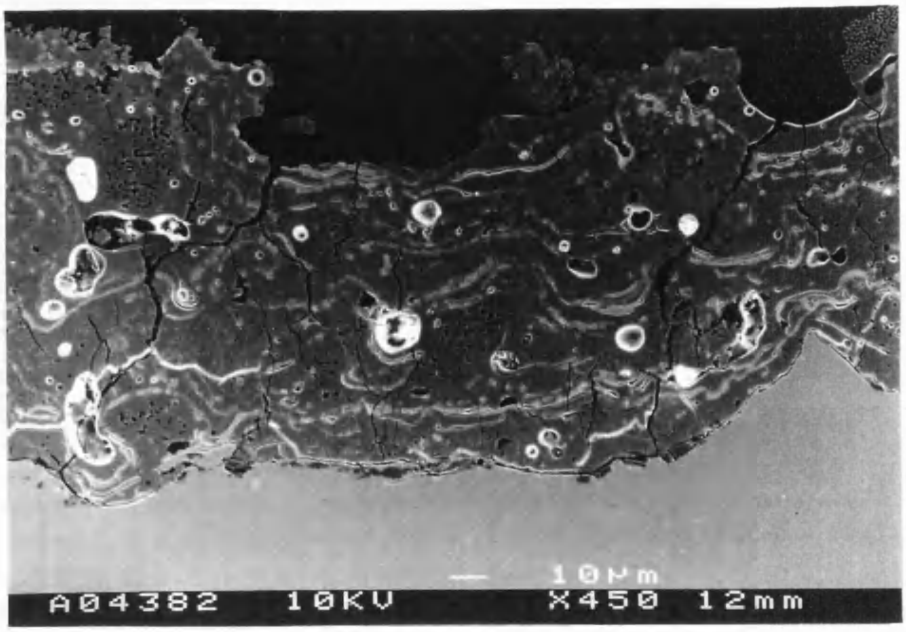

Figure 3.5.14. SEM micrograph of deformed HA coating APS2. Mag.x450.

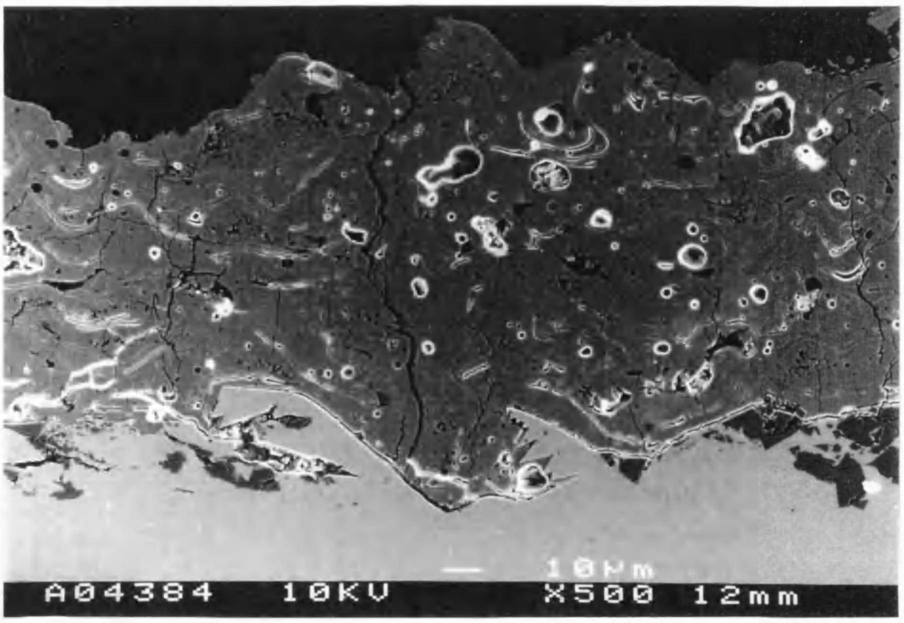

Figure 2.5.15. SEM micrograph of deformed HA coating APS3. Mag.x500.

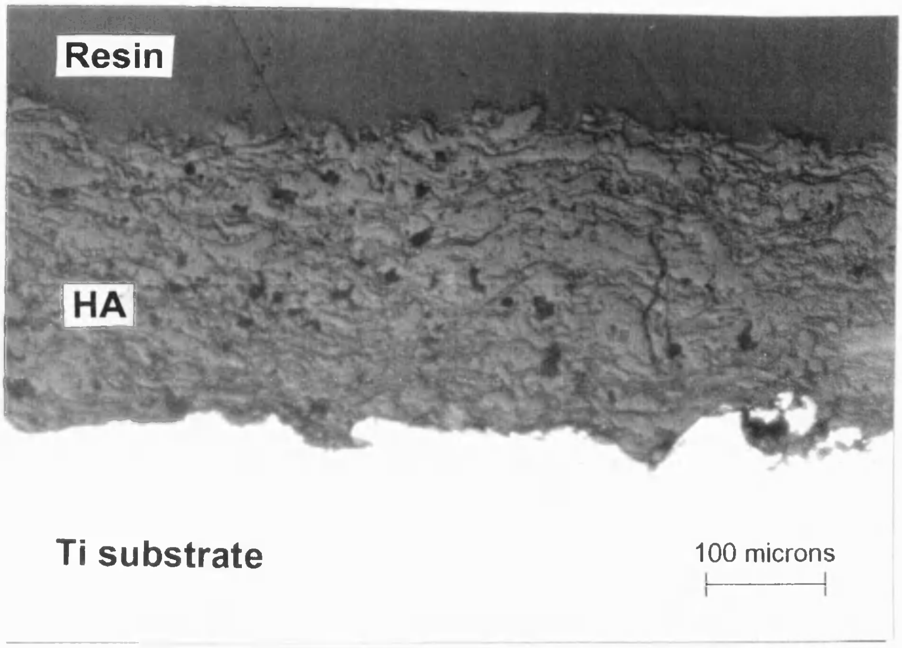

Figure 3.5.16. DIC optical micrograph of deformed HA coating APS4. Mag.x160.

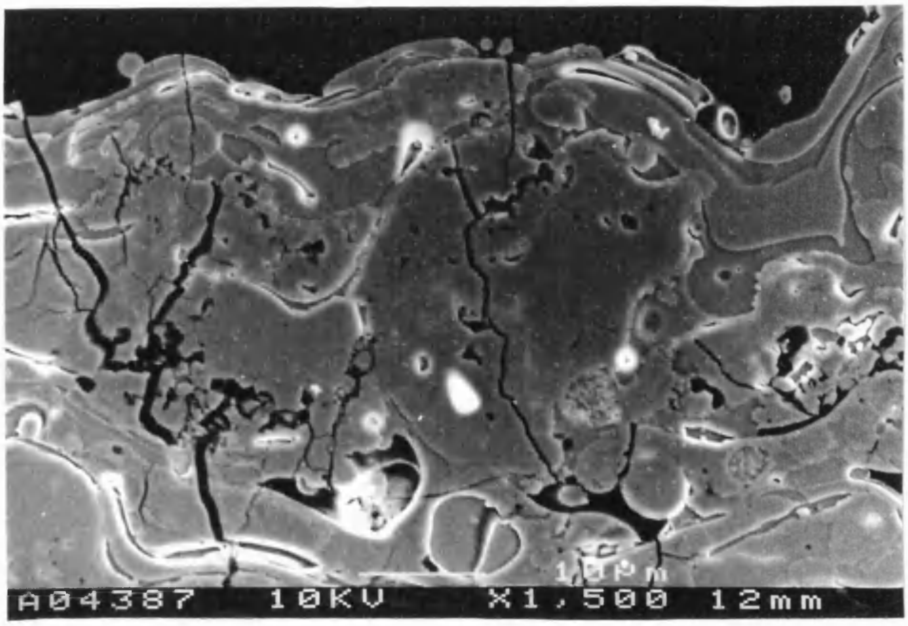

Figure 3.5.17. SEM micrograph of the surface layer of the deformed HA coatings APS4. Mag.x1500.

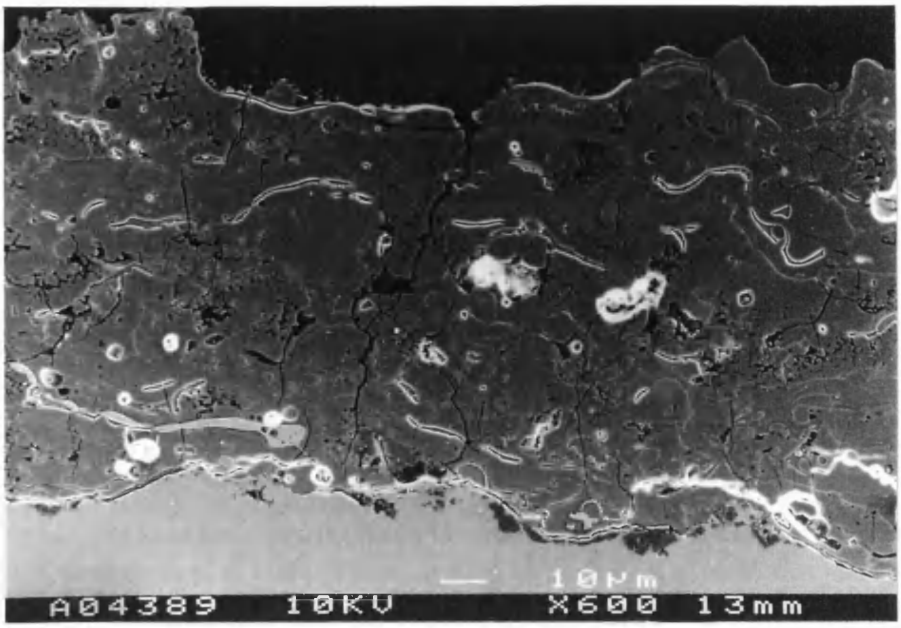

Figure 3.5.18. SEM micrograph of the deformed HA coating APS6. Mag.x600.

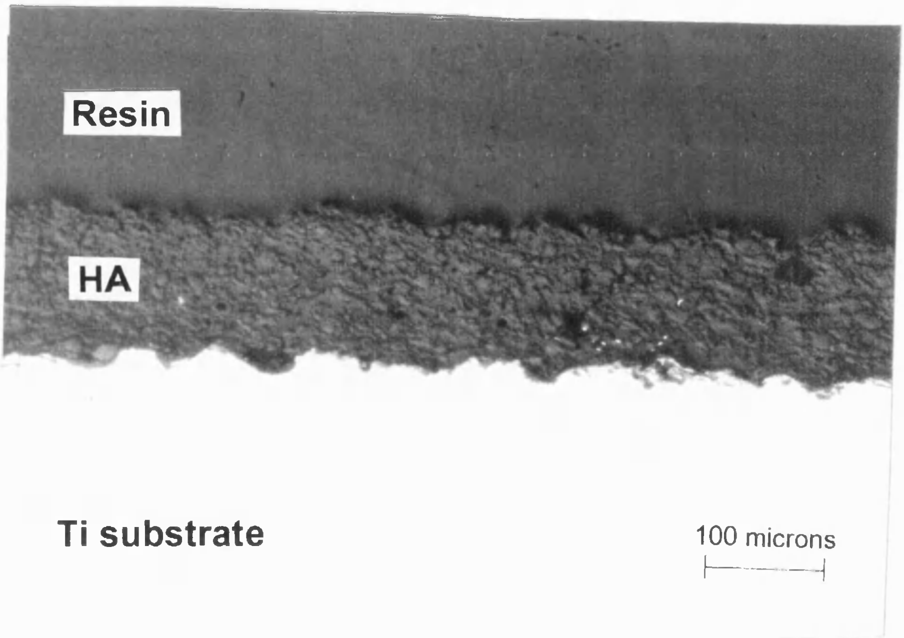

Figure 3.5.19. DIC optical micrograph of deformed HA coating CDS. Mag.x160.

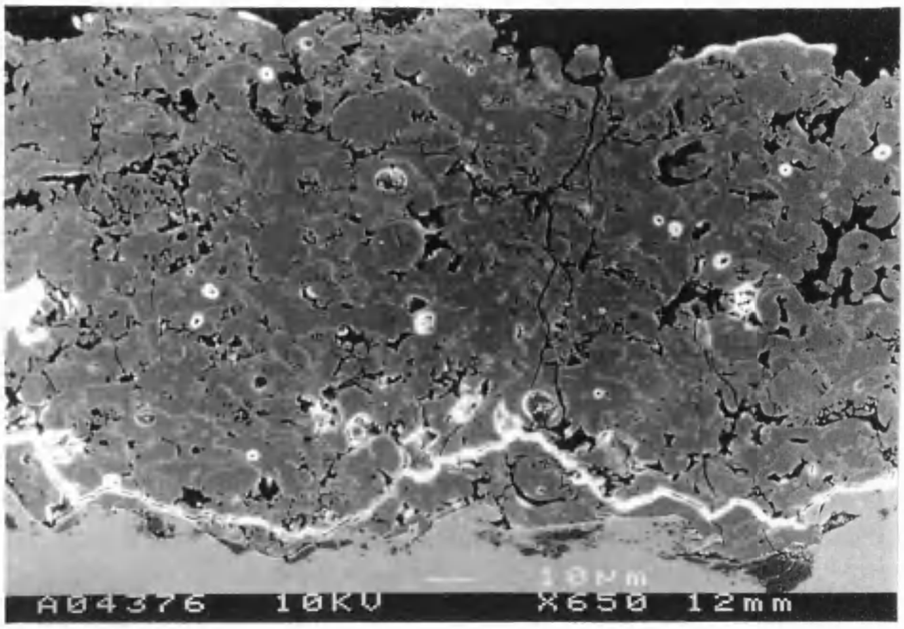

Figure 3.5.20 SEM micrograph of deformed HA coating CDS. Mag.x650.

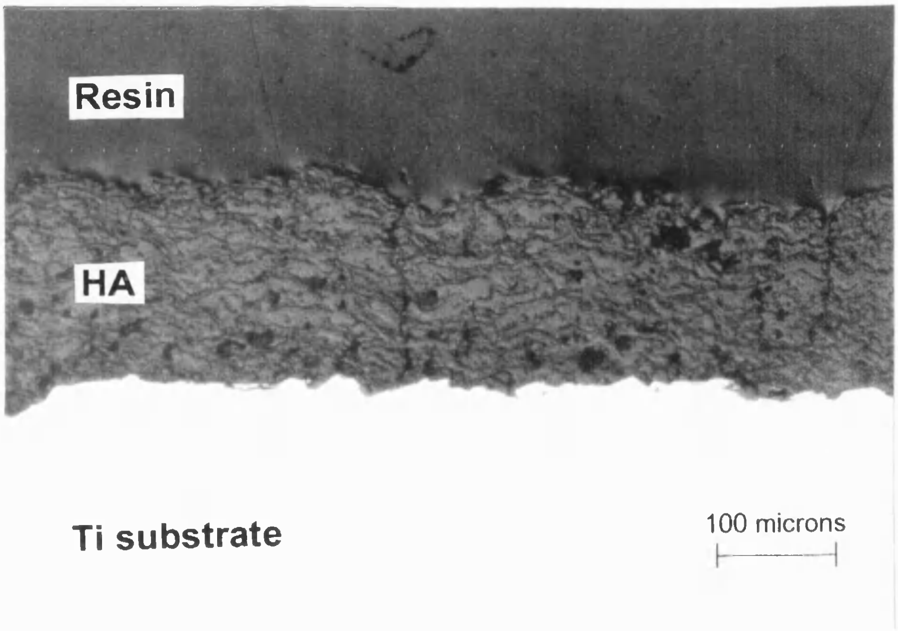

Figure 3.5.21. DIC optical micrograph of deformed HA coating VPS. Mag.x160

3.6 Heat-treatment of Hydroxyapatite Powders and Coatings.

3.6.1 Heat-treatment of HA Powders.

The powders used for thermal spraying were heat-treated as described in section 2.7. XRD was employed to characterise the powders after heat-treatment.

The XRD patterns for the powder HA044 after each heat-treatment showed a change in the percentage of β-TCP, which is illustrated in table 3.6.1. There was a small increase in the β-TCP % between 650°C and 750°C, and for the 850°C to 1150°C heat-treatments there is a significant increase in the % β-TCP. However above 1250°C there is a drop in the % β-TCP. At 1250°C to 1450°C the powder had sintered and required crushing for XRD analysis. Up to 1250°C the only two phases present in the powder were hydroxyapatite and β-TCP. At 1350°C a small amount of α-TCP is observed and the % β-TCP had decreased to 3.64%, figure 3.6.1. At 1450°C no β-TCP was detected and the two main phases present are α-TCP ($Ca_3(PO_4)_2$) and calcium oxide phosphate ($Ca_4O(PO_4)_2$), figure 3.6.2. Using the relative intensities of the peaks and assuming similar X-ray absorption coefficients between the phases there is approximately 13% hydroxyapatite present in the powder.

The peak widths decreased with increasing temperature up to 850°C after which no further change was observed. Between 1250°C and 1350°C some of the relative peak intensities had increased by 10-40 % in relation to the I_{100} hydroxyapatite peak.

Temperature (°C)	Intensity (counts/sec)		% β - TCP
	HA	β - TCP	
650	2304	46	2.21
750	2088	55	2.57
850	2079	71	3.30
950	1962	98	4.76
1050	2162	132	5.75
1150	2080	130	5.88
1250	2314	112	4.62
1350	1325	50	3.64

Table 3.6.1. Percentage β - TCP at each heat-treatment temperature.

Powder Amdry 6020 was also heat-treated between 650°C and 1450°C. It was found that at 650°C there was no difference between the unheat-treated and heat-treated powders. At 750°C there was a decrease in the peak width from 0.1° to 0.08°. The peak width remained constant on consecutive heat-treatments up to 1250°C. At 1350°C the peak width widened to 0.13°. At this temperature there was considerable sintering. At 1050°C there was a small peak corresponding to β-TCP, suggesting there was less than 1% β-TCP present in the powder. This increased to nearly 2% at 1150°C but without further increase at 1250°C. However all traces of β-TCP had disappeared after heat-treating at 1350°C, but a small peak corresponding to CaO was detected. Also at this temperature there was a variation in the peak intensities similar to that found in the XRD pattern for powder HA044. At

1450°C powder Amdry 6020 had decomposed into the same phases in approximately the same proportions to powder HA044, figure 3.6.3.

Heat-treatment of the VPS powder showed minimal change until the temperature of 1350°C was reached. At this temperature a small peak corresponding to a trace of α-Tri calcium phosphate was detected. At 1450°C the powder had started to break down into α-TCP and calcium oxide phosphate, but not to the same extent as powders HA044 and Amdry 6020. The XRD pattern for VPS powder at 1350°C and 1450°C can be seen in figure 3.6.4.

The crystallinity of the powders before heat-treatment was greater than 95% and therefore any increase in crystallinity was not measurable using XRD.

3.6.2. Heat-treatment of HA Coatings.

The hydroxyapatite coatings prepared by the different thermal spraying techniques were heat-treated as described in section 2.7.

The coatings were characterised using XRD, optical and scanning electron microscopy.

3.6.2.1. XRD of HA Coatings.

The XRD patterns of the heat-treated standard Ar/N APS coatings (APS1) can be seen in figure 3.6.5. The unheat-treated APS1 HA coating has approximately 5% β-TCP and a peak corresponding to CaO. As the heat-treatment temperature is increased the percentage β-TCP reduces to zero at 700°C. The CaO is not affected by the heat-treatment and is still present after the 900°C heat-treatment.

The crystallinity measurements for the heat-treated APS1 coatings are shown in table 3.6.2. The error on crystallinity measurement using the XRD technique is approximately ±3%. The crystallinity increases as the heat-treatment temperature rises. This is evident from the XRD patterns as the background emissions are reduced and the HA peaks are narrower and have a higher intensity.

Sample	Standard	600°C	700°C	800°C	900°C
Crystallinity %	70	75	82	88	92

Table 3.6.2. Crystallinity of heat-treated APS1 HA coatings.

The XRD patterns for the (004) peak of the heat-treated APS1 coatings can be seen in figure 3.6.6. This peak shifts to higher values of 2θ, which corresponds to a change in the residual stress in the coating. Using the shift of the (004) and the (300) peaks the residual stress in the coating has been calculated and these results are shown in figure 3.6.7. The tensile residual stress in the coating reduces as the heat-treatment temperature rises, apart from the 900°C heat-treatment where the residual stress has increased.

The XRD patterns of the heat-treated standard Ar/He APS coatings (APS4) can be seen in figure 3.6.8. This coating responded to the heat-treatment in a similar way to the APS1 coating. A trace of β-TCP and CaO are present in the as-sprayed coating. At 700°C the β-TCP is no longer present and there is a small increase in the quantity of CaO as the heat-treatment temperature rises.

The crystallinity measurements for the heat-treated APS4 coatings are shown in table 3.6.3. The crystallinity of the coating rises with the heat-treatment temperature similar to the result obtained from APS1.

Sample	Standard	600°C	700°C	800°C	900°C
Crystallinity %	61	68	82	88	90

Table 3.6.3. Crystallinity of heat-treated APS4 HA coatings.

The XRD patterns for the (004) peak of the heat-treated APS4 coatings can be seen in figure 3.6.9. The peak shifts to higher values of 2θ which corresponds to a reduction in the tensile residual stress in the coating as shown in figure 3.6.10.

The XRD patterns of the heat-treated standard CDS coatings can be seen in figure 3.6.11. The unheat-treated CDS coating has a small broad peak indicating approximately 2% β-TCP. As the heat-treatment temperature is increased this peak becomes sharper and larger, at 900°C the percentage β-TCP is approximately 8%.

The crystallinity measurements for the heat-treated CDS coatings are shown in table 3.6.3. The crystallinity increases by over 20% from the unheat-treated to the 600°C heat-treated sample. The crystallinity continues to rise to a maximum of 87% at 900°C.

Sample	Standard	600°C	700°C	800°C	900°C
Crystallinity %	43	67	80	82	87

Table 3.6.3. Crystallinity of heat-treated CDS HA coatings.

The XRD patterns for the (004) peak of the heat-treated CDS coatings can be seen in figure 3.6.12. The peak shifts to higher values of 2θ as the heat-treatment temperature rises until 900°C when the peak shifts back to near the original unheat-treated position. This result is similar to the APS coatings although the shift is not as large and the tensile residual stress in the coatings is smaller.

The residual stress measurements using XRD are shown in figure 3.6.13 for the heat-treated CDS coatings. The increase in residual stress observed at the 600°C heat-treatment is negligible as the peak position measurement is only accurate to ±15MPa of the residual stress. The 700, 800 & 900°C heat-treatments have resulted in compressive residual stresses in the coating.

The magnitude of these residual stresses are small and not significantly different within experimental measurement error.

The XRD patterns of the heat-treated VPS coatings can be seen in figure 3.6.14. The unheat-treated VPS coating only contained HA, no CaO or β-TCP was detected. CaO and β-TCP were not detected in any of the heat-treated coatings.

The crystallinity measurements for the heat-treated VPS coatings are shown in table 3.6.4. The crystallinity of the coating rises with the heat-treatment temperature similar to the result obtained from APS1. The 900°C heat-treated VPS coating showed large peak broadening, this does not necessarily indicate a reduction in crystallinity as the background noise around the peaks was very low. This result suggests that the coating is crystalline and the peak broadening was caused by another factor, i.e. residual stress.

Sample	Standard	600°C	700°C	800°C	900°C
Crystallinity %	72	83	89	91	94

Table 3.6.4. Crystallinity of heat-treated VPS HA coatings.

The XRD patterns for the (004) peak of the heat-treated VPS coatings can be seen in figure 3.6.15. The (004) peaks for the 600,700 & 800°C heat-treatments have shifted to significantly higher 2θ angles, this indicates a large reduction in residual stress which is shown in figure 3.6.16. The 900°C heat-treatment caused a phenomena unique to the VPS coating, with a negative 2θ peak shift which gave a higher tensile residual stress than the as sprayed coating.

3.6.2.2. Microscopy of Heat-treated HA Coatings.

Figure 3.6.17 - 3.6.21 shows the optical micrographs of the cross-section of the as-sprayed and heat-treated APS1 HA coatings. As the heat-treatment temperature increases the coating becomes more homogeneous and appears flat using the DIC technique. The 800°C heat-treated coating appears very flat and dense with a good contact with the substrate. At 900°C there appears to be a thin interfacial layer between the HA and the titanium alloy substrate. The coating has also developed a number of cracks running from the surface of the coating to the interface. The porosity seems to have increased although this could be damage induced on polishing due to the coating being more fragile because of the cracks running through it.

Figures 3.6.22 - 3.6.26 show the optical micrographs of the cross-section for the as-sprayed and heat-treated coatings APS4. There is a small difference between the as-sprayed and the 600°C heat-treated coating. The structure of the coating is still visible in the 600°C heat-treated coating but the sharpness between particle splats has been slightly reduced. The 700°C heat-treated coating appears homogenous with a few cracks near the surface of the coating. The 800°C heat-treated coating is similar to the 700°C heat-treated coating although there are larger cracks running from the surface of the coating to the interface with the titanium alloy substrate. At 900°C more cracks are apparent and a thin interfacial layer between the HA and titanium substrate is visible.

Figure 3.6.37 - 3.6.31 show the optical micrographs of the cross-section for the as-sprayed and heat-treated CDS HA coatings. There is very little difference between the as-sprayed and the 600°C heat-treated coatings. The 700°C heat-treated coating looks more homogenous than the as-sprayed coating, there are a few cracks which run through the coating from the surface to the HA / titanium alloy interface. The 800°C heat-treated coating shows a few more cracks than the 700°C heat-treated coating, and appears to be more homogenous. The coating heat-treated at 900°C is similar to the 800°C heat-treated coating although with slightly larger cracks and a thin interfacial layer similar to the APS coatings.

Figures 3.6.32 - 3.6.36 show the optical micrographs of the cross-sections for the as-sprayed and heat-treated VPS HA coatings. The 600°C heat-treated coating is different to the as-sprayed coating, the coating appears more homogenous and the porosity and cracks are larger. The 700°C and 800°C heat-treated coatings appear to be very similar to the 600°C heat-treated coating, the coatings appear to be homogenous and there are large cracks running from the surface of the coating to the HA / titanium alloy interface. The 900°C heat-treated coating has very large cracks traversing the coating and the porosity has increased. There is also a thin interfacial layer at the interface of the HA and titanium alloy substrate, similar to the other heat-treated coatings.

3.6.3. Discussion of Results.

It has been reported in several papers [54,56,57] that stoichiometric crystallised hydroxyapatite is stable up to 1250°C and β-TCP forms from amorphous calcium phosphate lower than 1250°C. This was found to be the case for powder HA044. The amorphous calcium phosphate could be present in powder HA044 from its preparation route. Electron microscope images of powder HA044 shows spherical particles and this morphology of particle is characteristic of spray dried powders. Spray drying has an inherently fast cooling rate which can cause amorphous material to form, and hence on heat-treating the powder, β-TCP is formed. A small amount of α-TCP is observed when powder HA044 is heat-treated at 1350°C, this could be due to either β-TCP or hydroxyapatite becoming unstable and transforming. Also at this temperature the percentage β-TCP had decreased to 3.64%, this suggests that β-TCP had transformed to α-TCP. This is confirmed when looking at the binary phase diagram for CaO and P_2O_5, figure 4.2.1, the stable phase at this temperature is α-TCP. The peak widths decreased with increasing temperature up to 850°C, probably due to increasing crystallinity in the powder. It has been reported in several papers that hydroxyapatite will crystallise before 750°C [54.57]. Between 1250°C and 1350°C some of the relative peak intensities had increased by 10-40% in relation to the I_{100} HA peak. This result has not been reported in other work and could possibly be due to the hydroxyapatite gradually dissociating or as the powder sinters at these temperatures, it is possible that during sintering the grains grow in preferential crystallographic directions. This would have the effect of altering the intensities in the XRD pattern. At 1450° C no β-TCP was detected and the two main phases present are α-TCP ($Ca_3(PO_4)_2$) and calcium oxide phosphate ($Ca_4O(PO_4)_2$), similar to the work published by Zhou et al. [56].

Powder Amdry 6020 was similar to powder HA044 when heat-treated. The main difference was that no β-TCP was detected in the powder until 1050°C. It has been reported that when hydroxyapatite is heated in a vacuum the OH molecule can be lost and TCP formed [52]. Although the powder was not heat-treated in a vacuum, the Argon atmosphere does have a similar effect to a vacuum by reducing the partial pressure of water vapour in the atmosphere and the loss of the OH molecules becomes more favourable. This also suggests that powder Amdry 6020 is crystalline, as no β-TCP was formed before this temperature like powder HA044. The formation of CaO at 1350°C is not reported in any other work, but the disappearance of the β-TCP suggests that the β-TCP has transformed into CaO. At 1350°C there was a variation in the peak intensities similar to that found in HA044, and the same explanation would apply. Powder Amdry 6020 dissociated into the same phases as powder HA044, as reported by Zhou et al. [56].

Powder XPT W 601 performed in a similar manner to Amdry 6020 when subjected to the heat-treatment temperatures in that no change was observed at the low heat-treatment temperatures. At 1350°C a small peak corresponding to α-TCP was detected and was probably caused by the degradation of hydroxyapatite, as according to the binary phase diagram of calcium phosphate, figure 4.2.1, α-TCP becomes more stable at this temperature. At 1450°C the powder degrades into the same phases as the other two powders, although more hydroxyapatite remains. This would suggest that powder XPT W 601 is the most stable of the three powders.

The APS coatings reacted in a similar manner when subjected to the heat-treatment process. The β-TCP reduced in quantity and the CaO remained in the coating. The heat-treatment results from the powders showed an increase in β-TCP at the lower heat-treatment temperatures. The heat-treatment of the powders and the coatings differed in that the powders were heat-treated using an Argon atmosphere whereas the coatings used an air atmosphere. The Argon atmosphere would have the effect of reducing the partial pressure of O_2 and H_2O increasing the probability of losing the OH group in the hydroxyapatite structure and encouraging the formation of TCP. When using an air atmosphere the partial pressures of O_2 and H_2O are higher and the loss of the OH group from the hydroxyapatite structure is less probable. Therefore when the amorphous phase in the coating crystallises hydroxyapatite is formed rather than TCP. The CaO present in the as-sprayed coating remains at a constant level for all the heat-treatments. CaO is a stable oxide and is unlikely to undergo a phase change or react with the coating elements at these temperatures. The crystallinity of the coating increases post heat-treatment and the higher heat-treatment temperatures cause a greater increase in crystallinity. There was an increase in crystallinity after the first heat-treatment of 600°C, which agreed with other authors work [50,55]. All the heat-treatments were for 30 minutes, if the heat-treatment was longer for the lower temperatures this would have the effect of increasing the crystallinity to a similar value to that of the 900°C heat-treatment. A coating with a high crystallinity would be expected to have a longer life span when exposed to body fluids, as it has been reported that crystalline HA is more stable than amorphous HA [23,24]. Therefore heat-treatment of the coatings should increase the longevity of the coating when used in the body. It has also been reported that hydroxyapatite is more stable than β-TCP and CaO when exposed to body fluids[33,34]. The heat-treatment of the APS coating reduced the quantity of β-TCP in the coating and this should also increase the longevity of the coating in the body.

Residual stress in the coating has been reduced by the heat-treatment process. XRD has shown that the coating is crystallising and this would involve atomic rearrangement, therefore if atoms have sufficient energy to move and form crystalline HA then the atoms would also move to reduce the residual stress in the coating. Also at these temperatures stress in the titanium alloy substrate would be relieved. For the APS coatings the residual stress decreases gradually as the heat-treatment temperature increased. For the VPS and CDS coatings the residual stress decreases rapidly after the first heat-treatment and remains low for the 700 and 800°C heat-treatments. The VPS coating shows an increase in the residual stress similar to the APS coatings although this increase is much larger and puts a residual stress in the coating higher than the residual stress post spraying. Also at this temperature the peaks are very broad suggesting a high increase in the residual stress. The increase in residual stress at 900°C could be due to a combination of factors :

I. A difference in the thermal expansion coefficients of the titanium alloy substrate and the hydroxyapatite coating.
II. A reaction may occur between the hydroxyapatite coating and the titanium alloy substrate.
III. Formation of an oxide layer at the titanium alloy hydroxyapatite interface.
IV. Degradation of the hydroxyapatite coating.

V. A phase transition in the titanium alloy substrate causing a change in thermal expansion coefficient.

Any one factor or combination of these factors could be contributing to the increase in residual stress, further work will be required to determine the main contributing factors.

The increase in β-TCP for the CDS coatings is unusual compared to the VPS and APS coatings. The VPS and APS spraying powders were similar in structure, although different in size, and showed similar properties when heat-treated. The CDS powder probably originated from a mixture of spraying dried and precipitated particles. Heat-treatment of these powders showed that the VPS and APS powders performed in a similar manner with only a small amount of TCP present. The CDS powder showed an increase in the TCP with heat-treatment similar to the heat-treatment of the coating. The CDS process is a lower temperature process than the APS and VPS techniques and therefore it is possible that the particles post spraying retain there original structural characteristics. The CDS coating was also the least crystalline of the coatings. Either of these factors could contribute to the increase in β-TCP observed when the CDS coating is heat-treated. The CDS coating also showed a negative residual stress after the heat-treatment process, this is effectively a positive compressive residual stress. The CDS coating has the lowest residual stress of the sprayed coatings and for an equivalent peak shift observed in the APS coatings a compressive residual stress would be observed. A compressive residual stress in the coating should be beneficial to the coating performance, as this stress would act to close cracks in the coating and improve the adhesion of the coating to the surface as spalling of the coating is less likely.

Microscopy of the heat-treated coatings showed that the heat-treatment resulted in a similar effect on all the coatings. As the heat-treatment temperature increases there is an increase in the number of cracks traversing the coating and porosity. The 900°C heat-treatment caused all of the coatings to form an interfacial layer between the coating and the titanium alloy. This interfacial layer is probably due to the growth of a titanium oxide layer or a possible reaction between the titanium and hydroxyapatite. Microscopy of the cross-section of the heat-treated coatings showed an apparent increase in the homogeneity of the coating as the heat-treatment temperature rises. This is due to the increase in crystallinity of the coating, as amorphous hydroxyapatite has a faster polishing rate than crystalline hydroxyapatite, due to the higher solubility of the amorphous to the crystalline hydroxyapatite. For the as sprayed coating the faster cooled hydroxyapatite is formed around the outside of splatted particles, this would polish preferentially to the slower cooled more crystalline centre of the splat. This shows up in the cross-section of coatings as layers which built up during spraying to form the coating. As the heat-treatment temperature increases these layer are harder to distinguish and not visible at the 800 & 900°C heat-treatment temperatures. The layers in the coating become harder to distinguish as the difference in crystallinity between the outside and centre of a spatted particles becomes less. The thickness of the layers in the coating will determine whether the morphology of the coating is still visible at higher temperatures. This explains why APS1 with a thicker layered structure than APS4 has a visible structure at 800°C whereas APS4 does not.

There are some large cracks visible in the cross-section of the VPS coating and this observation would correspond to the large residual stress measured in this coating. The porosity increase observed in most of the coatings as the heat-treatment temperature rises is probably due the crystallinity increase causing a rise in the brittleness of the coating and hence more damage occurs to the coating in the polishing procedure.

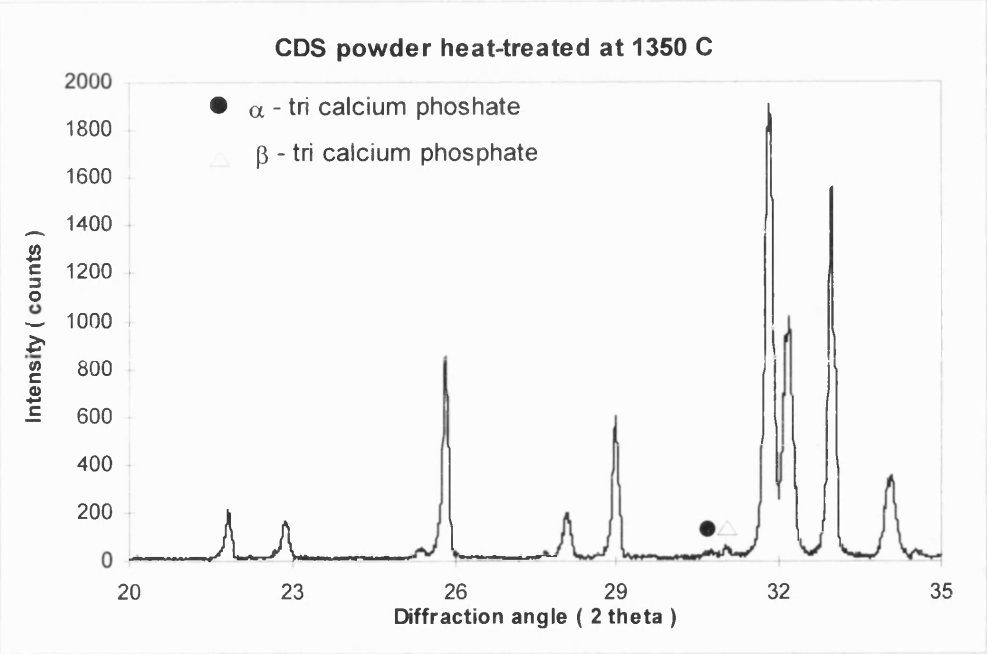

Figure 3.6.1. XRD pattern for powder HA044 heat-treated at 1350°C.

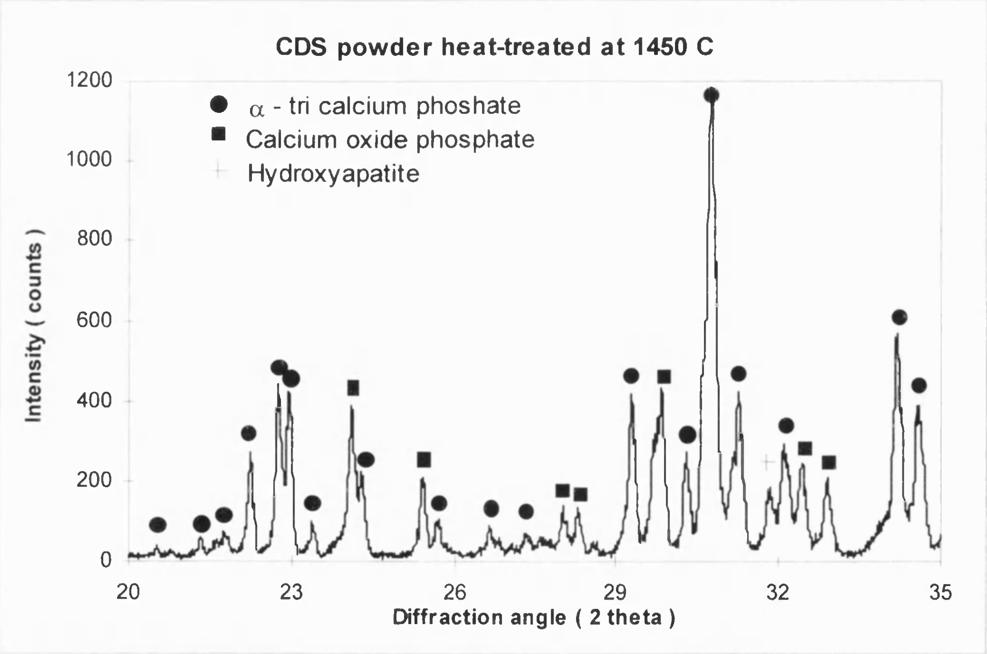

Figure 3.6.2. XRD pattern for powder HA044 heat-treated at 1450°C.

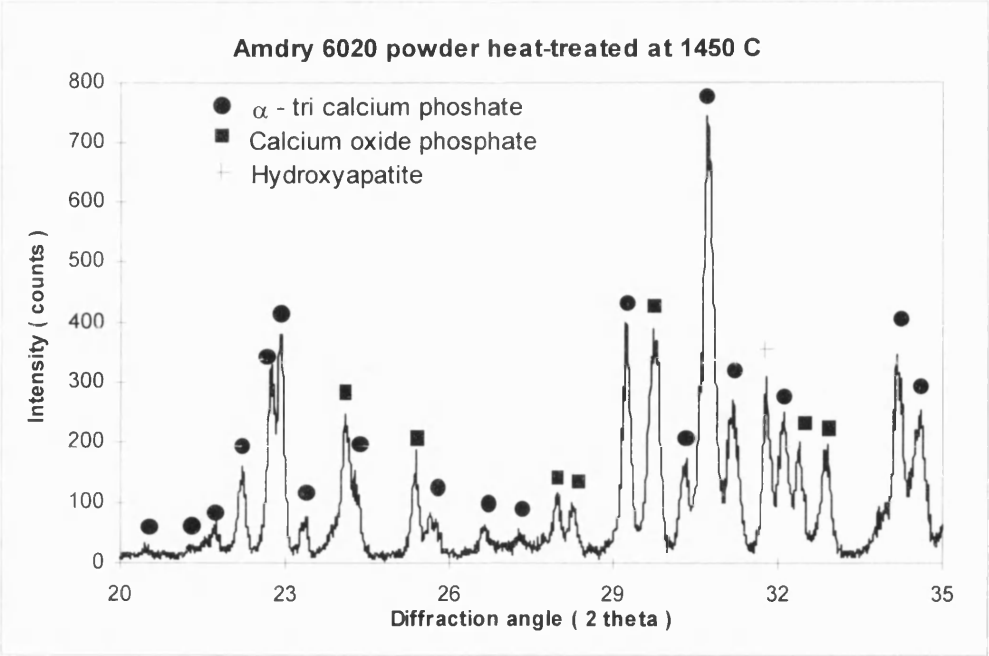

Figure 3.6.3. XRD pattern for powder Amdry 6020 heat-treated at 1450°C.

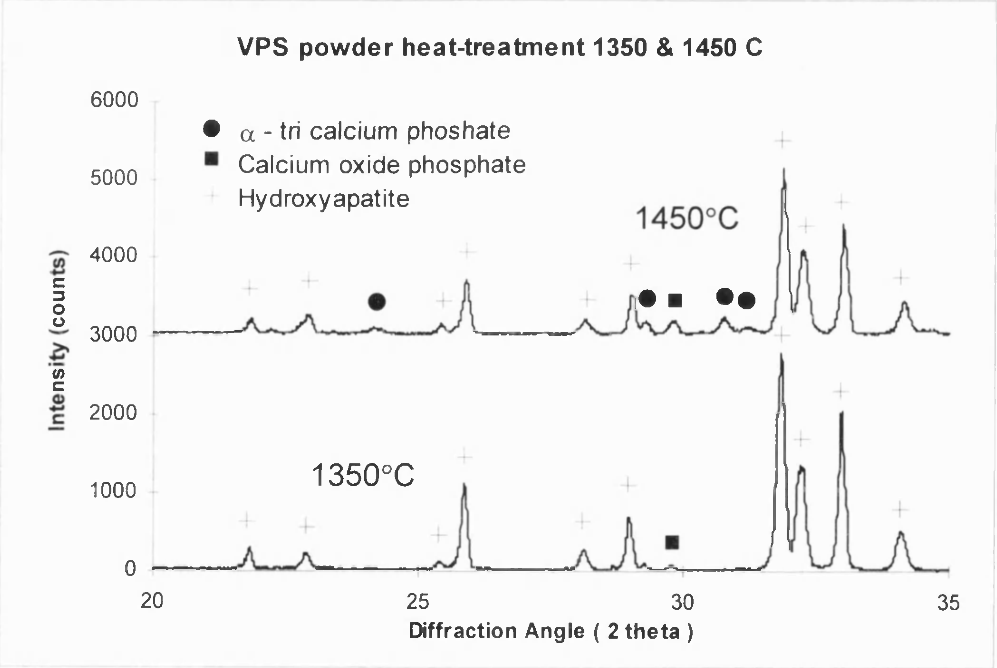

Figure 3.6.4. XRD pattern for VPS powder heat-treated at 1350°C and 1450°C.

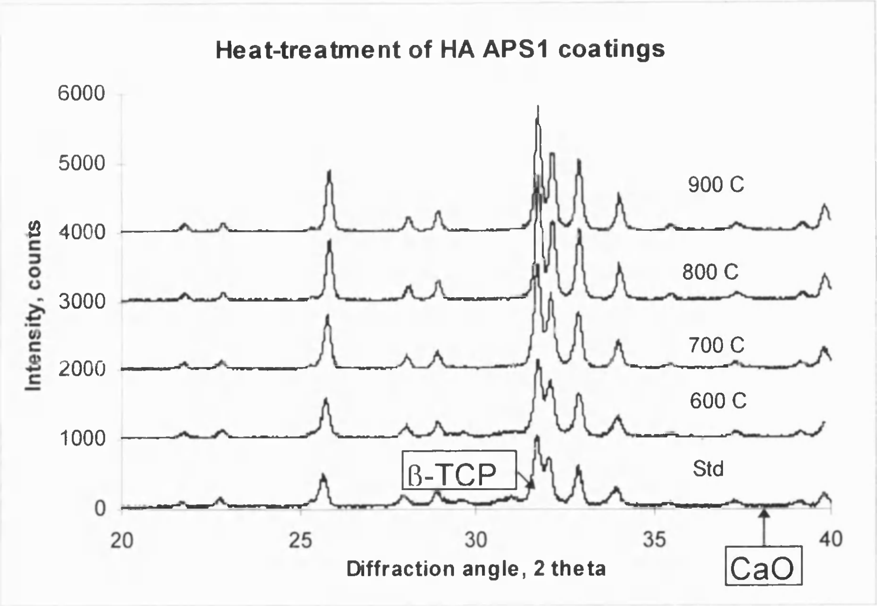

Figure 3.6.5. XRD patterns for heat-treated HA coating APS1.

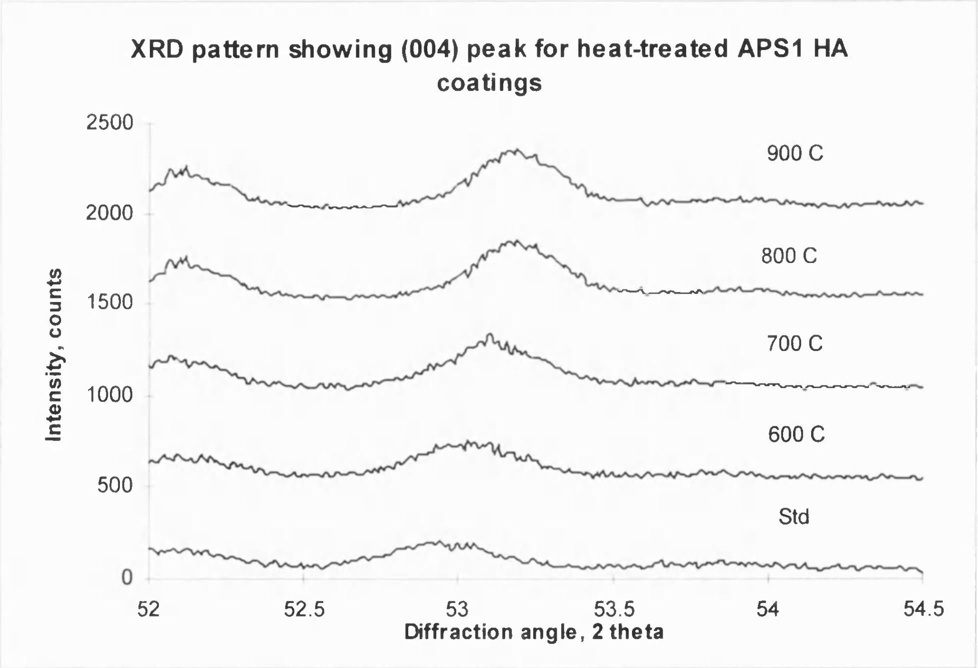

Figure 3.6.6. XRD pattern showing the (004) peak for the heat-treated APS1 HA coatings.

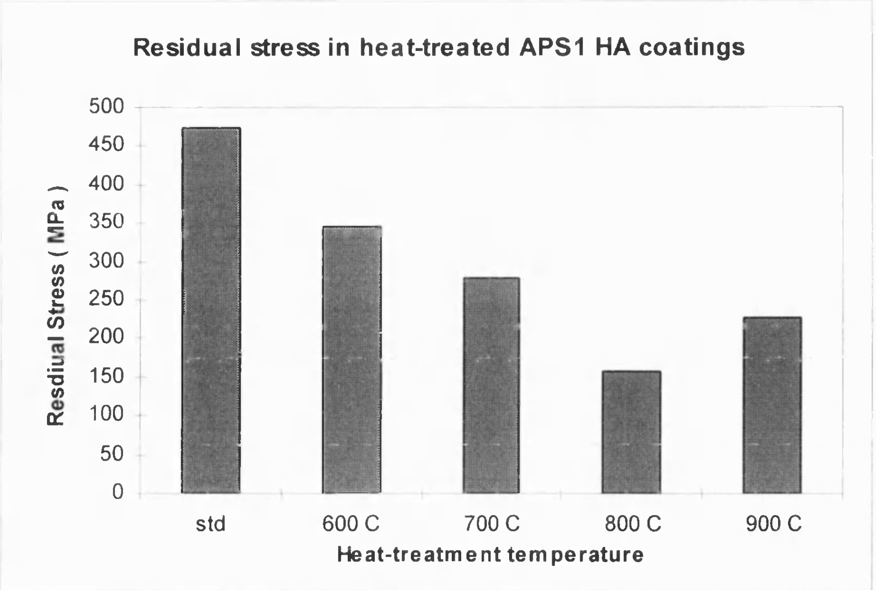

Figure 3.6.7. Residual stress measurement in heat-treated APS1 HA coatings.

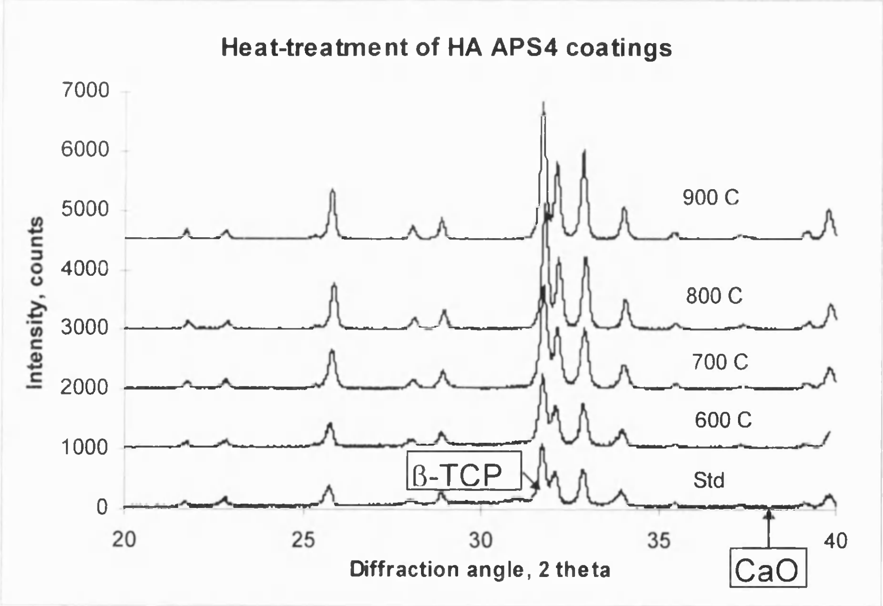

Figure 3.6.8. XRD patterns of heat-treated APS4 HA coatings.

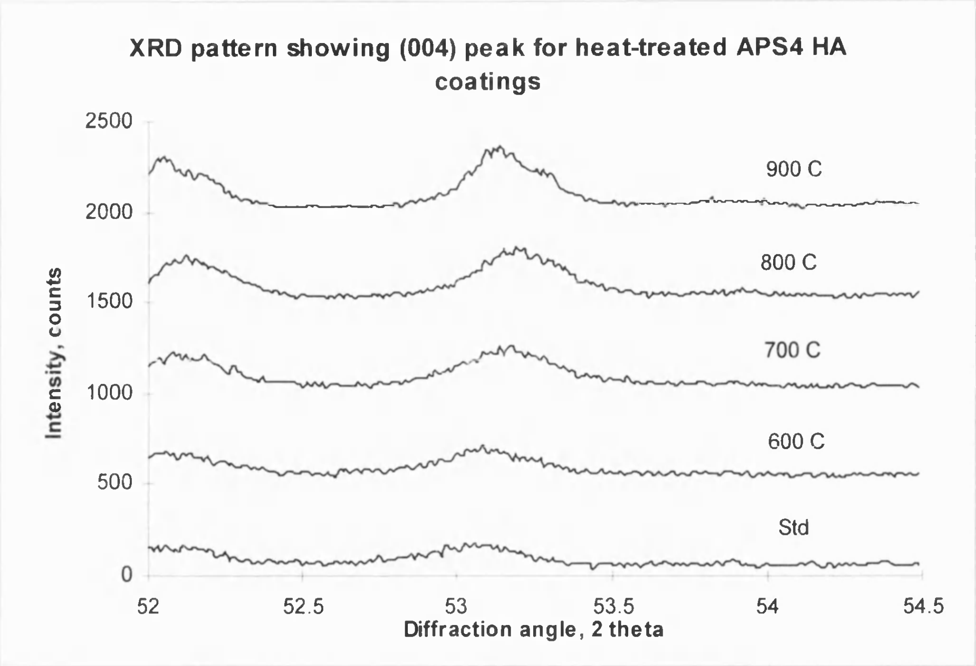

Figure 3.6.9. XRD patterns showing (004) peak for heat-treated APS4 HA coatings.

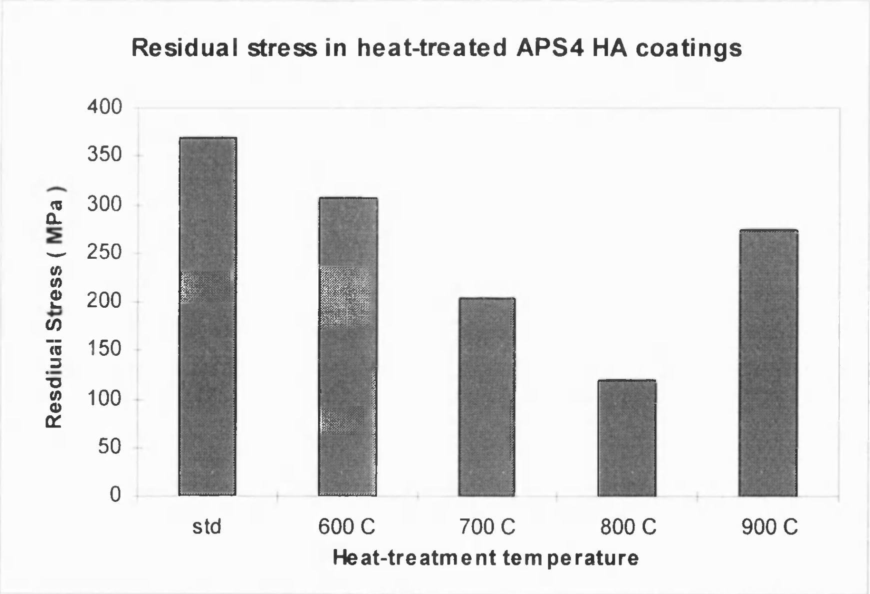

Figure 3.6.10. Residual stress measurement in heat-treated APS4 HA coatings.

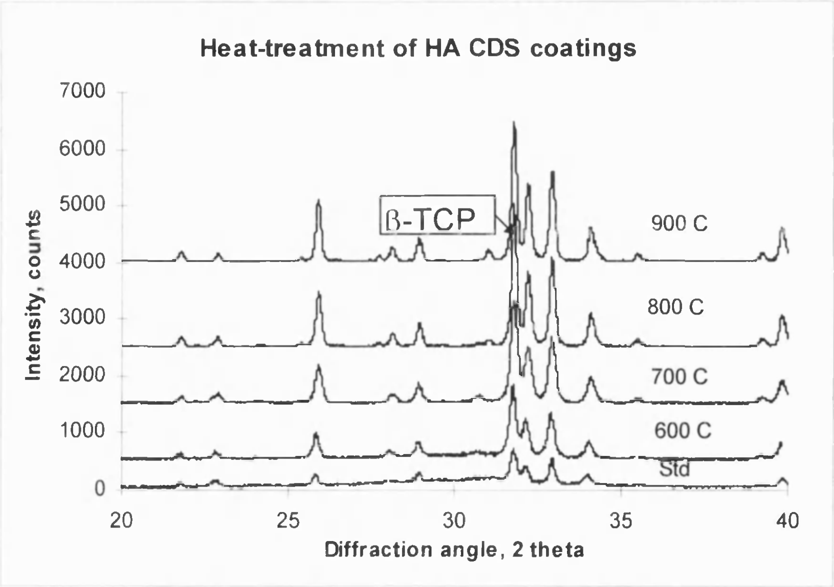

Figure 3.6.11. XRD patterns of heat-treated CDS HA coatings.

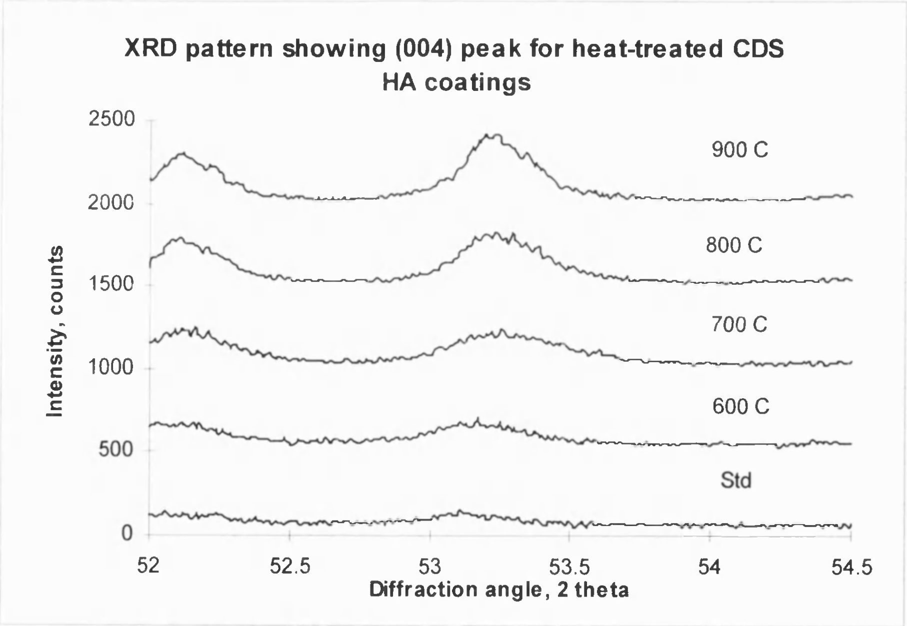

Figure 3.6.12. XRD patterns showing (004) peak of heat-treated CDS HA coatings.

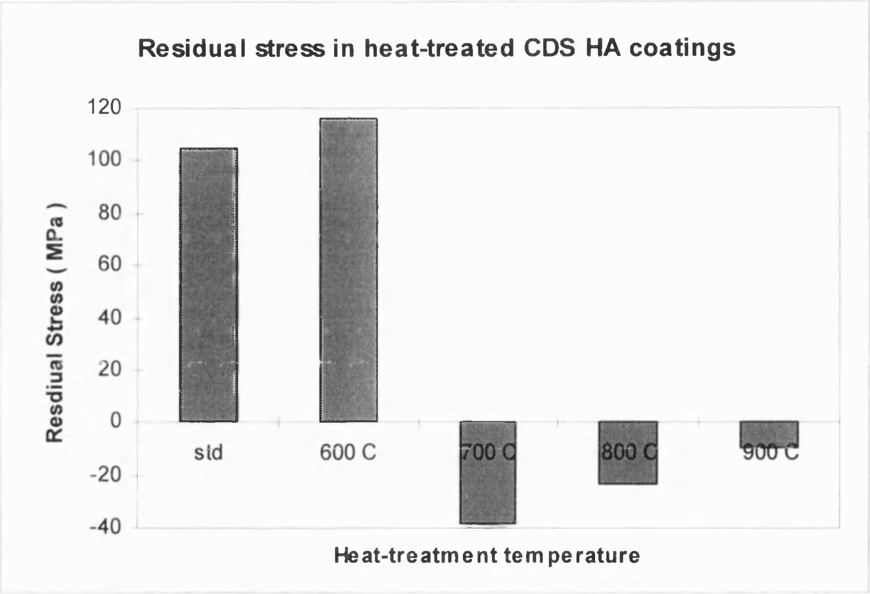

Figure 3.6.13. Residual stress measurement in heat-treated CDS HA coatings.

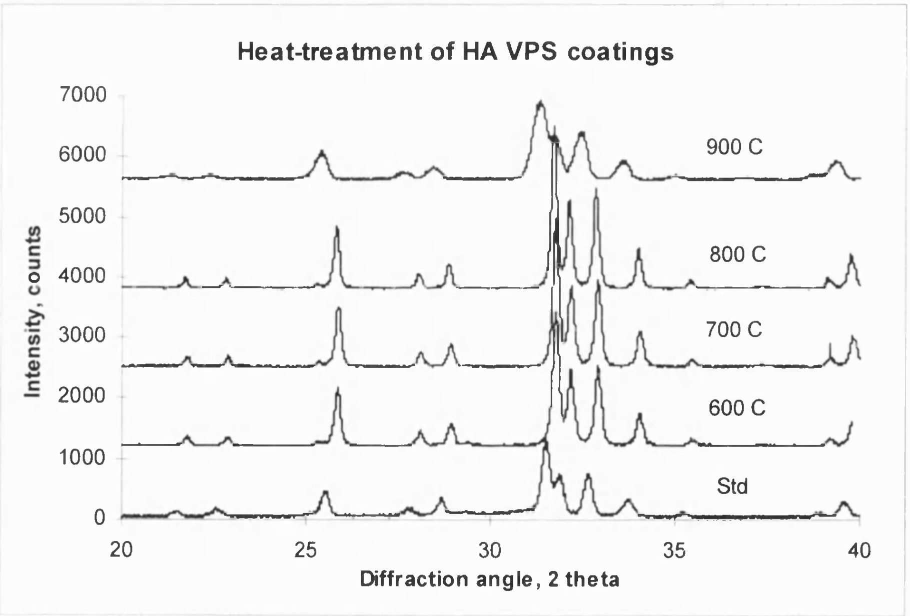

Figure 3.6.14. XRD patterns of heat-treated VPS HA coatings.

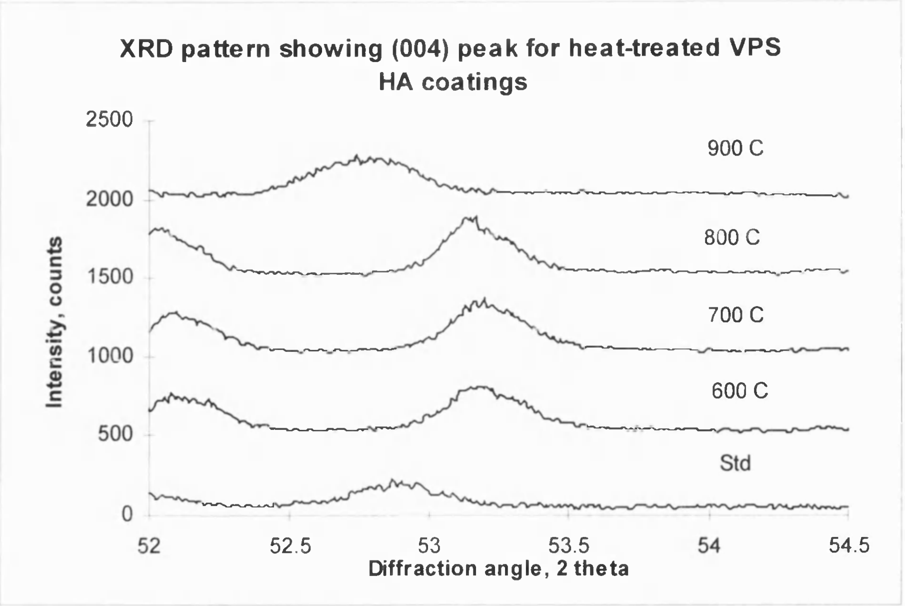

Figure 3.6.15. XRD patterns showing (004) peak for heat-treated VPS HA coatings.

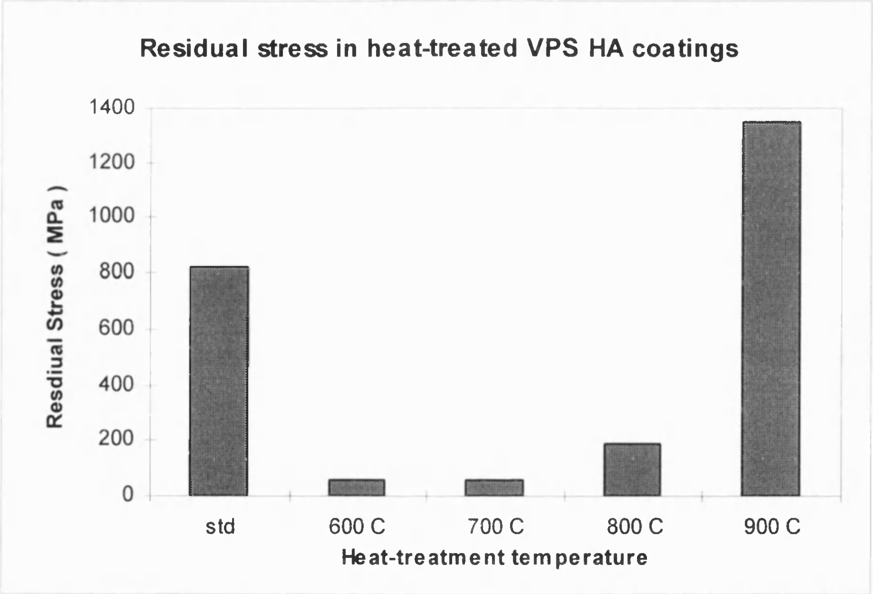

Figure 3.6.16. Residual stress measurement in heat-treated VPS HA coatings.

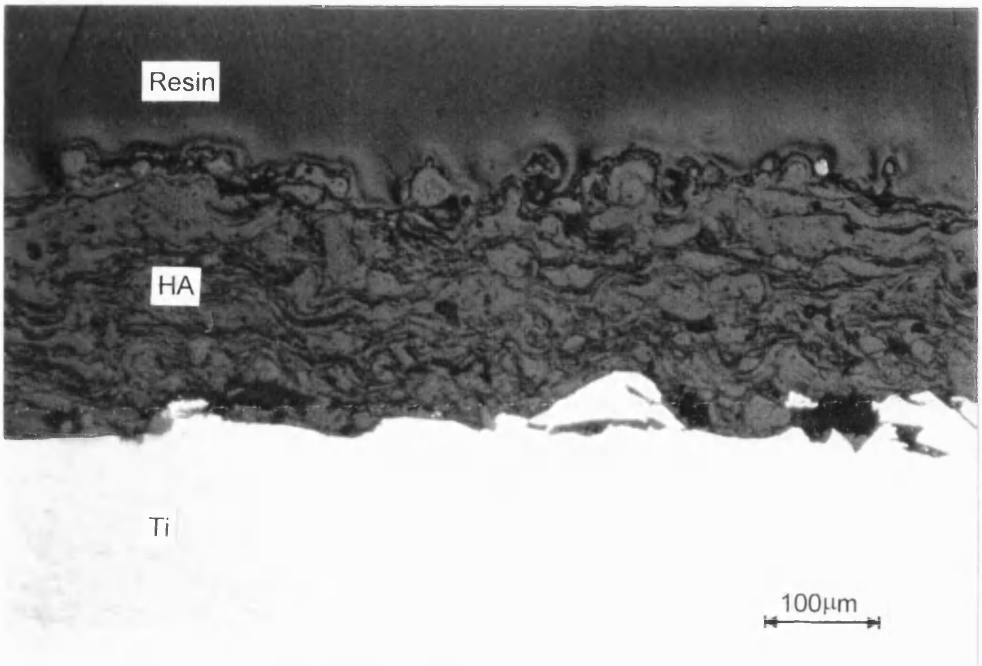

Figure 3.6.17. DIC optical micrograph of the cross-section of the as-sprayed HA coating APS1. mag ×160.

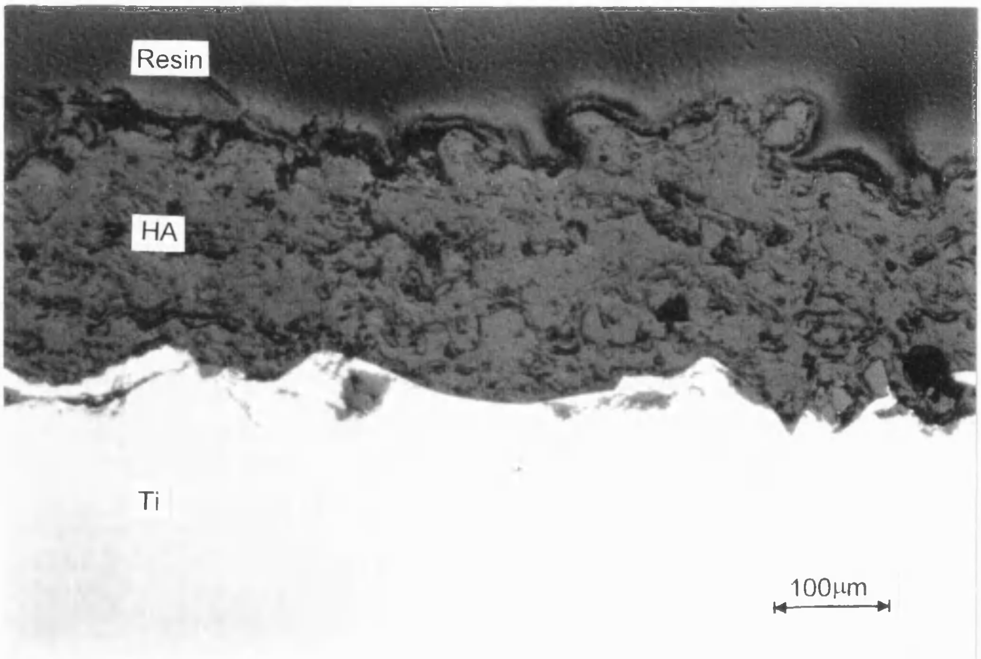

Figure 3.6.18. DIC optical micrograph of the cross-section of the HA coating APS1 heat-treated at 600°C. mag ×160.

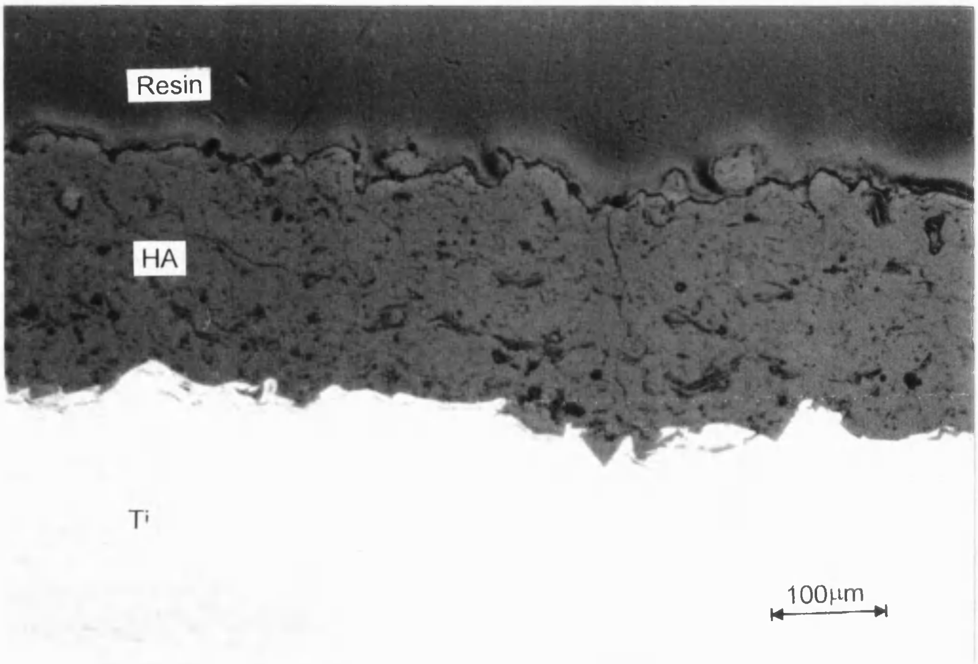

Figure 3.6.19. DIC optical micrograph of the cross-section of the HA coating APS1 heat-treated at 700°C. mag ×160.

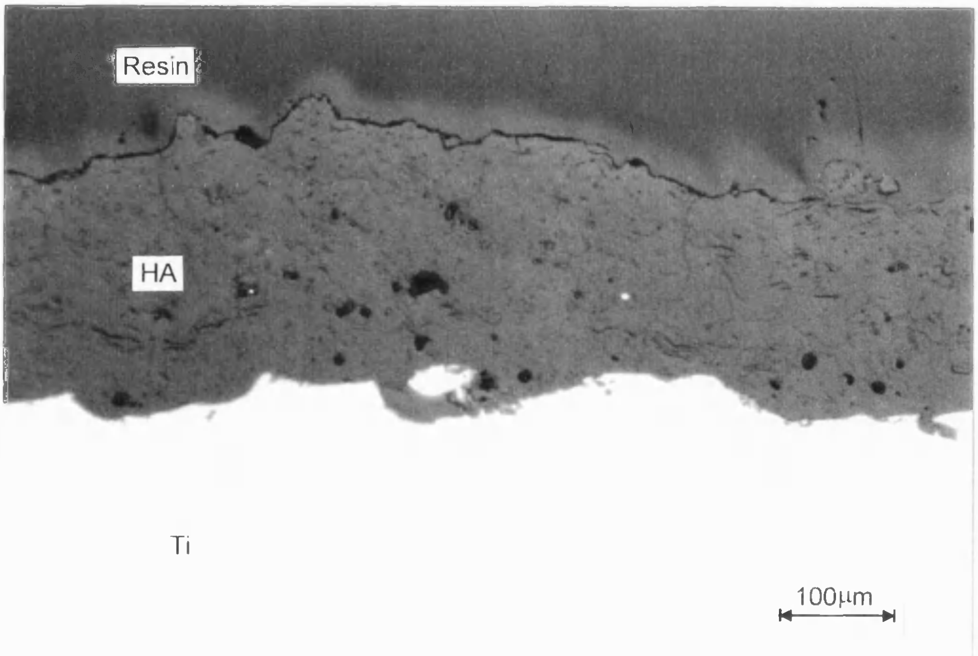

Figure 3.6.20. DIC optical micrograph of the cross-section of the HA coating APS1 heat-treated at 800°C. mag ×160.

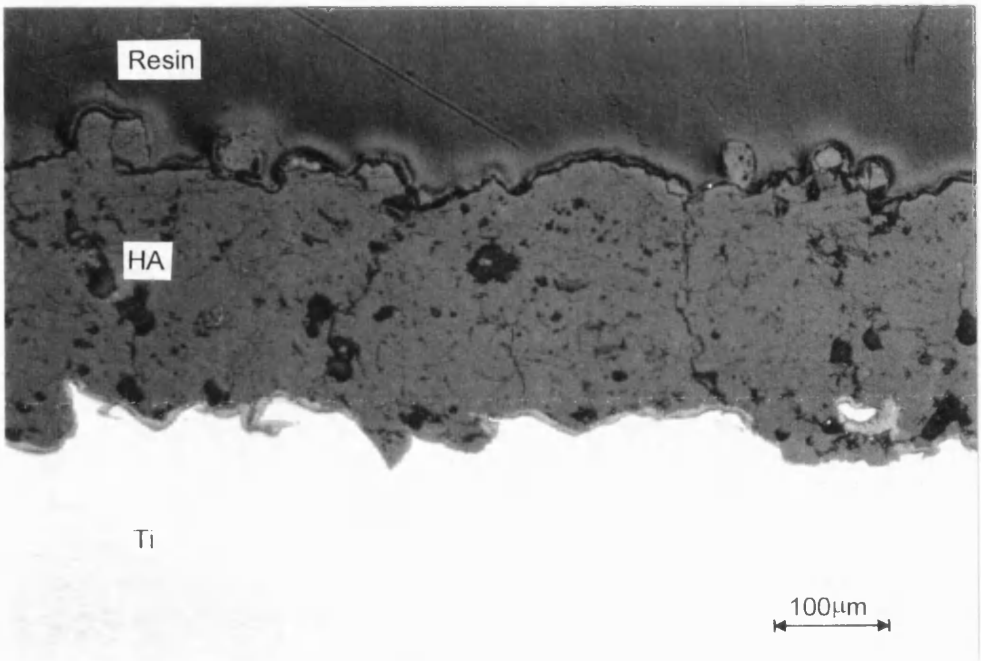

Figure 3.6.21. DIC optical micrograph of the cross-section of the HA coating APS1 heat-treated at 900°C. mag ×160.

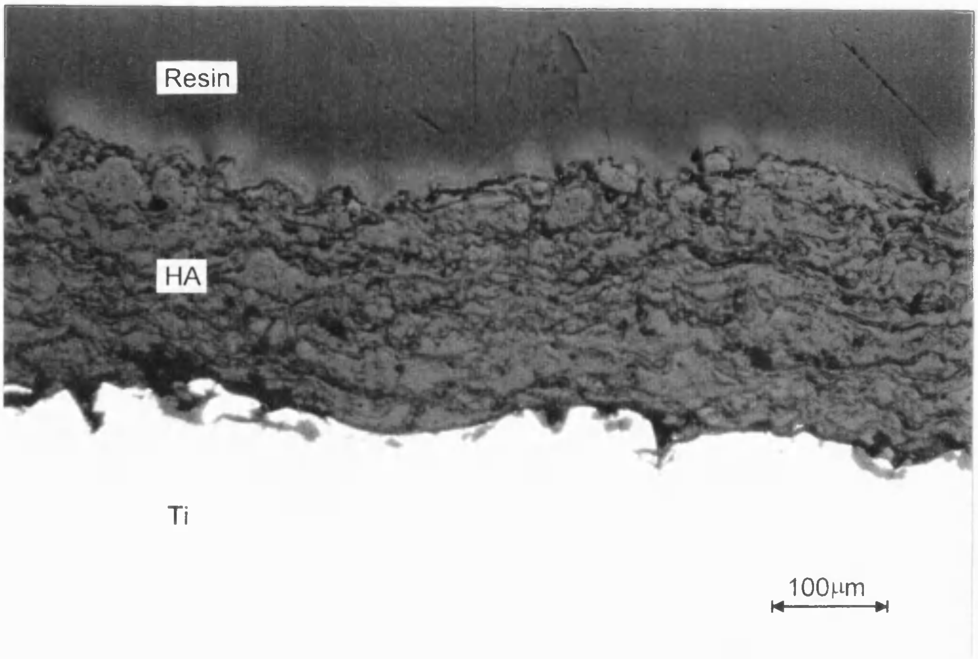

Figure 3.6.22. DIC optical micrograph of the cross-section of the as-sprayed HA coating APS4. mag ×160.

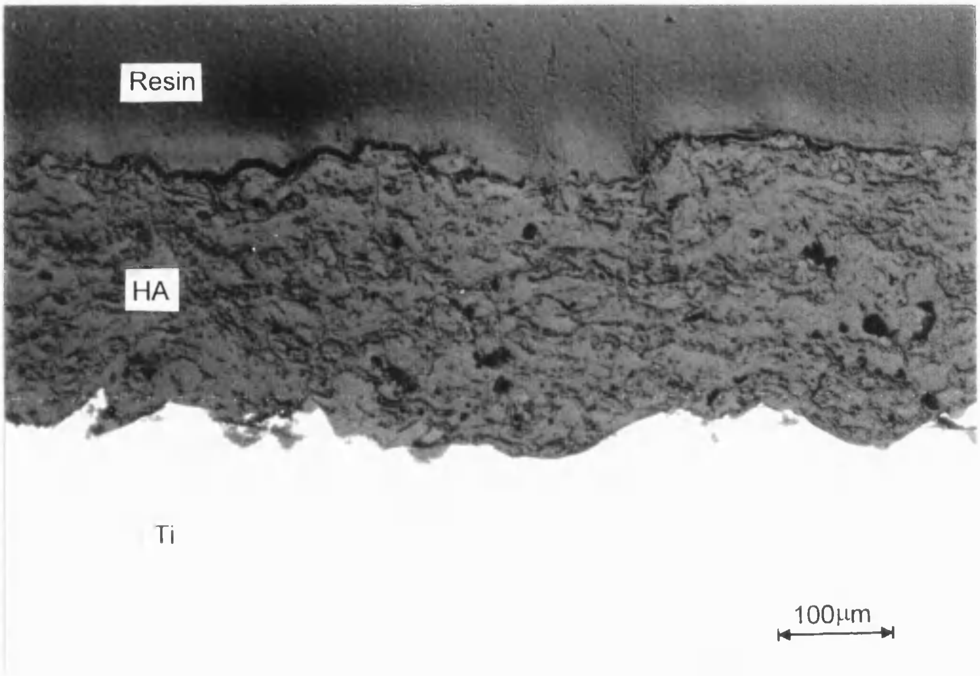

Figure 3.6.23. DIC optical micrograph of the cross-section of the HA coating APS4 heat-treated at 600°C. mag ×160.

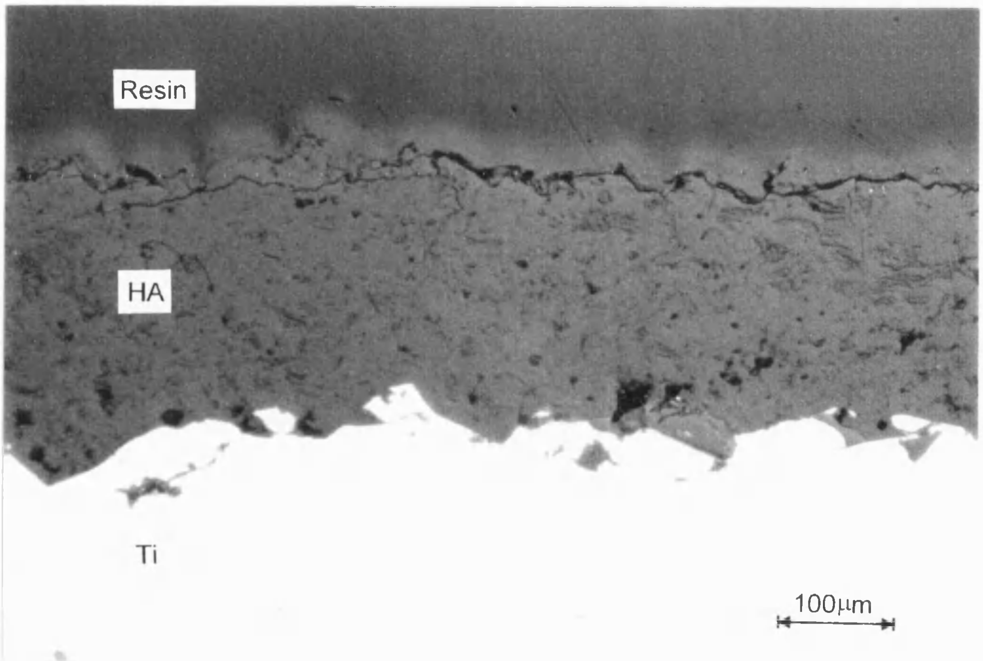

Figure 3.6.24. DIC optical micrograph of the cross-section of the HA coating APS4 heat-treated at 700°C. mag ×160.

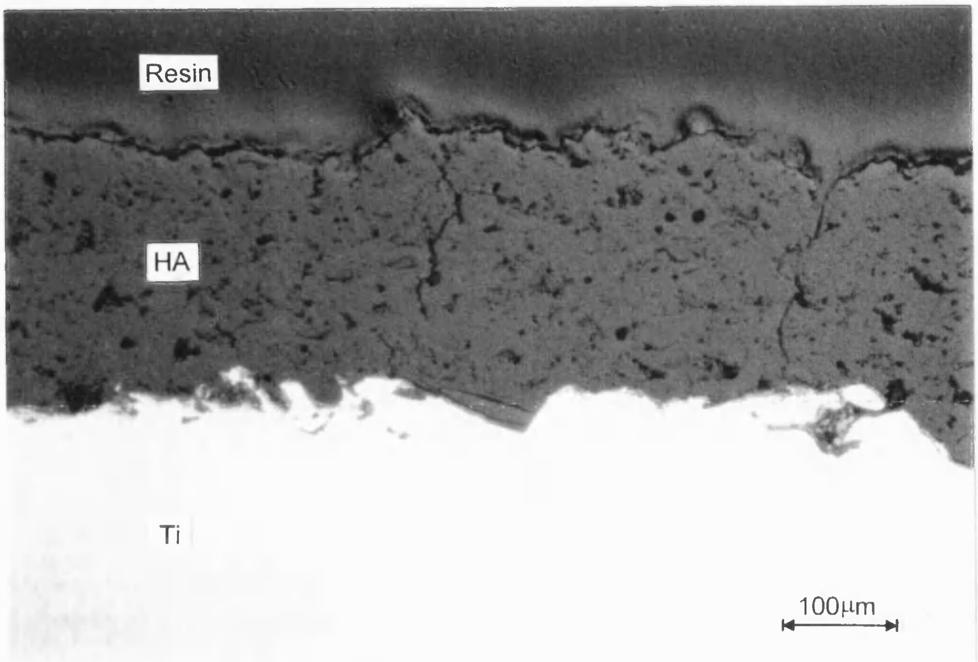

Figure 3.6.25. DIC optical micrograph of the cross-section of the HA coating APS4 heat-treated at 800°C. mag ×160.

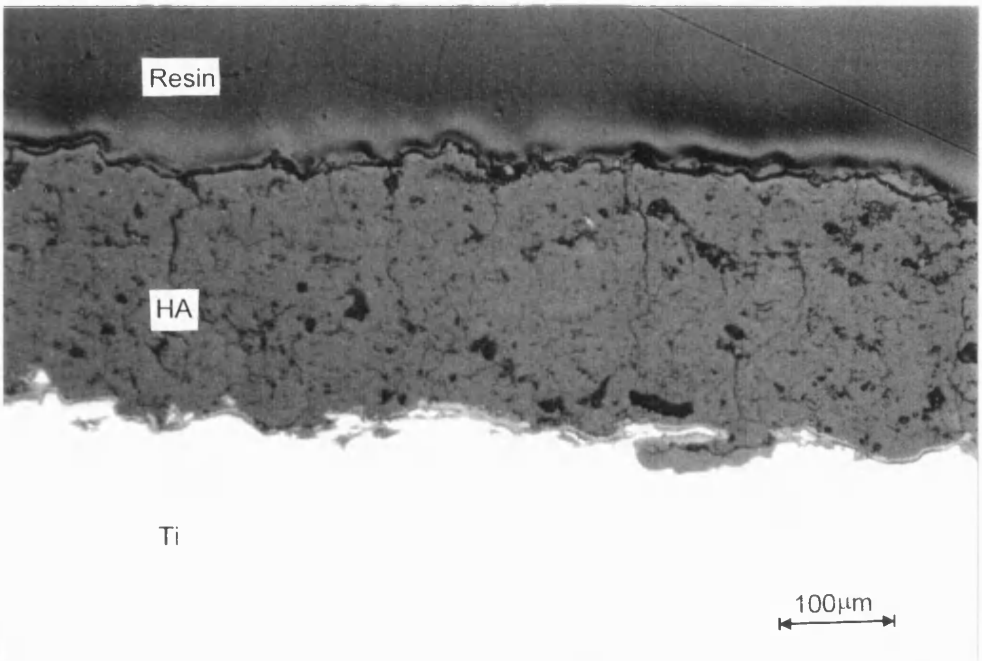

Figure 3.6.26. DIC optical micrograph of the cross-section of the HA coating APS4 heat-treated at 900°C. mag ×160.

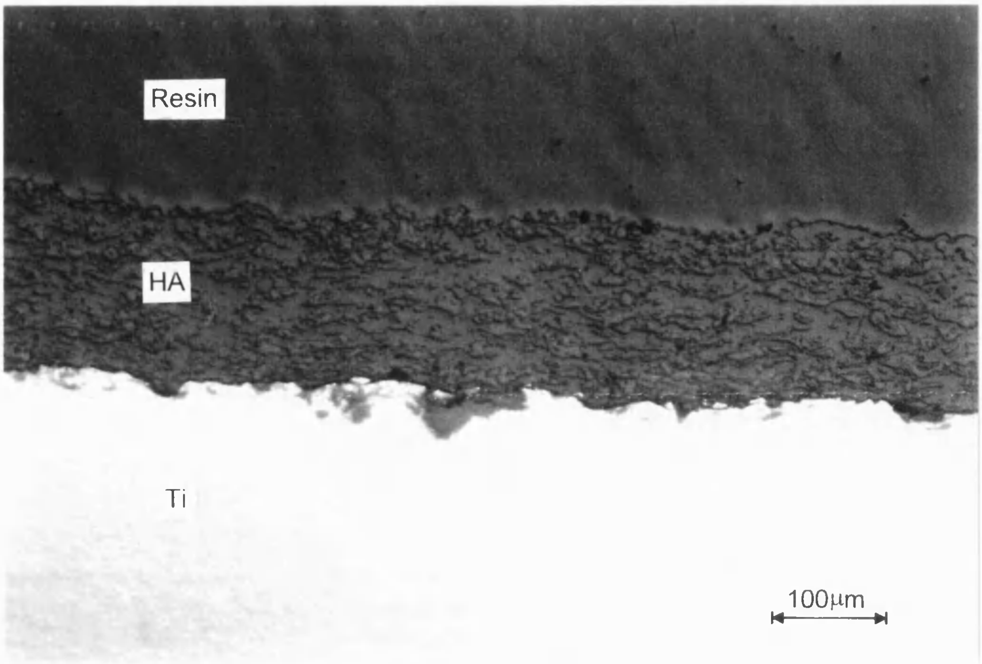

Figure 3.6.27. DIC optical micrograph of the cross-section of the as-sprayed CDS HA coating, mag ×160.

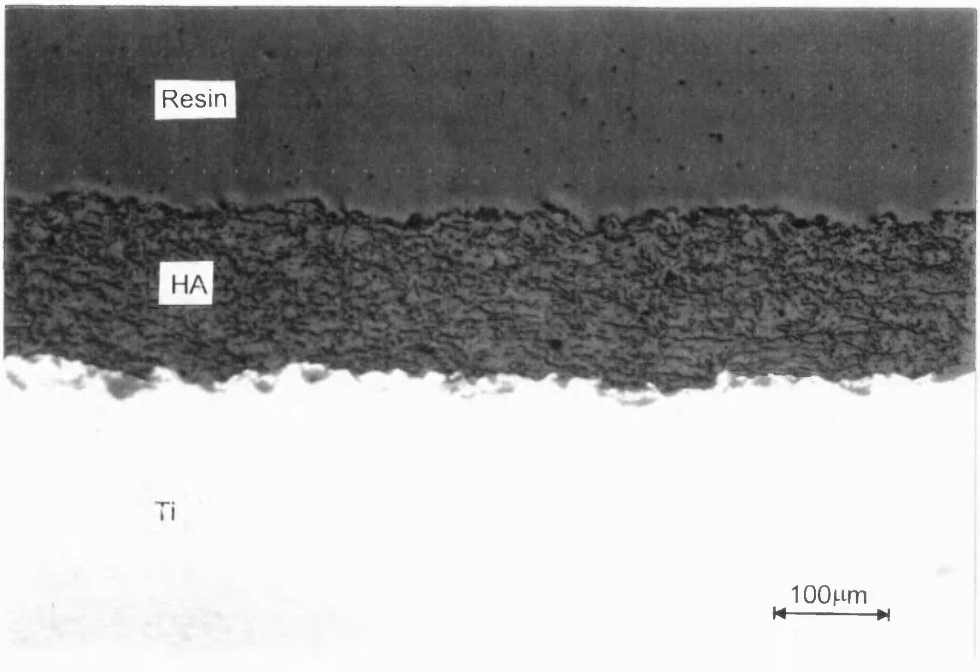

Figure 3.6.28. DIC optical micrograph of the cross-section of the CDS HA coating heat-treated at 600°C. mag ×160.

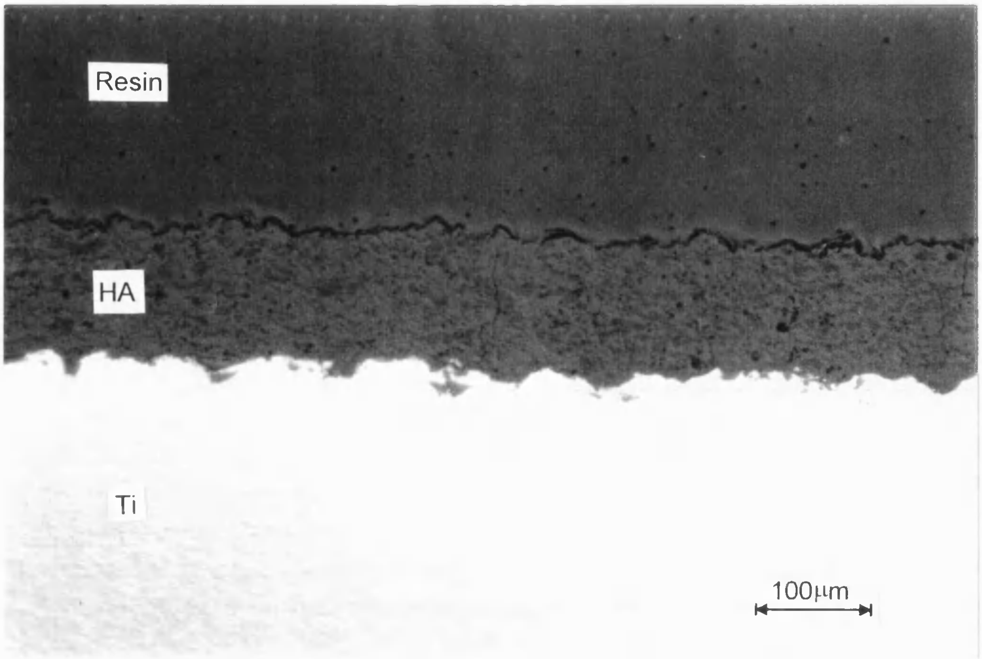

Figure 3.6.29. DIC optical micrograph of the cross-section of the CDS HA coating heat-treated at 700°C. mag ×160.

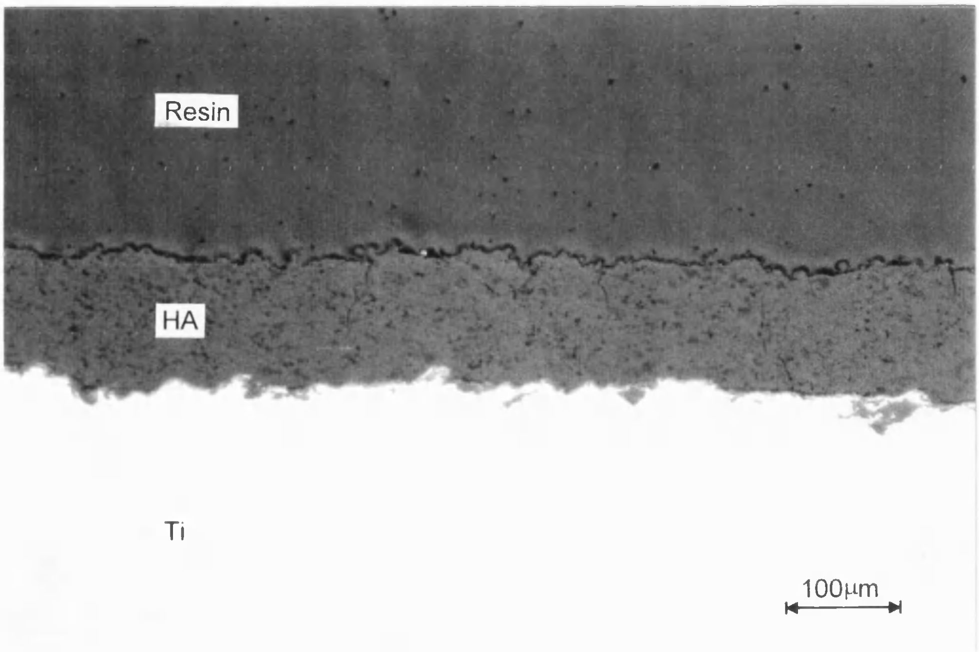

Figure 3.6.30. DIC optical micrograph of the cross-section of the CDS HA coating heat-treated at 800°C. mag ×160.

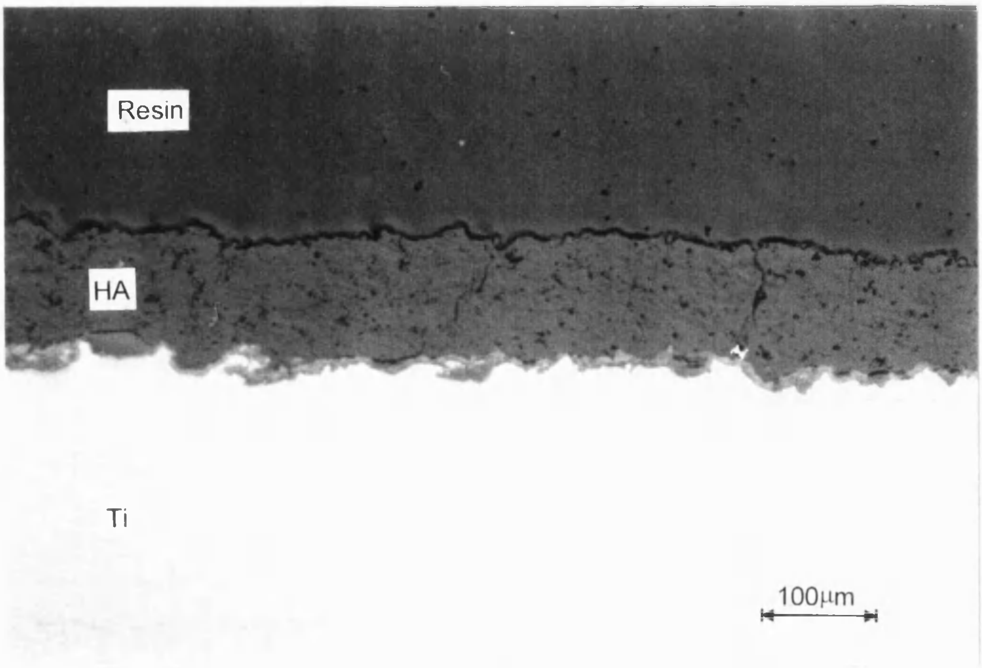

Figure 3.6.31. DIC optical micrograph of the cross-section of the CDS HA coating heat-treated at 900°C. mag ×160.

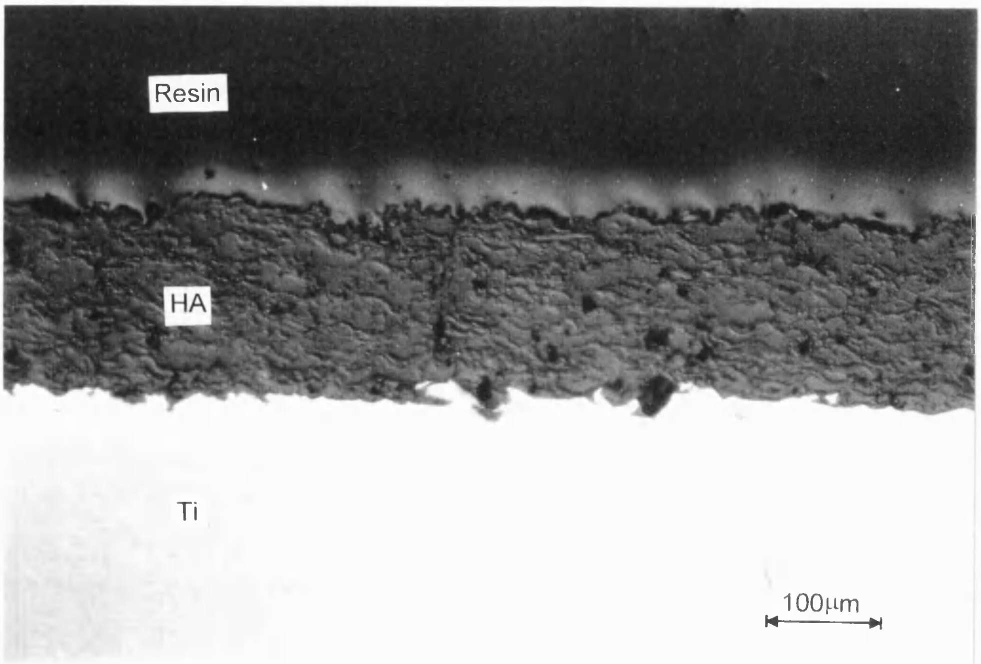

Figure 3.6.32. DIC optical micrograph of the cross-section of the as-sprayed VPS HA coating. mag ×160.

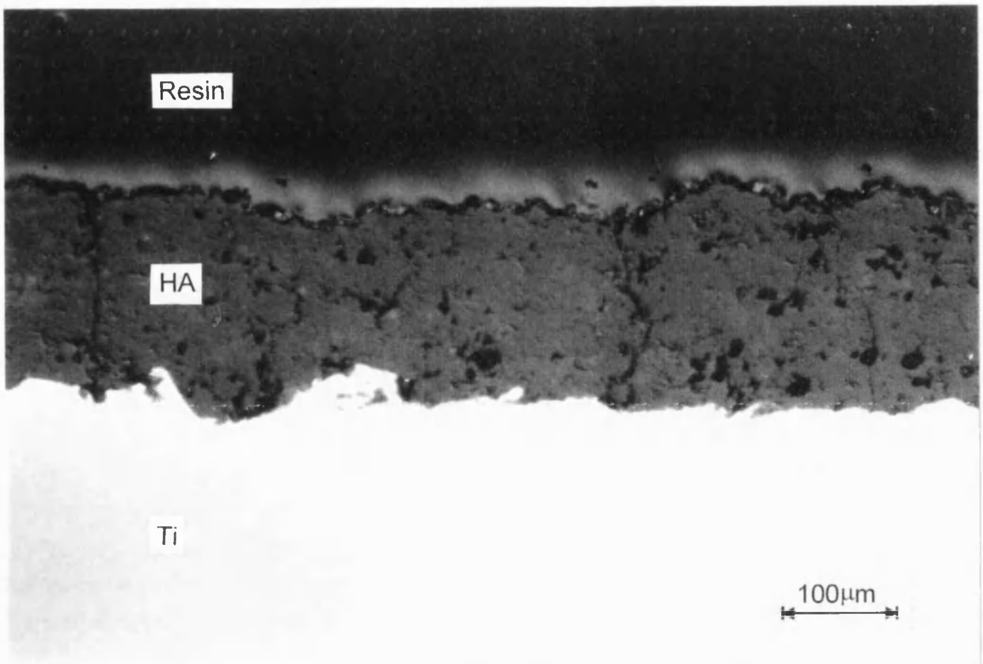

Figure 3.6.33. DIC optical micrograph of the cross-section of the VPS HA coating heat-treated at 600°C. mag ×160.

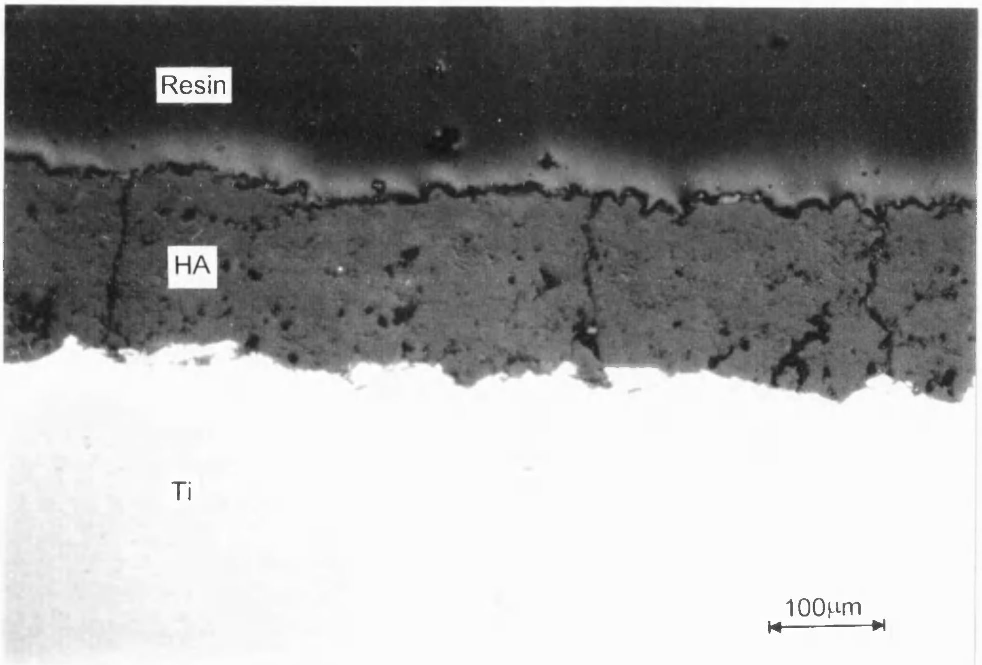

Figure 3.6.34. DIC optical micrograph of the cross-section of the VPS HA coating heat-treated at 700°C. mag ×160.

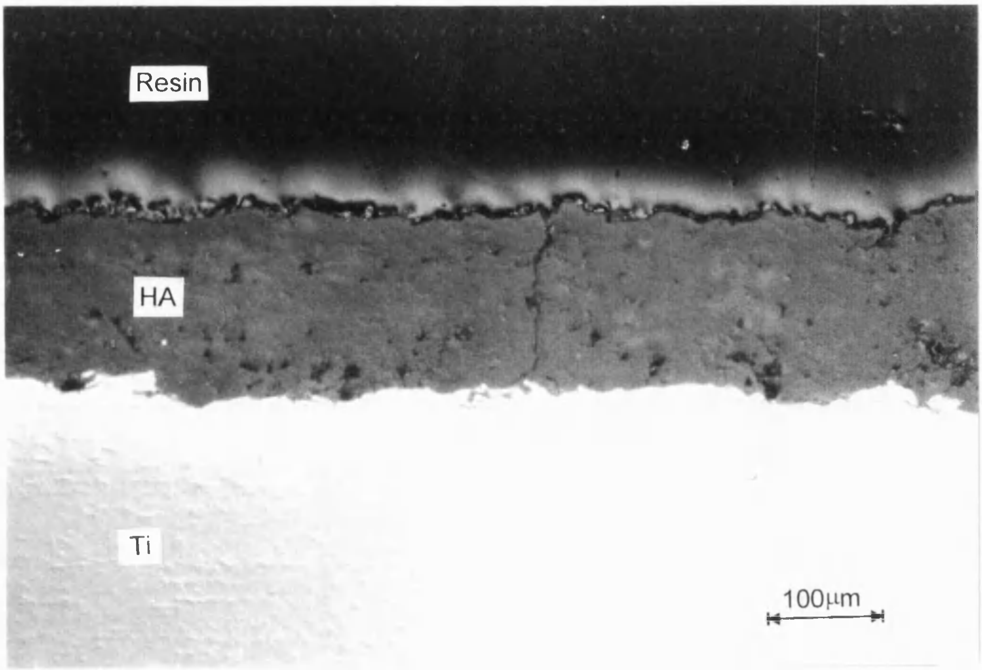

Figure 3.6.35. DIC optical micrograph of the cross-section of the VPS HA coating heat-treated at 800°C. mag ×160.

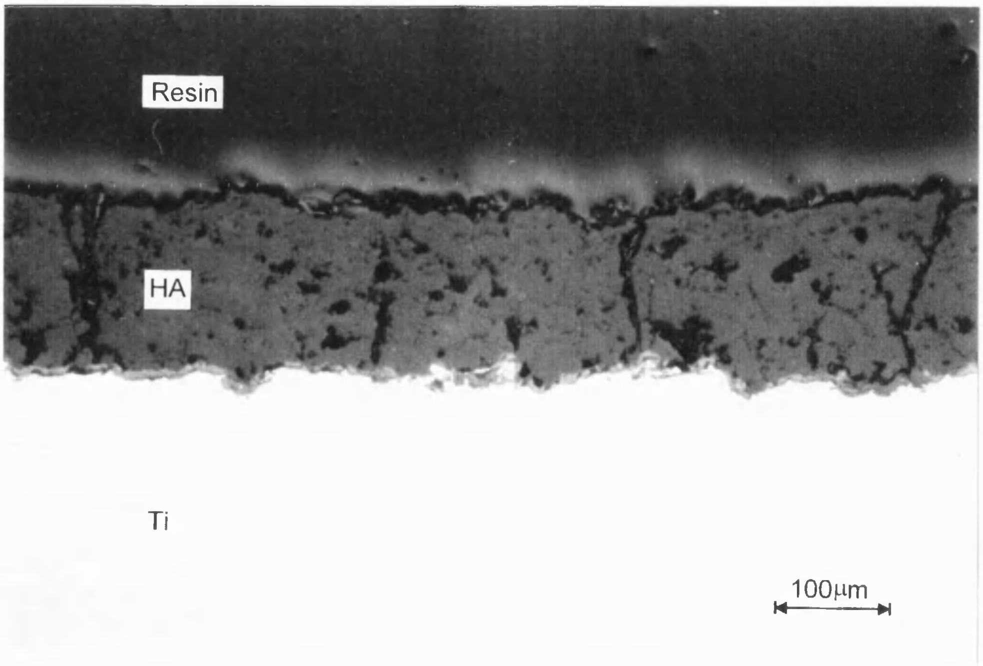

Figure 3.6.36. DIC optical micrograph of the cross-section of the VPS HA coating heat-treated at 900°C. mag ×160.

3.7 *In Vitro* Testing of Hydroxyapatite Coatings.

All the HA coatings were exposed in Ringer's solution at 37°C and either pH4.5 or pH7.2, as described in section 2.8. These coatings were examined for degradation using XRD, optical and scanning electron microscopy.

3.7.1 XRD of *In Vitro* Tested HA Coatings.

Sample Ar/N standard APS HA coating (APS1):

The APS1 HA coating exposed to the 4pH4.5 Ringer's solution showed an increase in crystallinity from 60% in the as-sprayed coating to >90% in the 1 week aged sample. Figure 3.7.1 shows the XRD pattern for the standard and 1 week aged APS1 HA coatings. There was minimal change in the XRD pattern between the 1, 2 & 4 week aged samples. The β-TCP and CaO present in the as-sprayed coating can not be detected in the exposed coatings.

The APS1 HA coating exposed in the pH7.2 Ringer's solution also showed an increase in crystallinity. The XRD pattern for the 1 week aged sample indicated a crystallinity of ~75%, the 2 & 4 week aged samples showed an increase in crystallinity to >90%, figure 3.7.2. The 1 week aged samples had a trace of β-TCP which was not detectable in the 2 & 4 week aged samples.

Sample Ar/N over-heated APS HA coating (APS2):

The as-sprayed APS2 HA coating was 68% crystalline, contained 8% β-TCP and a trace of CaO. The APS2 sample aged for 1 week at pH4.5 showed an increase in crystallinity to >90% and no β-TCP or CaO was detected, figure 3.7.3. The 2 & 4 week aged samples showed no significant difference from the 1 week aged sample.

The APS2 HA coating aged at 1 week at pH7.2 showed an increase in crystallinity to >80% and the β-TCP had reduced to ~3%. There was no CaO detected in this coating. The XRD pattern for the 2 week aged sample indicated a higher crystallinity of >90% and a trace of β-TCP was detected. The crystallinity of the 4 week aged sample had increased to >90% and no trace of β-TCP was detected. The XRD patterns for the APS2 HA coating aged at pH7.2 are shown in figure 3.7.4.

Sample Ar/N under-heated APS HA coating (APS3):

The APS3 HA coating exposed in the pH4.5 Ringer's solution showed a similar result to coatings APS1 and APS2. The crystallinity increased from 63% to >90% after 1 week of ageing and remained the same for the 2 & 4 week exposure periods. Also the CaO present in the as-sprayed coating was not detectable in the aged samples. Figure 3.7.5 shows the XRD patterns for the as-sprayed coating and the 1 week aged sample.

The APS3 HA coating aged for 1 week at pH7.2 showed an increase in crystallinity to ≈80% and no β-TCP or CaO was detected. The 2 & 4 week aged samples showed an increase in crystallinity to >90%. Figure 3.7.6 shows the XRD patterns for the 1,2 & 4 week aged samples at pH7.2.

Sample Ar/He standard APS HA coating (APS4):

The APS4 HA coating exposed in the pH4.5 solution for 1 week showed an increase in crystallinity from 67% in the as-sprayed coating to >90%. The crystallinity did not change at 2 or 4 weeks of ageing. There was no β-TCP or CaO detected in the as-sprayed coating or any of the aged coatings. Figure 3.7.7 shows the XRD patterns for the as-sprayed and the 1 week aged at pH4.5 coatings.

The APS4 HA coating exposed at pH7.2 showed an increase in crystallinity to ≈80% after 1 week of ageing and >90% at 2 & 4 weeks of ageing. There were no other phases detected in the aged coatings. Figure 3.7.8 shows the XRD patterns of the 1, 2 & 4 week HA coatings exposed at pH4.5.

Sample Ar/He over-heated APS HA coating (APS5):

The APS5 HA coatings aged at pH4.5 showed an increase in crystallinity from 76% in the as-sprayed coating to >90%. There was no significant difference between the 1, 2 & 4 week aged samples. Figure 3.7.9 shows the XRD pattern of the as-sprayed and 1 week aged coating.

The APS5 HA coating aged at pH7.2 showed a similar result to APS4 aged at pH7.2. There was an increase in crystallinity to ≈80% after 1 week of ageing and >90% at 2 & 4 weeks of ageing. There were no other phases detected in the aged coatings. Figure 3.7.10 shows the XRD patterns of the 1, 2 & 4 week HA coatings exposed at pH4.5.

Sample Ar/He under-heated APS HA coating (APS6):

The APS6 HA coatings exposed for 1, 2 & 4 weeks at pH4.5 all showed an increase in crystallinity from 74% in the as-sprayed coating to >90%. There were no phases other than HA detected in the as-sprayed and aged coatings. Figure 3.7.11 shows the XRD patterns of the as-sprayed and the 1 week aged HA coatings.

The APS6 HA coatings aged at pH7.2 for 1, 2 & 4 week showed an increase in crystallinity from the as-sprayed to >90%. There was no detectable β-TCP or CaO in these coatings. The XRD patterns for the 1, 2 & 4 week aged samples are shown in figure 3.7.12.

Sample standard CDS HA coating:

The CDS HA coatings exposed at pH4.5 for 1, 2 & 4 weeks showed an increase in crystallinity from 62% in the as-sprayed coating to >90% and no β-TCP was detected. Figure 3.7.13 shows the XRD patterns for the as-sprayed and the 1 week aged coatings.

The CDS HA coating exposed at pH7.2 for 1 week showed an increase in crystallinity to ≈75%. The broad β-TCP peak which was present in the as-sprayed coating, and corresponded to ≈4% β-TCP, has sharpened and indicates ≈6% β-TCP. At 2 & 4 weeks of ageing the crystallinity has increased to >85% and there is no detectable β-TCP. Figure 3.7.14 shows the XRD patterns of the 1,2 & 4 week aged samples.

Sample VPS HA coating:

The VPS HA coatings exposed at pH4.5 for 1, 2 & 4 weeks showed an increase in crystallinity from 70% in the as-sprayed coating to >90%. The β-TCP detected in the as-sprayed coating is not detectable in the aged samples. The XRD patterns for the as-sprayed coating and the 1 week exposed HA coating are shown in figure 3.7.15.

The VPS coating aged at pH7.2 1, 2 & 4 weeks showed an increase in crystallinity to >90%. The β-TCP detected in the as-sprayed coating is no longer detectable in the aged samples. The XRD patterns for the 1, 2 & 4 week aged coatings are shown in figure 3.7.16.

The XRD results for the pH4.5 exposed HA coatings are summarised in table 3.7.1 and the XRD results for the pH7.2 exposed HA coatings are summarised in table 3.7.2.

SAMPLE	STD	1 week	2 week	4 week
APS1	59% crystalline CaO 5% β-TCP	>90% crystalline no CaO no β-TCP	>90% crystalline	>90% crystalline
APS2	68% crystalline CaO 8% β-TCP	>90% crystalline no CaO no β-TCP	>90% crystalline	>90% crystalline
APS3	63% crystalline CaO Trace of β-TCP	>90% crystalline no CaO no β-TCP	>90% crystalline	>90% crystalline
APS4	67% crystalline no CaO no β-TCP	>90% crystalline no CaO no β-TCP	>90% crystalline	>90% crystalline
APS5	76% crystalline no CaO no β-TCP	>90% crystalline no CaO no β-TCP	>90% crystalline	>90% crystalline
APS6	74% crystalline no CaO no β-TCP	>90% crystalline no CaO no β-TCP	>90% crystalline	>90% crystalline
CDS	62% crystalline no CaO 4% β-TCP	>90% crystalline no CaO no β-TCP	>90% crystalline	>90% crystalline
VPS	70% crystalline no CaO 6% β-TCP	>90% crystalline no CaO no β-TCP	>90% crystalline	>90% crystalline

Table 3.7.1. Summary of XRD results for HA coatings exposed at pH4.5.

SAMPLE	STD	1 week	2 week	4 week
APS1	59% crystalline CaO 5% β-TCP	≈75% crystalline no CaO trace β-TCP	>90% crystalline no β-TCP	>90% crystalline
APS2	68% crystalline CaO 8% β-TCP	≈80% crystalline no CaO 3% β-TCP	>90% crystalline trace β-TCP	>90% crystalline no β-TCP
APS3	63% crystalline CaO Trace of β-TCP	≈80% crystalline no CaO trace β-TCP	>90% crystalline no β-TCP	>90% crystalline
APS4	67% crystalline no CaO no β-TCP	≈80% crystalline no CaO no B-TCP	>90% crystalline	>90% crystalline
APS5	76% crystalline no CaO no β-TCP	≈80% crystalline no CaO no β-TCP	>90% crystalline	>90% crystalline
APS6	74% crystalline no CaO no β-TCP	>90% crystalline no CaO no β-TCP	>90% crystalline	>90% crystalline
CDS	62% crystalline no CaO 4% β-TCP	≈75% crystalline no CaO 6% β-TCP	>85% crystalline no CaO no β-TCP	>85% crystalline
VPS	70% crystalline no CaO 6% β-TCP	>90% crystalline no CaO no β-TCP	>90% crystalline	>90% crystalline

Table 3.7.2. Summary of XRD results for HA coatings exposed at pH7.2

3.7.2 Microscopy of *In Vitro* Tested HA Coatings.

Sample Ar/N standard APS HA coating (APS1):

SEM analysis of the surface of the coating exposed at pH7.2 for 1, 2 & 4 weeks showed very little change from the as-sprayed coating. Figure 3.7.17 shows an SEM micrograph of the APS1 coating after 4 weeks ageing at pH7.2. The coating looks very similar to the as-sprayed coating, with little evidence of dissolution of the coating. Optical microscopy of the coating cross-section showed no noticeable change from the as-sprayed coating. The coating thickness was not reduced and the porosity remained constant. Figure 3.7.18 shows an optical micrograph of the cross-section of APS1 after ageing at pH7.2 for 4 weeks.

SEM examination of the HA coating APS1 aged for 1 week at pH4.5, figure 3.7.19, shows a difference from the as-sprayed coating. The surface of the coating shows areas of coral like appearance, which are caused by dissolution of the coating. After 2 weeks ageing at pH4.5 the coating surface appears to have increased in roughness by valleys being etched between outcrops of larger particles. At 4 weeks this effect is more apparent, figure 3.7.20. Some areas of the coating have been preferentially etched, one such area is shown in figure 3.7.21. After 2 weeks ageing the surface of the etched areas appears to consist of small agglomerated particles $\approx 1\mu m$ in size. Optical microscopy of the cross-section of HA coatings APS1 aged at 1, 2 & 4 weeks, figures 3.7.22, 3.7.23 & 3.7.24, showed a layer at the surface of the coating being etched by the *in vitro* solutions. As the ageing time increased the etched layer also increased in thickness. Figure 3.7.24 shows the thickness of coating etched at each ageing time for all HA coatings. The layer of coating which has been etched is highly porous and probably has much lower mechanical properties than the as-sprayed coating. This was evident when the coating surface was rubbed gently with the thumb, a powder would fall off the coating suggesting the coating surface was disintegrating.

Sample Ar/N over-heated APS HA coating (APS2):

SEM examination of the surface of HA coating APS2 after ageing for 1, 2 & 4 weeks in pH7.2 *in vitro* solutions, figures 3.7.25, 3.7.26 & 3.7.27, showed some etching of the surface of the coating. As the ageing time increased the amount of etching increased. The increase in etching is evident from the large areas of surface covered with agglomerates of particles ≈1μm in size rather than the smooth glassy appearance of as-sprayed HA. Optical microscopy of the cross-section of the APS2 HA coating aged in pH7.2 *in vitro* solution showed very little change from the as-sprayed coating.

SEM analysis of the surface of the APS2 HA coatings aged in pH4.5 *in vitro* solution showed a similar result to the APS1 HA coatings. The etched area on the surface consisted of an agglomerate of particles ≈1μm in size. An SEM micrograph of a etched area is shown in figure 3.7.28. Optical microscopy of the cross-section of the HA coating APS2 aged in pH4.5 *in* *vitro* solution showed a similar result to APS1 with a layer of etched coating increasing in thickness as the ageing time increased. The coating thickness of APS2 was less than that of APS1 and at 4 weeks of ageing the thickness of the etched layer had exceeded the thickness of the coating, figure 3.7.29.

Sample Ar/N under-heated APS HA coating (APS3):

SEM examination of the surface of the HA coating APS3 aged in pH7.2 *in vitro* solution showed a steady increase in the amount of surface etching as the ageing time increased. This is apparent form the large number of areas consisting of agglomerated 1μm particles which are only present in small quantities in the as-sprayed coating. Figure 3.7.30 shows the HA coating APS3 after ageing in pH7.2 *in vitro* solution for 4 weeks. Optical microscopy of the HA coating APS3 aged in pH7.2 *in vitro* solutions shows no significant change from the as-sprayed HA coating.

SEM examination of the surface of HA coating APS3 aged in pH4.5 *in vitro* solutions showed a similar result to APS1. The 1 week aged sample showed areas which were etched and unetched, figure 3.7.31. As the ageing time increases the etched areas increased in size and number. Optical microscopy showed an increase in the thickness of the etched layer similar to that of APS2. Figure 3.7.32 shows the 1 week aged sample, with the majority of the coating intact and an etched layer on the surface. As the coating thickness is less than APS1 the etched layer had penetrated to the Ti interface after the 4 weeks of ageing, figure 3.7.33.

Sample Ar/He standard APS HA coating (APS4):

SEM and optical microscopy analysis for both the pH7.2 and pH4.5 *in vitro* solution aged APS4 coatings showed very similar results to APS3. The SEM analysis of the pH7.2 aged coatings showed an increase of etched areas as the ageing time increased. The optical microscopy indicated a minimal change from the as-sprayed coating. The optical microscopy of the pH4.5 aged coatings showed an increase in the thickness of the etched layer as the ageing time increased. After 4 weeks of ageing in the pH4.5 *in vitro* solutions there is still a thin layer of intact coating at the interface with the titanium alloy substrate, figure 3.7.34.

Sample Ar/He over-heated APS HA coating (APS5):

Sample APS5 showed very similar results to APS3. The thickness of the etched layer had penetrated the full thickness of the coating after 4 weeks of ageing in pH4.5 *in vitro* solution.

Sample Ar/He under-heated APS HA coating (APS6):

Using SEM microscopy the appearance of the surface of coating APS6 was very similar to APS5 for pH 7.2 & 4.5 at all ageing times. The optical microscopy examination was also similar to APS5 with the coating being fully etched after the 4 week ageing time in pH4.5 *in vitro* solutions.

Sample standard CDS HA coating:

SEM examination of the surface of the CDS HA coating aged in pH7.2 *in vitro* solution for 1 week, figure 3.7.35, shows very little change form the as-sprayed coating. The 2 and 4 week aged samples shows evidence of some ageing although not as evident as the APS coatings, figure 3.7.36. The optical microscopy of the cross-section of the CDS coating shows very little change from the as-sprayed coating for the pH7.2 *in vitro* aged samples.

SEM examination of the surface of the CDS HA coatings aged in pH4.5 *in vitro* solution showed large cracks appearing on the surface of the coating after 1 week of ageing, figure 3.7.37. After 2 weeks of ageing these cracks had enlarged and etching was evident. At 4 weeks the coating was to fragile to view using the SEM. Optical microscopy of the cross-section of the CDS HA coating after ageing in pH4.5 *in vitro* solution showed that the etched layer had penetrated ≈50% of the thickness of the coating after 1 week of ageing, figure 3.7.38. After 2 weeks of ageing the etched layer had penetrated up to 80% of the coating thickness and at 4 weeks of ageing the full coating had been etched and had detached from the substrate leaving a thin layer of HA remaining on the substrate, figure 3.7.39.

Sample VPS HA coating:

SEM examination of the surface of the VPS HA coating aged in pH7.2 *in vitro* solution showed very little change from the as-sprayed coating. The optical microscopy of the cross-section of the VPS coating aged in pH7.2 *in vitro* solution showed no change from the as-sprayed coating.

SEM examination of the surface of the VPS HA coating aged in pH4.5 *in vitro* solution showed etching of the coating after 1 week, figure 3.7.40. The etched areas increased in size as the ageing time increased. The optical microscopy of the cross-section of the VPS coatings showed the etched layer penetrating almost to the interface with the titanium alloy substrate, figure 3.7.41.

3.7.3. Discussion of Results.

It has been reported that hydroxyapatite and other calcium phosphates are less stable at lower pH values [24, 45] and therefore the pH4.5 *in vitro* test is effectively an accelerated version of the pH7.2 tests. Wound healing conditions in the body result in a local pH of 4.5 and therefore the pH4.5 *in vitro* tests would also simulate the conditions the coating would experience when initially implanted into the body.

The XRD data for all of the HA coatings exposed in pH4.5 Ringer's solution showed very similar results. The crystallinity of the coating had increased to >90% and any impurity phases had been dissolved. The increase in crystallinity can be attributed to dissolution of amorphous calcium phosphate in preference to crystalline hydroxyapatite. The Ringer's solution initially acts on the surface of the coating and as amorphous calcium phosphate is less stable than crystalline hydroxyapatite the amorphous phase is preferentially dissolved leaving crystalline hydroxyapatite on the surface of the coating. The X-ray beam penetrates ≈5μm into the surface of the coating and is therefore a surface orientated technique. The unexposed coating has a mixture of crystalline and amorphous hydroxyapatite at the coating surface, after exposure to the pH4.5 Ringer's solution the majority of the surface is crystalline and hence the crystallinity measured by XRD increases. Although the unexposed coating below the affected zone probably has a similar crystallinity to the as-sprayed coating. The CaO and β-TCP have been reported to have a lower stability than hydroxyapatite when exposed *in vitro*, this explains the loss of these phases after exposure in Ringer's solution. In a similar way to the amorphous hydroxyapatite dissolving from the surface the CaO and β-TCP will also be dissolved preferentially to crystalline hydroxyapatite.

The XRD results for the pH7.2 *in vitro* tests showed a similar result to the pH4.5 *in vitro* tests, although the dissolution of the phases was at a slower rate. The crystallinity increases and attains a similar crystallinity to the pH4.5 1 week aged samples after 4 weeks of ageing. The β-TCP present in the Ar/N_2 gas mixture APS coatings and the CDS coating was not detectable at 2 weeks of ageing for all the coatings except for the overheated APS Ar/N_2 gas mixture coating (APS2) which had a trace of β-TCP at 2 weeks and this had dissolved by 4 weeks. The APS2 coating had the largest percentage β-TCP post spraying and this shows that the β-TCP dissolves at a relatively slow rate at pH7.2 and the more β-TCP present the longer it will remain in the coating post implantation. The CaO present in the Ar/N_2 APS coatings had dissolved after 1 week of ageing. The XRD results show that after 4 weeks of ageing at pH7.2 all the coatings have effectively the same surface composition. Hydroxyapatite coatings which have a high percentage of amorphous calcium phosphate or other calcium phosphate phases partially dissolve when implanted in the body. The rate of dissolution and quantity of coating dissolved depends on the ratio of hydroxyapatite to these other phases, the higher the percentage of other calcium phosphate phases the faster the coating will dissolve. One of the advantages of a coating which dissolves is that the new bone forming around the implant has a local supply of calcium and phosphate ions to aid bone growth. This can enhance the bone formation and speed of the fixation of the implant. The disadvantage of a coating that dissolves is that the structural integrity of the coating is reduced which can cause the coating to spall off the implant and produce potentially damaging wear particles.

The microscopy of all the HA coatings exposed at pH7.2 showed very minimal change to the as-sprayed coatings. There was no significant change in the coating thickness or an increase in porosity. The surface of the coatings when viewed using scanning electron microscopy showed minimal change despite the XRD results suggesting that some dissolution of the coating had occurred. Gross & Berndt [44] used Ringer's solution to *in vitro* test amorphous and crystalline HA coatings. They found the amorphous coating reduced in weight by ≈20% after 4 weeks of ageing and the surface of the coating when examined using SEM showed significant disintegration . The crystalline coatings showed a very minimal weight gain and the surface of the coating did not disintegrate. The hydroxyapatite coatings used in this work are all semi-crystalline and showed minimal change for the ageing at pH7.2 which is similar to the result found by Gross & Berndt for the crystalline hydroxyapatite coatings. At pH4.5 the degradation of the coatings was significant with cracks and etching appearing on the surface and through the cross-section of the coatings. The pH4.5 result is similar to the result obtained by Gross & Berndt for the amorphous coating exposed to Ringer's solution.

Scanning electron microscope images of the surface of the APS & VPS hydroxyapatite coatings which had been exposed in Ringer's solution at pH4.5 for a couple of weeks showed etched areas which appeared to consist of agglomerated particles ≈1μm in size. The powders which were used to spray these coatings, Amdry 6020 and XPTW601, were formed by a sintering and crushing technique. SEM micrographs of the powder particles, 3.1.8 & 3.1.13, showed that the particles were sintered from smaller particles ≈1μm in size. The structure of the etched surface of the coatings and the powder particles show some similarities. APS and VPS coatings consist of a mixture of fully melted and partially melted particles. The partially melted particles have a molten surface and a solid core. The molten surface of the particles enables it to adheres to the substrate while the core of the particle would remain unchanged. The surface of a molten particle experiences a very rapid cooling rate when impacting the substrate which would cause the surface to be almost totally amorphous hydroxyapatite. When the surface is exposed to the pH4.5 Ringer's solution the amorphous hydroxyapatite dissolves leaving the more crystalline core of the partially molten particle. This explains the correlation between the agglomerated etched structure on the surface of an exposed coating and the structure of the powder particles.

The CDS coating exposed at pH4.5 showed the splats on the surface splitting and cracking, fig. 3.7.37. This is similar to the result found by Gross & Berndt [44] with the amorphous APS hydroxyapatite coating exposed in Ringer's solution. The structural integrity of the surface layer of the CDS coating is severely reduced by ageing at pH4.5. This is evident when the coating can be rubbed from the substrate of the coating with a thumb. The cross-sectional microscopy of the CDS coating shows that the coating has rapidly dissolved, fig. 3.7.38. At 4 weeks of ageing the coating has completely detached from the substrate, due to dissolution, fig.3.7.39. The other hydroxyapatite coatings also show the dissolution of the coating at pH4.5, although not at such a rapid rate as the CDS coating. The dissolution appears to progress from the surface of the coating towards the hydroxyapatite/ titanium alloy substrate interface in a linear manner along the length of the coating. Cracks which propagate from the coating surface towards the hydroxyapatite / titanium alloy interface do not cause Ringer's solution to dissolve the hydroxyapatite from the interface which could result in the coating spalling off the substrate. For all of the coatings, the affected part of the coating is not completely dissolved and a highly porous layer is seen on top of a seemingly intact coating. The porous layer appears to have been etched around the edges of splatted particles which suggests that the amorphous hydroxyapatite around the edge of splatted particles is dissolved preferentially to the slower cooled more crystalline core.

The coating thickness dissolved in pH4.5 Ringer's solution at 2 weeks and the crystallinity of the as-sprayed coatings are plotted in figure 3.7.43. A relationship is apparent in that the more crystalline coatings dissolve at a slower rate. Although there is not a large difference in crystallinity between the hydroxyapatite coatings the dissolution rate is affected. The fact that amorphous coating dissolves at a faster rate than crystalline coatings has been reported in the literature. This work shows that small differences in crystallinity can make a difference to the dissolution rate of the coating, and the dissolution rate is fairly independent of spraying technique.

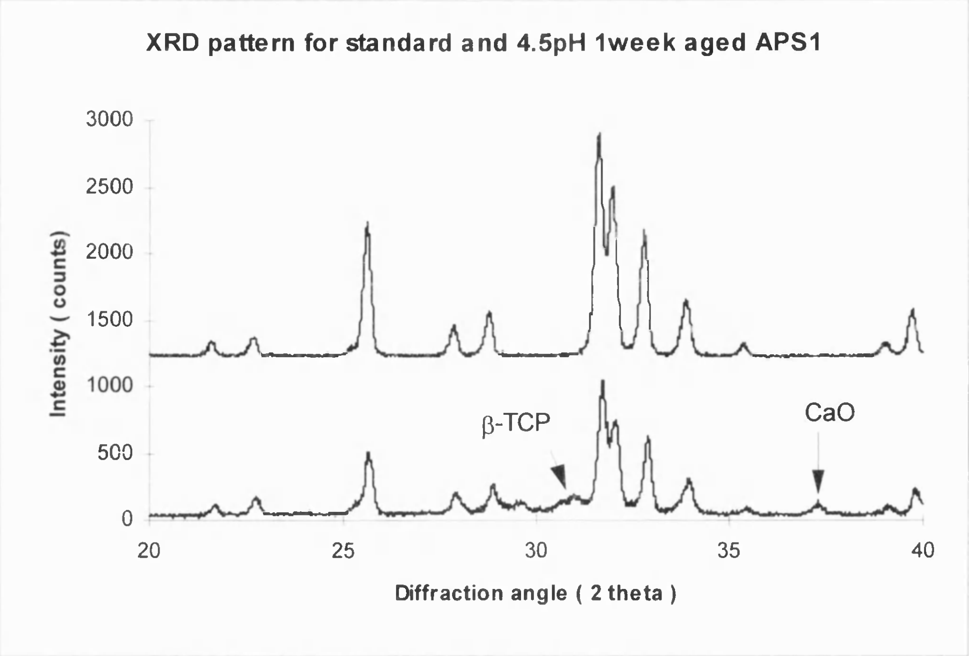

Figure 3.7.1. XRD patterns showing as-sprayed and 1 week aged in pH4.5 Ringer's solution APS1 HA coating.

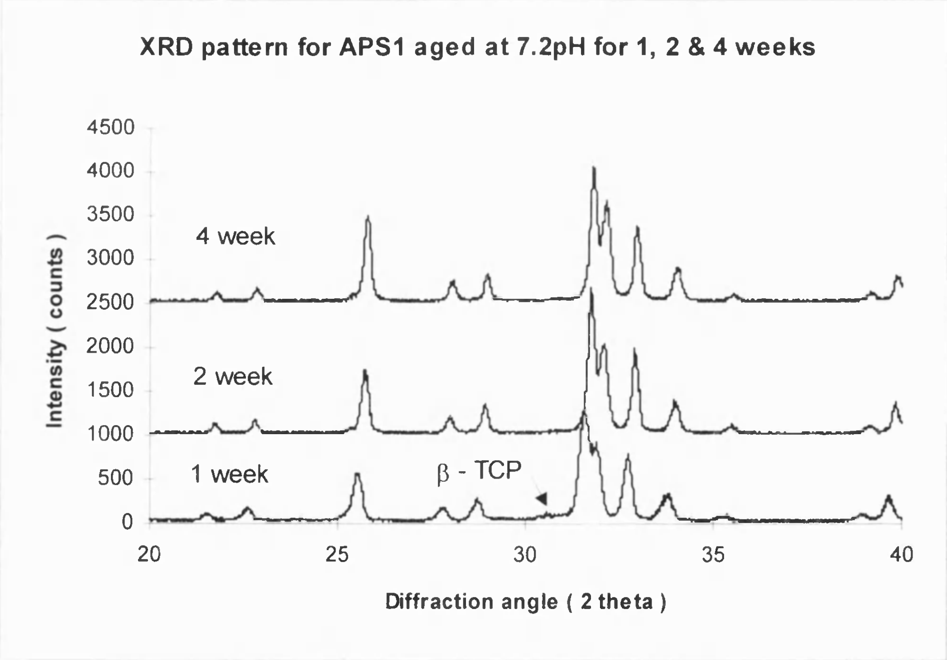

Figure 3.7.2. XRD patterns showing 1,2 & 4 week aged in pH7.2 Ringer's APS1 HA coatings.

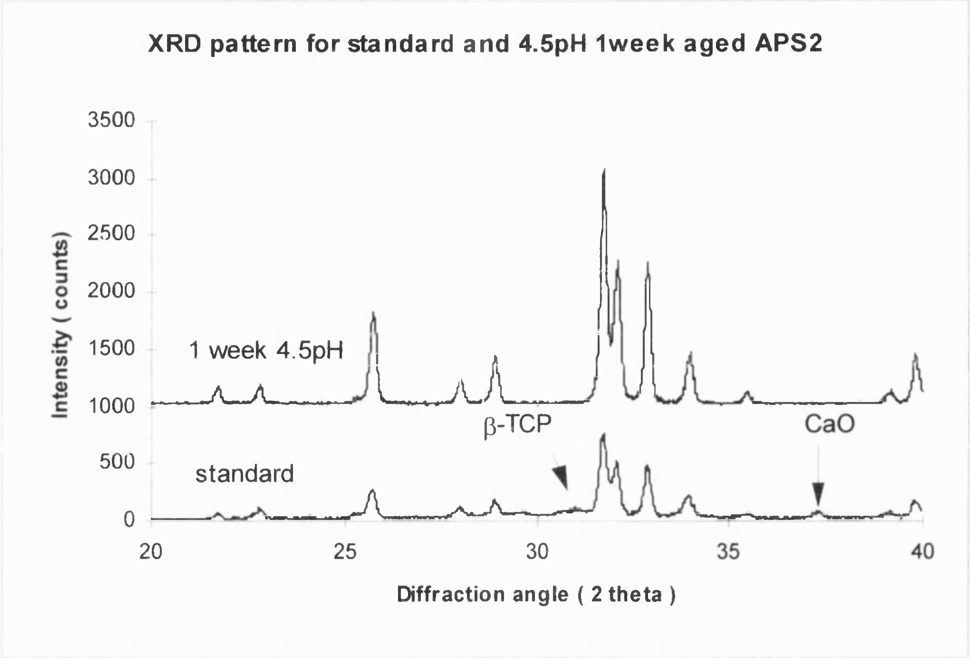

Figure 3.7.3. XRD patterns showing the as-sprayed and 1 week aged in pH4.5 Ringer's solution APS2 HA coating.

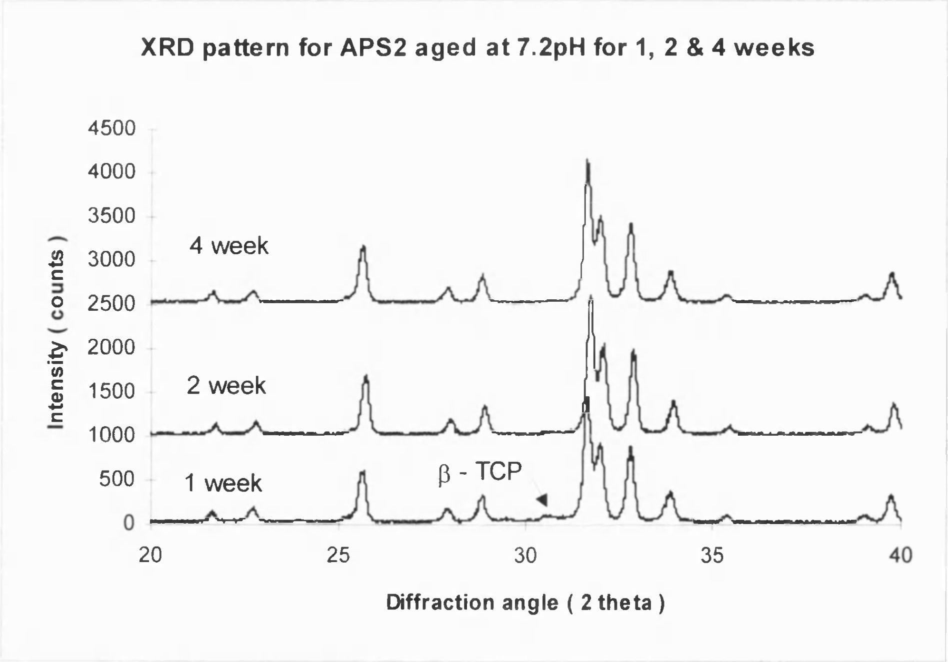

Figure 3.7.4. XRD patterns showing the 1,2, & 4 week aged in pH7.2 Ringer's solution APS2 HA coating.

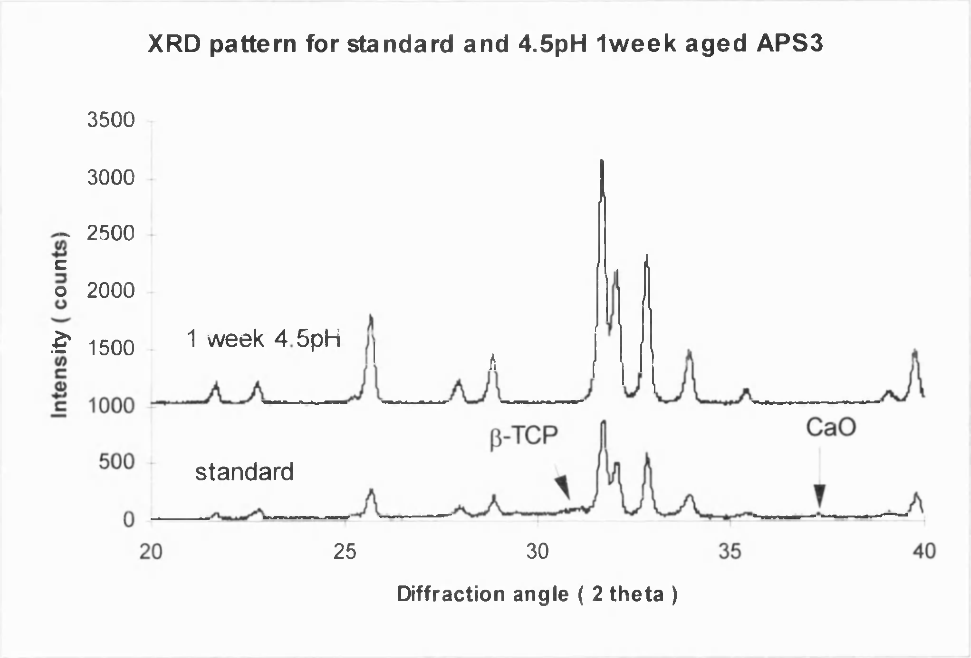

Figure 3.7.5. XRD patterns showing the as-sprayed and 1 week aged in pH4.5 Ringer's solution APS3 HA coating.

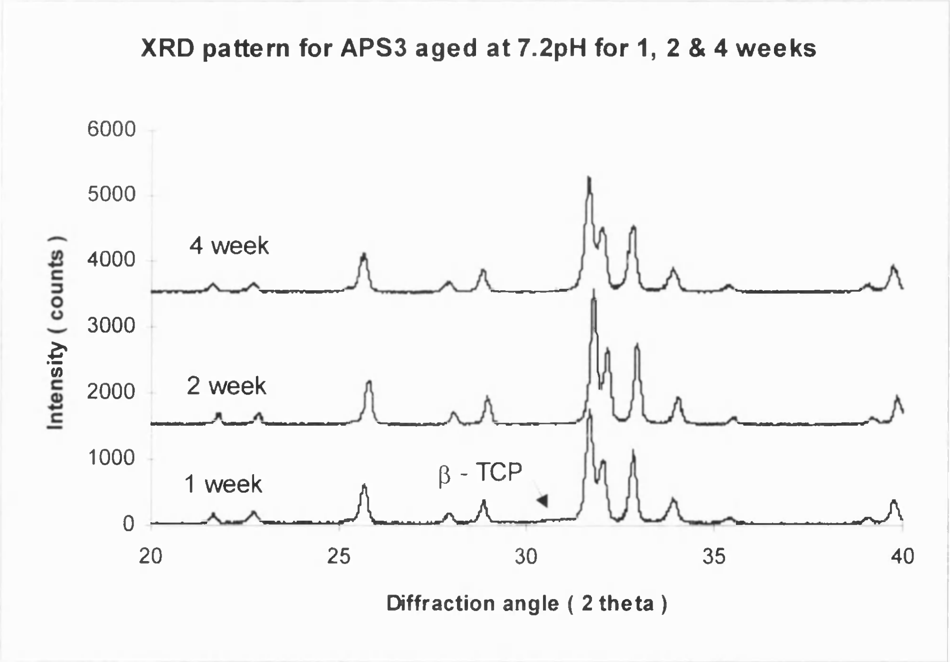

Figure 3.7.6. XRD patterns showing the 1,2 & 4 week aged in pH7.2 Ringer's solution APS3 HA coatings.

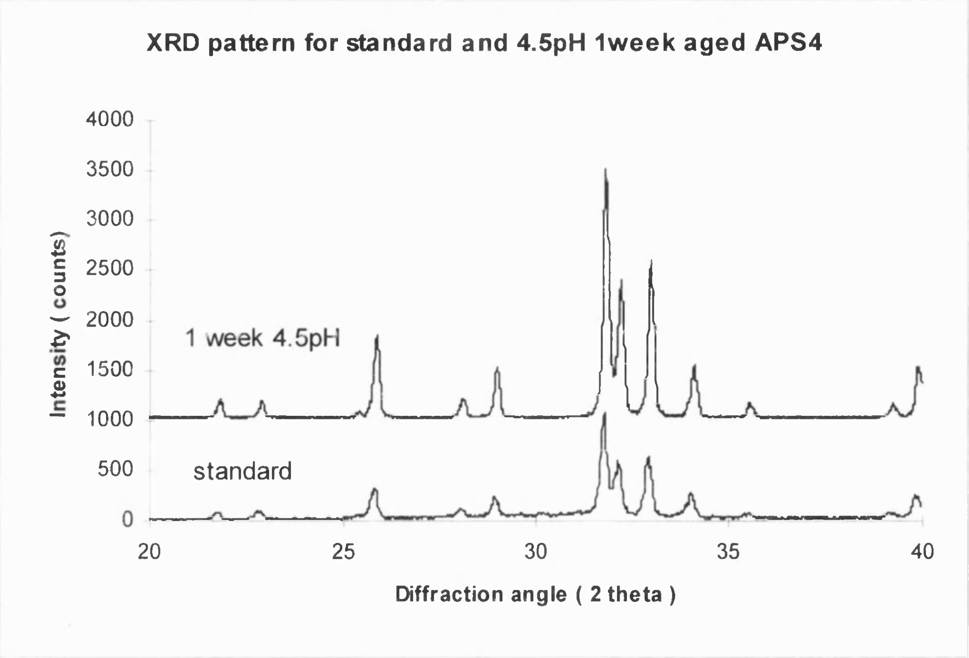

Figure 3.7.7. XRD patterns showing the as-sprayed and 1 week exposed in pH4.5 Ringer's solution APS4 HA coating.

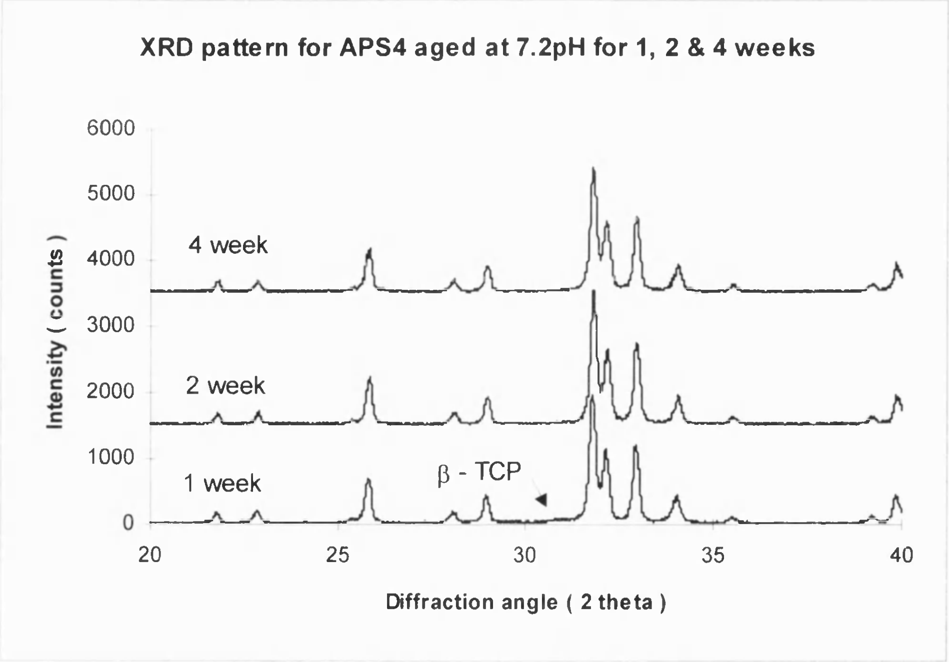

Figure 3.7.8. XRD patterns showing the 1,2 & 4 week aged in pH7.2 Ringer's solution APS4 HA coatings.

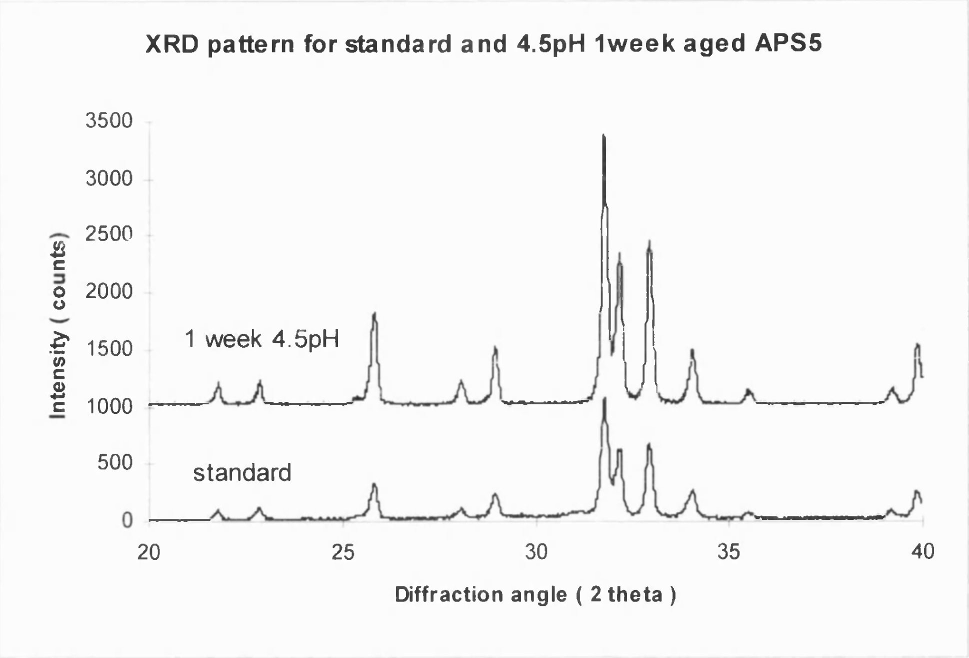

Figure 3.7.9. XRD patterns showing the as-sprayed and 1 week exposed in pH4.5 Ringer's solution APS5 HA coating.

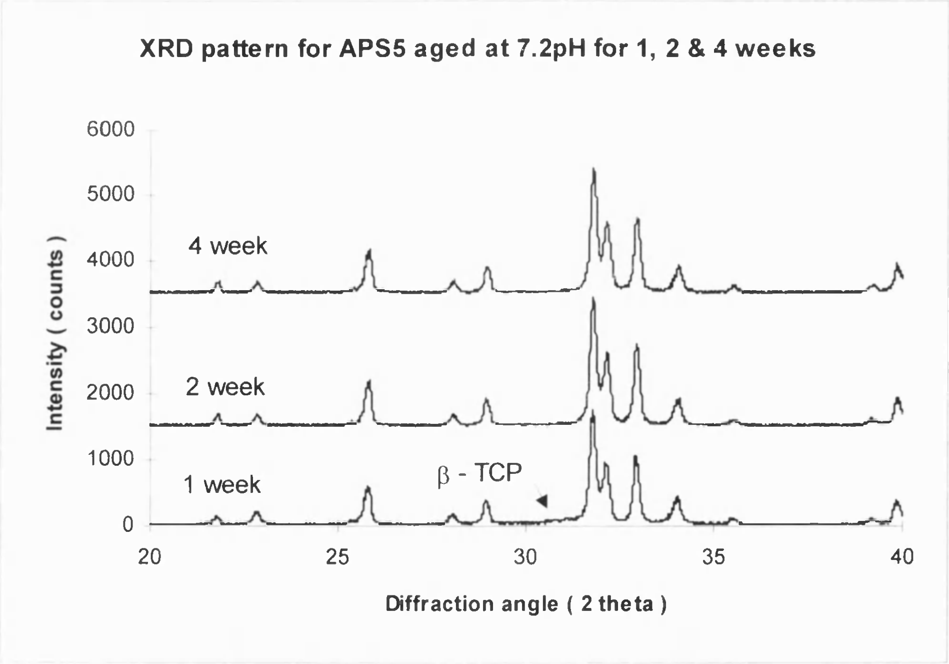

Figure 3.7.10. XRD patterns showing the 1,2 & 4 week aged in pH7.2 Ringer's solution APS5 HA coatings.

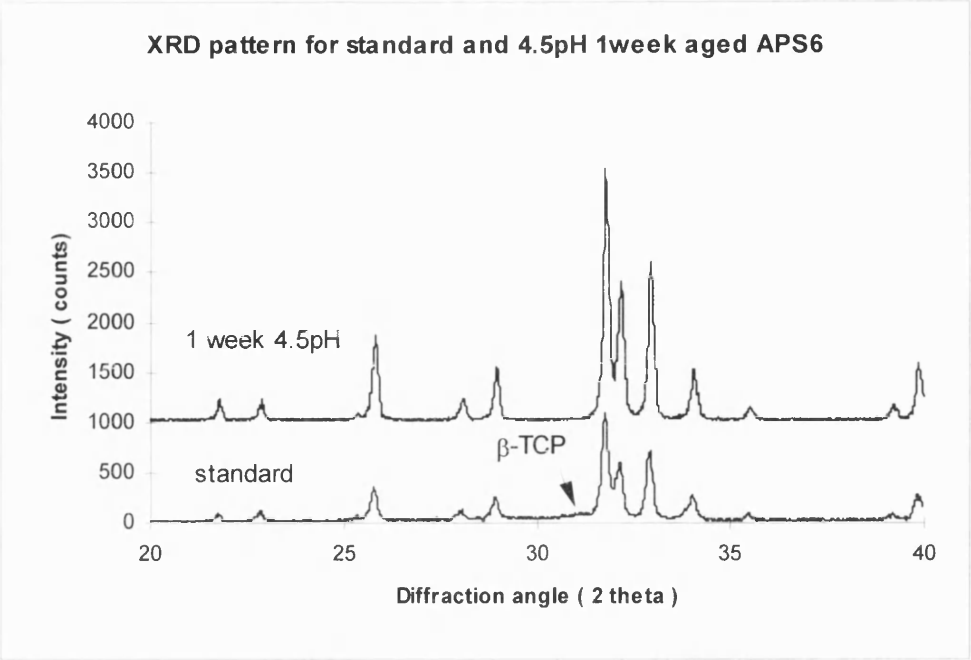

Figure 3.7.11. XRD patterns showing the as-sprayed and 1 week exposed in pH4.5 Ringer's solution APS6 HA coating.

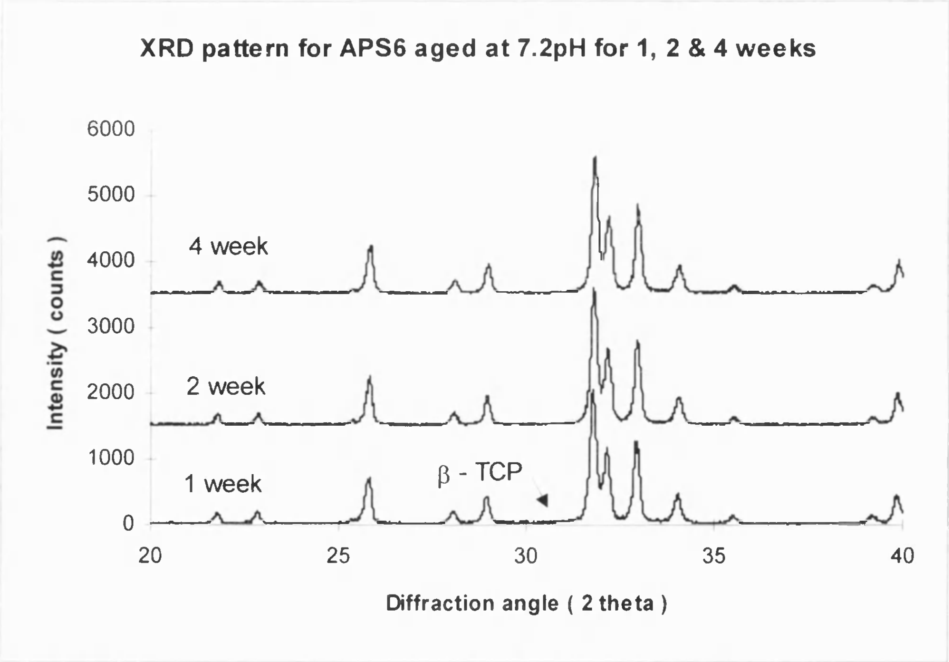

Figure 3.7.12. XRD patterns showing the 1,2 & 4 week aged in pH7.2 Ringer's solution APS6 HA coatings.

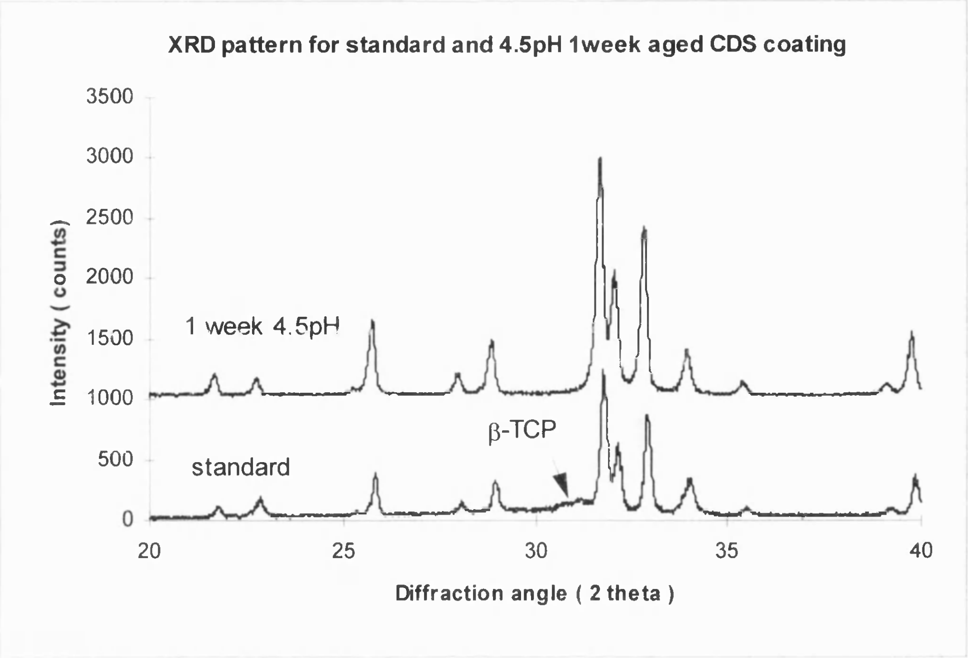

Figure 3.7.13. XRD patterns showing the as-sprayed and the 1 week aged in pH4.5 Ringer's solution CDS HA coatings.

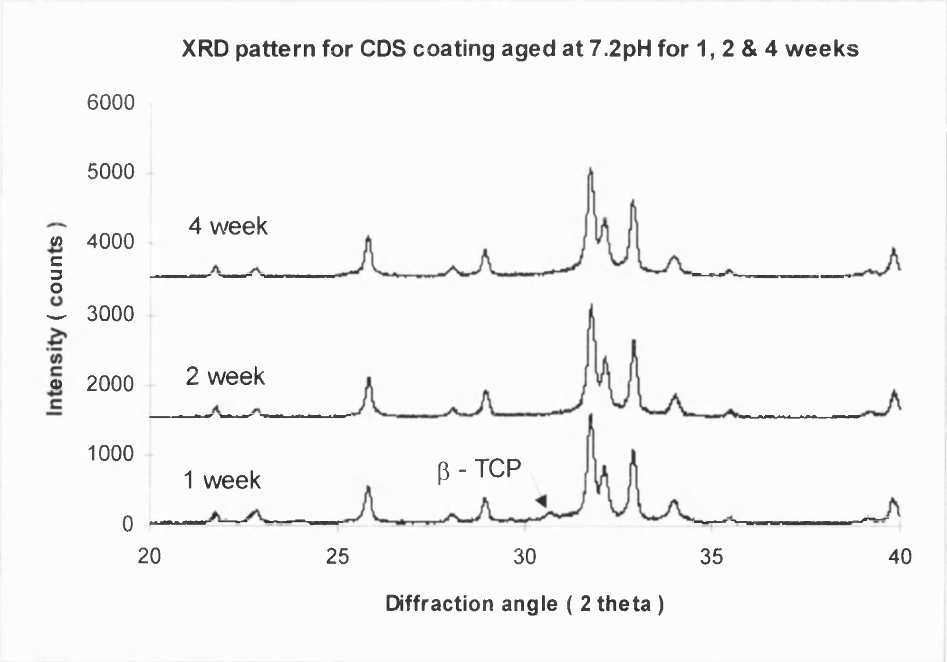

Figure 3.7.14. XRD patterns showing the 1,2 & 4 week aged in pH7.2 Ringer's solution CDS HA coatings.

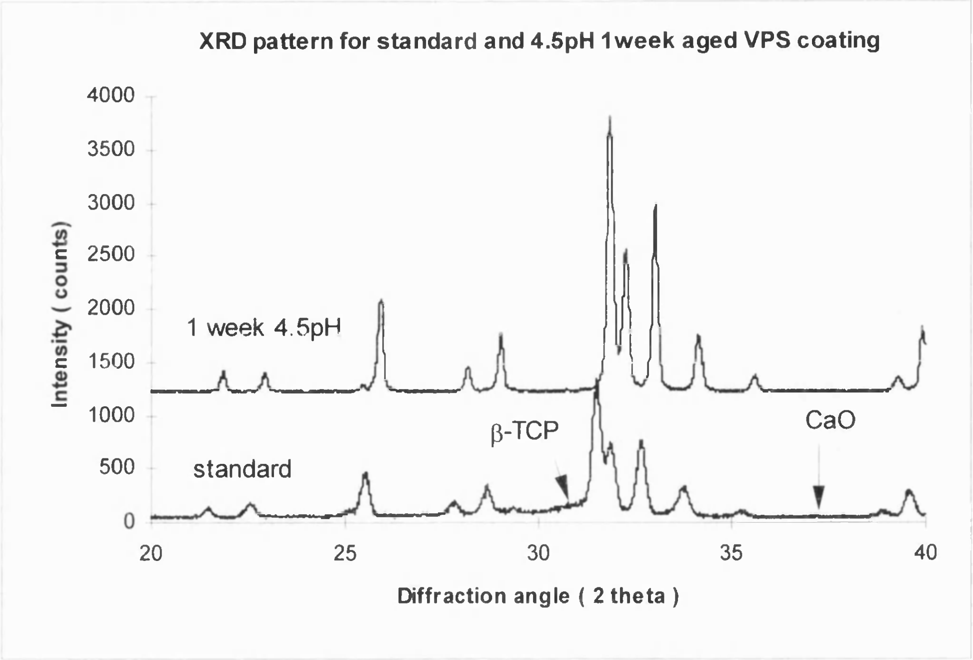

Figure 3.7.15. XRD patterns showing the as-sprayed and the 1 week aged in pH4.5 Ringer's solution VPS coating.

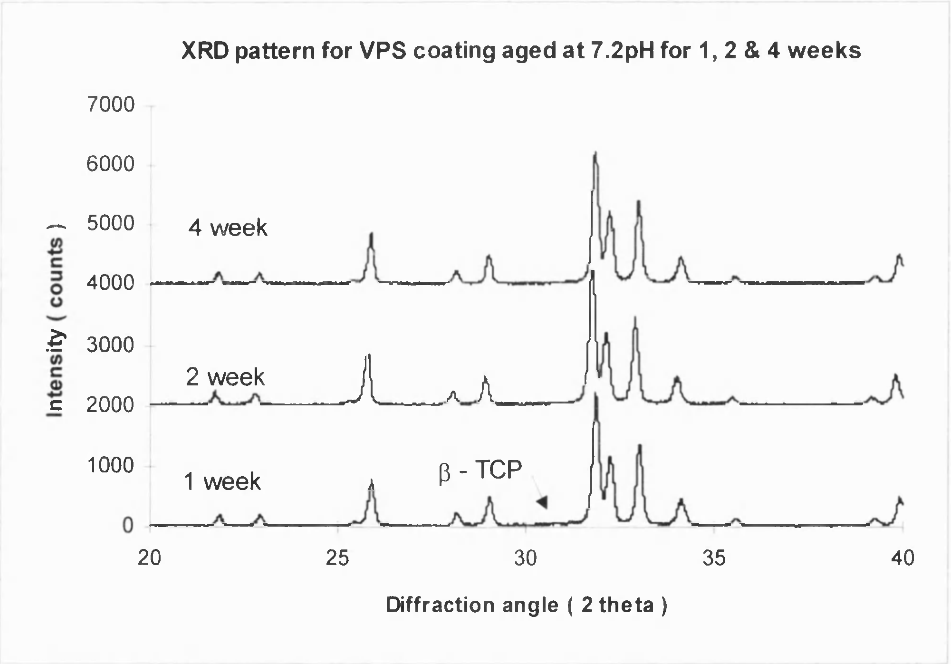

Figure 3.7.16. XRD patterns showing the 1,2 & 4 week aged in pH7.2 Ringer's solution VPS HA coatings.

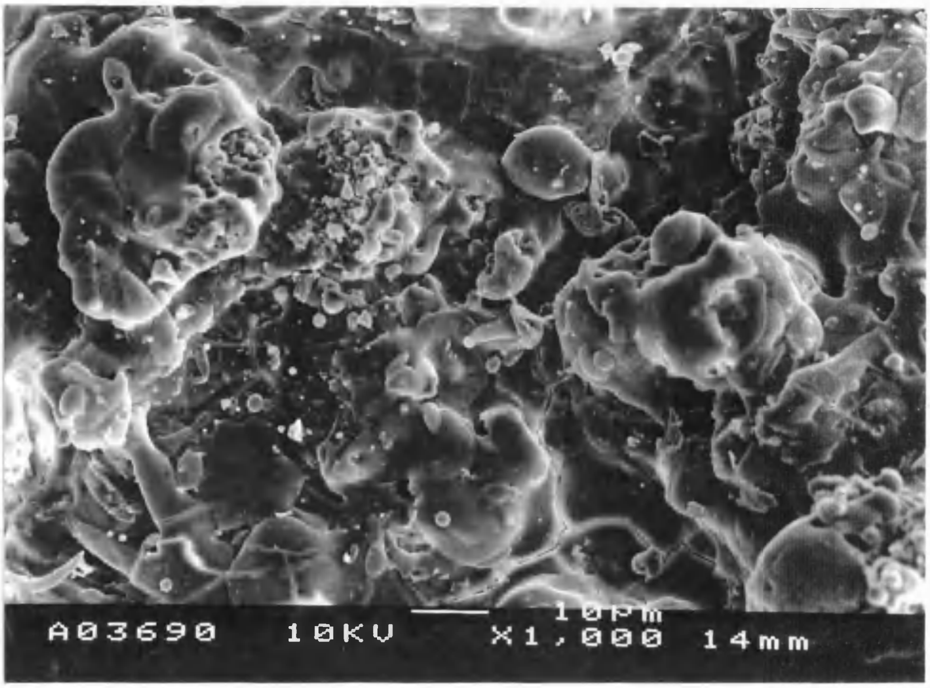

Figure 3.7.17. SEM micrograph of the surface of HA coating APS1 after ageing at pH7.2 for 4 weeks. mag. ×1000.

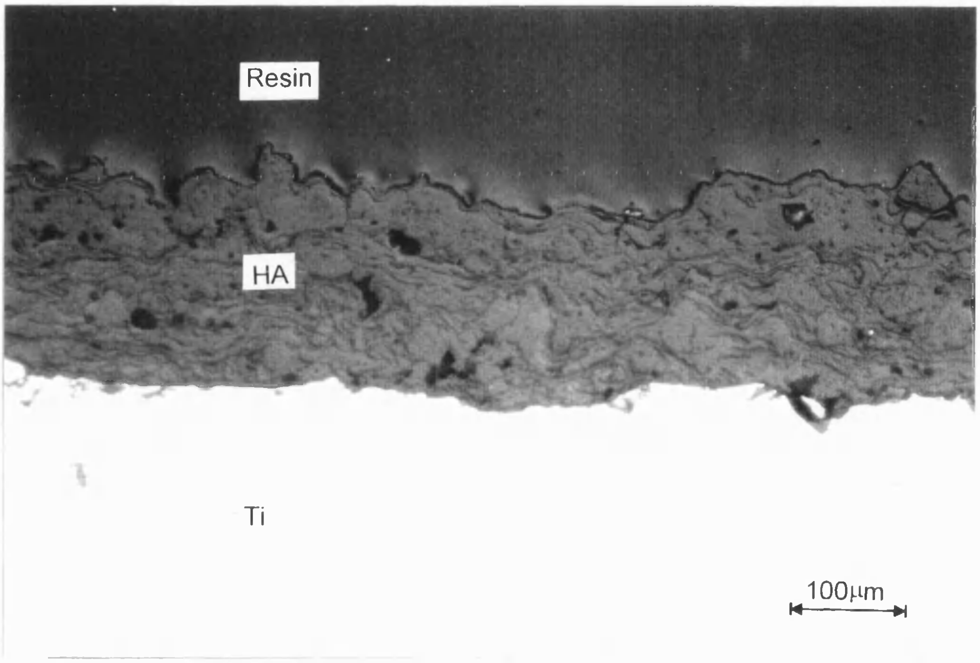

Figure 3.7.18. DIC optical micrograph of the cross-section of HA coating APS1 after ageing at pH7.2 for 4 weeks. mag. ×160.

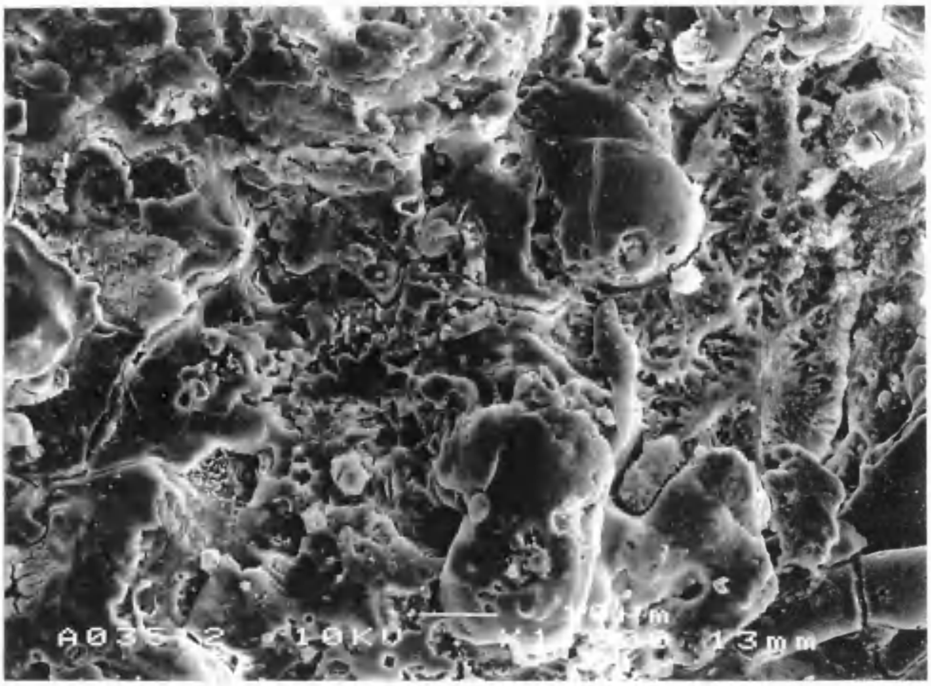

Figure 3.7.19. SEM micrograph of the HA coating APS1 aged for 1 week at pH4.5. mag. ×1000.

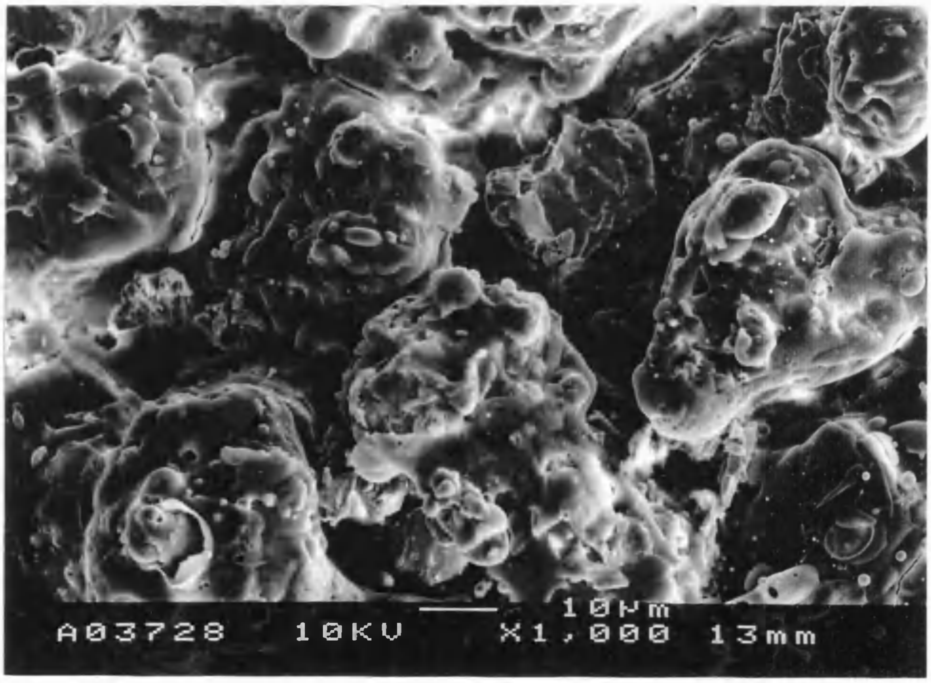

Figure 3.7.20. SEM micrograph of the HA coating APS1 aged for 4 weeks at pH4.5. mag. ×1000.

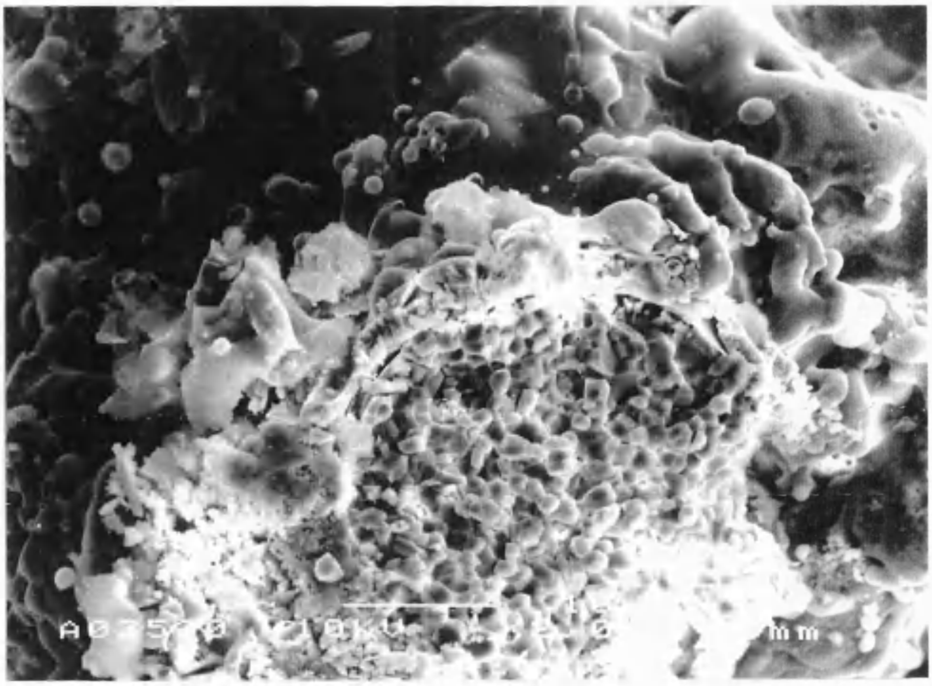

Figure 3.7.21. SEM micrograph of the HA coating APS1 aged for 2 weeks at pH4.5. mag. ×2000.

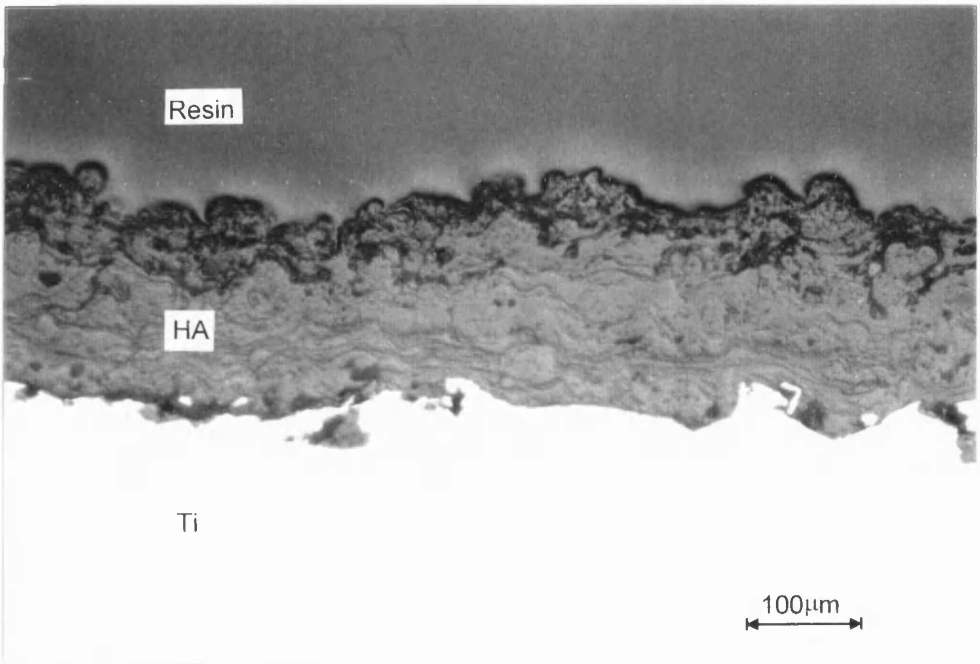

Figure 3.7.22. DIC optical micrograph of the cross-section of HA coating APS1 after ageing at pH4.5 for 1 weeks. mag. ×160.

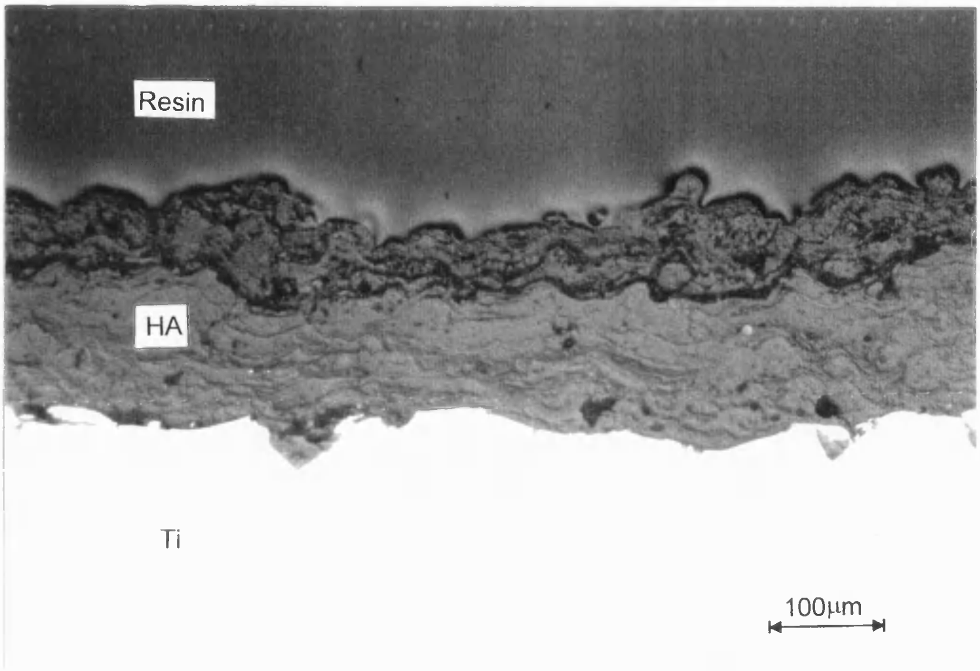

Figure 3.7.23. DIC optical micrograph of the cross-section of HA coating APS1 after ageing at pH4.5 for 2 weeks. mag. ×160.

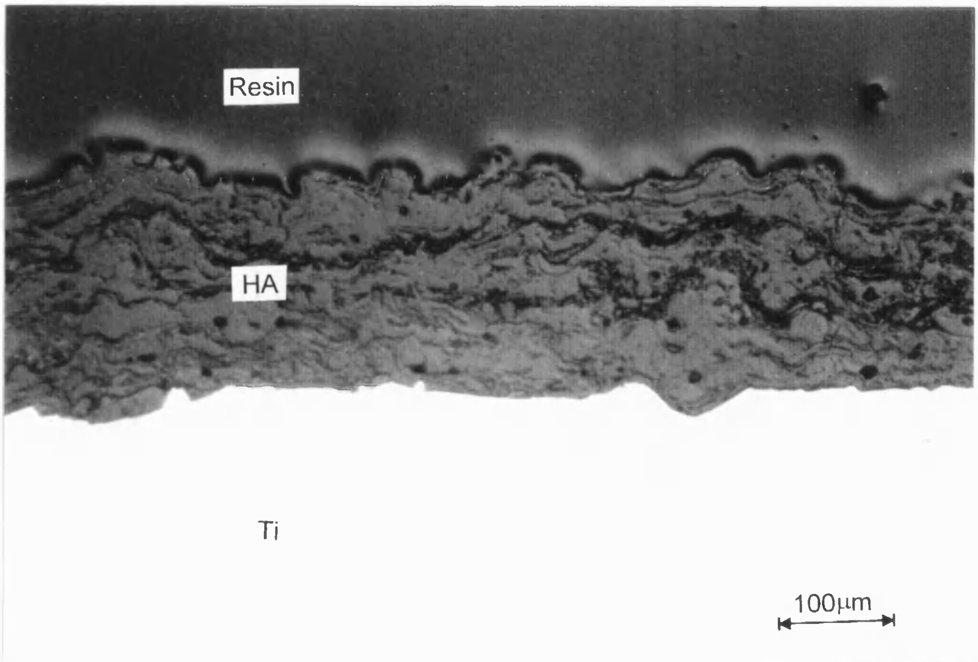

Figure 3.7.24. DIC optical micrograph of the cross-section of HA coating APS1 after ageing at pH4.5 for 4 weeks. mag. ×160.

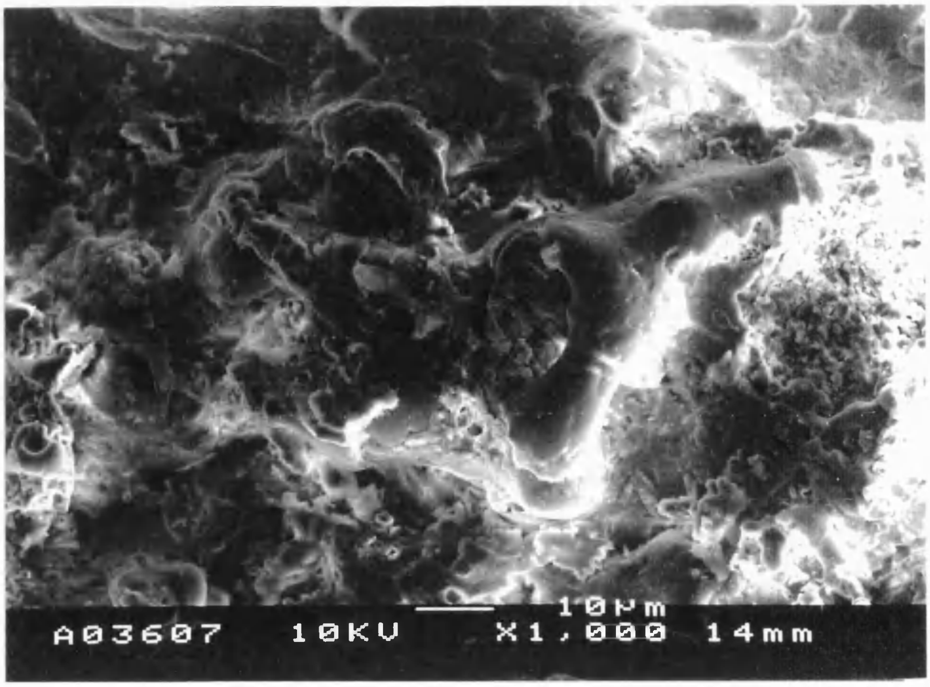

Figure 3.7.25. SEM micrograph of the HA coating APS2 aged for 1 weeks at pH4.5. mag. ×1000.

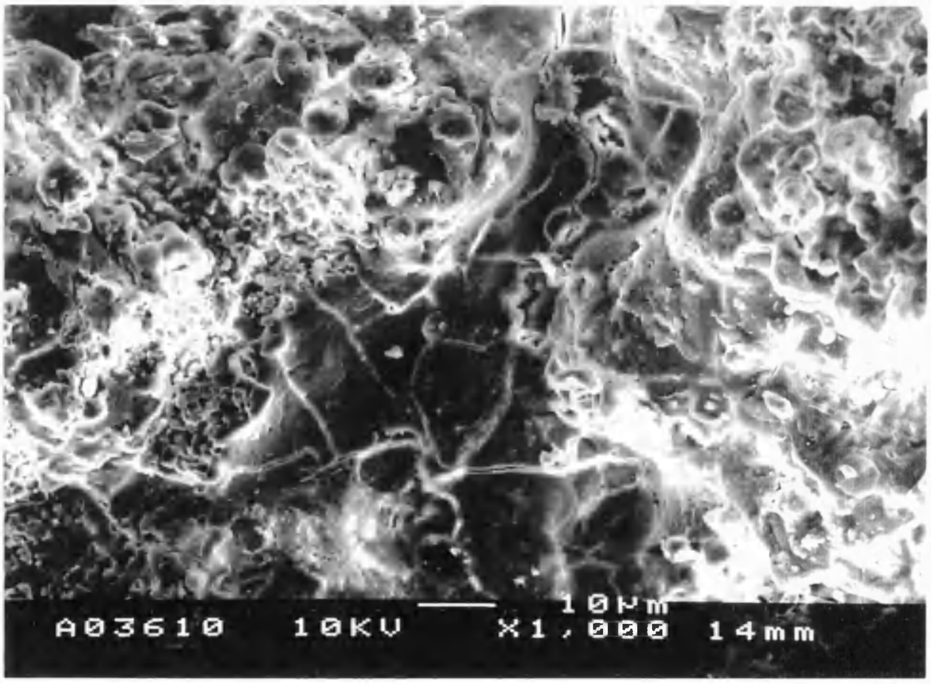

Figure 3.7.26. SEM micrograph of the HA coating APS2 aged for 2 weeks at pH4.5. mag. ×1000.

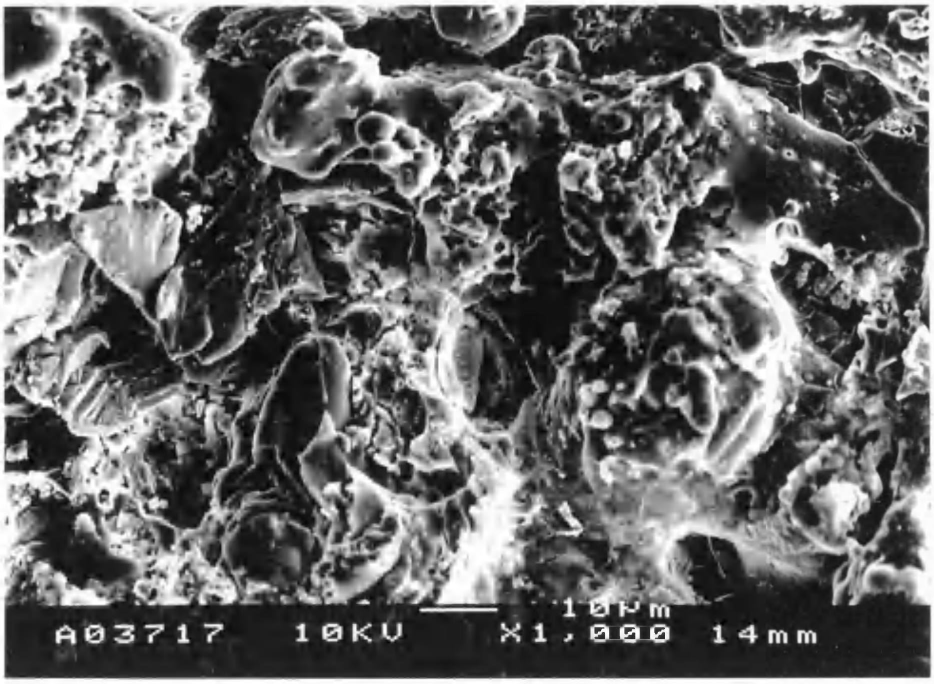

Figure 3.7.27. SEM micrograph of the HA coating APS2 aged for 4 weeks at pH4.5. mag. ×1000.

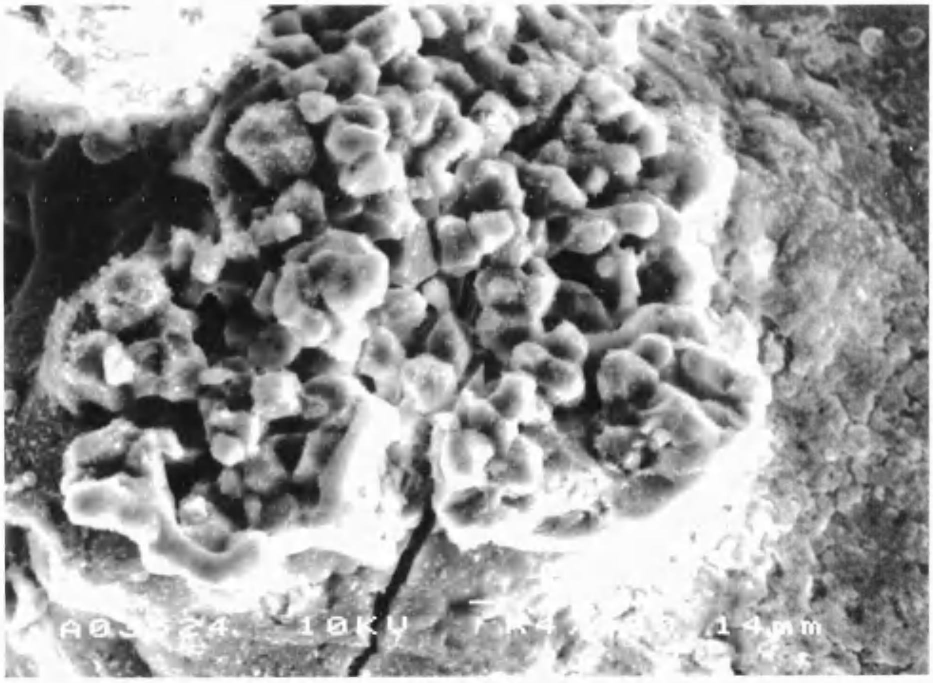

Figure 3.7.28. SEM micrograph of the HA coating APS2 aged for 1 week at pH4.5 showing an etched area. mag. ×4000.

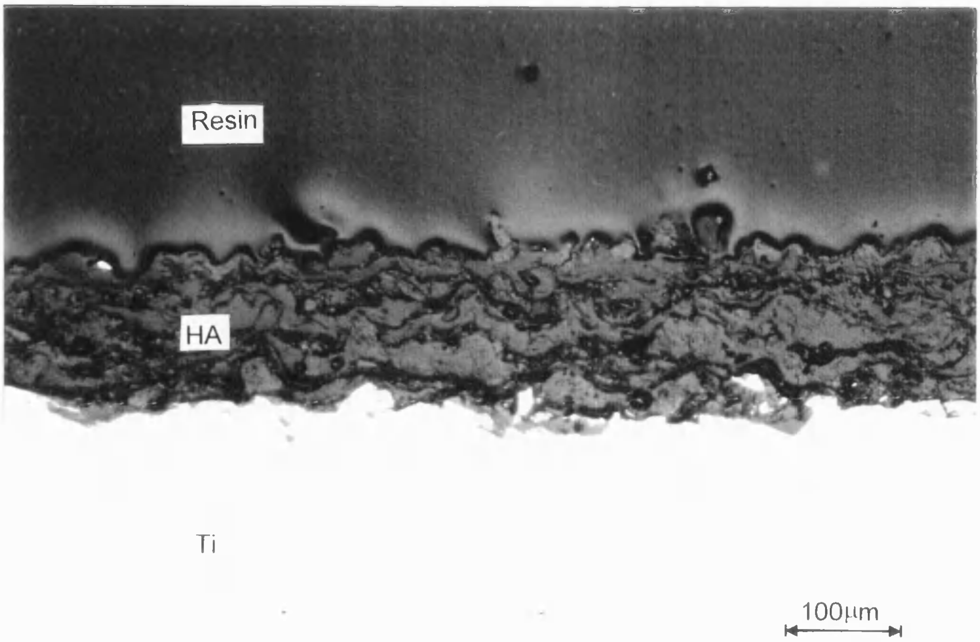

Figure 3.7.29. DIC optical micrograph of the cross-section of HA coating APS2 after ageing at pH4.5 for 4 weeks. mag. ×160.

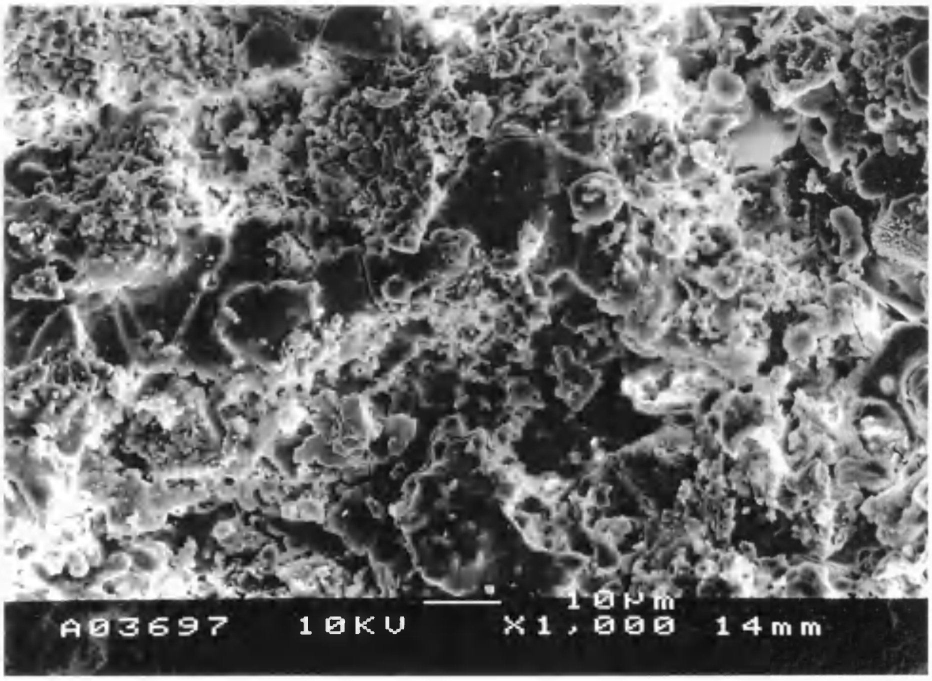

Figure 3.7.30. SEM micrograph of the HA coating APS3 aged for 4 weeks at pH7.2. mag. ×1000.

Figure 3.7.31. SEM micrograph of the HA coating APS3 aged for 1 week at pH4.5, showing etched and unetched areas. mag. ×2200.

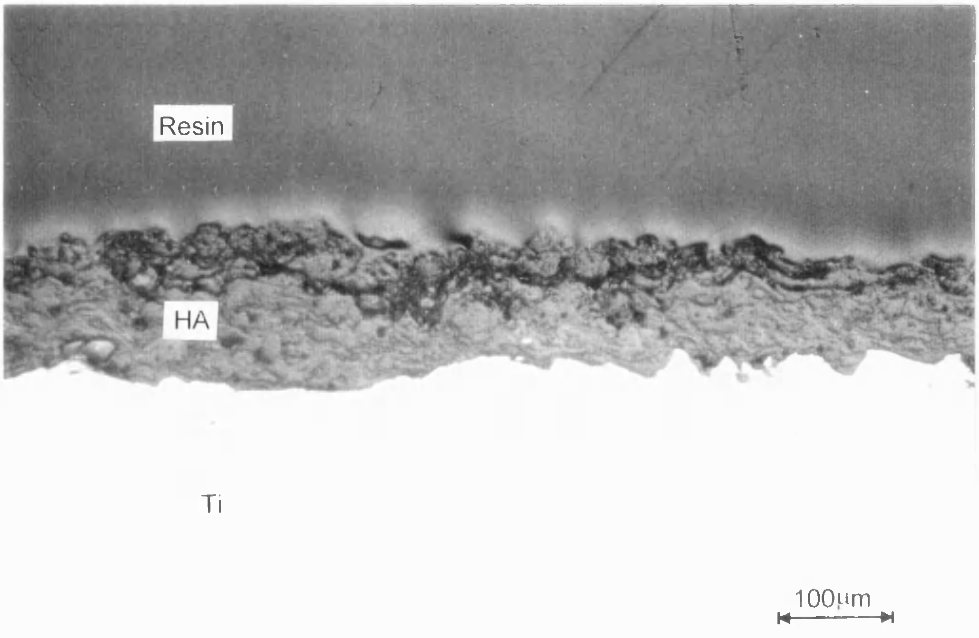

Figure 3.7.32. DIC optical micrograph of the cross-section of HA coating APS3 after ageing at pH4.5 for 1 weeks. mag. ×160.

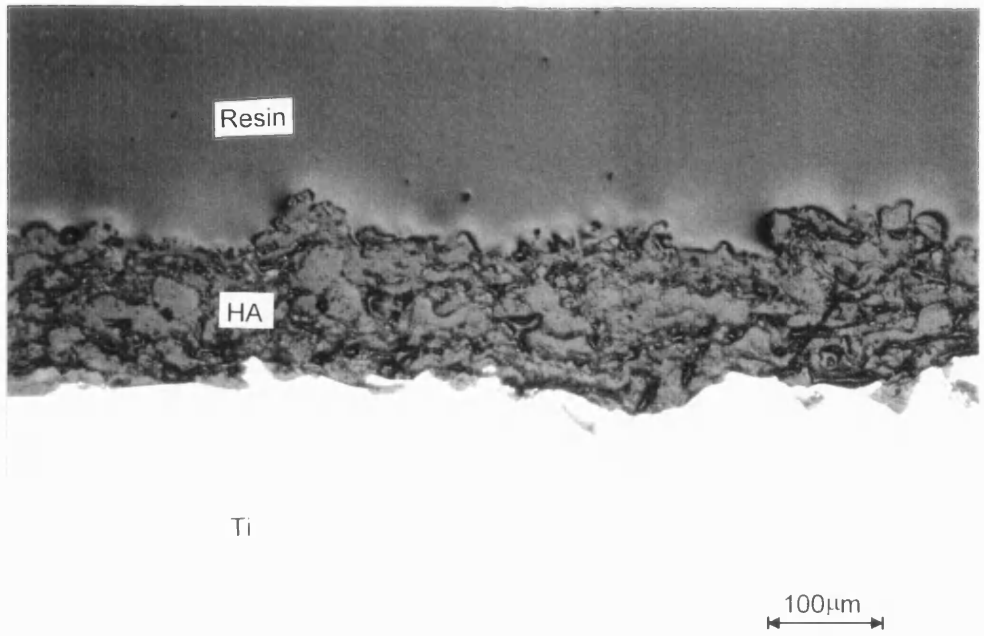

Figure 3.7.33. DIC optical micrograph of the cross-section of HA coating APS3 after ageing at pH4.5 for 4 weeks. mag. ×160.

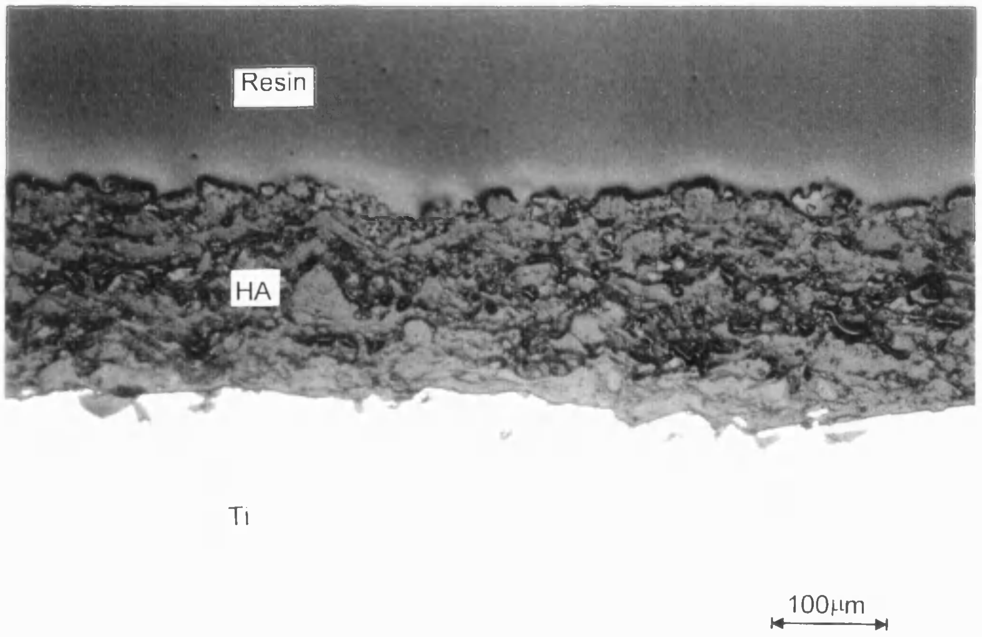

Figure 3.7.34. DIC optical micrograph of the cross-section of HA coating APS4 after ageing at pH4.5 for 4 weeks. mag. ×160.

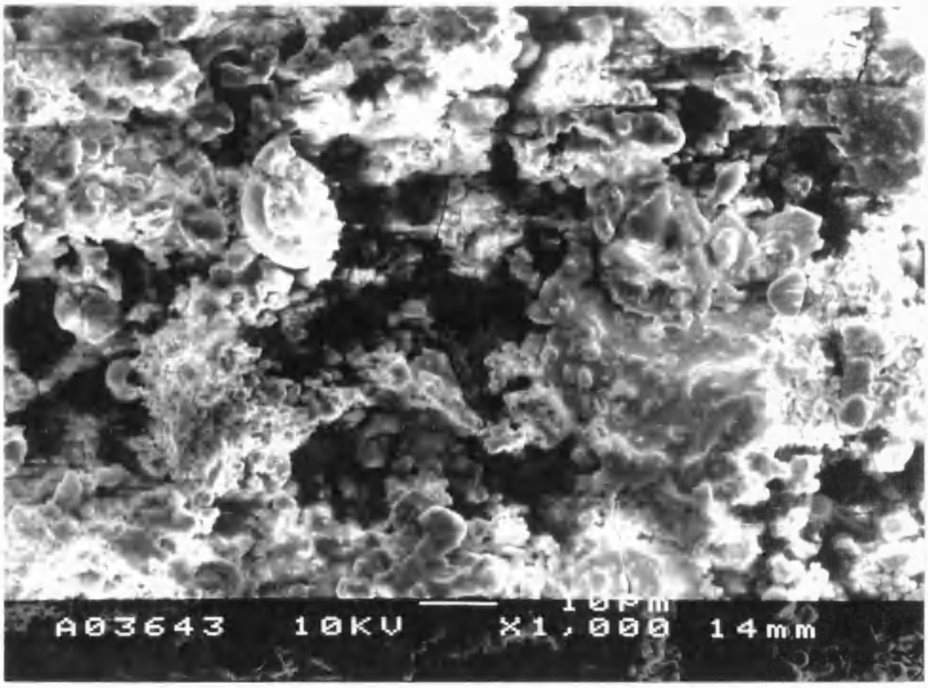

Figure 3.7.35. SEM micrograph of the HA coating CDS aged for 1 weeks at pH7.2. mag. ×1000.

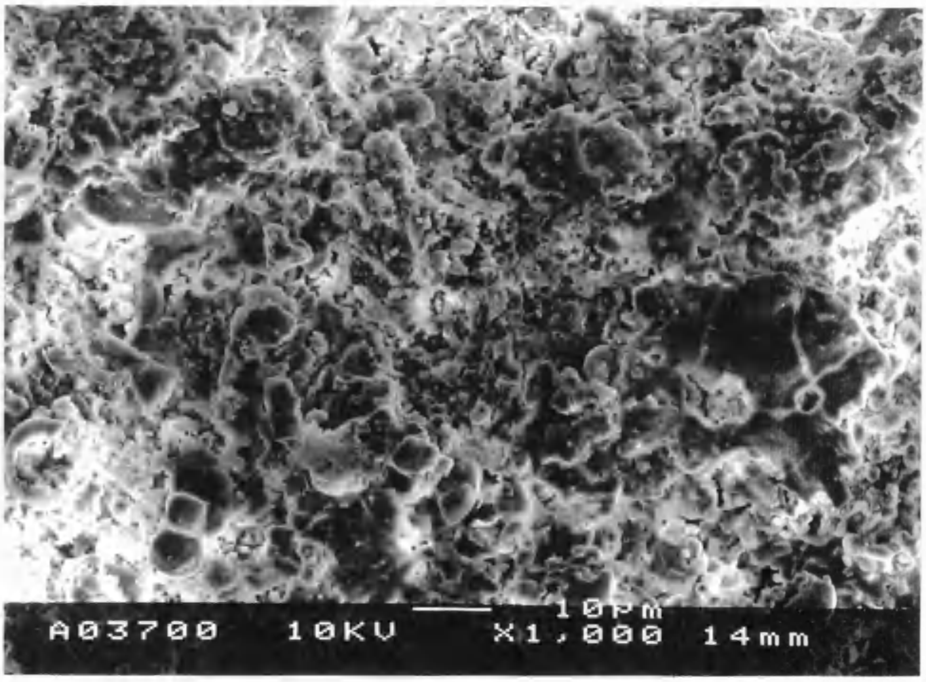

Figure 3.7.36. SEM micrograph of the HA coating CDS aged for 4 weeks at pH7.2. mag. ×1000.

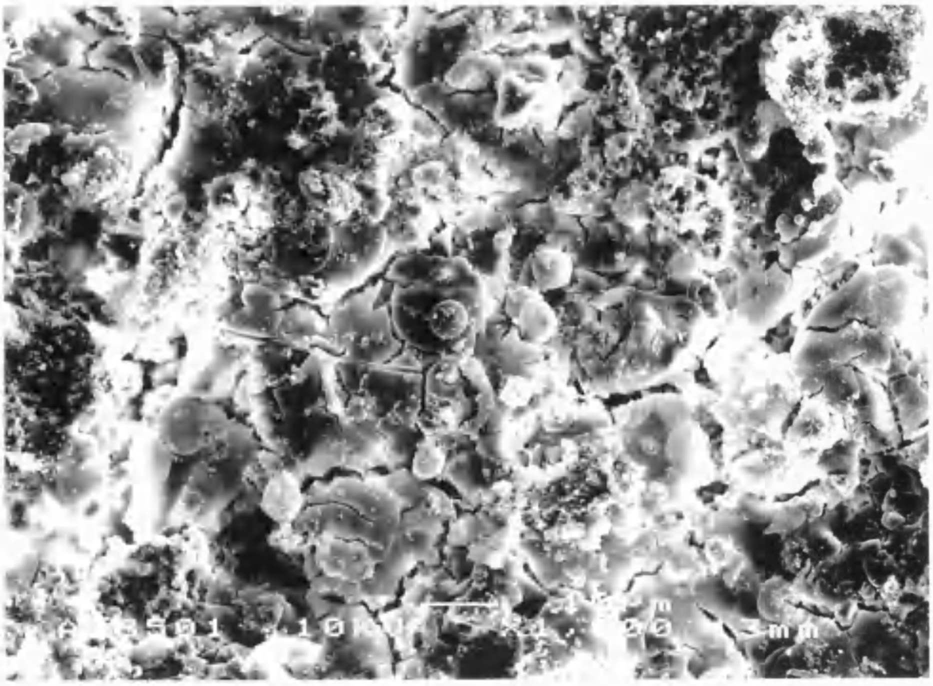

Figure 3.7.37. SEM micrograph of the HA coating CDS aged for 1 weeks at pH4.5. mag. ×1000.

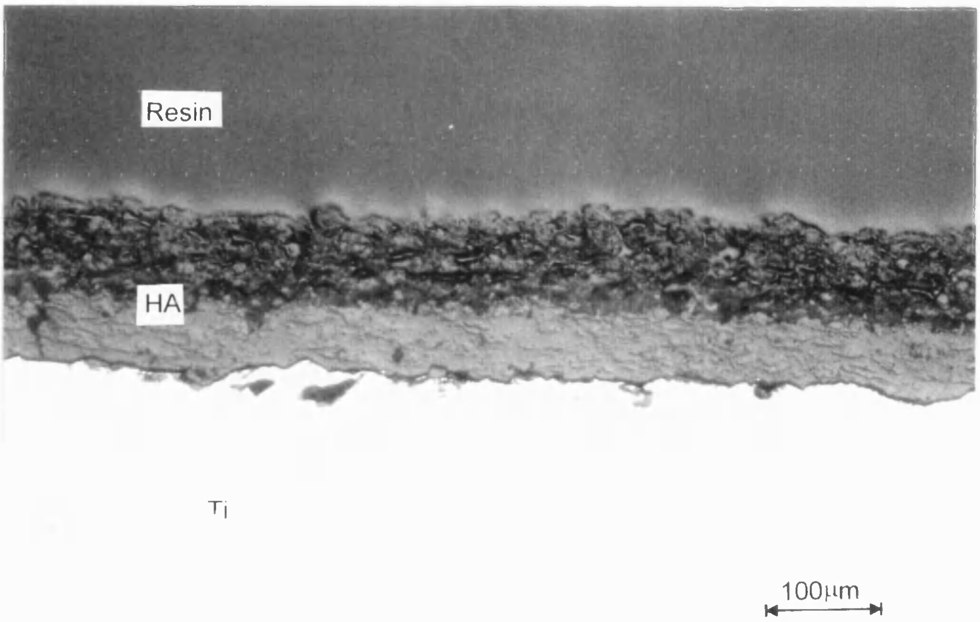

Figure 3.7.38. DIC optical micrograph of the cross-section of HA coating CDS after ageing at pH4.5 for 1 week. mag. ×160.

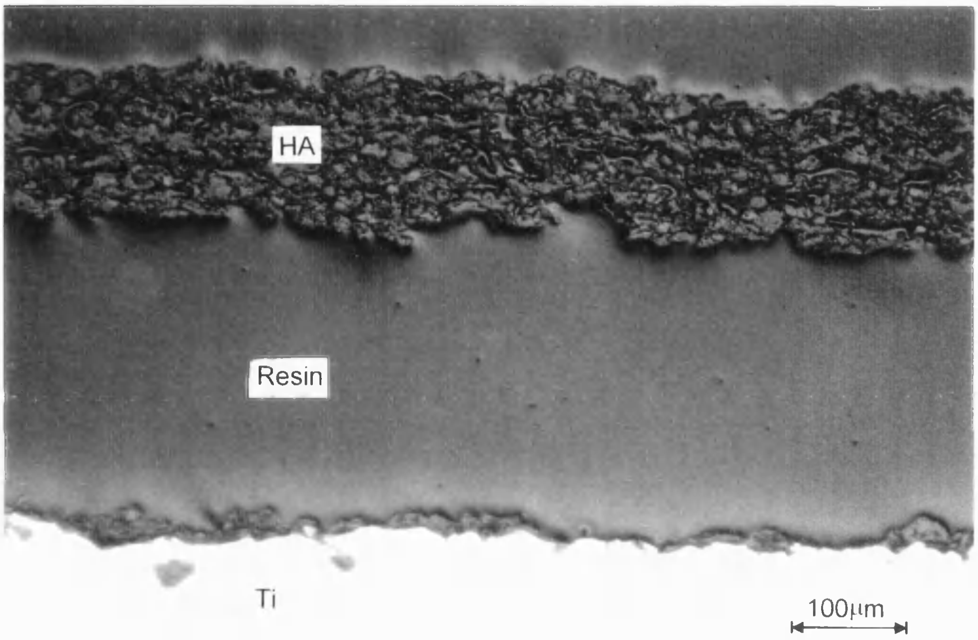

Figure 3.7.39. DIC optical micrograph of the cross-section of HA coating CDS after ageing at pH4.5 for 4 weeks. mag. ×160.

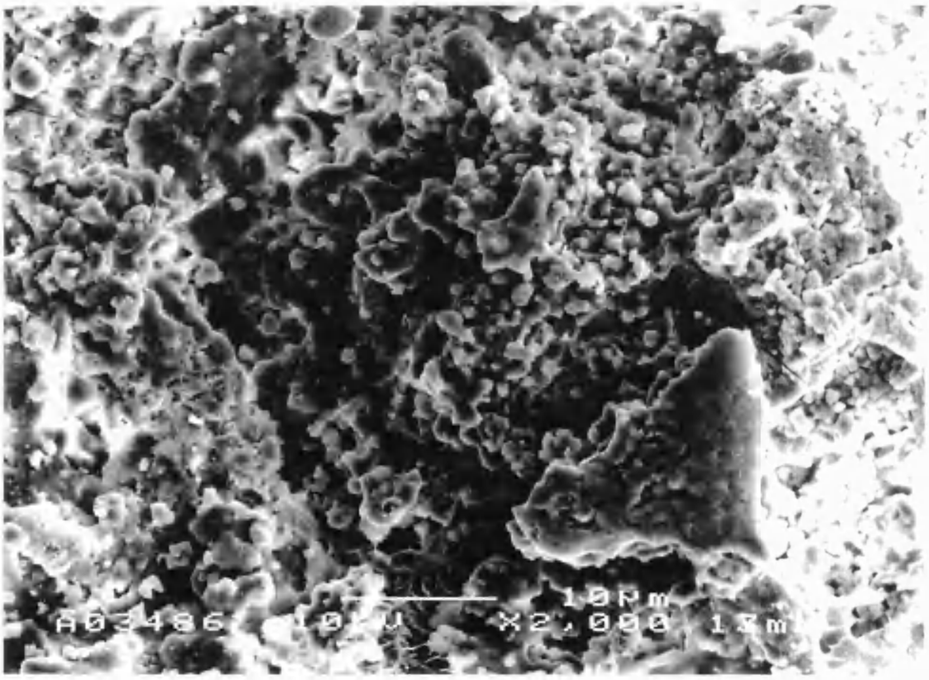

Figure 3.7.40. SEM micrograph of the HA coating VPS aged for 1 weeks at pH4.5. mag. ×2000.

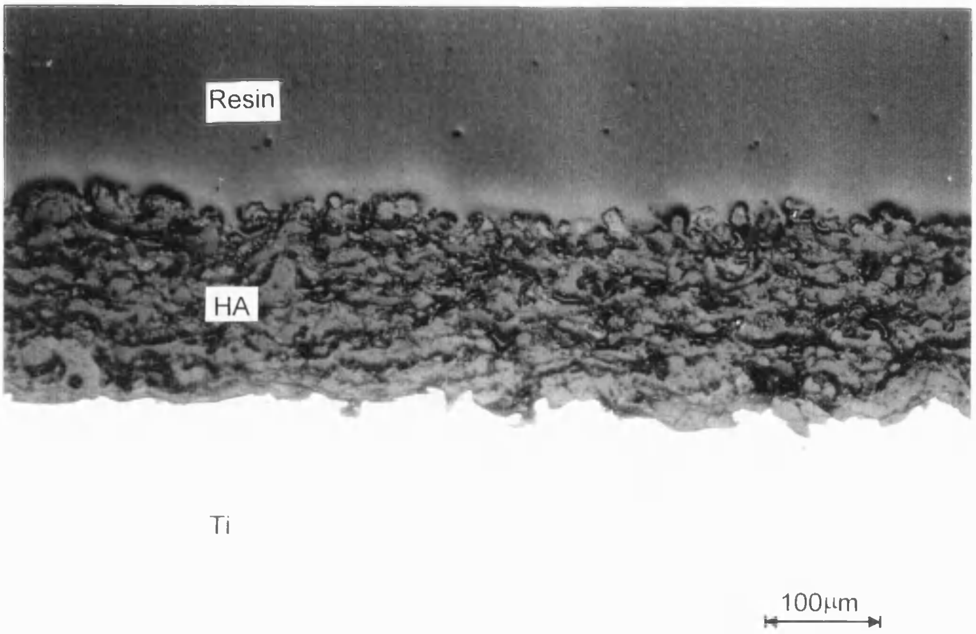

Figure 3.7.41. DIC optical micrograph of the cross-section of HA coating VPS after ageing at pH4.5 for 4 weeks. mag. ×160.

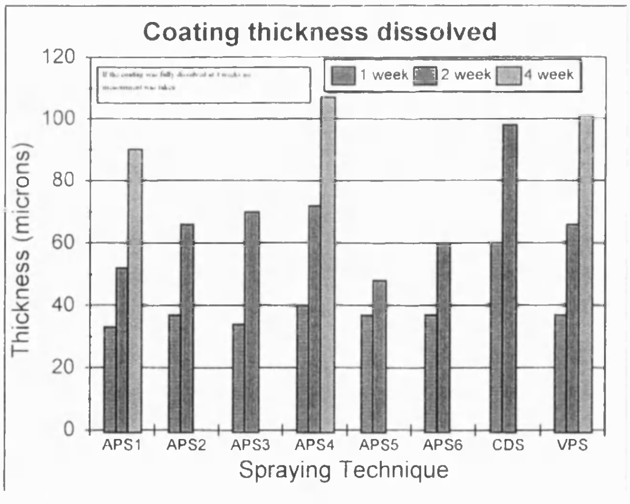

Figure 3.7.42. Thickness of etched layer from the pH4.5 *in vitro* solution aged HA coatings.

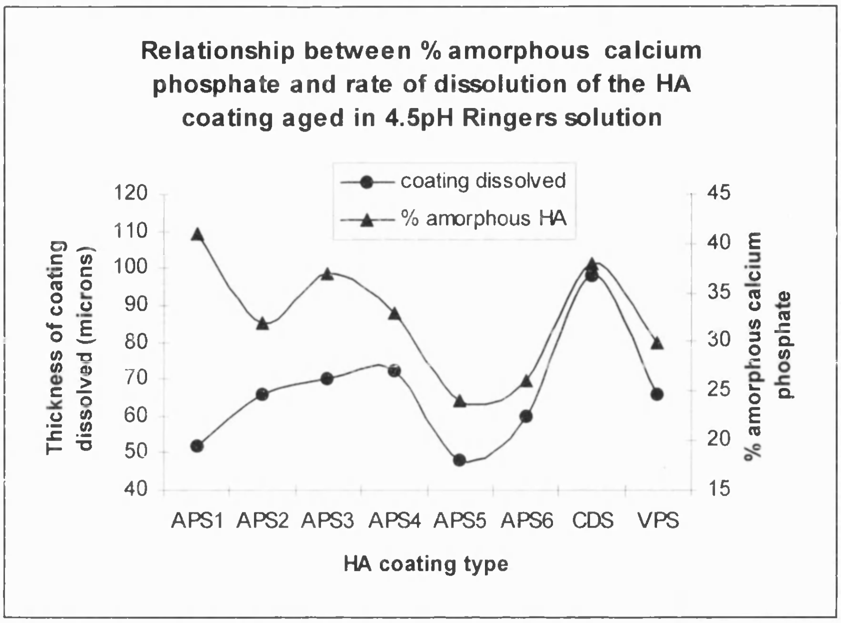

Figure 3.7.43. Relationship between % amorphous Ca/PO_4 and the rate of dissolution of the HA coating aged in pH4.5 Ringer's solution for 2 weeks.

4.0 Summary & Conclusions.

4.1 Powder Characterisation.

- Powders Amdry 6020 and XPT W 601 showed a crystalline hydroxyapatite which is characteristic of a powder which had been manufactured by a precipitation, sintering and crushing route.
- Powder HA 044 consisted of two particle morphologies, sponge like spherical particles and rectangular particles, the crystallinity of this powder was >90% and the manufacturing processes used were probably spray drying and precipitation.
- The particle size of the three powders was different due to the three spraying processes having different thermal energies and requiring particles to have a certain heat capacity to prevent particles from vaporising or not melting.
- The EDX technique showed no significant difference in the Ca/P ratio for the three powders.

4.2 Hydroxyapatite coating characterisation.

- The three spraying processes produced coatings with different structure and morphology.
- The morphology of all the coatings consists of a polyphase structure of crystalline and amorphous hydroxyapatite.
- Varying the spraying parameters of the APS process produced coatings with different morphologies.

- The VPS & CDS processes produced coatings with the lowest porosity.
- The highest power Ar/N APS coatings, APS2, showed the highest coating deposition efficiency and also the highest β-TCP %. Concluding that the higher the power of the plasma the greater the deterioration of the hydroxyapatite.
- By varying the spraying parameters the residual stress can be controlled.
- Residual stress increases with increasing coating thickness.
- The CDS process produced the lowest residual stress in the coating.

4.3 Shear Testing of HA Coatings.

- Shear testing of the hydroxyapatite coatings showed that the three spraying processes produced coatings with different shear strengths.
- The highest power processes APS2 and VPS produced the coatings with the strongest shear strength. The lowest shear strength was for the CDS process which is a relatively low temperature process.
- A relationship between crystallinity and shear strength has been shown. This relationship can be attributed to the power of the process effecting the molten state of the particles prior to coating deposition.

4.4 Tensile testing of HA coatings.

- Results obtained using this test method were inconclusive due to poor test sample alignment.

4.5 Acoustic emission of HA coatings.

- HA coatings fail by microcracking when subjected to a bending stress.
- Thin coatings withstand higher deformation before substantial microcracking occurs.
- The higher residual stress in the APS Ar/N gas mixture coatings results in higher **D** parameters for similar thickness coatings.
- SEM results show APS2 to have a large number of hairline microcracks, probably due to the higher power of the APS2 plasma producing a glassy coating which is more susceptible to brittle fracture.

4.6 Heat-treatment of Hydroxyapatite Powders and Coatings.

- Heat-treatment of all the powders showed similar results above 1350°C; all powders decomposed into α-TCP and calcium oxide phosphate with a small amount of hydroxyapatite remaining.
- Powder HA 044 showed an increase in β-TCP from 650°C to 1150°C, probably caused by crystallisation of amorphous calcium phosphate.
- Powders Amdry 6020 and XPT W 601 showed very little change until the temperature of 1350°C, where the hydroxyapatite showed signs of dissociation into α-TCP and calcium oxide phosphate.
- Heat-treatment of the coatings increased the crystallinity which would increase the longevity of the coating *in vivo.*
- Heat-treatment of the coatings below the temperature of 800°C reduced the tensile residual stress in the coating, which should improve the fatigue resistance of the coating.

- Microscopy of the coatings shows an increase in homogeneity of the coating as the heat-treatment temperature rises, due to the amorphous phase in the coating crystallising and therefore having a similar polishing rate to the crystalline phase.

- The 900°C heat-treatment temperature showed an increase in tensile residual stress and the formation of an interfacial layer at the interface between the hydroxyapatite and the titanium alloy substrate. The increase in residual stress could be due to a combination of factors:

I. A difference in the thermal expansion coefficients of the titanium alloy substrate and the hydroxyapatite coating.
II. A reaction may occur between the hydroxyapatite coating and the titanium alloy substrate.
III. Formation of an oxide layer at the titanium alloy hydroxyapatite interface.
IV. Degradation of the hydroxyapatite coating.
V. A phase transition in the titanium alloy substrate causing a change in thermal expansion coefficient.

4.7 *In Vitro* Testing of Hydroxyapatite Coatings.

- The pH4.5 *in vitro* test is effectively an accelerated test of pH7.2.

- The observed increase in crystallinity of the hydroxyapatite coatings aged at pH4.5 & 7.2 is related to dissolution of amorphous phase at surface of coating leaving the more stable crystalline hydroxyapatite exposed for analysis by the XRD technique..

- Hydroxyapatite coatings aged at pH7.2 showed an increase in crystallinity after 1 and 2 weeks and finally reached a similar crystallinity to pH4.5 after 1 week of ageing.
- Other calcium phases present in the coating dissolve rapidly at pH4.5.
- Other calcium phases dissolved at pH7.2 although at a slower rate than pH4.5.
- Optical microscopy indicated no significant change in the morphology of the coating for the hydroxyapatite coatings aged at pH7.2. SEM of the surface of pH7.2 aged coatings showed minimal change at 1 week and a small amount of dissolution at 2 & 4 weeks.
- Optical microscopy of pH4.5 aged coatings showed a partially dissolved layer on the surface of the coating which increased in thickness with ageing time.
- SEM microscopy of the surface of the VPS and APS aged coatings showed agglomerated particles on the surface of the coating which resembled the structure of the spraying powders used to produce these coatings.
- The aged CDS coating showed fracture of the particle splats on the surface of the coating and general coating disintegration.
- For the duration of the pH7.2 *in vitro* test the coating thickness remains unchanged.
- The coatings aged at pH4.5 show a partially dissolved layer of hydroxyapatite coating starting from the surface and progressing towards the interface.

- The rate of dissolution of the coating at pH4.5 is dependent on initial crystallinity of the coating.

In general :

- Varying the spraying parameters produces a coating with different properties.
- Varying the spraying powder can also effect the coating which is produced.
- Characterisation of thermal sprayed HA coatings has been successfully achieved using several conventional and novel techniques.
- By selecting a spraying process, an HA powder and varying the spraying parameters, one can achieve a coating with the structure and composition that is required.
- The new CDS process produced HA coatings of equivalent quality to those achieved by the conventional APS and VPS processes.

5.0 Further Work.

- Investigate the effect of varying spraying parameters and powder morphology for the VPS and CDS spraying techniques.
- Perform *in vitro* testing of heat-treated coatings to confirm that the increase in crystallinity results in a more stable coating.
- Investigate the effects of fatigue on as-sprayed, heat-treated and *in vitro* tested samples.
- Investigate the use of the acoustic emission **D** parameter for accessing the failure mechanism of other coatings and relate the **D** parameter to fatigue life of these coatings.
- Compare the XRD measurement of the residual stress with another residual stress measurement technique and relate the residual stress to adhesion and fatigue strength of the coatings.

Acknowledgements.

I would like to thank the EPSRC, Howmedica International and Plasma Technik Ltd for their financial support of this project.

I would also like to thank Dr I.G.Turner, Mr H. Reiter, Dr C. Doyle and Mr R. McIntyre for their advice and encouragement throughout the project.

References.

1. C.J.K.Bulstrode, V.Seagroatt, Heng Soon Tan, M. Goldacre, L.Gill, I.Nugent.
The epidemiology of total hip replacement.
IMechE. 1992. C441/009. p.1.

2. R.Fifield
New lives for painful hips.
New Scientist. 10 Dec. 1987. p.35 - 40.

3. W.Bonfield.
Materials for the replacement of osteoarthritic hip joints.
Metals and Materials. Dec. 1987. p.712-716.

4. J.H.Boss, I.Shajrawi, D.G.Mendes.
The nature of the bone - implant interface.
Medical Progress through Technology. 1994. Vol. 20, p.119 -142.

5. J.J.Callaghan.
Current concepts review. The clinical results and basic science of total hip arthroplasty with porous-coated prostheses
The Journal of Bone and Joint Surgery. Feb. 1993. Vol.75-A, No.2, p.299-309.

6. D.F.Williams.
Materials for surgical implants.
Metals & Materials: Materials in Medicine. Jan. 1991. p.24 - 29.

7. S.Downes, C.P.A.T.Klein, M.V.Kayser, L.Di Silvio.
The use of CaPO4 ceramics to deliver growth hormones and insulin-like-growth factor-I.
Fourth World Biomaterials Congress. April 24-28, 1992. p.178.

8. S.S.Kaplan.
Biomaterials-host interactions: consequences, determined by implant retrieval analysis.
Medical Progress through Technology. 1994. Vol.20. p.209-230.

10. R.D.Bloebaum, K.N.Bachus, N.G.Momberger, A.A.Hofmann.
Mineral apposition rates of human cancellous bone at the interface of porous coated implants.
J. Biomed. Mat. Res. 1994. Vol. 28, p.537-544.

11. A.Moroni V.Caja E.Egger M.Pompili E.Y.Chao.
Mechanical strength and bone ingrowth analysis of hydroxyapatite coated verses uncoated titanium porous bone ingrowth.
VIII meeting of the European Society of Biomechanics. Rome-Italy-June 21-24 1992.

12. A.Moroni, V.L.Caja, E.L.Egger, L.Trinchese, E.Y.S.Chao.
Histomorphometry of hydroxyapatite coated and uncoated porous titanium bone implants.
Biomaterials. 1994. Vol.15, No.11, p.926-930.

13. A.Moroni, V.L.Caja, C.Sabato, E.L.Egger, F.Gottsauner-wolf, E.Y.S.Chao.
Bone ingrowth analysis and interface evaluation of hydroxyapatite coated versus uncoated titanium porous bone implants.
Journal of Materials Science: Materials and Medicine. 1994. Vol.5, p.411-416.

14. W.J.A.Dhert, C.P.A.T.Klein, J.A.Jansen, E.A. van der Velde, R.C.Vriesde, P.M.Rozing. K. de Groot.
A histological and histomorphometrical investigation of fluorapatite, magnesiumwhitlockike, and hydroxylapatite plasma-sprayed coatings in goats.
Journal of Biomedical Materials Research. 1993. Vol. 27, p.127-138.

15. C.P.A.T.Klein, P.Patka, J.G.C.Wolke, J.M.A. de Blieck-Hogervorst, K. de Groot.
Long-term in vivo study of plasma-sprayed coatings on titanium alloys of tetracalcium phosphate, hydroxyapatite and a-tricalcium phosphate.
Biomaterials. 1994. Vol.15, No.2, p.146-150.

16. W.C.A.Vrouwenvelder, C.G.Groot, K. de Groot.
Histological and biochemical evaluation of osteoblasts cultured on bioactive glass, hydroxylapatite, titanium alloy, and stainless steel.
Journal of Biomedical Materials Research. 1993. Vol. 27, p.465-475.

17. R.B.Martin, M.W.Chapman, N.A.Sharkey, S.L.Zissimos, B.Bay, E.C.Shors.
Bone ingrowth and mechanical properties of coralline hydroxyapatite 1 yr after implantation.
Biomaterials. 1993. Vol. 14, No. 5, p.341-348.

18. M.Jarcho, C.H.Bolen, M.B.Thomas, J.Bobick, J.F.Kay, R.H.Doremus.
Hydroxyapatite synthesis and characterisation in dense polycrystalline form.
Journal of Materials Science. 11(1976) 2027-2035.

19. A.Osaka, Y.Miura, K.Takeuchi, M.Asada, K.Takahashi.
Calcium apatite prepared from calcium hydroxide and orthophosphoric acid.
Journal of Materials Science: Materials in Medicine. 1991. Vol.2, p.51-55.

20. K.de Groot R.Geesink C.P.A.T.Klein.
Plasma sprayed coatings of hydroxyapatite.
Journal of Biomedical Materials Research. 1987. Vol. 21, p.1375-1381.

21. P.Leali tranquilli, A.Merolli, O.Palmacci, C.Gabbi, A.Cacchioli, G.Gonizzi.
Evaluation of different preparations of plasma-spray hydroxyapatite coatings on titanium alloy and duplex stainless steel in the rabbit.
Journal of Materials Science: Materials and Medicine. 1994. Vol.5, p.345-349.

22. B.C.Wang, T.M.Lee, E.Chang, C.Y.Yang.
The shear strength and the failure mode of plasma-sprayed hydroxyapatite coating to bone: The effect of coating thickness.
Journal of Biomedical Materials Research.1993. Vol. 27, p.1315-1327.

23. S.H.Maxian, J.P.Zawadsky, M.G.Dunn.
Mechanical and histological evaluation of amorphous calcium phosphate and poorly crystallized hydroxyapatite coatings on titanium implants.
Journal of Biomedical Materials Research. 1993. Vol. 27, p.717-728.

24. S.H.Maxian, J.P.Zawadsky, M.G.Dunn.
Invitro evaluation of amorphous calcium phosphate and poorly crystallised HA coatings on Ti implants.
Journal of Biomedical Materials Research. 1993. Vol. 27, p.111-117.

25. J.A.D'Antonio, W.N.Capello, W.L.Jaffe.
Hydroxyapatite-Coated Hip Implants.
Clinical Orthopaedics and Related Research. Dec. 1992. No.285, p.102-114.

26. L.Carlsson, L.Regner, C.Johansson, M.Gottlander, P.Herberts.
Bone response to hydroxyapatite-coated and commercially pure titanium implants in the human arthritic knee.
Journal of Orthopaedics Research. 1994. Vol.12, p.274-285.

27. D.B.Burr, S.Mori, R.D.Boyd, T.C.Sun, J. David Blaha, L.Lane, J.Parr.
Histomorphometric assessment of the mechanisms for rapid ingrowth of bone to HA/TCP coated implants.
Journal of Biomedical Materials Research. 1993. Vol.27, p.645-653.

28. S.D.Cook, K.A.Thomas, J.F.Kay, M.Jarcho.
Hydroxyapatite coated porous titanium for use as an orthopeadic biological attachment system.
Clinical Orthopeadics Related Research. May 1988. No.230, p.303-312.

29. G.Daculsi, J.Delecrin.
Biological transformation of calcium phosphate coating in human implants: Micro-characterisation using scanning electron microscopy and high resolution transmission electron microscopy.
Cells and Materials. 1994. Vol.4, No.1, p.63-71.

30. K.de Groot, R.Geesink, C.P.A.T.Klein.
Plasma sprayed coatings of hydroxyapatite.
Journal of Biomedical Materials Research. 1987. Vol.21, p.1375-1381.

31. J.D. de Bruijin, C.A.van Blitterswijk, J.E.Davies.
Initial bone matrix formation at the hydroxyapatite interface in vivo.
Journal of Biomedical Materials Research. 1995. Vol.29, p.89-99.

32. J.Delecrin, G.Daculsi, N.Passuti, B.Duquet.
Specific resorbable calcium phosphate coating to enhance osteoconduction.
Cells and Materials. 1994. Vol.4, No.1, p.51-62.

33. W.J.A.Dhert, C.P.A.T.Klein, J.A.Jansen, E.A. van der Velde,
R.C.Vriesde, P.M.Rozing. K. de Groot.
A histological and histomorphometrical investigation of fluorapatite, magnesiumwhitlockike, and hydroxylapatite plasma-sprayed coatings in goats.
Journal of Biomedical Materials Research. 1993. Vol.27, p.127-138.

34. P.Frayssinet, J.L.Trouillet, N.Rouquet, E.Azimus, A.Autefage.
Osseointegration of macroporous calcium phosphate ceramics having a different chemical composition.
Biomaterials. 1993. Vol.14, No.6, p.423-429

35. K.Hayashi, T.Inadome, T.Masima, Y.Sugioka.
Comparison of bone-implant interface shear strength of solid hydroxyapatite and hydroxyapatite-coated titanium implants.
Journal of Biomedical Materials Research. 1993. Vol.27, p.557-563.

36. K.Hayashi, K.Uenoyama, T.Mashima, Y.Sugioka.
Remodelling of bone around hydroxyapatite and titanium in experimental osteoporosis.
Biomaterials. 1994. Vol.15, No.1, p.11.

37. J.A.Jansen, J.P.C.M. van der Waerden, J.G.C.Wolke.
Histologic investigation of the biologic behaviour of different hydroxyapatite plasma-sprayed coatings in rabbits.
Journal of Biomedical Materials Research. 1993. Vol.27. p.603-610.

38. C.P.A.T.Klein, P.Patka, J.G.C.Wolke, J.M.A. de Blieck-Hogervorst, K. de Groot.
Long-term in vivo study of plasma-sprayed coatings on titanium alloys of tetracalcium phosphate, hydroxyapatite and a-tricalcium phosphate.
Biomaterials. 1994. Vol.15, No.2, p146-150.

39. A.Ravaglioli, A.Krajewski, V.Biasini, R.Martinetti.
Interface between HA and mandibular human bone tissue.
Biomaterials. 1992. Vol. 13, No 3, p.162-167.

40. Y.Abe, T.Kokubo, T.Yamamuro.
Apatite coatings on ceramics, metals and polymers utilising a biological process.
Journal Materials Science: Materials in Medicine. 1990. Vol.1, p.233-238.

41. H.Ben-Bassat, B.Y.Klien, E.Lerner, R.Azoury, E.Rahamin, Z.Shlomai, S.Sarig.
An invitro biocompatability study of a new hydroxyapatite ceramic HA-SAL1: comparison to bioactive bone substitute ceramics.
Cells and Materials. 1994. Vol.4, No.1, p.37-50.

42. J.H.Chern Lin, M.L.Liu, C.P.Ju.
Morphologic variation in plasma-sprayed hydroxyapatite-bioactive glass composite coatings in Hank's solution.
Journal of Biomedical Materials Research. 1994. Vol.28, p723-230.

43. P.Ducheyne, S.Radin, M.Heughebaert, J.C.Heughebaert.
Calcium phosphate ceramic coatings on porous titanium: effect of structure and composition on electrophoretic deposition, vacuum sintering and invtiro dissolution.
Biomaterials. May 1990. Vol.11, p.244-254.

44. K.A.Gross, C.C.Berndt.
In vitro testing of plasma-sprayed hydroxyapatite coatings.
Journal Materials Science: Materials in Medicine. 1994. Vol.5, p.219-224.

45. M.Kohri, K.Miki, D.E.Waite, H.Nakajima, T.Okabe.
In vitro stability of biphasic calcium phosphate ceramics.
Biomaterials. 1993. Vol.14, No.4, p. 299-304

46. D.M.Liu, H.M.Chou, J.D.Wu.
Plasma-sprayed hydroxyapatite coatings: effect of different calcium phosphate ceramics.
Journal Materials Science: Materials in Medicine. 1994. Vol.5, p.147-153.

47. U.Saalfeld, N.M.Meenen, T.T.Jures, H.Saalfeld.
Solubility behaviour of synthetic hydroxyapatite in aqueous solution: influence of amorphous constituents on pH value.
Biomaterials. 1994. Vol.15, No.11, p.905-908.

48. C.C.P.M.Verheyen, W.J.A.Dhert, P.L.C.Petit, P.M.Rozing, K. de Groot.
In vitro study on the integrity of a hydroxylapatite coating when challenged with staphylococci.
Journal of Biomedical Materials Research.1993. Vol.27, p.775-781.

49. J.Weng, X.Liu, X.Zhang, Z.Ma, X.Ji, Z.Zyman.
Further studies on the plasma-sprayed amorphous phase in hydroxyxaptite coatings and its deamorphization.
Biomaterials. 1993. Vol.14, No.8, p.578-582.

50. J.Chen, J.G.C.Wolke, K.de Groot.
Microstructure and crystallinity in hydroxyapatite coatings.
Biomaterials. 1994. Vol.15, No.5, p.396.

51. L.G.Ellies, D.G.A.Nelson, J.D.B.Featherstone.
Crystallographic changes in calcium phospahte during plasma spraying
Biomaterials. 1992. Vol.13, No.5. p.313-316.

52. M.J.Filiaggi, R.M.Pilliar, N.A.Coombs.
Post-plasma-spraying heat-treatment of the HA coating/Ti-6Al-4V implant system.
Journal of Biomedical Materials Research. 1993. Vol.27, p.191-196.

53. H.Ji, P.M.Marquis.
Effect of heat treatment on the microstructure of plasma-sprayed hydroxyapatite coating.
Biomaterials. 1993. Vol.14, No.1, p.64-68

54. B.Locardi, U.E.Pazzaglia, C.Gabbi, B.Profilo.
Thermal behaviour of hydroxyapatite intended for medical applications.
Biomaterials. 1993. Vol.14, No.6, p.431-437.

55. G.V.Rodicheva, V.P.Orlovsky, Zh.A.Ezhova, G.E.Sukhanova.
Synthesis and structural transformations of hydroxyapatite within temperature range 100-1550C.
Fourth World Biomaterials Congress, April 24-28 1992. p.522. Berlin, Federal Republic of Germany.

56. J.Zhou, X.Zhang, J.Chen, S.Zeng, K. de Groot.
High temperature characteristics of synthetic hydroxyapatite.
Journal of Materials Science: Materials in Medicine. 1993. Vol.4, p.83-85.

57. Z.Zyman, J.Weng, X.Liu, X.Li, X.Zhang.
Phase and structural changes in hydroxyapatite coatings under heat treatment.
Biomaterials. 1994. Vol.15, No.2, p.151-155.

58. K.Ishikawa, P.Ducheyne, S..Radin.
Determination of the Ca/P ratio in calcium deficient hydroxyapatite using X-ray diffraction analysis.
Journal of Materials Science: Materials in Medicine. 1993. Vol.4, p.165-168.

59. Phase Diagrams for Ceramists.
American Chemistry Society: Ceramics International. Vol. 19, No. 5, p.320-324.

60. J.Weng, X.Liu, X.Zhang, Z.Ma, X.Ji, Z.Zyman.
Further studies on the plasma-sprayed amorphous phase in hydroxyxaptite coatings and its deamorphization.
Biomaterials. 1993. Vol.14, No.8, p.578-582.

61. Z.Zyman, J.Weng, X.Liu, X.Zhang, Z.Ma.
Amorphous phase and morphological structure of hydroxyapatite plasma coatings.
Biomaterials. 1993. Vol.14, No.3, p.225-228.

62. H.Herman.
Plasma-sprayed coatings.
Scientific American. Sept. 1988, p.78-83.

63. M.Vardelle, A.Vardelle, P.Fauchais.
Spray parameters and particle behaviour relationships during plasma spraying.
Journal of Thermal Spray Technology. Mar. 1993. Vol.2, No.1, p.79.

64. M.Vardelle, A.Vardelle, Ph.Roumilhac, P.Fauchais.
Influence of the surrounding atmosphere under plasma spraying conditions.
Journal of Thermal Spraying Technology. Mar. 1993, Vol.21, No.1, p.79-92.

65. O.Knotek, U.Schnaut.
Numerical simulation of the influences of HVOF spraying parameters on coating properties
Proceedings of the 1993 National Thermal Spray Conference, Anheim, CA, 7-11 Junes 1993. p7.

66. K.V.Rao, D.A.Somerville, D.A.Lee.
Properties and characterisation of coatings made using JET KOTE thermal spray technique.
Advances in Thermal Spraying. Canadian Welding Inst. p.873

67. R.J.Thorpe, M.L.Thorpe.
High pressure HVOF - An update.
Proceedings of the 1993 National Thermal Spray Conference, Anheim, CA, 7-11 Junes 1993. p199.

68. H. Oguchi, K.Ishikawa, K.Seto, G.Eguchi.
Histological evaluation of Ti alloy sprayed with HA using a high velocity flame-spraying technique.
4th World Biomaterilas Congress. April 24-28 1992. p.510.

69. H.Oguchi, Kanichi Seto, Y.Nakajima, S.Ojima.
High Velocity Flame Spraying Technique for hydroxyapatite.
4th World Biomaterials Congress. April 24-28 1992. p.509.

70. H.Oguchi, K.Ishikawa, S.Ojima, Y.Hirayama, K.Seto, G.Eguchi.
Evaluation of a high-velocity flame-spraying technique for hydroxyapatite.
Biomaterials. 1992. Vol.13, No.7, p.471-476.

71. R.Terashima, Isato Furata, T.Ichijo, S.Ojima, Y.Hirayama, H.Rudelt.
Apatite Coating implant by high velocity flame spraying and experimental study of the characterisation of the flame spraying layer and histological reactions.
4th World Biomaterials Congress. April 24-28 1992. p.505.

72. J.G.C.Wolke, K.de Groot, T.G.Kraak, W.Herlaar, J.M.A.de Blieck-Hogervorst.
The characterisation of hydroxyapatite coatings sprayed with VPS, APS and DJ systems.
Proceedings of the Fourth Thermal Spray Conference, Pitsburgh, PA, USA, 4-10 May 1991, p.481.

73. S.Best, W.Bonefield.
Processing behaviour of hydroxyapatite powders with contrasting morphology.
Journal of Materials Science: Materials in Medicine. 1994. Vol.5, p.516-521.

74. E.F.Bres, G.Moebus, H.J.Kleebe, G.pourroy, J.Werkmann, G.Ehret.
High resolution electron microscopy study of amorphous calcium phosphate.
Journal of Crystal Growth. 1993. Vol.129, p.149-162.

75. N.Pleshko, A.Boskey, R.Mendelsohn.
Novel infrared spectroscopic method for the determination of crystallinity of hydroxyapatite minerals.
Journal of Biophysics. Oct. 1991. Vol.60, p.786-793.

76. S.R.Radin, P.Ducheyne.
The effect of Calcium phosphate ceramic composition and structure on invitro behaviour. II . Precipitation .
Journal Biomedical Materials Research. 1993. Vol.27, p.35-45.

77. M.Y.Shareef, P.F.Messer, R. van Noort.
Fabrication, characterisation and fracture study of a machinable hydroxyapatite ceramic.
Biomaterials. 1993. Vol.14, No.1, p.69-75.

78. S.Amrah-Bouali, C.Rey, A.Lebugle, D.Bernache.
Surface modification of hydroxyapatite ceramics in aqueous media.
Biomaterials. 1994. Vol.15, No.4. p.269.

79. G.Spoto, E.Ciliberto, G.C.Allen.
A new synthetic route to hydroxyapatite coatings.
Journal of Materials Chemistry. 1994. Vol.4, No.12, p.1849-1850.

80. E.F.Bres, G.Moebus, H.J.Kleebe, G.pourroy, J.Werkmann, G.Ehret.
High resolution electron microscopy study of amorphous calcium phosphate.
Journal of Crystal Growth. 1993. Vol.129, p.149-162.

81. H.Ji, P.M.Marquis.
Preparation and characterisation of Al2O3 reinforced hydroxyapatite.
Biomaterials. 1992. Vol.13, No.11, p.744-748.

82. H.Ji, P.M.Marquis.
Modification of hydroxyapatite during transmission electron microscopy.
Journal of Materials Science Letters. 1991. Vol.10, p.132-134.

83. P.Ducheyne, L.L.Hench, A.Kagan II.
Effect of hydroxyapatite impregnation on skeletal bonding of porous coated implants.
Journal Biomedical Materials Research. 1980. Vol.14, p.225-237.

84. D.H.Kohn, P.Ducheyne, J.M.Cuckler, A.C.Chu, S.Radin.
Fractographic analysis of failed porous and surface coated cobalt-chromium alloy total joint replacements.
Medical Progress through Technology. 1994. Vol.20, p.169-177.

85. S.Kokubun, O.Kashimoto, Y.Tanaka.
Histological verification of bone bonding and ingrowth into porous hydroxyapatite spinous process spacer for cervical laminoplasty.
Tohoku Journal of Experimental Medicine. 1994. Vol.173, p.337-344.

86. S.H.Maxian, J.P.Zawadsky, M.G.Dunn.
Effect of Ca/P coating resorption and surgical fit on hte bone/implant interface.
Journal of Biomedical Materials Research. 1994. Vol.28, p.1311-1319.

87. A.Piattelli, P.Trisi.
A light and laser scanning microscopy study of bone/hydroxyapatite-coated titanium implants interface: Histochemical evidence of unmineralized material in humans.
J. Biomedical Materials Research. 1994. Vol.28, p.529-536.

88. J.D. de Bruijin, C.A.van Blitterswijk, J.E.Davies.
Initial bone matrix formation at the hydroxyapatite interface in vivo.
Journal of biomedical materials research. 1995. Vol. 29, p.89-99.

89. P.Ducheyne, S.Radin, M.Heughebaert, J.C.Heughebaert.
Calcium phosphate ceramic coatings on porous titanium: effect of structure and composition on electrophoretic deposition, vacuum sintering and invtiro dissolution.
Biomaterials. May 1990. Vol.11, p.244-254.

90. K.A.Khur, R.Cheang.
Characterisation of plasma sprayed hydroxyapatite powders and coatings
Proceedings of the 1993 National Thermal Spray Conference, Anheim, CA, 7-11 Junes 1993. P.347

91. D.H.Kohn, P.Ducheyne, J.M.Cuckler, A.C.Chu, S.Radin.
Fractographic analysis of failed porous and surface coated cobalt-chromium alloy total joint replacements.
Medical Progress through Technology. 1994. Vol.20, p.169-177.

92. A.Ravaglioli, A.Krajewski, V.Biasini, R.Martinetti.
Interface between HA and mandibular human bone tissue.
Biomaterials. 1992. Vol.13, No.162-167.

93. J.C.G.Wolke, C.P.A.T.Klein, J.M.A. de Blieck-Hogervorst, K.de Groot.
The biological and physical properties of apatite coatings.
Proceedings of the 1993 National Thermal Spray Conference, Anheim, CA, 7-11 June 1993, p.619.

94. I.Abrahams, J.C.Knowles.
Effects of sintering conditions on hydroxyapatite for use in medical applications: A powder diffraction study.
Journal of Materials Chemistry. 1994. Vol.4, No.2, p.185-188.

95. O.Babushkin, T.Lindback, A.Holmgren, J.Li, L.Hermansson.
Thermal expansion of hot isostatically pressed hydroxyapatite
Journal of Materials Chemistry. 1994. Vol.4, No.3, p.413-415.

96. F.Brossa, A.Cigada, R.Chiesa, L.Paracchini, C.Consonni.
Post-deposition treatment effects on hydroxyapatite vacuum plasma sprayed coatings.
Journal of Materials Science: Materials in Medicine. 1994. Vol.5, p.855-857.

97. R.L.Salsbury.
Quality control of hydroxylapatite coatings: Purity and crystallinity determination.
Proceedings of the Fourth Thermal Spray Conference, Pitsburgh, PA, USA, 4-10 May 1991, p.471.

98. P.E.Wang, T.K.Chaki.
Sintering behaviour and mechanical properties of hydroxyapatite and dicalcium phosphate.
Journal of Materials Science: Materials in Medicine. 1993. Vol.4, p.150-158.

99. P.Bialuski, W.Kaczmar, J.Gladysz.
Residual Stress Measurements of Plasma Sprayed Coatings.
Advances in Thermal Spraying. Canadian Welding Institute. p837.

100. R.Elsing, O.Knoteck, U.Balting.
Calculation of residual thermal stress in plasma-sprayed coatings.
Surface and Coating Technology. 1990. Vol.43, No.44, p. 416-425.

101. S.C.Gill, T.W.Clyne.
The effect of substrate temperature and thickness on residual stresses in plasma sprayed deposits.
Proceedings of the 2nd European conference on advanced materials and processes - EUROMAT 91. 1992, Vol.1, p.289-297.

102. M.K.Hobbs, H.Reiter.
Residual Stresses in ZrO2-8%Y2O3 Plasma-sprayed Thermal barrier Coatings
Surface and coatings technology. 1988. Vol.34, p.33-42.

103. R.Knight, R.W.Smith
Residual stress in thermally Sprayed Coatings.
Proceedings of the 1993 National Thermal Spray Conference, Anheim, CA, 7-11 June 1993, p.607.

104. S.R.Brown, I.G.Turner, H.Reiter.
Residual stress measurement in thermal sprayed hydroxyapatite coatings.
Journal of Materials Science: Materials in Medicine. 1994. Vol.5, p.756-759.

105. Acoustic Emission.
Symposium of the American Society for Testing and Materials. 7-8 December 1971. ASTM Special Publication 505.

106. C.Colin, M.Boussuge, D.Valentin, G.Desplanches.
Mechanical testing of plasma-sprayed coatings of ceramics.
Journal of Materials Science. 1988. Vol.23, p.2121-2128

Appendix 1

Differential Interference Contrast (DIC).

This can be described as phase contrast in colour. It converts the grey levels caused by optical path differences into chromatic differences. In reflected light it converts not differences in height but angles into colour differences. In transmitted light it is the refractive index difference that introduces the colours.

Principle of DIC.

Differential interference (after Nomarski) makes use of a birefringent beam-splitter (see figure A1.(a)), where the incident beam is split into two; the ordinary ray and the extraordinary ray. The shear or separation between these two rays is less than the limit of resolution for the objective being used; therefore no double image should be orthoscopically observed. These two rays are polarised, the planes of vibration being perpendicular to each other. Figure A1.(b) shows the modified beam-splitter consisting of two wedge shaped uniaxial prisms, whose optic axes are at right angles to each other. The incident polarised beam is still split into two but this time the second prism causes the two rays to intersect at the objective back focal plane. The ordinary and extraordinary rays will when recombined have travelled different optical path distances. In order to equalise the intensities of the two rays, the wedge is placed at 45° to the incident polarised light direction. These two rays when combined in the primary image plane, although of different optical path difference (OPD), will not interfere because their directions of vibration are perpendicular to each other. In order to observe colours the analyser must be introduced.

When this technique is utilised in the reflected light microscope, the polars are crossed and the wedge is at 45°. The background colour will no longer be extinguished but exhibits a

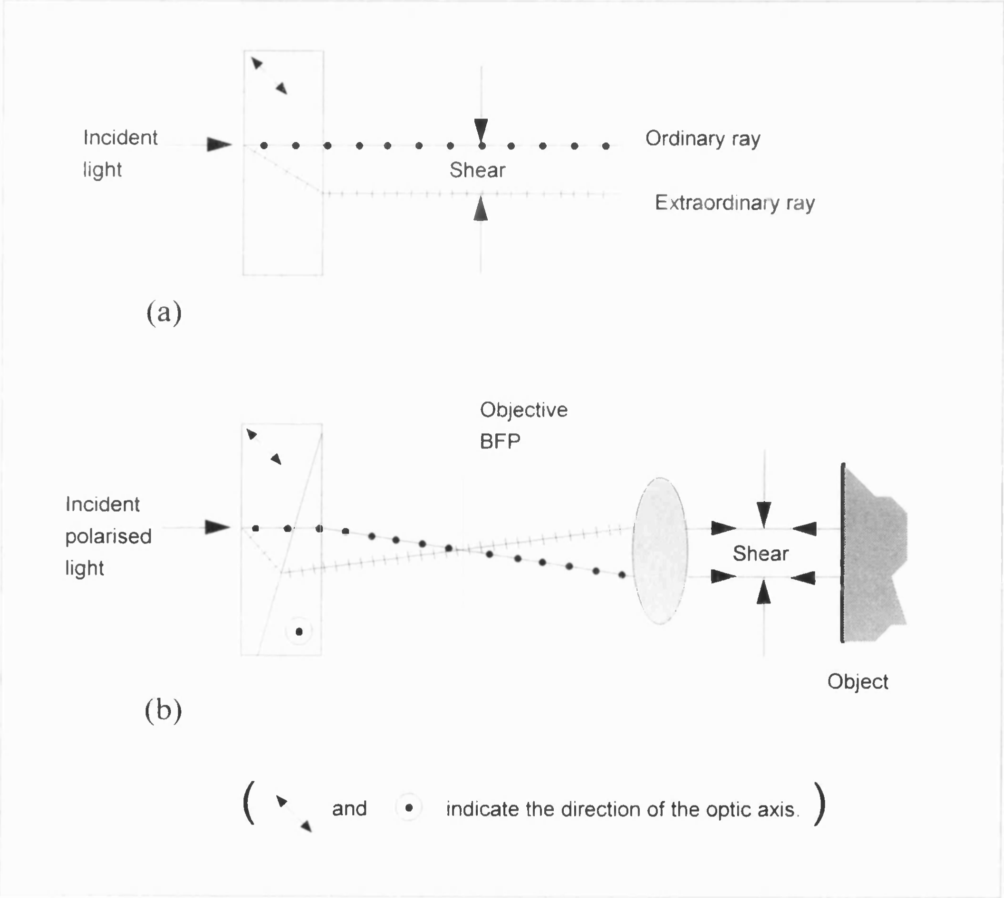

Figure A1. Creating the optical path difference. (a) Single beam-splitter and (b) modified beam-splitter.

colour relative to the OPD of the birefringent wedge, the background colour changing with every lateral movement of the wedge. In order to have one single colour across the whole field of view, the plane of fringe localisation must coincide with the objective back focal plane. Figure A2 show the reflected light microscope set up.

Observations in reflected light shows the background colour as indicative of the wedge position. Changes to this colour occur with every optical path difference. This being so the one will be able to detect slope or angle differences not, as is often portrayed, step difference.

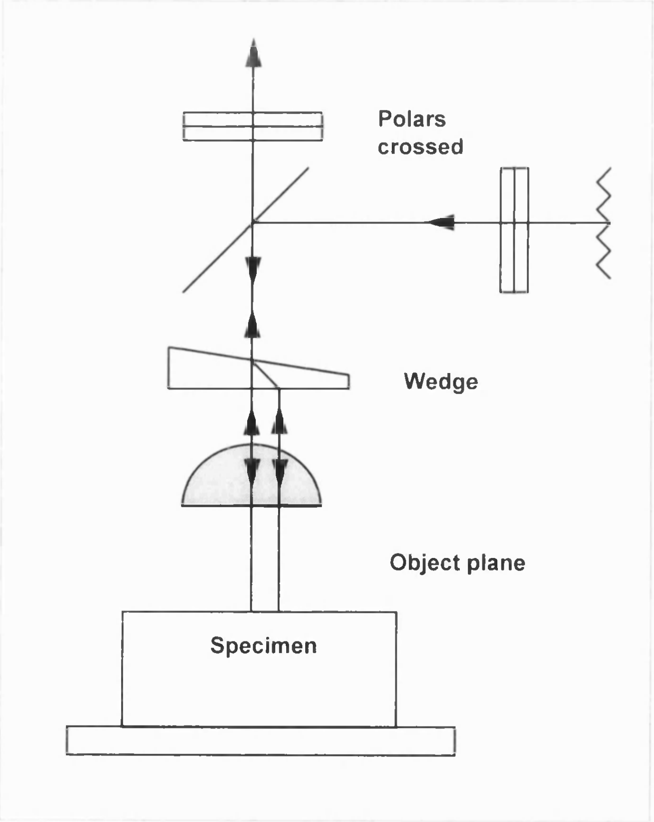

Figure A2. Reflected light Nomarski microscope.

Fortunately most surfaces being investigated by the materialographer constitute a series of curves. These curves are inevitable when mechanically preparing a two- or multiphase material, due to preferential polishing.

This qualitative study renders a sharply defined relief-like image with an excellent variable range contrast of zero-order to first-order interference colours. The interference relief-like images exhibit different colours with the degree of relief and will all change with a change in background colour.

Reference

Surface Preparation and Microscopy of Materials. Brian Bousfield.
Pub. J.Wiley, 1992. pg 282 - 285.